Double Parton Distributions in the Nucleon on the Lattice

Dissertation

zur Erlangung des Doktorgrades
der Naturwissenschaften (Dr. rer. nat.)
der Fakultät für Physik
der Universität Regensburg

vorgelegt von

Christian Zimmermann

aus Sulzbach-Rosenberg

im Jahr 2020

Promotionsgesuch eingereicht am: 12.08.2020
Die Arbeit wurde angeleitet von: Prof. Dr. Andreas Schäfer

Prüfungsausschuss:
Vorsitzender: Prof. Dr. Dieter Weiss
Erstgutachter: Prof. Dr. Andreas Schäfer
Zweitgutachter: Prof. Dr. Markus Diehl
weiterer Prüfer: Prof. Dr. Klaus Richter

Datum Promotionskolloquium: 28.10.2020

Dissertation advisor: Prof. Dr. Andreas Schäfer **Christian Zimmermann**

Double Parton Distributions in the Nucleon on the Lattice

Abstract

Modern scattering experiments involving hadrons are sensitive to parton correlations, which can be parameterized by double parton distributions (DPDs). These are non-perturbative objects, which are largely unknown in theory, detailed experimental access is quite challenging. This thesis provides a first non-perturbative study from first principles of light quark DPDs in the nucleon in the framework of lattice QCD. First of all, a brief review of Quantum Chromodynamics (QCD) is given, followed by definitions and relations regarding double parton distributions. After that, the evaluation of hadronic matrix elements in the framework of lattice QCD is explained. DPDs are related to two-current matrix elements, which can be calculated on the lattice by evaluating four-point functions. We describe the corresponding Wick contractions for the case of the proton and give details on the techniques being used for their simulation. These are performed on 990 configurations of the CLS ensemble H102 with $\beta = 3.4$, which corresponds to a lattice spacing of 0.0856 fm, and pseudoscalar masses $m_\pi = 355$ MeV and $m_K = 441$ MeV. The data is converted to the $\overline{\text{MS}}$ scheme at a renormalization scale of $\mu = 2$ GeV. Results of the bare Wick contractions, as well as physical combinations for specific flavor, are presented for the two-current matrix elements $\langle V^0 V^0 \rangle$ and $\langle A^0 A^0 \rangle$, where also lattice artifacts are explored. The data of two-current matrix elements is used for the determination of twist-2 functions, which are related to the first DPD Mellin moment for a specific quark polarization. Consistence of the results with the DPD number sum rule is verified. The dependence on the quark flavor and polarization is analyzed for the twist-2 functions, as well as for the extracted DPD Mellin moments. A further aspect to be investigated is the validity of factorization hypotheses which are often assumed in order to decompose DPDs in terms of single parton distribution functions (PDFs). This is e.g. the case in the well known pocket formula of double parton scattering. To this end, we derive factorized expressions for hadronic matrix elements of two operators, where we obtain convolutions of proton form factors, which can be obtained from lattice calculations. We implement two versions, the corresponding results are compared to those obtained from two-current matrix elements.

Contents

1 Introduction

Since it has become clear in the middle of the last century that hadrons are composed of more elementary particles, the study of the hadronic structure has evolved to one of the most diverse subjects in modern particle physics. Nowadays we know that the constituents of a hadron are quarks and gluons, which are elementary particles treated by the standard model. The theory describing the dynamics and interactions between quarks and gluons is known as Quantum Chromodynamics (QCD). Hadrons can be thought of being bound states of the QCD Hamiltonian. However, the exact internal structure in terms of quarks and gluons remains unknown. While we have gained a quite reasonable understanding of some aspects, like quark and gluon distributions, there are still many open questions.
Among others, this concerns e.g. the orbital angular momentum of the hadron's constituents and subsequently their contribution to the total hadron spin (proton spin puzzle) [1]. Related to this subject is the internal hadronic structure in the transverse plane in collisions with other particles. Experimental insight on these subjects should be provided by the future Electron Ion Collider (EIC) [2].
The subject being addressed by this work is the question how partons are correlated with each other in a hadron and how scattering processes are affected by these correlations. A reasonable understanding of this is necessary for the interpretation of experiments in order to test the Standard Model (SM) or find physics beyond it, as we explain in the following.

1.1 SM background at the LHC

Thanks to their relatively large mass to charge ratio, protons can be accelerated to highest energies in circular accelerators in order to create high-energy collisions. In this context they have been used e.g. in experiments at Tevatron and nowadays are collided at the Relativistic Heavy Ion Collider (RHIC) and the Large Hadron Collider (LHC).
Therefore, hadrons play also an essential role in experiments where the validity of the standard model is explored. A prominent example is the LHC, where proton-proton collisions with energies up to 13 TeV are used within the four experiments ATLAS, CMS, ALICE and LHCb. Their purpose is e.g. the investigation of standard model related subjects like the experimental proof of the existence of the Higgs boson, which has been achieved in 2012 [3, 4]. Further tasks are given by the search for physics beyond the Standard Model (BSM) like dark matter physics.
BSM-particles, which are hoped to be detected in LHC experiments, have to be very

massive, otherwise they would have been found already. They decay into particles having much lighter masses, which leads to a very large decay phase space. However, this is also characteristic for the phase space accessible by double parton scattering (DPS) events, an interaction of the two colliding hadrons where two partons of each hadron take part. This is part of the SM background.
Among others, the production of W^+W^- and ZZ are channels in which the Higgs boson has been detected in ATLAS and CMS. In both channels there may be background contributions by DPS events, e.g. double Drell-Yan (DDY) processes. Within a simplified and unrealistic model of the DDY process it was pointed out in the past that DDY contributions might be sufficient to describe the experimental data of W^+W^- and ZZ production without taking into account contributions by the Higgs particle [5]. To definitely exclude such scenarios, investigations on DPS and their contribution to the SM background in LHC experiments are crucial.

1.2 Double parton scattering

The simplest parton model description of hadron-hadron interactions is given by assuming that there is one hard parton-parton interaction, i.e. one parton of each hadron is involved. In the following, this type of interactions is referred to as single parton scattering (SPS). The corresponding cross section directly depends on the probability of finding a parton with a given longitudinal momentum, which is described by a parton distribution function. An example is the Drell-Yan (DY) process, where a quark from each of two colliding hadrons scatters, resulting in the production of a lepton-antilepton pair ($pp \to l\bar{l} + X$) [6]. The cross section depends on the probability of finding a quark with a given fraction x of the hadron's momentum. For a given parton a with a certain polarization this is parameterized by the corresponding parton distribution functions (PDFs) $f_a(x)$. Depending on the hadron, they are more or less known from experiment and lattice simulations [7, 8].
With decreasing momentum fraction x the parton density in a hadron increases. As a consequence interactions with two partons of each hadron become more probable. In particular, this is relevant at energy scales reached at the LHC. These types of interaction are known as double parton scattering (DPS), an example are the aforementioned DDY processes. DPS was established in pp collisions [9] and in $\bar{p}p$ collisions [10–13] a few decades ago, recent experimental observations of DPS can be found in [14–28].
However, detailed determinations of DPS contributions in experiment are challenging, since there is typically a large SPS background. A relatively clean process in this context has been found to be same-sign W-pair production, which is therefore a promising channel when looking for experimental DPS data [29–31].
We anticipate here the DPS cross section in terms of double parton distributions (DPDs) $F(x_1, x_2, \boldsymbol{y})$ and the parton level cross sections σ_i, which can be written as:

$$\frac{\mathrm{d}\sigma_{\mathrm{DPS}}}{\mathrm{d}x_1\mathrm{d}\bar{x}_1\mathrm{d}x_2\mathrm{d}\bar{x}_2} \propto \sum \int \mathrm{d}^2\boldsymbol{y}\ \sigma_1(x_1\bar{x}_1 s)\ \sigma_2(x_2\bar{x}_2 s)\ F(x_i, \boldsymbol{y})\ F(\bar{x}_i, \boldsymbol{y})\ , \tag{1.1}$$

where the sum represents contributions from all possible quark flavors, polarizations, etc. The DPD parameterizes the probability of finding two correlated quarks at a transverse distance $\boldsymbol{y}$ and longitudinal momentum fractions x_1 and x_2. More detailed expressions are given in chapter 2. In order to give an estimate for the size of the DPS contribution, this is often approximated by neglecting correlations in longitudinal dynamics, quark flavors and polarizations, and assuming a factorization of DPDs of the following form:

$$F(x_1, x_2, \boldsymbol{y}) = f(x_1)\ f(x_2)\ T(\boldsymbol{y})\ , \tag{1.2}$$

where $f(x)$ are PDFs and $T(\boldsymbol{y})$ is a function parameterizing the dependence on the transverse quark distance. As a result one obtains a relation often referred to as the pocket formula [32]

$$\begin{aligned} \frac{\mathrm{d}\sigma_{\mathrm{DPS}}}{\mathrm{d}x_1\mathrm{d}\bar{x}_1\mathrm{d}x_2\mathrm{d}\bar{x}_2} &= \frac{1}{C}\frac{\sigma_{1,\mathrm{SPS}}(x_1,\bar{x}_1)\ \sigma_{2,\mathrm{SPS}}(x_2,\bar{x}_2)}{\sigma_{\mathrm{eff}}}\ , \\ \sigma_{\mathrm{eff}} &:= \left[\int \mathrm{d}^2\boldsymbol{y}\,(T(\boldsymbol{y}))^2\right]^{-1}\ , \end{aligned} \tag{1.3}$$

where $\sigma_{i,\mathrm{SPS}}$ denote the SPS cross sections and $C = 2$ if the two scattering partons are the same, otherwise $C = 1$. The effective cross section σ_{eff} only contains the transverse correlation of the two partons and in the simplest case is assumed to be a universal constant. Estimates of σ_{eff} are given by experimental DPS studies in [9–28], where values between 1 mb and 28 mb have been found.
According to (1.1) DPS processes are sensitive to parton correlations parameterized by the DPDs. Like other kinds of parton distributions, DPDs are non-perturbative objects. They are largely unknown. In the past there have been studies on parton correlations employing several quark models [33–39], recently also for the pion [40–43].
A non-perturbative method for calculating quantities related to DPDs from first principles is provided by Monte Carlo simulations of QCD on a Euclidean lattice. The required quark-quark correlations are obtained from evaluating local two-current matrix elements, which are directly related to Mellin moments in x_i of DPDs:

$$M^{(n,m)}(\boldsymbol{y}) = \int \mathrm{d}x_1\ x_1^{n-1} \int \mathrm{d}x_2\ x_2^{m-1}\ F(x_1, x_2, \boldsymbol{y})\ . \tag{1.4}$$

The corresponding calculations have been worked out already in the past for the pion [44–46]

1.3 Outline

The purpose of this work is to study DPDs for the nucleon (in particular the proton) within the lattice QCD (LQCD) framework. When calculating proton matrix elements and subsequently determining the first DPD Mellin moment, we want to implement several factorization assumptions in order to test the validity of simplifications being

employed e.g. by the pocket formula (1.3). Parts of the results presented in this work have already been published in [47].
This thesis is organized as follows: In chapter 2 we discuss subjects concerning the structure of a hadron. First of all we consider the hadronic wave function in terms of valence quarks and its symmetries and constraints w.r.t. space, flavor, spin and color. Furthermore, we give a brief review of QCD, the fundamental theory of quark-gluon-interactions and hadron physics. After that, we introduce the factorization concept as generic description of hadrons during high-energy processes, where we introduce several kinds of parton distribution functions and discuss their meaning in certain physical contexts. Therein we also define DPDs and describe their role in the description of double hard interactions.
In chapter 3 we continue with introducing LQCD as a non-perturbative method to evaluate hadronic matrix elements, from which any kind of parton distribution functions can be defined. We describe the path integral formalism and the corresponding evaluation in discrete and finite Euclidean spacetime by employing Monte Carlo integration, a procedure, which is known as LQCD.
The matrix elements related to DPDs involve two currents and are introduced in chapter 4. After discussing their properties and decompositions in terms of Wick contractions, we explain in detail the methods and techniques being used for the calculation of each Wick contraction in LQCD. We also list some details of the employed CLS gauge ensembles and the general setup of lattice parameters. We conclude this chapter with presenting the data for specific current insertions.
We continue in chapter 5 with explaining the relations between Mellin moments of DPDs and two-current matrix elements. The extraction of the moments includes a Fourier transformation. Because of the finite hadron momenta we have to choose some model to be able to perform the integral. We motivate our choice of the model and describe the corresponding fits on the lattice data. Finally, we present the results for the moments and check whether DPD number sum rules are fulfilled.
Chapter 6 is dedicated to exploring the validity of naive factorization assumptions which are used e.g. in the aforementioned pocket formula. We establish two approaches of factorizing quantities involving two-current matrix elements. Both include a convolution of nucleon form factors, which are calculated on the same lattice as the two-current matrix elements.
This thesis is summarized in chapter 7, where we give some concluding remarks and perspectives for future research.

2 Hadron structure and DPDs

As already mentioned, describing the internal structure of hadrons is highly non-trivial. Within this chapter we shall give brief introductions to various common concepts that have been established in order to describe hadron properties. A first description of the hadronic wave function in terms of (valence) quarks is provided by the quark model, which is suitable for describing certain symmetries. We shall introduce Quantum Chromodynamics (QCD) to be able to describe the dynamics and interactions of the hadron's constituents. The corresponding discussions can be found in standard literature [48–50]. In a scattering process hadrons can be treated as a bunch of quasi-free particles (partons). This assumption was first use by Bjorken and Feynman in order to explain deep inelastic scattering (DIS) and is known as parton model. In this context we shall briefly explain the concepts going into the definition and interpretation of parton distributions. A special treatment is given to double parton distributions (DPDs), which are used in the description of double parton scattering.

2.1 Quarks and hadron symmetries

The standard model has six quark flavors and the corresponding antiquarks. They are spin-1/2 particles, i.e. fermions, and color charged forming a $SU(3)_{\text{color}}$ symmetric triplet, i.e. they couple to the strong force mediated by gluons. Together with the leptons they are grouped into three families, where the first family contains the lightest particles and the third the heaviest[1].
The quarks of the first family, u (up, $m_u \approx 2.2$ MeV) and d (down, $m_d \approx 4.7$ MeV), have very small masses compared to the hadronic mass scale, which is about a few hundred MeV. In analogy to spin-1/2 states one identifies the isospin doublet (u, d) with the fundamental representation of the $SU(2)$ group (often called $SU(2)_{\text{flavor}}$ to distinguish from other symmetries of the same group). Taking into account the s (strange, $m_s \approx$ 95 MeV) quark, this symmetry can be extended to $SU(3)_{\text{flavor}}$, which is less exact due to the heavier mass of the strange quark.
It seems natural to obtain a rough description of hadronic states by considering valance quarks coupled to multiplets w.r.t. spin, flavor and color. Since in nature one only observes color neutral states, i.e. color singlets (see discussion in section 2.2), hadrons have to be built from the combinations $q\bar{q}$ (mesons) and qqq (baryons), where the latter has to be totally antisymmetric in color.
Considering $SU(2)$, which is the symmetry group of spin and flavor, and taking into

[1] In this statement we neglect the neutrinos, where each one has a mass smaller than 2 eV.

account only u and d quarks, the mesons are decomposed in following multiplets:

$$2 \otimes \bar{2} = 3 \oplus 1 \ , \tag{2.1}$$

i.e. a triplet with (iso)spin 1 and a singlet with (iso)spin 0. Examples for the isospin-triplet are the pions (spin 0) and rho-mesons (spin 1). The flavor symmetry leads to very similar properties of the particles belonging to the same multiplet, e.g. their masses. Discrepancies can be explained with different masses and electric charges of the quarks. The breaking of the symmetry becomes more relevant if we consider $SU(3)_{\text{flavor}}$, where the mesons decompose into an octet and a singlet:

$$3 \otimes \bar{3} = 8 \oplus 1 \ , \tag{2.2}$$

where the mass spectrum of the octet strongly depends on strangeness, i.e. the number of strange quarks in the leading Fock state of the corresponding particles. Notice that the $SU(2)_{\text{flavor}}$-triplet is contained in the octet. Since the flavor symmetry is not exact, the corresponding singlet state turns out to mix with an octet state having the same quantum numbers, which results in the spin-0 mesons η and η'.
For baryons the situation is more involved. The total wave function has the structure

$$|\text{baryon}\rangle = |\text{space}\rangle \otimes |\text{flavor}\rangle \otimes |\text{spin}\rangle \otimes |\text{color}\rangle \ , \tag{2.3}$$

and has to be totally antisymmetric against permutation of quarks. In the ground state, where there is no orbital angular momentum, $|\text{space}\rangle$ has to be symmetric (s-waves) and $|\text{color}\rangle$ must be antisymmetric in order to obtain a color singlet. This implies that only symmetric combinations of $|\text{flavor}\rangle \otimes |\text{spin}\rangle$ are present in nature. The spins are coupled to spin-1/2 (mixed symmetry) or spin-3/2 (symmetric) states. Again considering the symmetry groups $SU(2)$ (spin, flavor) and/or $SU(3)_{\text{flavor}}$ we obtain:

$$\begin{aligned} 2 \otimes 2 \otimes 2 &= 4_{\text{S}} \oplus 2_{\text{M}} \oplus 2_{\text{M}} \ , \\ 3 \otimes 3 \otimes 3 &= 10_{\text{S}} \oplus 8_{\text{M}} \oplus 8_{\text{M}} \oplus 1_{\text{A}} \ , \end{aligned} \tag{2.4}$$

where the subscripts S (symmetric), M (mixed) and A (antisymmetric) label the symmetry of the corresponding states. Since the $SU(3)$-singlet is antisymmetric and there is no antisymmetric spin wave function, it does not occur in nature.
Nucleons, i.e. the proton and the neutron, are spin-1/2 particles, hence their flavor part can be written in terms of $SU(2)$-doublet ($I = 1/2$) or $SU(3)$-octet states, such that the overall spin-flavor wave function is symmetric. Notice that within this thesis we do not consider effects caused by electromagnetism and always assume that u and d quarks have the same mass, i.e. we consider an exact flavor symmetry of the group $SU(2)_{\text{flavor}}$. Hence, the results obtained for the proton can be mapped onto the neutron case by suitable symmetry operations. Omitting permutations of the quark spins, the proton

wave function can be written as:

$$|p^{\uparrow}\rangle = \frac{1}{\sqrt{6}}\left[|u^{\uparrow}u^{\downarrow}d^{\uparrow}\rangle + |u^{\downarrow}u^{\uparrow}d^{\uparrow}\rangle - 2\,|u^{\uparrow}u^{\uparrow}d^{\downarrow}\rangle\right] \ . \tag{2.5}$$

The description given so far takes into account only the simplest Fock state in each case and does neither give any information about spatial distributions or correlations of quarks in a hadron nor about its internal dynamics. Before we continue with more sophisticated descriptions of hadrons, it is necessary to discuss the dynamics and interactions of the hadron's constituents, i.e. quarks and gluons, which we do in the following section.

2.2 Quantum chromodynamics

In the following, we want to give a review of the fundamental theory of hadron physics, which is known as Quantum Chromodynamics (QCD). It provides a description of the dynamics and interactions of color charged particles, in particular the hadron's constituents, i.e. quarks and gluons. Like for other gauge theories one considers invariance of the physical system under a certain kind of local gauge transformations. As mentioned in the previous section, the gauge group of QCD is $SU(3)$, which is a non-Abelian group.
We start with considering free Dirac fermions with mass m, which are described by the Dirac equation:

$$(i\partial\!\!\!/ - m)\,\psi(x) = 0 \ , \tag{2.6}$$

with $\partial\!\!\!/ = \gamma^{\mu}\partial_{\mu}$. The Dirac matrices γ^{μ} are elements of the Clifford algebra $\{\gamma^{\mu}, \gamma^{\mu}\} = 2g^{\mu\nu}$. The solutions ψ are plane waves

$$\psi(x) = \begin{cases} u^{\lambda}(p)\ e^{-ixp} \\ v^{\lambda}(p)\ e^{+ixp} \end{cases} \ , \tag{2.7}$$

where u and v are Dirac spinors, which transform in a four dimensional representation of the Lorentz group. Therefore, the description is already relativistic. There are two types of spinor solutions, which are denoted by $u^{\lambda}(p)$ (particles) and $v^{\lambda}(p)$ (antiparticles), where λ labels the quark helicity. These solutions fulfill the completeness relations:

$$\begin{aligned} \sum_{\lambda} u^{\lambda}\bar{u}^{\lambda} &= p\!\!\!/ + m \ , \\ \sum_{\lambda} v^{\lambda}\bar{v}^{\lambda} &= p\!\!\!/ - m \ , \end{aligned} \tag{2.8}$$

where $\bar{\cdot}$ denotes Dirac conjugation, which is defined by $\bar{\psi} = \psi^{\dagger}\gamma_0$ for a given Dirac spinor ψ, such that the product $\bar{\psi}\psi$ is a Lorentz scalar.

The Dirac field is quantized by imposing anti-commutation relations, which are usually supposed to be fulfilled at equal time:

$$\begin{aligned} \left\{\hat{\psi}(x), \hat{\psi}^\dagger(y)\right\}\Big|_{x^0=y^0} &= \delta^{(3)}(\vec{x}-\vec{y}) \ , \\ \left\{\hat{\psi}^\dagger(x), \hat{\psi}^\dagger(y)\right\}\Big|_{x^0=y^0} &= \left\{\hat{\psi}(x), \hat{\psi}(y)\right\}\Big|_{x^0=y^0} = 0 \ . \end{aligned} \tag{2.9}$$

The operator $\hat{\psi}$ is understood to annihilate a particle and create an antiparticle, whereas $\hat{\bar{\psi}}$ creates a particle and annihilates an antiparticle. Throughout this work, we consider quarks, the corresponding operators are denoted by q and $\bar{q}$. Within the parton model, which will be introduced in the following section, the fields are considered to be quantized in an alternative way. The anti-commutation relations (2.9) are modified such that they are fulfilled at equal light-cone time $x^+ = (x^0 + x^3)/\sqrt{2} = y^+ = (y^0 + y^3)/\sqrt{2}$. This is known as light-cone or light-front quantization [51].
The Lagrangian being connected to (2.6) via the Euler-Lagrange equation reads:

$$\mathcal{L}_{\text{free}}(x) = \bar{\psi}(x)\,(i\partial\!\!\!/ - m)\,\psi(x) \ . \tag{2.10}$$

As mentioned before, we require the theory to be invariant under local $SU(3)$ transformations. The spinor fields ψ are considered to transform in the three-dimensional fundamental representation of $SU(3)$, i.e. :

$$\begin{aligned} \psi(x) &\to \Omega(x)\ \psi(x) \ , \\ \bar{\psi}(x) &\to \bar{\psi}(x)\ \Omega^\dagger(x) \ , \end{aligned} \tag{2.11}$$

where we define the local gauge transformation $\Omega(x)$ as:

$$\Omega(x) = e^{i\theta^j(x)t^j} \ , \tag{2.12}$$

with eight position dependent parameters $\theta^j(x)$ and the generators t^j of $SU(3)$, which obey:

$$\left[t^j, t^k\right] = i f^{jkl} t^l \ . \tag{2.13}$$

Usually one chooses the Gell-Mann basis for t^j. The constants f^{jkl} are called structure constants of $SU(3)$, which are totally anti-symmetric under permutations of their indices.
While the mass term in (2.10) is trivially invariant under $\Omega(x)$, we obtain an additional term $-t^j \partial\!\!\!/ \theta_j$ arising from the derivative on the local transformation. To restore gauge invariance we have to extend the derivative in a gauge covariant manner:

$$D_\mu(x) := \partial_\mu - i g_0 A^j_\mu(x) t^j \ , \tag{2.14}$$

where we have introduced a second kind of fields, the gauge fields A^j_μ called gluons. They transform in the adjoint representation of $SU(3)$ and are by construction of dimension $length^{-1}$:

$$t^j A^j_\mu(x) \to \Omega(x) \left(t^j A^j_\mu(x) + i g_0^{-1} \partial_\mu \right) \Omega^\dagger(x). \tag{2.15}$$

g_0 is the (bare) coupling constant. A consequence of the replacement by the covariant derivative (2.14) in (2.10) is the interaction of the fermions with the gauge fields, which is tuned by the coupling constant g_0.
To complete the theory, we also need to describe the free propagation of the gauge fields themselves, i.e. we have to construct a Lorentz and gauge invariant expression of dimension $length^4$ only built out of these fields. A suitable quantity is:

$$\mathcal{L}_\mathrm{G}(x) = -\frac{1}{4} F^j_{\mu\nu}(x) F^{j\mu\nu}(x) \ , \tag{2.16}$$

with the field strength tensor

$$F^j_{\mu\nu}(x) := \partial_\mu A^j_\nu(x) - \partial_\nu A^j_\mu(x) + g_0 f^{jkl} A^k_\mu(x) A^l_\nu(x) \ . \tag{2.17}$$

A fundamental difference to the electromagnetic field strength is that the last term, which arises from the non-Abelian property of $SU(3)$, includes self-interaction between the gluons. Adding (2.16) to the gauge covariant form of (2.10) and taking into account n_f quark flavors labeled by the index f, we finally obtain the Lagrangian of QCD:

$$\mathcal{L}_\mathrm{QCD}(x) = \sum_f \bar{\psi}^f(x) \left(i \not{D} - m_f \right) \psi^f(x) - \frac{1}{4} F^{j\mu\nu}(x) F^j_{\mu\nu}(x) \ . \tag{2.18}$$

Performing perturbative calculations to a given order of $\alpha_s = g_0^2/(4\pi)$, one will encounter divergences resulting from loop integrals, which have to be regularized in a suitable scheme. The essence is to isolate the divergent terms, which can be tuned by a regulator, and re-define the constants of the theory, e.g. the quark masses m_q or the coupling g_0, such that everything remains finite, once the regulator is removed. This is known as renormalization. Notice that this introduces a renormalization scale μ the constants subsequently depend on.
In the case of QCD (and similar for all non-Abelian gauge theories) one finds that the renormalized coupling $\alpha_s(\mu)$ reads at 1-loop order:

$$\frac{g_0^2}{4\pi} = \alpha_s \xrightarrow{\text{Renormalization}} \alpha_s(\mu) = \frac{2\pi}{\left(11 - \frac{2}{3} n_f\right) \log\left(\Lambda^{-1}_\mathrm{QCD} \mu\right)} \ , \tag{2.19}$$

with the mass scale Λ_QCD, where the coupling diverges. This is often referred to as the soft energy scale. Quantities involving this region of strong coupling cannot be calculated perturbatively. A non-perturbative method, LQCD, is described in chapter 3. In the strong coupling limit one can derive a linear potential between color charged parti-

cles, which is responsible for the phenomenon of confinement, i.e. color charged particles are always bound in a color singlet. On the other hand, in the limit of infinitely large energies or momentum transfers the coupling goes to zero. Therefore, color charged particles are asymptotically free at large scales, such that hard scattering processes, e.g. between quarks, are accessible by perturbation theory.

2.3 Parton correlation functions

Within the parton model, hadrons are treated as a cluster of quasi-free particles called partons. A hadronic scattering process is then described by an interaction of one or more partons with the scattering counter part. Within this scheme the process is separated into a hard process at parton level and a soft part concerning the hadronic structure. The hard process involves a high energy scale, which according to (2.19) allows a perturbative treatment.
In the following, we focus on the soft part, which is described by so-called parton correlation functions. These are non-perturbative objects and describe the appearance of partons with certain properties in a specific hadron. Throughout this work, we consider (anti)quarks. Gluons can be treated in an analogue way. For reviews on subjects regarding parton correlation functions and various types of parton distributions, as well as their interpretation, see [52, 53].

2.3.1 Definition

Within a typical scattering experiment hadrons are accelerated to very high energies $\sim Q$, which are much larger than the hadronic mass scale Λ, i.e. $\Lambda \ll Q$. Therefore, the hadron's four-momentum may be considered as almost light-like. Assuming that the hadron moves in 3-direction, we can express the momentum in light-cone coordinates $p = (p^+, p^-, \boldsymbol{p})$ (see also (A.13) for the notation), where

$$p^+ \sim Q \ , \qquad p^- \sim \frac{\Lambda^2}{Q} \ , \qquad \boldsymbol{p} = \boldsymbol{0} \ . \tag{2.20}$$

$\boldsymbol{p}$ denotes the transverse vector components $\boldsymbol{p} = (p^1, p^2)$. In this scenario a hadron turns into a flat bunch of partons due to Lorentz contraction. Time dilatation causes the system to be nearly frozen, i.e. the partons can be seen as quasi-free particles with momentum $k = (k^+, k^-, \boldsymbol{k})$, with $k^+ \sim p^+$ and $k^- \sim p^-$. k^+ can be expressed by the longitudinal momentum fraction x, which indicates how much of the hadron's momentum is carried by the parton:

$$k^+ = x p^+ \ . \tag{2.21}$$

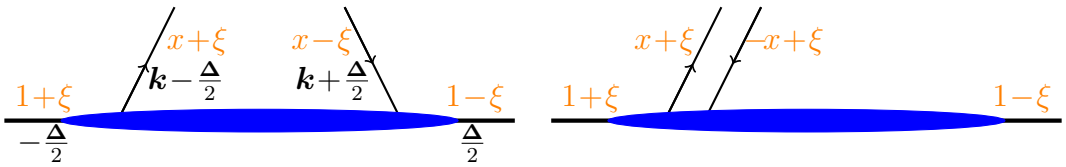

Figure 2.1: Diagrammatic illustration of a parton correlation function. The blue blob represents the hadron from which the quarks emerge. For the quarks and the hadron we indicate the corresponding momenta, where the longitudinal momenta are given in terms of the fraction w.r.t. p^+. The l.h.s. shows the situation if $x+\xi$, as well as $x-\xi$, is positive. The change of sign of one fraction turns the corresponding quark in the wave function to an antiquark in its complex conjugate and vice versa. For $x-\xi<0$ this is shown on the r.h.s. .

If the spectator partons are considered to be on mass shell, momentum conservation yields the constraint $0<x<1$. The transverse parton momenta are considered to be small, at most at the hadronic mass scale. In total we have the relations:

$$k^- \sim \frac{\Lambda^2}{Q}\,, \qquad |\boldsymbol{k}| \sim \Lambda\,. \tag{2.22}$$

With this setup we define the parton correlation function

$$\begin{aligned}\Phi_{\alpha\beta cd}(x,\boldsymbol{k},\xi,\boldsymbol{\Delta}) := \int \frac{\mathrm{d}^2\boldsymbol{z}\;\mathrm{d}z^-}{(2\pi)^3} e^{ixp^+z^-} e^{-i\boldsymbol{k}\boldsymbol{z}} \\ \times \langle p+\Delta/2|\,\bar{q}_{\alpha c}(-z/2) q_{\beta d}(z/2)\,|p-\Delta/2\rangle\big|_{z^+=0}\,.\end{aligned} \tag{2.23}$$

The initial and the final hadron state are parameterized symmetrically in terms of the momentum variables p and Δ. The two quark operators in (2.23), which are considered to be light-cone quantized, are evaluated at $z^+=0$, i.e. at equal light-cone time. This is equivalent to integrating over $-$-components of the quark momenta, such that the quarks created or annihilated by q and $\bar{q}$ are not on mass shell. Furthermore, the quark operators anti-commute, which can be seen as an implementation of the quasi-free partons considered within the parton model.
By considering the Fourier expansion of the light-cone quantized quark field q, we see that depending on the sign of the $+$-momentum it removes a quark from the hadron wave function or creates an antiquark in its complex conjugate. An analogue behavior is found for $\bar{q}$. If all quark $+$-momenta are positive, this can be interpreted as the emission of a quark with momentum $k-\Delta/2$ and the absorption of a quark with momentum $k+\Delta/2$. A changing sign in the $+$-momentum turns the quark in the wave function into an antiquark in the complex conjugate wave function and vice versa. This is depicted in Figure 2.1. The dependence on the longitudinal momentum change is parameterized

in terms of the fraction ξ w.r.t. p^+:

$$\xi = -\frac{\Delta^+}{2p^+} \ . \tag{2.24}$$

There are two kinds of processes which can be described by parton correlation functions. The first one is called (semi-)inclusive, which means that only a part of the scattering products is actually detected. The cross section involves matrix elements $\langle X|\, q\, |p\rangle$ describing the emission of a quark leaving a set of spectator partons which are not resolved in the measurement. They have to be included in the squared amplitude by a sum over all possible final states. Roughly sketched, the hadronic part of the squared amplitude has then the form $\sum_X \langle p|\, \bar{q}\, |X\rangle \langle X|\, q\, |p\rangle$. This is what we get if we insert a complete set of states in the matrix element appearing in (2.23) for $\Delta = 0$. On the other hand we consider exclusive processes with only the scattered hadron in the final state. In this case the amplitude involves hadronic matrix elements of the form $\langle p|\, \mathrm{T}\bar{q}q\, |p'\rangle$, where T denotes time ordering. The matrix element describes the emission of a quark and the subsequent absorption leading to a total momentum change $\Delta = p - p'$. It can be shown that the time ordering may be dropped if $\bar{q}$ and q are evaluated at equal light-cone time [54]. Again, the matrix element can be identified with (2.23).
The concept of quark correlation functions can be extended to n quarks, see [55]. With the additional average quark momenta k_i this introduces further degrees of freedom given by the differences r_i between the quark momenta. Within the chosen frame the introduced parton momenta scale similarly to (2.22):

$$\begin{aligned} p^+ \sim \ & k_i^+ \sim \ r_i^+ \sim \ Q \ , \\ p^- \sim \ & k_i^- \sim \ r_i^- \sim \ \frac{\Lambda^2}{Q} \\ & \boldsymbol{k}_i \sim \ \boldsymbol{r}_i \sim \ \Lambda \ . \end{aligned} \tag{2.25}$$

Since we shall only consider such correlation functions to represent the squared amplitude in the cross section, it is sufficient to consider $\Delta = 0$. The n-parton correlation function for quarks can be defined as:

$$\begin{aligned} &\Phi_{\alpha_i\beta_i c_i d_i}(x_i, \boldsymbol{k}_i, \zeta_i, \boldsymbol{r}_i) = (2p^+)^{n-1} \\ &\quad \times \left[\prod_i \int \frac{\mathrm{d}^2\boldsymbol{z}_i \ \mathrm{d}z_i^-}{(2\pi)^3} \mathrm{d}^2\boldsymbol{y}_i \ \mathrm{d}y_i^- \ e^{ix_i p^+ z_i^-} \ e^{-i\boldsymbol{k}_i \boldsymbol{z}_i} \ e^{-i\zeta_i p^+ y_i^-} \ e^{i\boldsymbol{r}_i \boldsymbol{y}_i}\right] \delta(y_n^-)\delta^{(2)}(\boldsymbol{y}_n) \\ &\quad \times \langle p|\, \prod_i \bar{q}_{i,c_i\alpha_i}(y_i - z_i/2) \ q_{i,d_i\beta_i}(y_i + z_i/2)\, |p\rangle \Big|_{\substack{z_i^+=0 \\ y_i^+=0}} \ . \end{aligned} \tag{2.26}$$

The quark momentum difference r_i is the Fourier conjugate variable to the average quark position y_i. Again we parameterize its longitudinal component as fraction w.r.t.

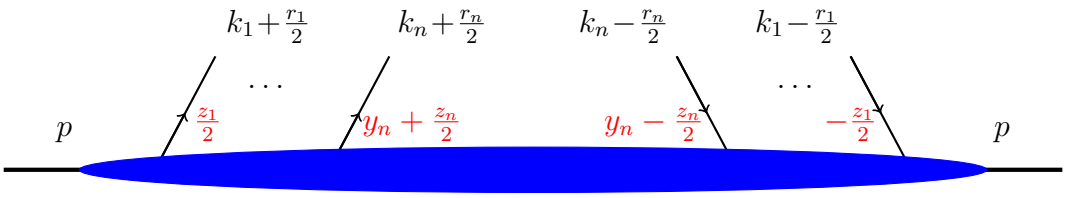

Figure 2.2: Depiction of a n-parton correlation function. The blue blob represents the hadron emitting and absorbing n partons. For each parton we show the corresponding momentum. Under the assumption that r_i is the Fourier conjugate variable to y_i and $y_n = 0$ we can assign $r_n = -\sum_{i=1}^{n-1} r_i$.

total hadron momentum p^+:

$$\zeta_i = \frac{r_i^+}{p^+} \,. \tag{2.27}$$

We are free to choose $y_n = 0$ because of translational invariance, i.e. y_i, with $i \neq n$ can be seen as the average distance to the n-th parton. Subsequently, only $n-1$ of the momentum variables r_i are independent. In the following we set $r_n = -\sum_{i=1}^{n-1} r_i$. The structure of the correlation function in terms of the involved momenta is depicted in Figure 2.2.

2.3.2 Twist-2 operators

Contracting (2.23) or (2.26) with $\Gamma_{\alpha\beta}$, where Γ is a suitable Dirac matrix, selects a certain quark polarization. A further contraction with a Kronecker delta δ_{cd} couples the corresponding quark fields to a color singlet. For the general n-parton correlation function (2.26) there are further possibilities for selecting different color representations as we will see when we discuss DPDs. The contracted operator $\bar{q}\Gamma q$ is classified by a number called twist, which was originally defined through the suppression by mass terms after applying the operator product expansion (OPE). In the present case we are interested in leading twist, i.e. twist 2, the corresponding operators are those with a maximal number of plus components. Matrix elements of these operators are most relevant, since by Lorentz invariance they scale with p^+, which is considered to be large. Furthermore, twist-2 operators represent only dynamically independent ("good") light-cone components of the quark fields, which allows a probabilistic interpretation within the parton model. For a detailed discussion on that we refer to [56]. There are three types of twist-2 operators, which correspond to the polarization of the quark. They can be constructed from helicity projection operators, $\gamma^+(1 \pm \gamma_5)/2$ or the projection operator for transverse spin s^j, which is $(\gamma^+ \pm s^j i\sigma^{j+}\gamma_5)/2$. For flavor q the twist-2

operators labeled by $a = q, \Delta q, \delta q$ are:

$$\mathcal{O}_a^{\perp}(y,z) := \bar{q}\,(y - z/2)\ \Gamma_a\ q(y + z/2)|_{z^+=0}\ , \tag{2.28}$$

with

$$\begin{aligned} \Gamma_q &= \frac{1}{2}\gamma^+ && \text{unpolarized quark ,} \\ \Gamma_{\Delta q} &= \frac{1}{2}\gamma^+\gamma_5 && \text{longitudinal polarization ,} \\ \Gamma^j_{\delta q} &= \frac{i}{2}\sigma^{j+}\gamma_5 && \text{transverse polarization .} \end{aligned} \tag{2.29}$$

The $\perp$-notation is introduced to distinguish between the operators (2.28) and those that are defined for vanishing transverse quark distance. These kind of operators we shall introduce later in this work. The operators (2.28) can be related to their analogue for antiquarks by considering charge conjugation $\mathcal{C}$, where we find:

$$\mathcal{O}_{\bar{a}}^{\perp}(y,z) := \mathcal{O}_a^{\perp,\mathcal{C}}(y,z) = \bar{q}\,(y + z/2)\ \Gamma_{\bar{a}}\ q(y - z/2)|_{z^+=0} = \eta_C^a \mathcal{O}_a^{\perp}(y,-z)\ , \tag{2.30}$$

such that

$$\Gamma_{\bar{a}} = \eta_C^a \Gamma_a\ , \tag{2.31}$$

where the sign factors η_C^a depend on the channel:

$$\eta_C^a = \begin{cases} 1 & a = \Delta q \\ -1 & a = q, \delta q \end{cases}\ . \tag{2.32}$$

Notice that the operators (2.28) and (2.30) are not invariant under local gauge transformations, since the quark fields are evaluated at different positions. In order to keep everything gauge invariant, it is necessary to introduce Wilson lines between the quark fields, i.e.

$$q(z) \to q^W(z,v) := W(z,v)\ q(z)\ . \tag{2.33}$$

The Wilson lines $W(z,v)$ represent collinear gluons and their explicit shape is specific to the considered process. For a detailed discussion see [57] and in the context of multi parton interactions [55]. For semi-inclusive DIS (SIDIS) and DY one finds

$$W(z,v) = \mathrm{P}\exp\left\{\pm ig\int_0^\infty \mathrm{d}\eta\ v\ t^j A^j(z \mp \eta v)\right\}\ , \tag{2.34}$$

where v is a space-like vector and P denotes path ordering. The two possible signs in (2.34) are specific to the process and correspond to future (SIDIS) and past (DY,DDY) pointing Wilson lines.

2.3.3 GPDs and form factors

In the following, we consider correlation functions involving a single light-cone quark operator. In addition to the integral over k^- we also integrate out the transverse quark momentum with the results that there is no sensitivity to transverse dynamics in the hadron. The resulting quantity is called generalized parton distribution (GPD). For reviews on subjects concerning GPDs, see [58, 59], where in the latter the term off-forward parton distribution (OFPD) is used. The GPD is defined as:

$$\begin{aligned} f_a(x,\xi,t) &:= (\Gamma_a)_{\alpha\beta}\,\delta_{cd}\int \mathrm{d}^2\boldsymbol{k}\;\Phi_{\alpha\beta cd}(x,\boldsymbol{k},\xi,\Delta) \\ &= \int \frac{\mathrm{d}z^-}{2\pi} e^{ixp^+z^-}\,\langle p+\Delta/2|\,\mathcal{O}_a(0,z)\,|p-\Delta/2\rangle\ , \end{aligned} \tag{2.35}$$

with

$$\mathcal{O}_a(y,z) := \bar{q}(y-z/2)\Gamma_a q(y+z/2)|_{z^+=0,\boldsymbol{z}=\boldsymbol{0}}\ . \tag{2.36}$$

Again Γ_a selects the quark polarization. Note that in the case $\boldsymbol{z}=\boldsymbol{0}$ the Wilson lines are just straight gauge links between the quark fields. In light cone gauge $A^+=0$ the links become trivial. As mentioned in the previous section, GPDs enter the calculations for the cross sections of exclusive scattering processes like deeply virtual Compton scattering (DVCS). For particles with zero spin or after taking the spin average, it can be shown that by Lorentz invariance the GPDs only depend on the following variables [58]:

$$\begin{aligned} x &= \frac{k^+}{p^+}\ , \qquad \xi = -\frac{\Delta^+}{2p^+}\ , \\ t &= \Delta^2 = -\frac{4\xi^2 m^2+\boldsymbol{\Delta}^2}{1-\xi^2}\ . \end{aligned} \tag{2.37}$$

As already discussed, emitted quarks with negative +-momentum are interpreted as absorbed antiquarks. Therefore, it depends on the sign of $x-\xi$ ($x+\xi$) whether a quark is emitted (absorbed) or an antiquark absorbed (emitted). Notice that the momentum fraction is restricted by $|x|<1$. Otherwise momentum conservation would imply spectator partons with negative +-momentum. However, this is not possible, since the spectator partons are considered to be on mass shell.
For spin-1/2 particles like the nucleon we have an additional quantum number characterizing the initial and final state, which is the helicity λ, i.e. the longitudinal hadron polarization. The corresponding GPD matrix elements $f^{\lambda\lambda'}$ depend on $\boldsymbol{\Delta}$, i.e. not only on t. They can be parameterized in terms of two independent functions, as we will discuss later.
If we consider a GPD for $\Delta=0$, we obtain a simple parton distribution function (PDF)

$$f_a(x) = f_a(x,\xi=0,t=0)\ , \tag{2.38}$$

which yields the probability to find a parton with longitudinal momentum xp^+ and polarization a. As mentioned in the previous section, the cross sections of inclusive processes like DIS can be written in terms of PDFs.
GPDs are related to form factors $F_a(t)$, which can be identified with a Fourier transform of the charge density in the transverse plane in the infinite momentum frame [60]. More precisely, it is the first Mellin moment in x of a GPD. The n-th Mellin moment is defined by

$$F_a^{(n)}(\xi,t) := \int_{-1}^{1} \mathrm{d}x\ x^{n-1} f_a(x,\xi,t)\ . \tag{2.39}$$

In the case of $n = 1$, which is equivalent to integrating the GPD over x, we find that the Mellin moment is independent of ξ, which is a consequence of Lorentz invariance:

$$F_a^{(1)}(\xi,t) = F_a(t) := \int_{-1}^{1} \mathrm{d}x\ f_a(x,\xi,t)\ . \tag{2.40}$$

Higher Mellin moments $F^{(n)}(\xi,t)$ in general decompose into an even polynomial in ξ of at most n-th degree. The corresponding coefficients, which depend on t, are called generalized form factors (GFFs). Integrating over x yields a delta function in z^-, which fixes z^- to zero. Therefore, the form factor can be defined by the hadronic matrix element of a local quark current.

$$p^+\ F_a(t) = \langle p+\Delta/2|\, \bar{q}(0)\ \Gamma_a\ q(0)\, |p-\Delta/2\rangle\ . \tag{2.41}$$

Replacing +-components by a Lorentz index, this equation can be brought into a Lorentz covariant form.
Let us now consider hadrons having non-zero total spin, which is the case for all baryons. In the following, we want to consider spin-1/2 hadrons, like the nucleon. The corresponding hadron states are classified by an additional quantum number referring to the longitudinal hadron spin (helicity) $\lambda = \pm 1/2$. Since spin-1/2 particles are represented by Dirac spinors, matrix elements of an operator $\mathcal{O}$ can be expressed in terms of Dirac spinors and a specific decomposition $\mathcal{J}[\mathcal{O}]$ of the operator:

$$\langle p+\Delta/2,\lambda|\, \mathcal{O}\, |p-\Delta/2,\lambda'\rangle = \bar{u}^{\lambda}(p+\Delta/2)\ \mathcal{J}[\mathcal{O}]\ u^{\lambda'}(p-\Delta/2)\ . \tag{2.42}$$

Explicit expressions for the decomposition $\mathcal{J}[\mathcal{O}]$ follow from Lorentz symmetry. This is discussed e.g. in [59]. In the following, we concentrate on the cases of vector currents $\bar{q}\gamma^\mu q$ and axial vector currents $\bar{q}\gamma^\mu\gamma_5 q$. For these currents a decomposition is given by:

$$\begin{aligned} \mathcal{J}[\bar{q}\gamma^\mu q] &= F_1(t)\gamma^\mu + F_2(t)\frac{i\sigma^{\mu\nu}\Delta_\nu}{2m}\ , \\ \mathcal{J}[\bar{q}\gamma^\mu\gamma_5 q] &= g_A(t)\gamma^\mu\gamma_5 + g_P(t)\frac{\gamma_5\Delta^\mu}{2m}\ . \end{aligned} \tag{2.43}$$

For each channel there are two independent form factors, in the vector case F_1, F_2 and in the axial vector case g_A and g_P (depending on the literature the latter is also denoted by $g_{\tilde{P}}$). At $t = 0$, $\sum_q e_q F_1^q$ and $\sum_q e_q F_2^q$ correspond to the hadron charge and the anomalous magnetic moment, respectively
The extension of the GPD (2.35) to spin-1/2 hadrons works analogously to that of the form factors. Here one finds the following parameterization [58]:

$$\begin{aligned} f_a^{\lambda\lambda'}(x,\xi,\boldsymbol{\Delta}) &= \int \frac{\mathrm{d}z^-}{2\pi} e^{ixp^+z^-} \langle p+\Delta/2,\lambda|\, \mathcal{O}_a(0,z)\, |p-\Delta/2,\lambda'\rangle \\ &= \frac{1}{2p^+} \bar{u}^\lambda(p+\Delta/2)\ \mathcal{J}_a(x,\Delta)\ u^{\lambda'}(p-\Delta/2)\ , \end{aligned} \tag{2.44}$$

with

$$\begin{aligned} \mathcal{J}_q(x,\Delta) &= H^q(x,\xi,t)\gamma^+ + E^q(x,\xi,t)\frac{i\sigma^{+j}\Delta_j}{2m}\ , \\ \mathcal{J}_{\Delta q}(x,\Delta) &= \tilde{H}^q(x,\xi,t)\gamma^+\gamma_5 + \tilde{E}^q(x,\xi,t)\frac{\gamma_5\Delta^+}{2m}\ . \end{aligned} \tag{2.45}$$

In analogy to (2.40) the form factors F_1, F_2, g_A and g_P can be identified as Mellin moments of the GPDs H, E, $\tilde{H}$ and $\tilde{E}$

$$\begin{aligned} F_1(t) &= \int \mathrm{d}x\ H(x,\xi,t)\ , & F_2(t) &= \int \mathrm{d}x\ E(x,\xi,t)\ , \\ g_A(t) &= \int \mathrm{d}x\ \tilde{H}(x,\xi,t)\ , & g_P(t) &= \int \mathrm{d}x\ \tilde{E}(x,\xi,t)\ . \end{aligned} \tag{2.46}$$

2.3.4 Evolution

The matrix elements appearing in (2.23) and (2.26) involve so-called rapidity divergences. These are removed in the collinear case, i.e. by integrating over transverse momenta, however, this causes divergences due to infinitely large transverse parton momenta, i.e. ultraviolet divergences. Both kinds of divergences require an appropriate regularization and renormalization procedure. As a consequence the distribution functions we considered so far depend on the renormalization scale μ and (in the transverse momentum dependent (TMD) case) on rapidity cut-off parameters. The dependence on these parameters and the scale is referred to as evolution and is describe by the Dokshitzer Gribow Lipatow Altarelli Parisi (DGLAP) equations in the collinear case or by Collins-Soper evolution in the TMD case.
Considering e.g. the GPDs (2.35), where we have collinear evolution, the corresponding dependence on the scale μ is described by the differential equation:

$$\frac{\partial}{\partial \log\mu} f_a(x,\xi,t;\mu) = \sum_{a'} \int_{-1}^{1} \mathrm{d}x'\ P_{aa'}(x,x',\xi,\alpha_s(\mu))\ f_{a'}(x',\xi,t;\mu)\ , \tag{2.47}$$

which is a generalization of the DGLAP equation for PDFs. The functions $P_{aa'}$ are called evolution kernels.

2.4 Double parton distributions

Now we want to give definitions and relations regarding the DPDs, which are the objects we want to investigate in this work. We shall focus on DPDs of quarks only. Furthermore, we only assume the unpolarized case, i.e. hadrons with spin zero or the spin average.

2.4.1 Definition for quarks

DPDs are given by the k^--integrated 2-parton correlation function. In the following, we concentrate on quark distributions and the corresponding spin structure, again only considering color singlet operators. The corresponding DPD ${}^1F$ is obtained from (2.26), considering $n = 2$:

$$\begin{aligned} {}^1F^{\perp}_{ab}(x_i, \boldsymbol{k}_i, \zeta, \boldsymbol{y}) &= (\Gamma_a)_{\alpha_1\beta_1} (\Gamma_b)_{\alpha_2\beta_2} \delta_{c_1d_1}\delta_{c_2d_2} \int \frac{\mathrm{d}^2\boldsymbol{r}}{(2\pi)^2}\, e^{-i\boldsymbol{y}\boldsymbol{r}} \Phi_{\alpha_i\beta_i c_i d_i}(x_i, \boldsymbol{k}_i, \zeta, \boldsymbol{r}) \\ &= 2p^+ \int \mathrm{d}y^- e^{-i\zeta p^+ y^-} \left[\prod_{i=1,2} \frac{\mathrm{d}^2\boldsymbol{z}_i \mathrm{d}z_i^-}{(2\pi)^3} e^{ix_i p^+ z_i^-} e^{-i\boldsymbol{z}_i\boldsymbol{k}_i} \right] \\ &\quad \times \langle p| \mathcal{O}^{\perp}_a(y, z_1) \mathcal{O}^{\perp}_b(0, z_2) |p\rangle \Big|_{y^+=0} \ , \end{aligned} \tag{2.48}$$

where ζ is defined as:

$$\zeta = \frac{r^+}{p^+} \ . \tag{2.49}$$

In contrast to one-parton distributions the quark bilinears can be coupled to a color-octet, the corresponding DPD is denoted by ${}^8F$. It is obtained by replacing the Kronecker deltas $\delta_{c_i d_i}$ by a sum over Gell-Man matrices $t^a_{c_1d_1} t^a_{c_2d_2}$. From now on we restrict ourselves to the color-singlet DPDs ${}^1F$ and drop the index 1 for simplicity.
Interchanging the spinor and color indices such that $(\Gamma_a)_{\alpha_1\beta_1}\ (\Gamma_b)_{\alpha_2\beta_2}\ \delta_{c_1d_1}\ \delta_{c_2d_2} \to (\Gamma_a)_{\alpha_1\beta_2}\ (\Gamma_b)_{\alpha_2\beta_1}\ \delta_{c_1d_2}\ \delta_{c_2d_1}$ yields distribution functions corresponding to fermion number interference. This is not discussed in detail within this work.
If $\zeta \neq 0$, the DPD is called non-forward or skewed, meaning that the emitted quarks have different longitudinal momenta than the absorbed ones. Within the DPS phenomenology this case is not relevant, as is discussed later in this section.
F_{ab} is related to the probability of finding two quarks of polarization a and b simultaneously. Since the transverse quark momenta $\boldsymbol{k}_i$ and the transverse distance $\boldsymbol{y}$ cannot be measured at the same time due to the uncertainty principle, the DPDs we defined above do not have a direct probabilistic interpretation. However, integrating over the

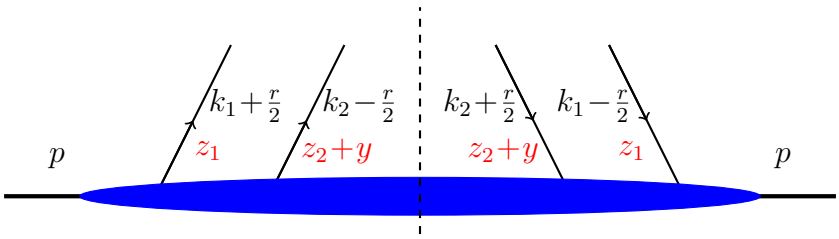

Figure 2.3: Structure of a DPD, where we show the parton momenta, as well as the corresponding Fourier conjugated (average) variables in position space (red). In an inclusive DPS process DPDs represent the hadronic part of the squared amplitude, which is represented by the blue blob. Therefore, we also show the final state cut (dashed line).

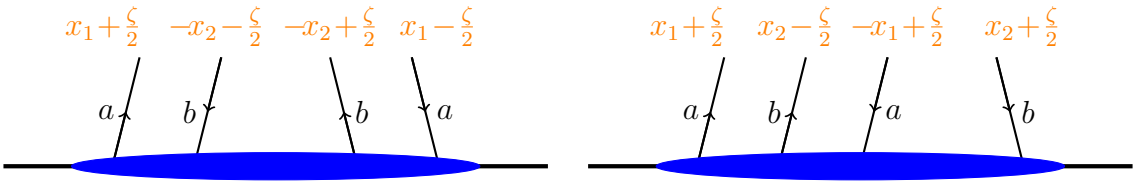

Figure 2.4: Different kinematic situations regarding the DPD $F_{ab}(x_1, x_2, \zeta, \boldsymbol{y})$, which correspond to different interpretations whether there are quarks or antiquarks in the wave function or its complex conjugate. Left: $x_1 \pm \zeta/2 \geq 0$, $x_2 \pm \zeta/2 \leq 0$, i.e. a quark and an antiquark are emitted and reabsorbed. Right: $x_2 \pm \zeta/2 \geq 0$, $x_1 + \zeta/2 \geq 0$, $x_1 - \zeta/2 \leq 0$, i.e. two quarks and one antiquark are emitted and one quark is absorbed.

transverse momenta yields a probability function. The resulting functions are called collinear DPDs:

$$\begin{aligned} F_{ab}(x_1, x_2, \zeta, \boldsymbol{y}) &:= \int \mathrm{d}^2\boldsymbol{k}_1 \, \mathrm{d}^2\boldsymbol{k}_2 \; F_{ab}^{\perp}(x_i, \boldsymbol{k}_i, \zeta, \boldsymbol{y}) \\ &= 2p^+ \int \mathrm{d}y^- e^{-i\zeta p^+ y^-} \left[\prod_{i=1,2} \frac{\mathrm{d}z_i^-}{2\pi} e^{i x_i p^+ z_i^-} \right] \langle p | \, \mathcal{O}_a(y, z_1) \mathcal{O}_b(0, z_2) \, | p \rangle |_{y^+=0} \; . \end{aligned} \tag{2.50}$$

These can be seen as an extension of the one-parton PDFs (2.38) to two partons. There is also a representation in momentum space, given by a simple Fourier transform w.r.t. to the transverse parton distance:

$$F_{ab}(x_1, x_2, \zeta, \boldsymbol{r}) := \int \mathrm{d}^2\boldsymbol{y} \; e^{i\boldsymbol{r}\boldsymbol{y}} F_{ab}(x_1, x_2, \zeta, \boldsymbol{y}) \; . \tag{2.51}$$

If the considered hadron carries non-zero spin the formalism has to be adapted accordingly. At the moment we always consider DPDs for unpolarized hadrons, meaning that

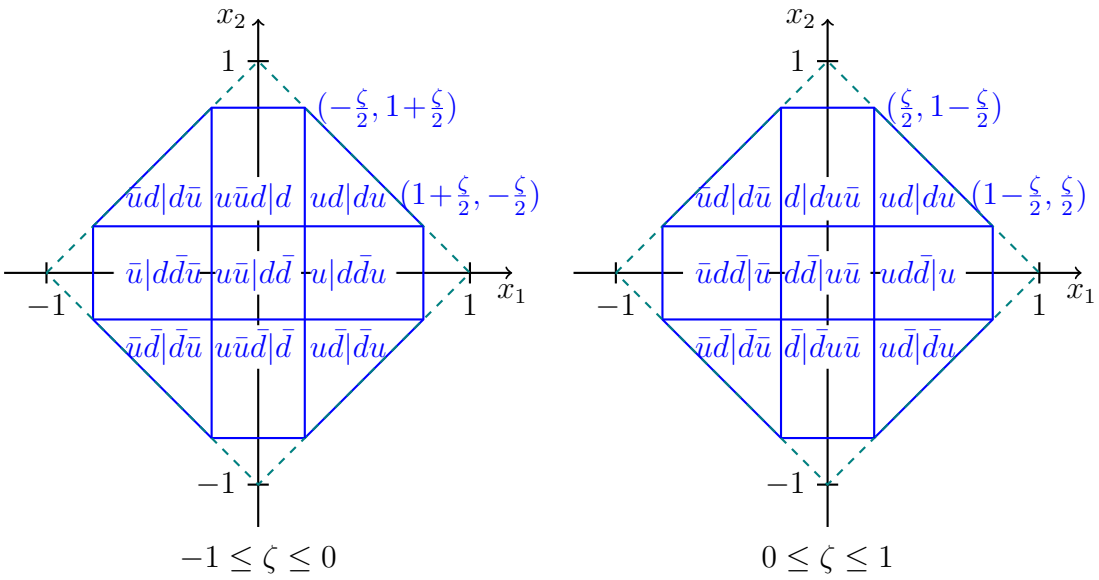

Figure 2.5: Support region for the skewed DPD $F_{ud}(x_1, x_2, \zeta, \boldsymbol{y})$ for $-1 \leq \zeta \leq 0$ (left) and $0 \leq \zeta \leq 1$ (right) in the (x_1, x_2)-plane. For each sub-region we specify whether the quarks are assigned to the hadron wave function or its complex conjugate. The notation $u|d\bar{d}u$ indicates an u-quark in $|p\rangle$ and $d\bar{d}u$ in $\langle p|$. The corners restricting the support region are located at $(|\zeta/2|, 1-|\zeta/2|)$, whereas those of the inner box are $(|\zeta/2|, |\zeta/2|)$. The dashed line is defined by $|x_1| + |x_2| = 1$.

we take the spin average. For spin-1/2 particles, like the nucleon, this is:

$$F_{ab}(x_1, x_2, \zeta, \boldsymbol{y}) := p^+ \sum_\lambda \int \mathrm{d}y^- e^{-i\zeta p^+ y^-} \left[\prod_{i=1,2} \frac{\mathrm{d}z_i^-}{2\pi} e^{ix_i p^+ z_i^-} \right] \times \langle p, \lambda | \, \mathcal{O}_a(y, z_1) \mathcal{O}_b(0, z_2) \, |p, \lambda\rangle|_{y^+=0} \ . \tag{2.52}$$

2.4.2 Properties of collinear color-singlet DPDs

In the following, we consider the collinear, skewed quark DPDs defined in (2.50) for spin-0 hadrons or in (2.52) for spin averaged hadrons. In the forward case $\zeta = 0$ they describe the probability of finding two quarks with momentum fractions x_1 and x_2 at a relative transverse distance $\boldsymbol{y}$. The variable ζ describes the difference between the momentum fractions in the amplitude and those in its complex conjugate. The quarks being emitted or absorbed have momentum fractions $x_1 \pm \zeta/2$ and $x_2 \mp \zeta/2$. Figure 2.4 shows different kinematic situations in this context. If a momentum fraction becomes negative, the corresponding emitted quark is again interpreted as an absorbed antiquark and vice versa. This is similar to GPDs, where we considered $x \pm \xi$ instead. Again the quarks cannot carry more than the total hadron momentum. Therefore, the absolute value of the total momentum fraction of a quark $x_i \pm \zeta/2$ is restricted to be smaller

than one. Furthermore, the sum of all momentum fractions has to be at most one. Otherwise one quark or both together would carry more momentum than the hadron itself. Therefore, the DPDs have to be zero outside the region defined by

$$\begin{aligned} |x_i \pm \zeta/2| &\leq 1 \ , \\ |x_1| + |x_2| &\leq 1 \ . \end{aligned} \tag{2.53}$$

The support region is sketched in Figure 2.5 for F_{ud}, where we also indicate whether there are quarks or antiquarks in the wave function or its complex conjugate. DPDs of antiquarks are related to those of the corresponding quark. By considering (2.30), one can give the following relations w.r.t. the arguments x_i:

$$\begin{aligned} F_{ab}(x_1, x_2, \zeta, \boldsymbol{y}) &= \eta_C^a F_{\bar{a}b}(-x_1, x_2, \zeta, \boldsymbol{y}) \ , \\ F_{ab}(x_1, x_2, \zeta, \boldsymbol{y}) &= \eta_C^b F_{a\bar{b}}(x_1, -x_2, \zeta, \boldsymbol{y}) \ . \end{aligned} \tag{2.54}$$

Furthermore, from PT invariance we find:

$$F_{ab}(x_1, x_2, \zeta, \boldsymbol{y}) = \eta_{PT}^a \eta_{PT}^b F_{ab}(x_1, x_2, -\zeta, -\boldsymbol{y}) \ . \tag{2.55}$$

with

$$\eta_{PT}^a = \begin{cases} 1 & a = q \\ -1 & a = \Delta q, \delta q \end{cases} \tag{2.56}$$

For each quark polarization combination we are able to give decompositions of DPDs in terms of functions being rotationally invariant w.r.t. the transverse quark distance $\boldsymbol{y}$. This is achieved by considering parity and transformation properties. In total we find:

$$\begin{aligned} F_{qq'}(x_i, \zeta, \boldsymbol{y}) &= f_{qq'}(x_i, \zeta, y^2) \ , & F_{\Delta q \Delta q}(x_i, \zeta, \boldsymbol{y}) &= f_{\Delta q \Delta q'}(x_i, \zeta, y^2) \ , \\ F_{q\Delta q'}(x_i, \zeta, \boldsymbol{y}) &= 0 \ , & F_{\Delta q q'}(x_i, \zeta, \boldsymbol{y}) &= 0 \ , \\ F^j_{q\delta q'}(x_i, \zeta, \boldsymbol{y}) &= \epsilon^{jl} y^l m f_{q\delta q'}(x_i, \zeta, y^2) \ , & F_{\Delta q \delta q'}(x_i, \zeta, \boldsymbol{y}) &= 0 \ , \\ F^j_{\delta q q'}(x_i, \zeta, \boldsymbol{y}) &= \epsilon^{jl} y^l m f_{\delta q q'}(x_i, \zeta, y^2) \ , & F_{\delta q \Delta q'}(x_i, \zeta, \boldsymbol{y}) &= 0 \ , \\ F^{jk}_{\delta q \delta q'}(x_i, \zeta, \boldsymbol{y}) &= \delta^{jk} f_{\delta q \delta q'}(x_i, \zeta, y^2) + \left(2y^j y^k - \delta^{jk}\boldsymbol{y}^2\right) m^2 f^t_{\delta q \delta q'}(x_i, \zeta, y^2) \ . \end{aligned} \tag{2.57}$$

The first line readily follows from the property that the DPDs $F_{qq'}$ and $F_{\Delta q \Delta q'}$ have even parity. This is different for $F_{\Delta q q'}$ and $F_{q\Delta q'}$, which have odd parity. An integration over transverse momenta yields zero in that case. $F_{\Delta q \delta q'}$ and $F_{\delta q \Delta q'}$ are $\mathcal{T}$-odd, invariance under time reflection then implies that they have to vanish. The remaining relations in (2.57) concern DPDs that involve transverse polarizations and are obtained by decomposing the DPDs in terms of transverse vectors. Inserting (2.57) into (2.55), we find:

$$f_{ab}(x_i, \zeta, y^2) = f_{ab}(x_i, -\zeta, y^2) \ , \tag{2.58}$$

i.e. $f_{ab}(x_i, \zeta, y^2)$ are even functions in ζ.
In analogy to the discussion in section 2.3.4 one has to regularize ultraviolet divergences involved by the collinear DPDs. This introduces an evolution w.r.t. each momentum fraction involving in general two scales μ and μ'. For ${}^1F$ this is [61]:

$$\frac{\partial}{\partial \log \mu^2} F_{ab}(x_i, \boldsymbol{y}; \mu, \mu') = \sum_{a'} \int_{x_1}^{1-x_2} \frac{\mathrm{d}x_1'}{x_1'} P_{aa'}\left(\frac{x_1}{x_1'}; \mu\right) F_{a'b}(x_1', x_2, \boldsymbol{y}; \mu, \mu') \tag{2.59}$$

At small quark distances a (forward) DPD is dominated by a perturbative effect known as $1 \to 2$ splitting of a parton a into two partons a', b'. The corresponding contribution can be written as:

$$F_{a'b'}(x_1, x_2, \boldsymbol{y})|_{\text{splitting}} = \frac{\alpha_s}{2\pi^2 y^2} P_{a\to a'b'}\left(\frac{x_1}{x_1 + x_2}\right) \frac{f_a(x_1 + x_2)}{x_1 + x_2} \ , \tag{2.60}$$

where f_a is an ordinary PDF as defined in (2.38) and $P_{a\to a'b'}$ parameterizes the splitting. The divergence caused by the factor $1/y^2$ in (2.60) is referred to as splitting singularity, which can be regularized by a cut-off. A commonly used choice is $y > b_0/\mu$, where μ is the renormalization scale and

$$b_0 = 2e^{-\gamma} \ , \tag{2.61}$$

where $\gamma \approx 0.577$ is the Euler-Mascheroni constant. In the forward case $\zeta = 0$, the DPD $F(x_1, x_2, \zeta, \boldsymbol{y})$ fulfills the number sum rule, which is a consequence of fermion number conservation. It has been formulated in [62] and finally proven in [63] and relates the Mellin moment in one fraction, e.g. x_2, with a PDF $f(x_1)$ depending on the remaining fraction:

$$\begin{aligned} &\int_{-1}^{1} \mathrm{d}x_2 \int_{b_0/\mu} \mathrm{d}^2\boldsymbol{y} \ F_{qq'}(x_1, x_2, \boldsymbol{y}; \mu) = \\ &\qquad = (N_{q'} + \delta_{q\bar{q}'} - \delta_{qq'})\, f_q(x_1) + \mathcal{O}(\alpha_s(\mu)) + \mathcal{O}((b_0\Lambda/\mu)^2) \ , \end{aligned} \tag{2.62}$$

where $N_{q'}$ corresponds to the number of valence quarks of flavor q' appearing in the considered hadron. The $\mathcal{O}(\alpha_s)$-term arises from the previously described splitting contribution and the correction of order $\mathcal{O}((b_0\Lambda/\mu)^2)$ is caused by the cutoff in the $\boldsymbol{y}^2$-integral. A similar relation is known for the single PDF $f_q(x)$, where the integral over x again yields the number of valence quarks of flavor q.

2.4.3 Double parton scattering and DPDs

A scattering process involving two partons of each hadron is sensitive to correlations of these partons. The corresponding information is provided by DPDs, which directly appear in the cross section. We will discuss at the end of this section that there are further contributions in the cross sections beyond those related to DPDs. Again we only consider the part concerning quarks. In the following, we consider two hadrons moving

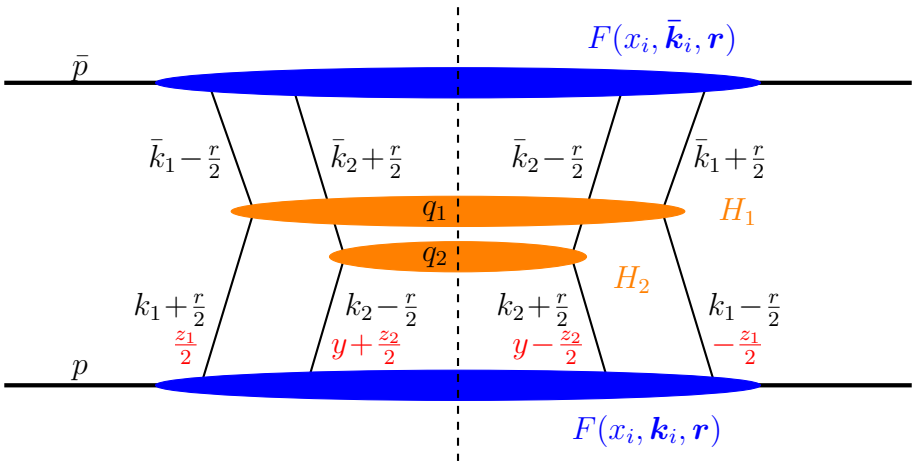

Figure 2.6: Leading order graph for a DPS process. Each of the two hadrons emits two partons, each of them interact with one parton of the other hadron. These interactions are represented by the hard scattering matrix elements H_i (orange blobs), which depend on the squared c.m. energy q_i^2. The emission of the parton is described by DPDs F of each hadron depicted by the blue blobs. The dashed line is the final state cut, which separates the scattering amplitude and its complex conjugate.

in opposite 3-direction at high energy Q. For the corresponding momenta p and $\bar{p}$ in the c.m. frame we can give the relations:

$$\begin{aligned} p^+ \sim \bar{p}^- &\sim Q \,, \\ p^- \sim \bar{p}^+ &\sim \frac{\Lambda^2}{Q} \,, \\ \boldsymbol{p} = \bar{\boldsymbol{p}} &= \boldsymbol{0} \,. \end{aligned} \tag{2.63}$$

For the parton momenta of the hadron moving in $-$-direction we obtain a similar scaling behavior as in (2.25) with $+$-components replaced by $-$-components. The double parton scattering process is shown in Figure 2.6. We have two quarks emerging from each hadron and scattering with one quark of the other hadron. This hard scattering subprocess is described by the hard scattering matrix element H_i, which includes all possible final states for momentum transfer q_i. Because of momentum conservation it is clear that $q_i = k_i + \bar{k}_i$, which implies

$$q_i^+ \approx k_i^+ \qquad q_i^- \approx \bar{k}_i^- \,. \tag{2.64}$$

Furthermore, momentum conservation forces light-cone components of r to be small:

$$r^+ \sim r^- \sim \frac{\Lambda^2}{Q} \,. \tag{2.65}$$

For the cross section it is therefore sufficient to consider $\zeta = r^+/p^+ \approx 0$. With $q_i^2 \approx q_i^+ q_i^- \approx x_i\bar{x}_i p^+\bar{p}^- \approx x_i\bar{x}_i(p+\bar{p})^2 = x_i\bar{x}_i s$ we can give an expression for the double parton scattering cross section in the quark sector. Resolving the longitudinal and transverse final momenta of the hard scattering products, the cross section reads [55]:

$$\begin{aligned}\frac{\mathrm{d}\sigma_{\mathrm{DPS}}}{\prod_{i=1,2}\mathrm{d}x_i\mathrm{d}\bar{x}_i\mathrm{d}^2\boldsymbol{q}_i} &= \frac{1}{C}\sum_{ab\bar{a}\bar{b}}\left[\prod_{i=1,2}\int \mathrm{d}^2\boldsymbol{k}_i\ \mathrm{d}^2\bar{\boldsymbol{k}}_i\ \delta^{(2)}\left(\boldsymbol{q}_i-\boldsymbol{k}_i-\bar{\boldsymbol{k}}_i\right)\right]\int \mathrm{d}^2\boldsymbol{y} \\ &\times\Big[\sigma_{1,a\bar{a}}\left(x_1\bar{x}_1 s\right)\ \sigma_{2,b\bar{b}}\left(x_2\bar{x}_2 s\right)\ F_{ab}\left(x_i,\boldsymbol{k}_i,\zeta,\boldsymbol{y}\right)\ F_{\bar{a}\bar{b}}\left(\bar{x}_i,\bar{\boldsymbol{k}}_i,\zeta,\boldsymbol{y}\right) \\ &\quad+\ \sigma_{1,a\bar{a}}\left(x_1\bar{x}_1 s\right)\ \sigma_{2,\bar{b}b}\left(x_2\bar{x}_2 s\right)\ F_{a\bar{b}}\left(x_i,\boldsymbol{k}_i,\zeta,\boldsymbol{y}\right)\ F_{\bar{a}b}\left(\bar{x}_i,\bar{\boldsymbol{k}}_i,\zeta,\boldsymbol{y}\right)\Big]\Big|_{\zeta=0} \\ &+\text{ octet }+\text{ interference terms }\,,\end{aligned} \tag{2.66}$$

where $C=2$ if the two scattering partons are the same and $C=1$ otherwise. The hard scattering cross sections $\sigma_{i,a\bar{a}}(x_i\bar{x}_i s)$ corresponds to the spin projected hard scattering matrix $H_i(q_i^2)$:

$$\sigma_{i,a\bar{a}}(x_i\bar{x}_i s) = \frac{1}{2q_i^2}k_i^+\left(\Gamma_a^-\right)_{\alpha\beta}H_{i,\beta\alpha\bar{\alpha}\bar{\beta}}(q_i^2)\left(\Gamma_{\bar{a}}^+\right)_{\bar{\beta}\bar{\alpha}}\bar{k}_i^-\ . \tag{2.67}$$

The contraction with the spin indices has been replaced by a sum over polarizations via a Fierz transformation, where we neglect higher twist contributions. The indices a, b are supposed to run over q, Δq, δq, while $\bar{a}$, $\bar{b}$ label the corresponding antiquark channels. The Dirac structures $\Gamma_a^\pm$ are defined as

$$\Gamma_q^\pm = \frac{1}{2}\gamma^\pm \qquad \Gamma_{\Delta q}^\pm = \frac{1}{2}\gamma_5\gamma^\pm \qquad \Gamma_{\delta q}^{\pm,j} = \frac{1}{2}\gamma_5\gamma^\pm\gamma^j \qquad \Gamma_{\bar{a}}^\pm = -\eta_C^a\Gamma_a^\pm\ . \tag{2.68}$$

If we do not desire to be sensitive to transverse effects, we can integrate over $\boldsymbol{q}_i$ eliminating the transverse parton momenta. This yields a similar formula as before, which involves collinear DPDs:

$$\begin{aligned}\frac{\mathrm{d}\sigma_{\mathrm{DPS}}}{\mathrm{d}x_1\mathrm{d}x_2\mathrm{d}\bar{x}_1\mathrm{d}\bar{x}_2} &= \frac{1}{C}\sum_{ab\bar{a}\bar{b}}\int \mathrm{d}^2\boldsymbol{y} \\ &\times\Big[\sigma_{1,a\bar{a}}\left(x_1\bar{x}_1 s\right)\ \sigma_{2,b\bar{b}}\left(x_2\bar{x}_2 s\right)\ F_{ab}\left(x_i,\zeta,\boldsymbol{y}\right)\ F_{\bar{a}\bar{b}}\left(\bar{x}_i,\zeta,\boldsymbol{y}\right) \\ &\quad+\ \sigma_{1,a\bar{a}}\left(x_1\bar{x}_1 s\right)\ \sigma_{2,\bar{b}b}\left(x_2\bar{x}_2 s\right)\ F_{a\bar{b}}\left(x_i,\zeta,\boldsymbol{y}\right)\ F_{\bar{a}b}\left(\bar{x}_i,\zeta,\boldsymbol{y}\right)\Big]\Big|_{\zeta=0} \\ &+\text{ octet }+\text{ interference terms }\,.\end{aligned} \tag{2.69}$$

Notice that these results are obtained from a leading order analysis. The expressions for the cross sections (2.69) and (2.66) are factorized in terms of hard scattering matrix elements and a soft part represented by the DPDs. In higher order analyses one has to take into account effects of collinear and soft gluons. We already mentioned collinear

gluons, which are represented by the Wilson line of the light cone operators. Soft gluons are taken into account by including a so-called soft factor in the definition of the DPD. Furthermore, one has to compensate double-counting of sub-processes being already included by the SPS description. This is related to perturbative splitting, which we mentioned in the previous section.
In order to show that factorization holds at all orders, it is crucial to prove that gluons in the so-called Glauber region cancel, which has been shown for DDY processes by [64]. There are processes, where there is no such cancellation, e.g. for hadronic final states and measured transverse momenta $\boldsymbol{q}_i$ [65]. For a review on DPS factorization subjects and the current status of factorization proofs, see [61].
Beyond the previous discussion there are certain interference contributions w.r.t. the fermion number and quark flavor, which are possibly contributing to the DPS process. In the cross sections (2.66) and (2.69) the corresponding contributions appear among the part described by DPDs. Fermion number interference is described by interference distributions, which we already mentioned when defining DPDs. For flavor interference one has to treat matrix elements of operators that do not conserve flavor.
Notice that there are also contributions involving the color-octet DPDs ${}^8F$, which we have not considered so far. These contributions, as well as the previously mentioned interference effects, are assumed to be Sudakov-suppressed [66].

3 Matrix elements and lattice QCD

In the previous chapter we defined several kinds of parton distribution functions for the case of quarks. All of them share as kernel a hadronic matrix element of quark operators. As already mentioned in the previous chapter, the QCD coupling constant becomes very large at the hadronic scale. Therefore, the perturbative ansatz is not applicable in order to perform a calculation of hadronic matrix elements from first principles. We will introduce a non-perturbative tool based on the path integral formalism on discrete and finite spacetime. The path integral is solved by Monte Carlo simulations. This methods is referred to as lattice field theory or, in our case, lattice QCD (LQCD) and was originally developed by Wilson [67]. A complication is that these lattice calculations are only feasible in Euclidean spacetime, which makes a direct access to dynamical processes impossible. However, the Euclidean correlation functions can be directly related to matrix elements we are interested in. This will be discussed at the end of this chapter. For the subjects being discussed in this chapter we refer to [68, 69], for details concerning field theoretical aspects, see e.g. [48].

3.1 The path integral formalism

A standard method of evaluating physical quantities within quantum mechanics is provided by functional quantization. The formalism basically corresponds to the principle that any transition is realized by a superposition of each possible path of intermediate states. The contribution of each state depends on the action of the theory. In the classic limit the contributions from all but the classical path vanish. Furthermore, the theory is represented by the Lagrangian. As a consequence the symmetry of the Lagrangian is reflected by the path integral. In the following, we will give a brief introduction of the formalism, a detailed derivation and discussion can be found in standard literature, e.g. [48].

3.1.1 The concept

The path integral formalism is based on the concept of considering infinitesimal slices w.r.t. the dynamic variable (time) and the insertion of complete sets of intermediate states between all of these slices. Let us consider a system with generalized coordinates $\phi_i(t)$ and conjugate momenta $\pi_i(t)$. For the transition from an initial state $|\phi_a\rangle$ to a final state $|\phi_b\rangle$ one can show that for any Hamiltonian of the form $\mathcal{H}(\phi_i, \pi_i) = c\pi_i^2 + f(\phi_i)$,

where c is some constant, the transition matrix element reads up to a normalization constant:

$$\langle\phi_b|\, e^{-i\mathcal{H}T}\, |\phi_a\rangle = \left[\prod_{i,t}\int \mathrm{d}\phi_{i,t}\right]_{\substack{\phi_{i,T}=\phi_b\\ \phi_{i,0}=\phi_a}} \exp\left\{i\int_0^T \mathrm{d}t\ \mathcal{L}\right\}\ , \tag{3.1}$$

with the Lagrangian

$$\mathcal{L} = \sum_i \pi_i\dot{\phi}_i - \mathcal{H}(\phi_i,\pi_i)\ . \tag{3.2}$$

From now on we will use the conventional notation $\mathrm{D}\left[\phi_{i,t}\right] = \prod_{i,t}\mathrm{d}\phi_{i,t}$. For our purpose we have to adapt the formalism to fields $\phi_i(x)$ being defined on each coordinate x in Minkowski spacetime. In this case we can rewrite (3.1):

$$\langle\phi_i'(\vec{x})|\, e^{-i\mathcal{H}T}\, |\phi_i''(\vec{x})\rangle = \int_{\substack{\phi_i(\vec{x},T/2)=\phi_b''(\vec{x})\\ \phi_i(\vec{x},-T/2)=\phi_a'(\vec{x})}} \mathrm{D}\left[\phi_i(\vec{x},t)\right] \exp\left\{i\int_{-T/2}^{T/2}\mathrm{d}t\int \mathrm{d}^3\vec{x}\ \mathcal{L}\right\}\ . \tag{3.3}$$

Notice that we shifted the time variable such that the integration boundaries are $\pm T/2$ instead of 0 and T. The expression (3.3) can be generalized to vacuum expectation values of a time ordered product of field operators $\hat{\phi}_i(x)$ in the Heisenberg picture, i.e. the operator itself is time dependent. $x = (t,\vec{x})$ is a four-vector. Assuming that the fields overlap with the vacuum, it can be shown that, in the limit $T\to\infty(1-i\epsilon)$, a vacuum expectation value can be related to the following path integral:

$$\left\langle \mathrm{T}\hat{\phi}_1(x_1)\cdots\hat{\phi}_n(x_n)\right\rangle = Z^{-1}\int \mathrm{D}\left[\phi_i\right]\phi_1(x_1)\cdots\phi_n(x_n)\ e^{iS[\phi_i]}\ , \tag{3.4}$$

with the partition function

$$Z = \int \mathrm{D}\left[\phi_i\right] e^{iS[\phi_i]}\ , \tag{3.5}$$

and the action

$$S[\phi_i(x)] = \int \mathrm{d}^4x\ \mathcal{L}\ . \tag{3.6}$$

The small imaginary part in the limit of the time extension T suppresses excited states by a factor e^{-ET}, where E is the energy difference between the vacuum state and the excited state. Hence, in this limit only the ground (vacuum) state is represented, which is exactly what we are interested in. The corresponding limit in Euclidean spacetime will be discussed more detailed in section 3.3.
The l.h.s. of (3.4) is the general form of quantities we want to investigate within this work by calculating the r.h.s. . This is feasible through Monte Carlo simulations if we consider a finite number of degrees of freedom, i.e. a discrete and finite spacetime. The

necessary discretization process will be explained in section 3.2.

3.1.2 The Wick rotation

We will see in section 3.2.6 that the oscillatory factor $e^{iS[\phi_i]}$ appearing in (3.4) makes Monte Carlo simulations unfeasible. In the following, we want to introduce the concept of Euclidean time, which is connected to Minkowski time by the so-called Wick rotation of the integration path in the action. This rotation is formally defined by

$$\int_{-\infty}^{\infty} \mathrm{d}t \to \int_{-i\infty}^{i\infty} \mathrm{d}t = \int_{-\infty}^{\infty} \mathrm{d}t_E \ , \tag{3.7}$$

leading to the definition of the Euclidean time t_E, which is a component of a Euclidean four-vector x_E

$$x_E^4 = t_E = -it = -ix^0 \ . \tag{3.8}$$

Considering the invariant distance $x^2 = -t_E^4 - \vec{x}_E^2 = -x_E^\mu x_E^\nu g_{E,\mu\nu}$, we can identify the Euclidean metric $g_{E,\mu\nu} = \delta_{\mu\nu}$. To distinguish between Euclidean and Minkowski time components the corresponding index of any four vector will be labeled by 4 instead of 0. The Euclidean four vector reads $x_E = (\vec{x}, t_E)$. As a consequence of the Wick rotation the argument $iS[\phi_i]$ in the exponential appearing in (3.4) and (3.5) becomes $-S_E[\phi_i]$, where S_E is the action in Euclidean spacetime. Since the exponent is a purely real function, the exponential itself is real and positive. Therefore, it can be treated as a weight factor, which is essential for Monte Carlo integration. After applying the Wick rotation to the expressions given in (3.4), (3.5) and (3.6), we obtain their Euclidean versions:

$$\begin{aligned} \left\langle \hat{\phi}_1(x_{E,1}) \cdots \hat{\phi}_n(x_{E,n}) \right\rangle &= Z^{-1} \int \mathrm{D}\left[\phi_i\right] \phi_1(x_{E,1}) \cdots \phi_n(x_{E,n}) \ e^{-S_E[\phi_i]} \ , \\ Z &= \int \mathrm{D}\left[\phi_i\right] e^{-S_E[\phi_i]} \ , \\ S_E[\phi_i] &= \int \mathrm{d}^4 x_E \ \mathcal{L}_E \ . \end{aligned} \tag{3.9}$$

From now on we only consider a Euclidean spacetime structure and drop the subscript E for better readability.

3.1.3 Grassmann variables and Wick's theorem

We already mentioned that a canonical way to solve a path integral is given by Monte Carlo integration. However, we want to discuss the special case, where parts of the degrees of freedom are represented by so-called Grassmann with the property that they anti-commute, i.e. :

$$\eta_i \eta_j = -\eta_j \eta_i \ , \tag{3.10}$$

for two Grassmann valued variables η_i and η_j. In our context this is the case, whenever we treat fermionic fields. If the path integral is taken w.r.t. such variables, the corresponding part can be evaluated exactly. A typical expression we have to deal with later in this work has the following form:

$$\int \mathrm{D}[\eta_i]\mathrm{D}[\bar{\eta}_i]\eta_{k_1}\bar{\eta}_{\bar{k}_1}\cdots\eta_{k_n}\bar{\eta}_{\bar{k}_n}\exp\left\{\bar{\eta}_i A_{il}\eta_l\right\} = \frac{\partial}{\partial j_{k_1}}\frac{\partial}{\partial \bar{j}_{\bar{k}_1}}\cdots\frac{\partial}{\partial j_{k_n}}\frac{\partial}{\partial \bar{j}_{\bar{k}_n}} Z[j,\bar{j}]\Big|_{j,\bar{j}=0} \ . \tag{3.11}$$

The r.h.s. shows the representation of the expectation value in terms of the generating functional $Z[\bar{j}, j]$, which is defined as:

$$Z[j,\bar{j}] = \int \mathrm{D}[\eta_i]\mathrm{D}[\bar{\eta}_i]\exp\left\{\bar{\eta}_i A_{il}\eta_l + \bar{j}_i\eta_i + \bar{\eta}_i j_i\right\} \ . \tag{3.12}$$

η_i and $\bar{\eta}_i$ are two sets of Grassmann valued degrees of freedom and A is an invertible matrix. $\bar{j}_i$ and j_i are Grassmann valued source terms. By applying the derivatives on the r.h.s. in (3.11), it can be shown that the expressions in (3.11) are equivalent to

$$(-1)^n \sum_{P\in S_n} \mathrm{sign}(P)\left(A^{-1}\right)_{k_1\bar{k}_{P(1)}}\cdots\left(A^{-1}\right)_{k_n\bar{k}_{P(n)}}\det\{A\} \ . \tag{3.13}$$

In a discrete field theory the analogue to the matrix A is given by a discretized differential operator $\mathcal{D}$, e.g. the Dirac operator in the case of QCD. The differential operator itself may depend on further fields ϕ_i which are not Grassmann valued. Defining the propagator $M[\phi_i] = \mathcal{D}^{-1}[\phi_i]$, the path integral expression related to the vacuum expectation value of anti-commuting field operators $\hat{\psi}$ takes the form:

$$\begin{aligned}\left\langle \hat{\psi}_1(x_1)\hat{\bar{\psi}}_1(x'_1)\cdots\hat{\psi}_n(x_n)\hat{\bar{\psi}}_n(x'_n)\right\rangle &= \frac{(-1)^n}{Z}\sum_{P\in S_n}\mathrm{sign}(P) \\ &\times\int \mathrm{D}[\phi_i]M[\phi_i](x_1|x'_{P(1)})\cdots M[\phi_i](x_n|x'_{P(n)})\det\{\mathcal{D}[\phi_i]\}e^{-S_\phi[\phi_i]} \ .\end{aligned} \tag{3.14}$$

The relation above is known as Wick's theorem. Later in this work, we will refer to the individual summands as Wick contractions.

3.2 QCD on the lattice

Our aim is to calculate expectation values by evaluating the corresponding path integral, which we have introduced in section 3.1. We already mentioned that a feasible way is to perform the calculation in discrete and finite Euclidean spacetime via Monte Carlo simulations. This section concerns the appropriate formulation of QCD on the lattice as discussed by Wilson [67]. Introductory literature is given by [68, 69].

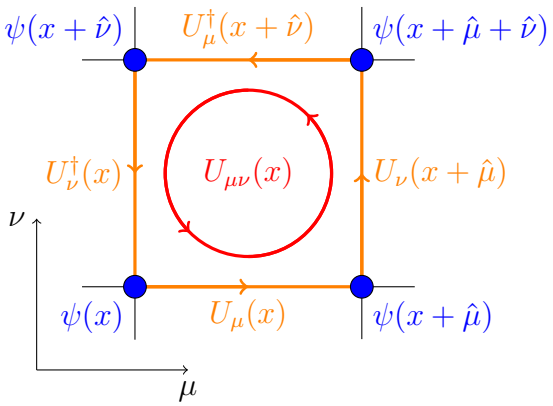

Figure 3.1: Degrees of freedom of QCD on the lattice shown for a two-dimensional subslice in the (μ, ν)-plane. The blue circles at the grid points represent the (anti)quark fields, while the orange lines are the gauge links. The product of all depicted gauge links yields the plaquette $U_{\mu\nu}$, which is represented by the red circle.

3.2.1 Discretization of the QCD action

We construct the lattice QCD Lagrangian in the same manner as we have derived the continuous version (2.18), i.e. we start with the relativistic non-interacting fermion Lagrangian. In Euclidean space the free Lagrangian for one quark flavor can be written as

$$\mathcal{L}_{\text{free}}(x) = \bar{\psi}(x)(\partial_\mu \gamma^\mu + m)\psi(x) \ , \tag{3.15}$$

where γ^μ are the Euclidean gamma matrices (an explicit choice of the basis we use in this work is given in (A.5)).
Now let us define the lattice Λ, where we consider the fermion fields to be placed at the corresponding grid points.

$$\Lambda := \left\{ x = an = a(n^1, n^2, n^3, n^4) | n^\mu \in \mathbb{N}, 0 \leq n^1, n^2, n^3 < L, 0 \leq n^4 < T \right\}, \tag{3.16}$$

i.e. we consider a regular lattice with spatial volume $L^3 a^3$ and time extension Ta, where a is the lattice spacing. The vector connecting two neighboring grid points in μ direction is denoted by $\hat{\mu}$. To recover at least discrete translational invariance under $x \to x + \hat{\mu}$ for all x, one often chooses periodic boundary conditions, i.e. $\psi(x) = \psi(x + L\hat{\mu})$. The Poincaré group, i.e. the original symmetry group, is reduced to the hypercubic group $H(4)$. Naively, the free fermion action $S[\bar{\psi}, \psi]$ is obtained by replacing integrals by sums

over spacetime points and derivatives by differential quotients. Explicitly, this is:

$$\begin{aligned} \int \mathrm{d}^4x\ \bar{\psi}(x)\left(\partial_\mu\gamma^\mu + m\right)\psi(x) \to a^4 \sum_{x,y\in\Lambda} \bar{\psi}(x)\mathcal{D}_{\text{free}}(x|y)\psi(y)\ , \\ \mathcal{D}_{\text{free}}(x|y) = \sum_\mu \frac{\gamma^\mu}{2a}\left(\delta_{x,y+\hat{\mu}} - \delta_{x,y-\hat{\mu}}\right) + m\delta_{x,y}\ . \end{aligned} \tag{3.17}$$

Applying the gauge transformation (2.12), we again notice that the derivative term in the Dirac operator $\mathcal{D}_{\text{free}}$ needs to be corrected in order to restore gauge invariance. This leads to the introduction of the gauge links $U_\mu(x)$ fulfilling the following behavior under gauge transformations:

$$U_\mu(x) \to \Omega(x)U_\mu(x)\Omega^\dagger(x+\hat{\mu})\ . \tag{3.18}$$

Some properties and relations on these gauge links will be discussed later in this work. Using the newly defined gauge links U_μ, we are able to construct a gauge covariant discretized Dirac operator:

$$\mathcal{D}_{\text{naive}}(x|y) = \frac{\gamma^\mu}{2a}\left(\sum_\mu U_\mu(x)\delta_{x,y+\hat{\mu}} - U_\mu^\dagger(x-\hat{\mu})\delta_{x,y-\hat{\mu}}\right) + m\delta_{x,y}\ . \tag{3.19}$$

The definition (3.19) introduces some non-physical artifacts, which is why we call it the "naive" lattice Dirac operator. This issue we shall explain in the following.

3.2.2 Doublers and chiral symmetry

In continuum field theory the Green's function of the Dirac operator describes the propagation of a free Dirac fermion. Therefore, it is called propagator and has exactly as many poles as the number of fermions it is considered to describe. For the massless case this is exactly one fermion, for non-vanishing mass there a two poles, which represent the particle and the antiparticle.
This is crucially different for the naive lattice Dirac operator we have constructed before. To illustrate that, we compare the continuum propagator for massless non-interacting Dirac fermions with the analogue obtained from an inversion on (3.19) with $U_\mu = \mathbb{1}$. Furthermore, we go to momentum space, where we obtain:

$$\mathcal{D}^{-1}_{\text{cont}}(p) = -\frac{i\not{p}}{p^2} \qquad \leftrightarrow \qquad \mathcal{D}^{-1}_{\text{naive}}(p) = -\frac{ia\sum_\mu \gamma^\mu \sin(p_\mu a)}{\sum_\mu \sin(p_\mu a)^2}\ . \tag{3.20}$$

The appearance of sine functions on the r.h.s. is a consequence of the discretization of spacetime, where the accessible momenta are restricted to the range $p^\mu \in (-\pi/a, \pi/a]$. Adding $2\pi/a$ to a given momentum leaves physics invariant. Considering the r.h.s. of (3.20), we find a second pole, located at the boundary of the accessible momentum range at $p^\mu = \pi/a$. This additional pole is identified with an unphysical particle called

doubler. In four dimensions there are 16 poles, i.e. 15 unphysical doublers one has to decouple from the theory in some manner. This is exactly, what is achieved by adding the Wilson term

$$(2a)^{-1} \sum_{\pm\mu} \left(U_\mu(x) \delta_{x+\hat{\mu},y} - 2\delta_{x,y}\ \mathbb{1} \right) \tag{3.21}$$

to $\mathcal{D}_{\text{naive}}$, which has the effect that the doublers acquire an additional mass $\propto a^{-1}$, such that they become infinitely heavy for $a \to 0$. In (3.21) we use negative Lorentz indices to abbreviate $U_{-\mu} = U_\mu^\dagger(x - \hat{\mu})$, see also (A.20). Adding (3.21) to the naive Dirac operator (3.19), we obtain the Wilson-Dirac operator

$$\mathcal{D}_{\text{Wilson}}[U_\mu](x|y) = \frac{1}{2a\kappa} \left[\mathbb{1}\delta_{xy} - \kappa H_{\text{W}}[U_\mu](x|y) \right] \ , \tag{3.22}$$

with the so-called hopping term, which connects neighboring grid points:

$$H_{\text{W}}[U_\mu](x|y) := \sum_{\pm\mu} (\mathbb{1} - \gamma_\mu) U_\mu(x) \delta_{x+\hat{\mu},y} \ . \tag{3.23}$$

The parameter κ is the so-called hopping parameter, which is defined by:

$$2am = \frac{1}{\kappa} - \frac{1}{\kappa_c} \ . \tag{3.24}$$

κ_c is the critical value of κ, where the quark mass vanishes. In the free field case it is $\kappa_c = 1/8$. Once we include interactions, we have to distinguish between the bare quark mass and the renormalized (physical) quark mass. Therefore, κ_c is different from the free case. Through the chiral relation $m_\pi^2 \propto m$ the value of κ_c is equal to the value of κ, where the pion becomes massless.
Adding the Wilson term as in (3.22) comes with a big price: In the massless case the continuous Dirac operator, as well as the naive lattice Dirac operator, was invariant under chiral rotations $\psi \to e^{i\alpha\gamma_5}\psi$ where α denotes the chiral angle. Any mass-like term in the Lagrangian breaks this symmetry explicitly. When adding the Wilson term, we introduced a mass-like expression, such that we loose chiral symmetry even in the massless case. It was shown in the past [70] that it is not possible to remove doublers and retain chiral symmetry at the same time. This fact is known as Nielsen-Ninomiya theorem. Only in the continuum limit $a \to 0$ chiral symmetry is restored.

3.2.3 Discrete symmetries

Having defined the theory on a Euclidean lattice, we want to list some properties of the fields under discrete symmetry operations.
The previously derived Wilson-Dirac operator is γ_5-Hermitian

$$\gamma_5 \mathcal{D}(x|y)[U_\mu]^\dagger \gamma_5 = \mathcal{D}(x|y)[U_\mu] \ . \tag{3.25}$$

We anticipate here that this will also hold, when we add the clover term later. An important implication of this relation is that the determinant $\det\{\mathcal{D}\}$ is real-valued.
The symmetry operation interchanging the role of quarks and antiquarks is known as charge conjugation. The fermion fields and gauge links are transformed in the following way under charge conjugation:

$$\psi(x) \xrightarrow{\mathcal{C}} C^{-1}\bar{\psi}^T(x) \ , \qquad \bar{\psi}(x) \xrightarrow{\mathcal{C}} -\psi^T(x)C \ , \qquad U_\mu(x) \xrightarrow{\mathcal{C}} U_\mu^*(x) \ . \tag{3.26}$$

C is a Dirac matrix that has to fulfill the following relation

$$C\gamma_\mu C^{-1} = -\gamma_\mu^T \ . \tag{3.27}$$

The explicit form of C depends on the chosen Dirac basis.
Two further discrete symmetry operations are parity

$$\mathcal{P}x = (La - x_1, La - x_2, La - x_3, x_4) \ , \tag{3.28}$$

and time reflection

$$\mathcal{T}x = (x_1, x_2, x_3, La - x_4) \ . \tag{3.29}$$

Under parity operations the fermion fields and gauge links transform as:

$$\psi(x) \xrightarrow{\mathcal{P}} \gamma_4\psi(\mathcal{P}x) \ , \qquad \bar{\psi}(x) \xrightarrow{\mathcal{P}} \bar{\psi}(\mathcal{P}x)\gamma_4 \ , \qquad U_\mu \xrightarrow{\mathcal{P}} \begin{cases} U_\mu(\mathcal{P}x) & \mu = 4 \\ U_\mu^\dagger(\mathcal{P}x - \hat{\mu}) & \text{else} \end{cases} \ . \tag{3.30}$$

The discussion of time reflection is more involved. The corresponding operation is understood to be anti-unitary. By considering the path integral in Euclidean spacetime, it can be shown that the fermion fields ψ, $\bar{\psi}$ transform as

$$\psi(x) \xrightarrow{\mathcal{T}} -T^{-1}\bar{\psi}^T(\mathcal{T}x) \ , \qquad \bar{\psi}(x) \xrightarrow{\mathcal{T}} \psi^T(\mathcal{T}x)T \ , \tag{3.31}$$

where the T is a Dirac matrix fulfilling

$$-T = T^\dagger = T^T = T^{-1} = \gamma_5 T \gamma_5 \ . \tag{3.32}$$

By considering invariance under time reflections, one finds for the gauge links:

$$U_\mu(x) \to \begin{cases} U_\mu^T(\mathcal{T}x - \hat{\mu}) & \mu = 4 \\ U^*(\mathcal{T}x) & \text{else} \end{cases} \ . \tag{3.33}$$

For the discussion on time reflection in Euclidean spacetime we refer to [71].
Considering the lattice quark propagator $M(x|y)[U_\mu]$ obtained from an inversion of the

Wilson-Dirac operator, the symmetry relations stated above imply:

$$\begin{aligned} M(x|y)[U_\mu] &= \gamma_5 M^\dagger(y|x)[U_\mu]\gamma_5 \ , \\ M(x|y)[U_\mu] &\xrightarrow{\mathcal{C}} C^{-1} M^T(y|x)[U_\mu^*]C \ , \\ M(x|y)[U_\mu] &\xrightarrow{\mathcal{P}} \gamma_4 M(\mathcal{P}x|\mathcal{P}y)[U_\mu^{\mathcal{P}}]\gamma_4 \ , \\ M(x|y)[U_\mu] &\xrightarrow{\mathcal{T}} T^{-1} M^T(\mathcal{T}y|\mathcal{T}x)[U_\mu^{\mathcal{T}}]T \ . \end{aligned} \tag{3.34}$$

Explicit expressions for the Dirac matrices C and T in our basis are given in (A.7).

3.2.4 The Wilson gauge action

With the definition of the gauge covariant derivative on the lattice, we introduced the gauge links U_μ obeying the transformation behavior (3.18). In order to derive the free gauge action, we want to discuss relations to the gauge fields A_μ being used for the continuum formulation.
The transformation (3.18) is the same as for gauge transporters in the continuum, which connect two points via a certain path. Therefore, it seems natural to interpret the gauge link $U_\mu(x)$ as a gauge transporter from x to $x+\hat{\mu}$ through a straight line, which is exact up to $\mathcal{O}(a)$. Hence, we identify

$$U_\mu(x) = e^{iaA_\mu(x)} \xrightarrow{a\to 0} \mathbb{1} + iaA_\mu(x) \ . \tag{3.35}$$

After rescaling the gauge fields $A(x) \to g_0^{-1}A(x)$, inserting (3.35) in the gauge covariant lattice Dirac operator, e.g. (3.19), and taking the limit $a \to 0$ reproduces the same expression as given by the continuum Lagrangian (2.18).
Each closed product of gauge links is gauge invariant by construction and, therefore, a candidate in the formulation of the free gauge Lagrangian on the lattice. The simplest expression is the so-called plaquette

$$U_{\mu\nu}(x) := U_\mu(x)U_\nu(x+\hat{\mu})U_{-\mu}(x+\hat{\mu}+\hat{\nu})U_{-\nu}(x+\hat{\nu}) \ , \tag{3.36}$$

which is the smallest loop in the (μ,ν)-plane, meaning that it is built only from four links. Notice that in this formula we used the notation (A.20). Again considering the continuum limit, we find that the following expression yields the continuum Lagrangian:

$$S_{\mathrm{G}}[U_\mu] := \frac{\beta}{3}\sum_x \sum_{\mu<\nu} \mathrm{Re}\ \mathrm{tr}\left\{\mathbb{1} - U_{\mu\nu}(x)\right\} \ , \tag{3.37}$$

where β is proportional to the inverse squared bare coupling g_0^2. In four dimensions its exact relation to the coupling is

$$\beta = \frac{6}{g_0^2} \ . \tag{3.38}$$

In Figure 3.1 the plaquette (3.36) is depicted by a red circle.

3.2.5 Symanzik improvement

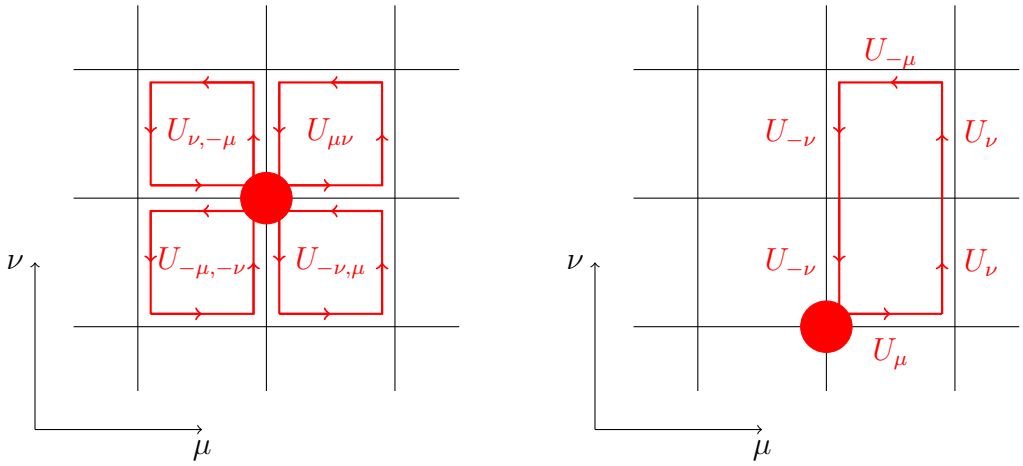

Figure 3.2: The clover term $Q_{\mu\nu}(x)$ (left) and the rectangle $\tilde{U}_{\mu\nu}(x)$ (right), shown in the (μ,ν)-plane. The red circle shows the position x, where Q and $\tilde{U}$ are defined.

The formulation of QCD in discrete spacetime is an approximation which is good up to a certain order of the lattice spacing a. In the case of Wilson fermions the discretization errors are of order $\mathcal{O}(a)$. However, errors of order $\mathcal{O}(a^n)$ may be removed by adding correction terms sharing the symmetries of the improved quantity and having dimension $energy^{4+n}$. The systematic identification of those correction terms is known as Symanzik improvement program. In the following, we want to give the corresponding expression for $\mathcal{O}(a)$ improvements. It was shown by Sheikholeslami and Wohlert [72] that the only correction term for Wilson fermions is the so-called clover term, which is illustrated in Figure 3.2:

$$C[U_\mu](x|y) := -\frac{i}{16a^2}\sigma^{\mu\nu}Q_{\mu\nu}(x)\delta_{xy} \ , \tag{3.39}$$

with the sum over all plaquettes in the (μ,ν)-plane that include the site x:

$$Q_{\mu\nu}(x) := U_{\mu,\nu}(x) + U_{\nu,-\mu}(x) + U_{-\mu,-\nu}(x) + U_{-\nu,\mu}(x) \ . \tag{3.40}$$

The origin of the name is deduced from the shape of the contributing plaquettes around x in the (μ,ν)-plane. Putting everything together, we can write the $\mathcal{O}(a)$-improved Wilson-Dirac operator as:

$$\mathcal{D}_{\mathrm{SW}}[U_\mu](x|y) = \frac{1}{2a\kappa}\left[\mathbb{1}\delta_{xy} - \kappa H_{\mathrm{W}}[U_\mu](x|y)\right] + ac_{\mathrm{SW}}C[U_\mu](x|y) \ . \tag{3.41}$$

c_{SW} is the Sheikholeslami-Wohlert coefficient, which can be determined non-perturbatively as described in [73] for $n_f = 3$.
For the pure gauge part of the action S_{G} there also exist improvements. In the context of this work we want to point out the Lüscher-Weisz action [74], which is tree level improved to $\mathcal{O}(g^2a^2)$:

$$S_{\mathrm{LW}}[U_\mu] = \frac{c_0}{2} S_{\mathrm{G}}[U_\mu] + \frac{c_1\beta}{6} \sum_x \sum_{\mu\neq\nu} \mathrm{Re}\,\mathrm{tr}\left\{\mathbb{1} - \tilde{U}_{\mu\nu}(x)\right\} \ , \tag{3.42}$$

where $\tilde{U}_{\mu\nu}$ is an object built from gauge links in the shape of a rectangle, as depicted in Figure 3.2:

$$\tilde{U}_{\mu\nu}(x) := U_\mu(x) U_\nu(x+\hat{\mu}) U_\nu(x+\hat{\mu}+\hat{\nu}) U_\mu^\dagger(x+2\hat{\nu}) U_\nu^\dagger(x+\hat{\nu}) U_\nu^\dagger(x) \ . \tag{3.43}$$

Finally, we want to give a complete expression of the lattice action including $\mathcal{O}(a)$-improved Sheikholeslami-Wohlert fermions and the tree-level improved gauge action:

$$S[\psi, \bar{\psi}, U_\mu] = a^4 \sum_f \bar{\psi}^f \mathcal{D}^f_{\mathrm{SW}}[U_\mu] \psi^f + S_{\mathrm{LW}}[U_\mu] \ . \tag{3.44}$$

This action we use for the simulation described in chapter 4.

3.2.6 Monte Carlo simulations and lattice QCD

The evaluation of an expectation value according to (3.9) requires the calculation of a high-dimensional integral over all relevant degrees of freedom. A suitable method for that is Monte Carlo Integration. In one dimension it is based on the principle that any integral can be approximated by a sum over integrand values that correspond to randomly chosen points x_n being uniformly distributed within the integration range:

$$\int_a^b \mathrm{d}x \ f(x) = \lim_{N\to\infty} \frac{b-a}{N} \sum_{x_n\in[a,b]} f(x_n) \ . \tag{3.45}$$

The result yields the integral value within an error which decreases like $\propto 1/\sqrt{N}$ when the number of samples N is increased. The convergence can be improved by importance sampling if the function f may be decomposed in the form $f(x) = g(x)w(x)$, where $w(x) > 0$ is a real function. This can be used as weight function, when choosing the points where the function is evaluated. The integral is then obtained by:

$$\frac{1}{Z_w} \int_a^b \mathrm{d}x \ f(x) = \int_a^b \mathrm{d}P(x) \ g(x) = \lim_{N\to\infty} \frac{1}{N} \sum_{x_n\in[a,b]} g(x_n) \ , \tag{3.46}$$

with x_n distributed according to $\mathrm{d}P(x)$:

$$\mathrm{d}P(x) = Z_w^{-1} w(x)\ \mathrm{d}x\ , \qquad Z_w = \int_a^b \mathrm{d}x\ w(x)\ . \tag{3.47}$$

The path integrals appearing in QCD calculations require the integration over gauge fields only. The fermionic part is evaluated using Wick's theorem (3.14). At this point we again want to emphasize the importance of employing Euclidean spacetime. Considering the path integral in Minkowski time (3.4), there is no term that can be taken as a suitable weight factor, whereas in Euclidean spacetime such a function is given by the action term e^{-S}.
The evaluation of the fermionic path integral by applying Wick's theorem yields further terms involving the determinant of the Dirac operator. These can be treated as part of the distribution weight. Here one has to take the product w.r.t. all considered flavors.
In total, Monte Carlo integration in the context of QCD expectation values is realized by evaluating the observable on a gauge ensemble, i.e. a set of gauge configurations U_μ^i being distributed according to:

$$P[U_\mu] = \mathrm{D}[U_\mu]\ e^{-S_{\mathrm{LW}}[U_\mu]} \prod_f \det\left\{\mathcal{D}^f_{\mathrm{SW}}[U_\mu]\right\}\ . \tag{3.48}$$

The expectation value is then obtained by a sum over all samples $\mathcal{O}(U_\mu^i)$ of the observable $\mathcal{O}$.

$$\langle\mathcal{O}\rangle_U = \frac{1}{N}\sum_i \mathcal{O}(U_\mu^i)\ . \tag{3.49}$$

Notice that, although γ_5-hermiticity seems to guarantee positivity, the fermion determinant in (3.48) can become negative due to fluctuations, which would inhibit us from using it as a suitable weight. This is in particular the case if the corresponding quark mass is very small. However, if there are two quark flavors of degenerate mass spectrum, as it is assumed for the u and d quark, $\mathcal{D}^u = \mathcal{D}^d$ and therefore $\det\{\mathcal{D}^u\}\det\{\mathcal{D}^d\} \geq 0$. If the mass is high enough, as it is considered in the case of the strange quark, negative eigenvalues are unlikely.
The gauge ensembles are generated by so-called Markov chains of gauge configurations, where the configuration U_n is obtained from U_{n-1} by random modifications and accepted according to a transition probability $T(U_n|U_{n-1})$ which satisfies:

$$0 \leq T(U_n|U_{n-1}) \leq 1\ , \qquad \sum_U T(U|U_{n-1}) = 1\ . \tag{3.50}$$

The procedure must be strongly ergodic, meaning that every possible configuration has to be accessible by the algorithm.
Once the Markov chain has reached equilibrium, the possibility of accessing a specific state has to be equal to that of leaving this state. This property can be achieved by

requiring $T(U_n|U_{n-1})$ to fulfill detailed balance:

$$T(U_n|U_{n-1})P(U_{n-1}) = T(U_{n-1}|U_n)P(U_n) \ , \tag{3.51}$$

where $P(U)$ refers to probability of the configuration U, which in our case is given by (3.48). This condition is employed e.g. by the Metropolis algorithm, which is frequently used for the generation of gauge ensembles. Here the configuration U_{n-1} is updated by a small modification of the gauge fields causing a change of the action ΔS. The resulting configuration is accepted with a probability $\propto \min(1, \exp\{\Delta S\})$. The simulation of fermionic fields is technically challenging because of the non-locality of the fermion determinant. A suitable method to handle fermions is given by the hybrid Monte Carlo (HMC) algorithm [75], where the updating procedure is realized by trajectories given by an iterative evolution of the molecular dynamics equations. Furthermore, the Grassmann integral is replaced by a Gaussian integral over pseudofermionic fields.
In practice the gauge ensembles are not generated using the distribution (3.48), but rather one uses a modified version in order to increase performance and stability. For the ensemble we use in our simulations this is described in detail in [76]. We give a brief overview of the modifications and list the subsequent reweighting factors that have to be included in the calculation of observables. As described before, the two light quarks, which are approximated as having the same mass, are simulated together, where the combined fermion determinant $\det\{\mathcal{D}\}\det\{\mathcal{D}\} = \det\{\gamma_5\mathcal{D}\gamma_5\}\det\{\mathcal{D}\} = \det\{\gamma_5\mathcal{D}\gamma_5 D\} = \det\{Q^2\}$ is used. Here $Q := \gamma_5\mathcal{D}$ denotes the Hermitian Dirac operator. The Dirac operator may have eigenvalues close to zero, which leads to a reduced stability of the algorithm. In order to separate these low modes of the Dirac operator, an infra-red cutoff is introduced by a so-called twisted mass μ term [77]. This is applied to the Schur complement of the asymmetrically even-odd preconditioned Dirac operator [78]. Following the notation of [76], it is denoted by $\hat{Q}$. The low modes are re-included by multiplying each sample of the observable by the reweighting factor W_0, which is defined as:

$$W_0 = \det\left\{ \frac{\left(\hat{Q}^2 + 2\mu^2\right)\hat{Q}^2}{\left(\hat{Q}^2 + \mu^2\right)^2} \right\} \ . \tag{3.52}$$

For the simulation of the strange quark the rational HMC (RHMC) algorithm [79] is employed, where in the calculation of the corresponding fermion determinant one uses a rational function to approximate the involved matrix square root. The introduced deviations have to be compensated by another reweighting factor W_1, which is implicitly defined by (3.5) in [79].
For each observable being calculated on an ensemble that is generated in the described manner, we have to reweight each sample corresponding to a given gauge configuration

U_μ^i:

$$\langle \mathcal{O} \rangle_U = \frac{1}{N} \sum_i \mathcal{O}_i = \frac{1}{N} \sum_i W_0^i \; W_1^i \; \mathcal{O}(U_\mu^i) \; . \tag{3.53}$$

3.3 Euclidean correlation functions

Let us now take a closer look at correlation functions of two or more operators separated in Euclidean time direction. As already mentioned, this cannot be related to a dynamic variable, because we switched to imaginary time. However, such correlation functions provide physical information we are interested in. This we want to describe in the following.
We consider a theory described by its Hamiltonian $\mathcal{H}$ with an orthonormal set of eigenstates $|n\rangle$ with energy eigenvalues E_n. These are supposed to be sorted such that $E_n < E_{n+1}$ for each n. Without loss of generality, we are free to shift the energy spectrum, such that the vacuum energy is $E_0 = 0$. Starting from (3.9) we can give an expression for a Euclidean correlation function of two operators $\mathcal{O}_1$ and $\mathcal{O}_2$ constructed from the field operators $\hat{\phi}_i$. In a finite spacetime with time extension T this reads:

$$\begin{aligned} \langle \mathcal{O}_2(t) \mathcal{O}_1(0) \rangle &= Z^{-1} \int \mathrm{D}\left[\phi_i\right] \mathcal{O}_2(t) \mathcal{O}_1(0) e^{-S[\phi_i]} \\ &= \frac{\mathrm{tr}\left\{ e^{-(T-t)\mathcal{H}} \; \mathcal{O}_2 \; e^{-t\mathcal{H}} \; \mathcal{O}_1 \right\}}{\mathrm{tr}\left\{ e^{-T\mathcal{H}} \right\}} \; . \end{aligned} \tag{3.54}$$

In the last line we assume periodic boundary conditions in time of the fields ϕ_i, i.e. $\phi_i(T, \vec{x}) = \phi_i(0, \vec{x})$. The integral over the fields at the boundary can then be identified with the trace of the operator product. The same applies for the partition function in the denominator. Expressing the trace in terms of energy eigenstates yields:

$$\langle \mathcal{O}_2(t) \mathcal{O}_1(0) \rangle = Z^{-1} \sum_n \langle n | \, e^{-(T-t)\mathcal{H}} \; \mathcal{O}_2 \; e^{-t\mathcal{H}} \; \mathcal{O}_1 \, | n \rangle \; , \tag{3.55}$$

with the partition function

$$Z = \sum_n \langle n | \, e^{-T\mathcal{H}} \, | n \rangle = \sum_n e^{-TE_n} \; . \tag{3.56}$$

We call the expression on the l.h.s. in (3.55) two-point function. Inserting a complete set of eigenstates on the r.h.s. , we can pull out the exponentials by replacing the Hamiltonian by the corresponding energy eigenvalue. Considering the limit of an infinite time extension, we find a suppression of each term containing T in the exponential except for the cases, where the energy is zero. The partition function becomes $Z \to 1$ in this

case. Hence, we can write:

$$\begin{aligned}\langle \mathcal{O}_2(t)\mathcal{O}_1(0)\rangle &= Z^{-1}\sum_{n,m}\langle n|\,\mathcal{O}_2\,|m\rangle\,\langle m|\,\mathcal{O}_1\,|n\rangle\,e^{-(T-t)E_n}\;e^{-tE_m}\\ &\xrightarrow{T\to\infty}\sum_{m}\langle 0|\,\mathcal{O}_2\,|m\rangle\,\langle m|\,\mathcal{O}_1\,|0\rangle\,e^{-tE_m}\;.\end{aligned} \tag{3.57}$$

In the last line we see that Euclidean correlation of the two operators decomposes in terms of the eigenstates $|m\rangle$. The higher their energy is, the stronger the corresponding contribution decays with increasing time separation. If t is sufficiently large, we are able to relate the slope of the correlation function in t to the energy of the eigenstate with the lowest eigenvalue, i.e. the ground state.
In the same manner we can treat correlation functions of three or more operators. For our purpose we need to consider three operators or products of operators at three distinct times. These we choose to be t, τ and 0. Performing similar steps as we did for the derivation of (3.57) we find:

$$\langle \mathcal{O}_3(t)\mathcal{O}_2(\tau)\mathcal{O}_1(0)\rangle|_{T=\infty} = \sum_{m,l}\langle 0|\,\mathcal{O}_3\,|l\rangle\,\langle l|\,\mathcal{O}_2\,|m\rangle\,\langle m|\,\mathcal{O}_1\,|0\rangle\,e^{-(t-\tau)E_l}\;e^{-\tau E_m}\;. \tag{3.58}$$

Again it holds that, if the time separations appearing in the exponentials are large, the entire expression is dominated by the states with the lowest energy eigenvalue. In this case the r.h.s. is directly related to the ground state matrix element. Therefore we can use Euclidean correlation functions to extract hadronic matrix elements, given that we find operators $\mathcal{O}_1$ and $\mathcal{O}_3$ which have non-vanishing overlap with the corresponding hadron ground state. This will be discussed in the following section.

3.4 Hadronic matrix elements on the lattice

We conclude this chapter by describing the procedure of the calculation of matrix elements for certain hadrons by using the formalisms and techniques we presented before. Furthermore, we introduce a certain kind of operators we want to consider within this study and describe how they are renormalized in order enable a physical interpretation.

3.4.1 Basic evaluation procedure

The operators $\mathcal{O}_1$ and $\mathcal{O}_3$ appearing in (3.58) are supposed to annihilate or create states having the same quantum numbers as the state we are interested in. For hadron physics these are spin, parity and flavor quantum numbers like isospin and, if the hadron is free of charge, the charge conjugation phase. These operators, also called hadron interpolators, usually create the simplest Fock state, i.e. a quark-antiquark (mesons) or three-quark state (baryons), respectively. E.g. for baryons they can be written as:

$$|qqq\rangle = \alpha_0\,|b\rangle + \sum_n \alpha_n\,|b^{(n)}\rangle\,, \tag{3.59}$$

where $|b\rangle$ describes the baryon to be investigated, which has a certain overlap α_0 with the three-quark state $|qqq\rangle$. The remaining contributions appearing in (3.59) correspond to excitations. There are methods to increase the overlap α_0, while the other coefficients α_n, i.e. the excited state contributions, are reduced. These are referred to as smearing techniques, where the originally local three-quark state receives a spatial wave function. This increases the overlap with the baryonic state. The smearing method used in our analysis shall be introduced in section 4.3.1.
In the following, we consider the interpolators $\overline{\mathcal{J}}_h(x)$, $\mathcal{J}_h(x)$ creating or annihilating the hadron h. These interpolators are formulated in position space. For definite momentum we have to project them by a discrete Fourier transform:

$$\mathcal{J}_h(\vec{p},t) = a^3 \sum_{\vec{x}} e^{-i\vec{p}\vec{x}}\, \mathcal{J}_h(\vec{x},t)\ , \qquad \overline{\mathcal{J}}_h(\vec{p},t) = a^3 \sum_{\vec{x}} e^{i\vec{p}\vec{x}}\, \overline{\mathcal{J}}_h(\vec{x},t)\ . \tag{3.60}$$

The interpolators may carry further indices according to their transformation behavior in the Lorentz group. For spinless particles they are scalar, whereas for spin-1/2 particles they are Dirac spinors, etc.
In the following, we denote the ground state by $|p,\lambda\rangle$, where λ is used for labeling a possible degeneracy in the energy spectrum, e.g. states with different spin quantum number. Furthermore, we consider an operator or a product of operators $\mathcal{O}$, which corresponds to the operator $\mathcal{O}_2$ in (3.58). The type of operators being relevant in this work is introduced in section 3.4.2. Taking the limit as described in the previous section, we arrive at the expression:

$$\sum_{\lambda\lambda'} U(p,\lambda)\, \langle p,\lambda|\, \mathcal{O}(\tau)\, |p,\lambda'\rangle\, \overline{U}(p,\lambda') e^{-(t-\tau)E_h(\vec{p})}\ e^{-\tau E_h(\vec{p})}\ , \tag{3.61}$$

with the interpolator overlap terms

$$\begin{aligned} U(p,\lambda) &:= \langle 0|\, \mathcal{J}_h(\vec{p},t)\, |p,\lambda\rangle\ , \\ \overline{U}(p,\lambda) &:= \langle p,\lambda|\, \overline{\mathcal{J}}_h(\vec{p},t)\, |0\rangle\ . \end{aligned} \tag{3.62}$$

To isolate the desired matrix element, we have to eliminate the exponentials and overlap terms, which can be achieved by a division by a two-point function of hadron interpolators. Since the overlap terms are in general not scalar, we have to project out the desired quantity by a suitable operator P. This can be e.g. a certain polarization or parity. The relation to the matrix element is given by:

$$\begin{aligned} &\frac{\sum_{\lambda\lambda'} \left[\overline{U}(p,\lambda') P U(p,\lambda)\right]\, \langle p,\lambda|\, \mathcal{O}\, |p,\lambda'\rangle|_{\text{latt}}}{\sum_{\lambda} \left[\overline{U}(p,\lambda) P U(p,\lambda)\right]} \\ &\quad = \left.\frac{\left\langle \text{tr}\left\{P \mathcal{J}_h(\vec{p},t)\ \mathcal{O}(\tau)\ \overline{\mathcal{J}}_h(\vec{p},0)\right\}\right\rangle}{\left\langle \text{tr}\left\{P \mathcal{J}_h(\vec{p},t)\ \overline{\mathcal{J}}_h(\vec{p},0)\right\}\right\rangle}\right|_{0\ll\tau\ll t} . \end{aligned} \tag{3.63}$$

The [.] notation indicates a scalar quantity and traces are taken w.r.t. spin indices. Notice that, if the initial and final state momenta are different, the ratio to be calculated has to be extended accordingly. The subscript "latt" is for distinguishing the normalization of states for a given momentum on the lattice or in the continuum, respectively. Expressing the matrix elements in the continuum causes an extra factor $2V\sqrt{\vec{p}^2+m^2}$, where $V = L^3a^3$ is the spatial lattice volume. The continuum value of the matrix element is given by:

$$\langle p,\lambda|\,\mathcal{O}\,|p,\lambda'\rangle|_{\text{cont}} = 2V\sqrt{\vec{p}^2+m^2}\;\;\langle p,\lambda|\,\mathcal{O}\,|p,\lambda'\rangle|_{\text{latt}}\;\;. \tag{3.64}$$

Finally, let us consider fermionic (anti-commuting) fields in the correlation function. We already mentioned that the interpolators are constructed from quark fields and also the operator $\mathcal{O}$ may contain fermions. Hence, we can apply Wick's theorem (3.14). We again write down the corresponding formula, considering the degrees of freedom of the LQCD Lagrangian (3.44). These are the fermions $\psi^f_{\alpha a}(x)$ of flavor f with spinor index α and color index a. Notice that the LQCD Lagrangian is diagonal w.r.t. flavor indices, which is why the propagator M has to conserve the quark flavor. The remaining degrees of freedom are represented by the gauge links $U_\mu(x)$, which we still have to integrate over:

$$\begin{aligned}\left\langle \hat{\psi}^{f_1}_{\alpha_1 a_1}(x_1)\hat{\bar{\psi}}^{f'_1}_{\beta_1 b_1}(x'_1)\cdots\hat{\psi}^{f_n}_{\alpha_n a_n}(x_n)\hat{\bar{\psi}}^{f'_n}_{\beta_n b_n}(x'_n)\right\rangle &= \frac{(-1)^n}{Z}\sum_{P\in S_n}\text{sign}(P)\int \mathrm{D}[U_\mu]\\ &\times\left(M^{f_1}[U_\mu]\right)^{a_1 b_{P(1)}}_{\alpha_1\beta_{P(1)}}(x_1|x'_{P(1)})\cdots\left(M^{f_n}[U_\mu]\right)^{a_n b_{P(n)}}_{\alpha_n\beta_{P(n)}}(x_n|x'_{P(n)})\\ &\times\delta_{f_1 f'_{P(1)}}\cdots\delta_{f_n f'_{P(n)}}\;e^{-S_{\text{LW}}[U_\mu]}\;\prod_f\det\{\mathcal{D}^f_{\text{SW}}[U_\mu]\}\;.\end{aligned} \tag{3.65}$$

The propagator M^f is obtained by solving the equation

$$\mathcal{D}^f_{\text{SW}}M^f = \mathbb{1}\;, \tag{3.66}$$

where $\mathcal{D}_{\text{SW}}$ is the $\mathcal{O}(a)$-improved Wilson-Dirac operator (3.41). The Kronecker deltas appearing in (3.65) guarantee the aforementioned flavor conservation of the propagators. The integral (3.65) is evaluated by Monte Carlo integration w.r.t. the gauge fields U_μ according to description in section 3.2.6.

3.4.2 Local operators

Within this study we consider matrix elements involving local quark bilinears that do not contain derivative terms. These are operators of the form:

$$\mathcal{O}^{qq'}_j(y) := \bar{q}(y)\;\Gamma_j\;q'(y)\;, \tag{3.67}$$

where Γ_i corresponds to a certain Dirac structure. We distinguish between three types of operators:

$$\begin{aligned} V^{\mu}_{qq'}(y) &= \bar{q}(y)\ \gamma^{\mu}\ q'(y) && \text{(vector)}\ , \\ A^{\mu}_{qq'}(y) &= \bar{q}(y)\ \gamma^{\mu}\gamma_5\ q'(y) && \text{(axial vector)}\ , \\ T^{\mu\nu}_{qq'}(y) &= \bar{q}(y)\ \sigma^{\mu\nu}\ q'(y) && \text{(tensor)}\ . \end{aligned} \tag{3.68}$$

There are two further operators types that are known as scalar and pseudoscalar currents. These we shall not consider in this work. We are interested in matrix elements of these operators defined in Minkowski spacetime, where they obey the following transformation behavior under charge conjugation and the combination of time reflection and parity:

$$\begin{aligned} \mathcal{O}_j^{qq'}(y) &\xrightarrow{C} \eta_C^j \mathcal{O}_j^{q'q}(y)\ , \\ \mathcal{O}_j^{qq'}(y) &\xrightarrow{PT} \eta_{PT}^j \mathcal{O}_j^{q'q}(-y)\ , \end{aligned} \tag{3.69}$$

with

$$\eta_C^j \in \begin{cases} 1 & j = A \\ -1 & j = V, T \end{cases}\ , \tag{3.70}$$

and

$$\eta_{PT}^j \in \begin{cases} 1 & j = V \\ -1 & j = A, T \end{cases}\ . \tag{3.71}$$

Furthermore, we can write down the Hermitian conjugate

$$\mathcal{O}_j^{qq'\dagger}(y) = \mathcal{O}_j^{q'q}(y)\ , \tag{3.72}$$

i.e. the operator is Hermitian in the case, where it conserves the quark flavor.
Since the calculation is performed in imaginary time, one should also discuss how the operators are translated when going to Euclidean spacetime. For $y^0 = 0$ we can give the following relation between the operators in Euclidean and Minkowski spacetime [80]:

$$\mathcal{O}_{j,E}^{qq'}(y) = i^n \eta_E^j \mathcal{O}_{j,M}^{qq'}(y)\ , \tag{3.73}$$

where the subscript E and M denote the versions in Euclidean or Minkowski spacetime, respectively. The power n of the imaginary unit is equal to the number of Lorentz indices

being 0 (or 4 in Euclidean notation). η_E^i takes the following values:

$$\eta_E^j \in \begin{cases} -i & j = V \\ i & j = A \\ -1 & j = T \end{cases} . \tag{3.74}$$

3.4.3 Renormalization

Field theoretical calculations in the continuum involve ultraviolet divergences, which have to be regularized appropriately. Physical interpretations require a subsequent renormalization procedure, which depends on the regularization scheme. In continuum calculations a frequently used scheme is dimensional regularization followed by renormalization within the $\overline{\text{MS}}$ scheme.
The discretization of spacetime introduces a regularization scheme where divergences are controlled by the lattice spacing a, which acts as an ultraviolet cutoff. In order to obtain the physical quantities from the objects being evaluated in such scheme, they have to be renormalized appropriately. In particular, this concerns quark fields and the operators (3.67). These operators are renormalized multiplicatively at a renormalization scale μ:

$$\mathcal{O}_\mu^R = Z_\mathcal{O}(\mu)\mathcal{O} \ , \tag{3.75}$$

The renormalization constants $Z_\mathcal{O}(\mu)$ are determined by imposing certain renormalization conditions given by the renormalization scheme. In the following, we sketch the scheme that we use for the renormalization of the lattice operators (3.67). The method is based on the so-called regularization independent (RI) scheme, which has been proposed in [81]. In the present case the RI′ scheme [82] is used, which differs from the RI scheme in the determination of the quark field renormalization constant. In the previously mentioned schemes one considers the renormalized amputated quark bilinear vertex function in Landau gauge

$$\Lambda_\Gamma(p) = S^{-1}(p) G_\Gamma(p) S^{-1}(p) \ , \tag{3.76}$$

with

$$\begin{aligned} G_\Gamma(p) &= \frac{1}{V} \sum_{xyz} e^{-ip(x-y)} \left\langle M(x|z) \Gamma M(z|y) \right\rangle \\ S(p) &= \frac{1}{V} \sum_{xy} e^{-ip(x-y)} \left\langle M(x|y) \right\rangle \end{aligned} \tag{3.77}$$

The renormalization condition in the RI′ scheme is given by imposing $\Lambda_\Gamma(p)$ to be equal to its tree-level counterpart, i.e. :

$$\frac{Z'_\Gamma}{Z'_q}\Lambda_\Gamma(p)\bigg|_{p^2=\mu^2} = \Gamma \ , \tag{3.78}$$

where Z'_q denotes the quark field renormalization constant. It is directly obtained by relating the free propagator $M^{\text{free}}(p)$ in momentum space with its interacting analogue $S(p)$:

$$Z'_q(\mu) = \frac{1}{12}\,\text{tr}\left\{S^{-1}(p)M^{\text{free}}(p)\right\}\bigg|_{p^2=\mu^2} \ , \tag{3.79}$$

where the trace is taken over spin and color, which is why we have to include the normalization by a factor 12. The renormalization scale is given by $\mu^2 = p^2$. Altogether, the renormalization constant reads:

$$Z'_\Gamma(\mu) = \frac{12Z'_q}{\text{tr}\left\{\Lambda_\Gamma(p)\Gamma^{-1}\right\}}\bigg|_{p^2=\mu^2} \ . \tag{3.80}$$

The RI′ scheme can be implemented in continuum perturbation theory, which allows a conversion of the renormalization factors to the aforementioned $\overline{\text{MS}}$ scheme .

4 Two-current correlations in the proton on the lattice

In contrast to single-current matrix elements, two-current matrix elements are sensitive to charge correlations. Therefore, evaluating matrix elements of two operators provides an important piece of information describing the internal hadron structure. In the past, hadronic matrix elements involving two currents have been investigated on the lattice in the context of various physical aspects like confinement [83, 84], the size of hadrons [85–88], spatial quark distributions and comparisons with quark models [89, 90], or the shape of hadrons [91–93]. Within recent studies two-current matrix elements in the short distance limit have been used to directly access PDFs in position space [94].
Our motivation to study two-current correlations is their relation to double parton distributions. In the following, we want to introduce matrix elements of two operator insertions for the proton and describe their evaluation on the lattice. We give an overview of all contributing Wick contractions and the techniques that are used for the calculation. We present some properties of the CLS ensemble that is used for this first study, before some results on two-current correlations in the proton are shown. A similar study of two-current correlations in the pion has been performed in [45].

4.1 Definition and properties

For the proton at momentum p we define the matrix element of two currents being represented by local quark bilinears defined in (3.67), which are separated by the purely spatial vector y, i.e. $y^0 = 0$. In this first study we do not aim to investigate effects arising from the proton polarization. Instead we always take the spin average:

$$\mathcal{M}_{ij}^{q_k}(p,y) := \frac{1}{2}\sum_{\lambda} \langle p,\lambda|\, \mathcal{O}_i^{q_1 q_2}(0)\; \mathcal{O}_j^{q_3 q_4}(y)\, |p,\lambda\rangle \Big|_{y^0=0} \,. \tag{4.1}$$

The operators (3.67) are understood to commute if y is space-like, which is the case in our framework, since $y^0 = 0$. Therefore, it holds that

$$\mathcal{M}_{ij}^{q_1 q_2 q_3 q_4}(p,y) = \mathcal{M}_{ji}^{q_3 q_4 q_1 q_2}(p,-y) \,. \tag{4.2}$$

Together with the hermiticity relation (3.72) it follows that

$$\left[\mathcal{M}_{ij}^{q_1 q_2 q_3 q_4}(p,y)\right]^* = \mathcal{M}_{ij}^{q_2 q_1 q_4 q_3}(p,y) \,. \tag{4.3}$$

This implies that the matrix element of two flavor conserving currents is real-valued. Another useful relation follows from PT invariance, where the second line of (3.69) implies

$$\mathcal{M}_{ij}^{q_1 q_2 q_3 q_4}(p, y) = \eta_{PT}^{ij} \mathcal{M}_{ij}^{q_2 q_1 q_4 q_3}(p, -y) \ , \tag{4.4}$$

where

$$\eta_{PT}^{ij} = \eta_{PT}^{i} \eta_{PT}^{j} \ , \tag{4.5}$$

with the sign factors η_{PT}^{i} defined in (3.71). The results obtained on the lattice for the matrix elements (4.1) have to be translated to Minkowski time by multiplying with a factor according to (3.73).

4.2 Evaluation on the lattice

In the following, we describe the evaluation of two-current matrix elements on the lattice according to the discussion given in section 3.4. This involves the so-called four-point functions, which decompose into a set of Wick contractions by applying Wick's theorem. We shall discuss their contributions to a physical matrix element of operators with definite flavor.

4.2.1 Four-point correlation functions

The matrix element (4.1) can be obtained by calculating the ratio of correlation functions (3.63). The interpolators $\overline{\mathcal{J}}$, $\mathcal{J}$ have to be constructed in such a way that they correspond to the desired quantum numbers like spin and parity.
Using the general form of baryonic interpolators, see e.g. [68], we can define for the proton with isospin $I = 1/2$

$$\begin{aligned} \mathcal{P}(\vec{x}, t) &:= \epsilon_{abc} \ \Gamma_A u_a(x) \left[u_b^T(x) \ \Gamma_B \ d_c(x) \right] \Big|_{x_4 = t} \ , \\ \overline{\mathcal{P}}(\vec{x}, t) &:= \epsilon_{abc} \ \left[\bar{u}_a(x) \ \Gamma_B \ \bar{d}_b^T(x) \right] \bar{u}_c(x) \Gamma_A \Big|_{x_4 = t} \ . \end{aligned} \tag{4.6}$$

$\overline{\mathcal{P}}$ is called source, while $\mathcal{P}$ is referred to as the sink. Notice that each of the interpolators carries an open spinor index, which is introduced by the quark field u_a or $\bar{u}_c$, respectively. This is consistent with the fermionic character of baryons. In order to obtain spin $J = 1/2$, Γ_A and Γ_B are taken to be:

$$\Gamma_A = \mathbb{1} \ , \qquad \Gamma_B = C\gamma_5 \ , \tag{4.7}$$

with the charge conjugation matrix C. Furthermore, we define the operator P_+

$$P_+ = \frac{1}{2}\left(\mathbb{1} + \gamma_4\right) \ , \tag{4.8}$$

which projects a baryon at rest onto positive parity. The matrix elements $\langle p, \lambda | \, \overline{\mathcal{P}} \, |0\rangle$ and $\langle 0 | \, \mathcal{P} \, | p, \lambda \rangle$ correspond to the overlap terms in (3.62). Up to some normalization constant, which cancels in the ratio in (3.63), they are Dirac spinors $\bar{u}^\lambda$ and u^λ, which are defined by (2.7). With the projection operator P_+ we can evaluate the l.h.s. of (3.63) using that

$$\bar{u}^{\lambda'}(p) P_+ u^\lambda(p) = \delta_{\lambda\lambda'} \frac{p^0 + m}{2} \ . \tag{4.9}$$

For a matrix element of a product of two operators $\mathcal{O}_i$ we readily obtain the spin average (4.1):

$$\frac{\sum_{\lambda\lambda'} \bar{u}^{\lambda'}(p) P_+ u^\lambda(p) \, \langle p, \lambda | \, \mathcal{O}_i \mathcal{O}_j \, | p, \lambda' \rangle}{\sum_\lambda \bar{u}^\lambda(p) P_+ u^\lambda(p)} = \mathcal{M}_{ij} \ . \tag{4.10}$$

With the continuum normalization (3.64) we obtain the relation between the desired matrix element (4.1) and the ratio of correlation functions to be calculated on the lattice:

$$\mathcal{M}_{ij}(p,y)|_{y^0=0} = 2V\sqrt{m^2 + \vec{p}^{\,2}} \left. \frac{C_{\mathrm{4pt}}^{ij,\vec{p}}(\vec{y}, t, \tau)}{C_{\mathrm{2pt}}^{\vec{p}}(t)} \right|_{0 \ll \tau \ll t} \ , \tag{4.11}$$

where $V = L^3 a^3$ is the spatial volume. The four-point function C_{4pt} and the two point C_{2pt} are defined as:

$$\begin{aligned} C_{\mathrm{4pt}}^{ij,\vec{p}}(\vec{y}, t, \tau) &:= a^6 \sum_{\vec{z}', \vec{z}} e^{-i\vec{p}(\vec{z}' - \vec{z})} \ \left\langle \mathrm{tr}\left\{ P_+ \mathcal{P}(\vec{z}', t) \ \mathcal{O}_i(\vec{0}, \tau) \ \mathcal{O}_j(\vec{y}, \tau) \ \overline{\mathcal{P}}(\vec{z}, 0) \right\} \right\rangle \ , \\ C_{\mathrm{2pt}}^{\vec{p}}(t) &:= a^6 \sum_{\vec{z}', \vec{z}} e^{-i\vec{p}(\vec{z}' - \vec{z})} \ \left\langle \mathrm{tr}\left\{ P_+ \mathcal{P}(\vec{z}', t) \ \overline{\mathcal{P}}(\vec{z}, 0) \right\} \right\rangle \ , \end{aligned} \tag{4.12}$$

i.e. we use the convention that the source is placed at $z = (\vec{z}, 0)$, the sink at $z' = (\vec{z}', t)$, the insertion Γ_i at $x = (\vec{0}, \tau)$ and Γ_j at $y = (\vec{y}, \tau)$.
The trace in (4.12) is taken over the open spinor indices of the proton interpolators. The expressions in (4.12) are expectation values of quark operators, which can be calculated using Wick's theorem (3.14). The contributing Wick contractions are described in the following.

4.2.2 Wick contractions and physical matrix elements

In order to calculate the correlation functions defined in (4.12), we apply Wick's theorem (3.14), which yields a sum of Wick contractions. To this end, it is necessary to

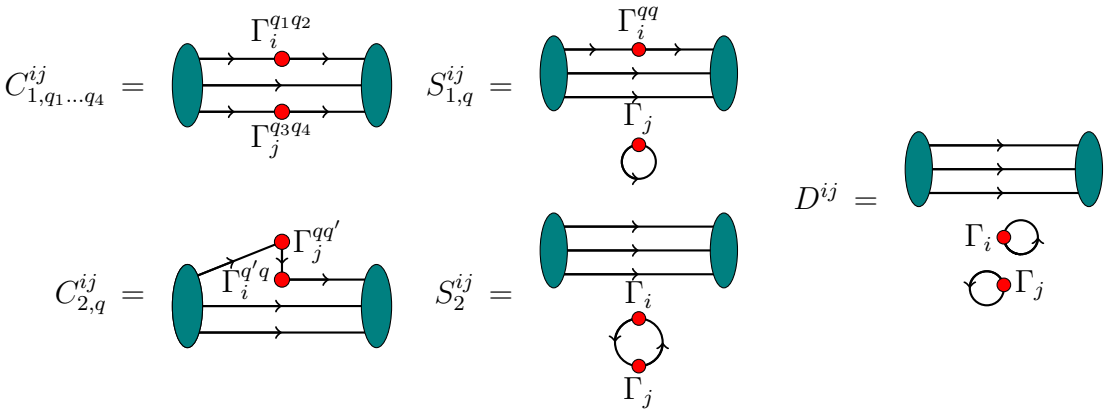

Figure 4.1: Depiction of the five types of Wick contractions contributing to baryonic four-point function. In the case of C_1, C_2 and S_1 the explicit contraction depends on the quark flavor. As long as all quark flavors have the same mass, the C_2 contractions do not depend on the flavor of the propagator connecting the two currents. Hence, the corresponding index is not written.

distinguish specific orderings of the quark fields. Therefore, we assign numbers to the fields appearing in the baryon interpolators (4.6) and the insertion operators (3.67) in the following way:

$$\begin{aligned}
&(\bar{1}) \text{ creating diquark part}\\
&(\bar{2}) \text{ creating diquark part (transposed)}\\
&(\bar{3}) \text{ creating quark (open)}\\
&(1) \text{ annihilating diquark part (transposed)}\\
&(2) \text{ annihilating diquark part}\\
&(3) \text{ annihilating quark (open)}\\
(4)&(\bar{4}) \text{ fields of first insertion } (i)\\
(5)&(\bar{5}) \text{ fields of second insertion } (j)
\end{aligned} \tag{4.13}$$

This numbering will be used again in section 4.3.1. The connected part of a generic baryon Wick contraction can be written in terms of the expressions (traces and transpositions are taken w.r.t. to spinor indices):

$$G^{123}[X,Y,Z] := \epsilon^{abc}\epsilon^{a'b'c'}\,\mathrm{tr}\left\{\left(\Gamma^B\right)^T X_{a'a}\Gamma^B Y^T_{b'b}\right\}\mathrm{tr}\left\{Z_{c'c}P\Gamma^A\right\}\ ,$$

$$
\begin{aligned}
G^{213}[X,Y,Z] &:= -\epsilon^{abc}\epsilon^{c'b'a'}\,\mathrm{tr}\left\{\Gamma^B X_{b'a}\Gamma^B Y^T_{a'b}\right\}\mathrm{tr}\left\{Z_{c'c}P\Gamma^A\right\}\ ,\\
G^{321}[X,Y,Z] &:= -\epsilon^{abc}\epsilon^{c'b'a'}\,\mathrm{tr}\left\{P\Gamma^A X_{c'a}\Gamma^B Y^T_{b'b}\left(\Gamma^B\right)^T Z_{a'c}\right\}\ ,\\
G^{132}[X,Y,Z] &:= -\epsilon^{abc}\epsilon^{c'b'a'}\,\mathrm{tr}\left\{\left(\Gamma^B\right)^T X^T_{a'a}\Gamma^B Z_{b'c}P\Gamma^A Y_{c'b}\right\}\ ,\\
G^{231}[X,Y,Z] &:= \epsilon^{abc}\epsilon^{a'b'c'}\,\mathrm{tr}\left\{\left(\Gamma^B X_{b'a}\Gamma^B\right)^T Z_{a'c}P\Gamma^A Y_{c'b}\right\}\ ,\\
G^{312}[X,Y,Z] &:= \epsilon^{abc}\epsilon^{a'b'c'}\,\mathrm{tr}\left\{P\Gamma^A X_{c'a}\Gamma^B Y^T_{a'b}\Gamma^B Z_{b'c}\right\}\ ,
\end{aligned}
\tag{4.14}
$$

where Γ^A, Γ^B are Dirac structures originating from the baryon interpolators (4.6) and P projects onto definite parity. For the nucleon, where $\Gamma^B = C\gamma_5$, $P\Gamma^A = P_+$, we can relate:

$$
G^{321}[X,Y,Z] = G^{132}[Y,X,Z]\ , \qquad G^{312}[X,Y,Z] = G^{231}[Y,X,Z]\ . \tag{4.15}
$$

X, Y and Z are either a propagator $M(z'|z)$ connecting the source at z and the sink at z' or one of the following pieces:

$$
\begin{aligned}
K_1^i(z'|y|z) &:= M(z'|y)\Gamma_i M(y|z)\ ,\\
K_2^{ji}(z'|y|z) &:= M(z'|0)\Gamma_i M(0|y)\Gamma_j M(y|z)\ ,\\
\overline{K}_2^{ij}(z'|y|z) &:= M(z'|y)\Gamma_j M(y|0)\Gamma_i M(0|z) = K_2^{ij}(z'|-y|z)\ .
\end{aligned}
\tag{4.16}
$$

The second identity in the last line follows from translational invariance. Since it is clear that the end points are connected to the source and the sink placed at z and z', respectively, we shall not write the corresponding arguments of $K_{1,2}$ and $\overline{K}_2$ in the following for brevity. Furthermore, we define the loops:

$$
\begin{aligned}
L_1^i(y) &:= \mathrm{tr}\left\{\Gamma_i M(y|y)\right\}\ ,\\
L_2^{ij}(y) &:= \mathrm{tr}\left\{\Gamma_i M(0|y)\Gamma_j M(y|0)\right\}\ .
\end{aligned}
\tag{4.17}
$$

For a baryonic four-point function we find five types of Wick contractions. Following the notation of [45], we call them C_1, C_2, S_1, S_2 and D. These are represented by the graphs depicted in Figure 4.1. The explicit contribution of a certain contraction type depends on the flavor of the inserted operators and the baryon, which in our case is

considered to be a proton. For C_1-type graphs we can define:

$$\begin{aligned}
C^{ij}_{1,uudd}(z,z',y) &:= \Big\langle G^{123}[K_1^i(0),K_1^j(y),M] + G^{321}[K_1^i(0),K_1^j(y),M] \\
&\quad + G^{321}[M,K_1^j(y),K_1^i(0)] + G^{123}[M,K_1^j(y),K_1^i(0)]\Big\rangle \ , \\
C^{ij}_{1,uuuu}(z,z',y) &:= \Big\langle G^{123}[K_1^i(0),M,K_1^j(y)] + G^{321}[K_1^i(0),M,K_1^j(y)] \\
&\quad + G^{321}[K_1^j(y),M,K_1^i(0)] + G^{123}[K_1^j(y),M,K_1^i(0)]\Big\rangle \ , \\
C^{ij}_{1,uddu}(z,z',y) &:= \Big\langle G^{213}[K_1^i(0),K_1^j(y),M] + G^{231}[K_1^i(0),K_1^j(y),M] \\
&\quad + G^{312}[M,K_1^j(y),K_1^i(0)] + G^{132}[M,K_1^j(y),K_1^i(0)]\Big\rangle \\
&= C^{ij}_{1,duud}(z,z',-y) \ .
\end{aligned} \tag{4.18}$$

In section 4.3.1 we shall see that each of the quantities $C_{1,uudd}$, $C_{1,uuuu}$ and $C_{1,uddu}$ can be calculated at once, avoiding the evaluation of each single term on the r.h.s. of (4.18) and, therefore, saving computer time. However, this makes the resulting expressions flavor dependent. Notice that the contractions are still defined in position space. According to (3.60), the projection onto definite proton momentum is given by:

$$C^{ij,\vec{p}}_{1,uudd}(\vec{y},t,\tau) := a^6 \sum_{\vec{z}\,\vec{z}'} e^{-i\vec{p}(\vec{z}'-\vec{z})} C^{ij}_{1,uudd}(z,z',y)|_{y^4=\tau,z^4=0,z'^4=t} \ , \tag{4.19}$$

and analogously for the remaining contractions, which we define in the following. The expressions for C_2 and S_1 read:

$$\begin{aligned}
C^{ij}_{2,u}(z,z',y) &:= \Big\langle G^{123}[K_2^{ji}(y),M,M] + G^{321}[K_2^{ji}(y),M,M] \\
&\quad + G^{321}[M,M,K_2^{ji}(y)] + G^{123}[M,M,K_2^{ji}(y)]\Big\rangle \ , \\
C^{ij}_{2,d}(z,z',y) &:= \Big\langle G^{123}[M,K_2^{ji}(y),M] + G^{321}[M,K_2^{ji}(y),M]\Big\rangle \ , \\
S^{ij}_{1,u}(z,z',y) &:= -\Big\langle \Big[G^{123}[K_1^i(0),M,M] + G^{321}[K_1^i(0),M,M] \\
&\quad + G^{321}[M,M,K_1^i(0)] + G^{123}[M,M,K_1^i(0)]\Big] L_1^j(y)\Big\rangle \ , \\
S^{ij}_{1,d}(z,z',y) &:= -\Big\langle \Big[G^{123}[M,K_1^i(0),M] + G^{321}[M,K_1^i(0),M]\Big] L_1^j(y)\Big\rangle \ .
\end{aligned} \tag{4.20}$$

Finally, we introduce the two contractions where both insertions are disconnected from the proton source and sink:

$$\begin{aligned}
S^{ij}_2(z,z',y) &:= -\Big\langle \Big[G^{123}[M,M,M] + G^{321}[M,M,M]\Big] L_2^{ij}(y)\Big\rangle \ , \\
D^{ij}(z,z',y) &:= \Big\langle \Big[G^{123}[M,M,M] + G^{321}[M,M,M]\Big] L_1^i(0) L_1^j(y)\Big\rangle \ .
\end{aligned} \tag{4.21}$$

For completeness we also write down the expression of the two-point function:

$$C_{2\mathrm{pt}}(z,z') := \Big\langle G^{123}[M,M,M] + G^{321}[M,M,M]\Big\rangle \ . \tag{4.22}$$

Using (A.21) and (A.24) and considering $\mathcal{PT}$ invariance and invariance under shifts in time direction we are able to deduce the relation

$$\begin{aligned} G^{ij,\vec{p}}(y) &= \eta_{PT}^{ij} G^{ij,\vec{p}}(-y) \qquad \text{for } G = C_{1,uudd}, C_{1,uuuu}, S_{1,u}, S_{1,d}, S_2, D \ , \\ G^{ij,\vec{p}}(y) &= \eta_{PT}^{ij} G^{ji,\vec{p}}(y) \qquad \text{for } G = C_{2,u}, C_{2,d} \ , \end{aligned} \tag{4.23}$$

where η_{PT}^{ij} is defined in (3.71). Furthermore, invariance under $\mathcal{C}$ and $\mathcal{P}$ transformation, as well as the relations (A.21) and (A.23), imply for all contractions:

$$\left[G^{ij,\vec{p}}(y)\right]^* = \eta_4^{ij} \eta_{PT}^{ij} G^{ij,\vec{p}}(-y) \ , \tag{4.24}$$

with

$$\eta_4^i = \begin{cases} 1 & i = V, T \\ -1 & i = A \end{cases} \ , \qquad \eta_4^{ij} = \eta_4^i \eta_4^j \ . \tag{4.25}$$

If $\eta_4^{ij} = 1$, which is the case for the current combinations investigated within this work, the relations (4.23) and (4.24) imply that $C_{1,uudd}$, $C_{1,uuuu}$, $S_{1,u}$, $S_{1,d}$, S_2, D are real-valued, whereas $C_{2,u}, C_{2,d}$ might have non-vanishing imaginary parts. For these contractions we find

$$\begin{aligned} 2\,\mathrm{Re}\left\{C_{2,q}^{ij,\vec{p}}(y)\right\} &= C_{2,q}^{ij,\vec{p}}(y) + C_{2,q}^{ji,\vec{p}}(-y) \\ 2i\,\mathrm{Im}\left\{C_{2,q}^{ij,\vec{p}}(y)\right\} &= C_{2,q}^{ij,\vec{p}}(y) - C_{2,q}^{ji,\vec{p}}(-y) \ , \end{aligned} \tag{4.26}$$

Moreover, because of translational invariance it holds that

$$G^{ij,\vec{p}}(y) = G^{ji,\vec{p}}(-y) \ , \qquad \text{for } G = S_2, D \ . \tag{4.27}$$

A physical matrix element corresponding to a certain quark flavor is obtained by a linear combination of a specific set of contractions. Taking into account only the light quarks u and d, we find for proton matrix elements:

$$\begin{aligned} \langle p|\, \mathcal{O}_i^{uu}(\vec{0})\ \mathcal{O}_j^{dd}(\vec{y})\, |p\rangle &= C_{1,uudd}^{ij,\vec{p}}(\vec{y}) + S_{1,u}^{ij,\vec{p}}(\vec{y}) + S_{1,d}^{ji,\vec{p}}(-\vec{y}) + D^{ij,\vec{p}}(\vec{y}) \ , \\ \langle p|\, \mathcal{O}_i^{uu}(\vec{0})\ \mathcal{O}_j^{uu}(\vec{y})\, |p\rangle &= C_{1,uuuu}^{ij,\vec{p}}(\vec{y}) + C_{2,u}^{ij,\vec{p}}(\vec{y}) + C_{2,u}^{ji,\vec{p}}(-\vec{y}) \\ &\quad + S_{1,u}^{ij,\vec{p}}(\vec{y}) + S_{1,u}^{ji,\vec{p}}(-\vec{y}) + S_2^{ij,\vec{p}}(\vec{y}) + D^{ij,\vec{p}}(\vec{y}) \ , \\ \langle p|\, \mathcal{O}_i^{dd}(\vec{0})\ \mathcal{O}_j^{dd}(\vec{y})\, |p\rangle &= C_{2,d}^{ij,\vec{p}}(\vec{y}) + C_{2,d}^{ji,\vec{p}}(-\vec{y}) + S_{1,d}^{ij,\vec{p}}(\vec{y}) + S_{1,d}^{ji,\vec{p}}(-\vec{y}) \\ &\quad + S_2^{ij,\vec{p}}(\vec{y}) + D^{ij,\vec{p}}(\vec{y}) \ , \\ \langle p|\, \mathcal{O}_i^{ud}(\vec{0})\ \mathcal{O}_j^{du}(\vec{y})\, |p\rangle &= C_{1,uddu}^{ij,\vec{p}}(\vec{y}) + C_{2,u}^{ij,\vec{p}}(\vec{y}) + C_{2,d}^{ji,\vec{p}}(-\vec{y}) + S_2^{ij,\vec{p}}(\vec{y}) \ . \end{aligned} \tag{4.28}$$

Z_V	Z_A	Z_T
0.7128	0.7525	0.8335

Table 4.1: Renormalization constants for each operator type for $\beta = 3.4$. The factors have been determined for a scale $\mu = 2$ GeV, including the conversion to the $\overline{\text{MS}}$ scheme.

In the expression above the contributions are understood to be defined in the limit given in (4.11) and accordingly normalized by the two-point function, i.e.

$$C^{ij,\vec{p}}_{1,uudd}(\vec{y}) = 2V\sqrt{m^2+\vec{p}^2}\,\left.\frac{C^{ij,\vec{p}}_{1,uudd}(\vec{y},t,\tau)}{C^{\vec{p}}_{2\text{pt}}(t)}\right|_{0\ll\tau\ll t}\,, \tag{4.29}$$

and analogously for all other contractions. Notice that, according to (4.26), the combination $C^{ij,\vec{p}}_{2,q}(\vec{y}) + C^{ji,\vec{p}}_{2,q}(-\vec{y})$ in (4.28) can be identified with the real part $2\,\text{Re}\left\{C^{ij,\vec{p}}_{2,q}(y)\right\}$. Isospin symmetry allows us to relate these matrix elements to those of the neutron:

$$\begin{aligned}
\langle p|\,\mathcal{O}_i^{dd}\mathcal{O}_j^{uu}\,|p\rangle_n &= \langle p|\,\mathcal{O}_i^{uu}\mathcal{O}_j^{dd}\,|p\rangle_p\ , \qquad & \langle p|\,\mathcal{O}_i^{dd}\mathcal{O}_j^{dd}\,|p\rangle_n &= \langle p|\,\mathcal{O}_i^{uu}\mathcal{O}_j^{uu}\,|p\rangle_p\ ,\\
\langle p|\,\mathcal{O}_i^{uu}\mathcal{O}_j^{uu}\,|p\rangle_n &= \langle p|\,\mathcal{O}_i^{dd}\mathcal{O}_j^{dd}\,|p\rangle_p\ , \qquad & \langle p|\,\mathcal{O}_i^{du}\mathcal{O}_j^{ud}\,|p\rangle_n &= \langle p|\,\mathcal{O}_i^{ud}\mathcal{O}_j^{du}\,|p\rangle_p\ .
\end{aligned} \tag{4.30}$$

In our calculations these relations are exact, since we consider u and d quarks to be mass degenerate and do not take into account electrodynamic effects.
In this work we, will concentrate on flavor conserving operators, i.e. we will consider only the first three matrix elements in (4.28).

4.2.3 Renormalization

According to the discussion in section 3.4.3 the operators appearing in (4.1) have to be renormalized multiplicatively, involving the renormalization factors Z_V, Z_A and Z_T. The corresponding values have been determined within the RI′ scheme and converted to the $\overline{\text{MS}}$ scheme for the scale $\mu = 2$ GeV [95]. Additionally, it is improved perturbatively w.r.t. to lattice artifacts. The values of the factors Z_i for $\beta = 3.4$ being used for our analysis are listed in table 4.1. The renormalization of the two operator insertions implies for the two-current matrix element:

$$\mathcal{M}^{\text{ren}}_{ij} = Z_i Z_j \mathcal{M}^{\text{latt}}_{ij}\ . \tag{4.31}$$

4.3 Simulation details

We now describe the technical details concerning the simulation. In particular, we give the explicit quantities being implemented on the lattice, including all used improve-

ments. Furthermore, we list all parameters and settings being used for the calculations and give some computational information.

4.3.1 Details on the Wick contractions

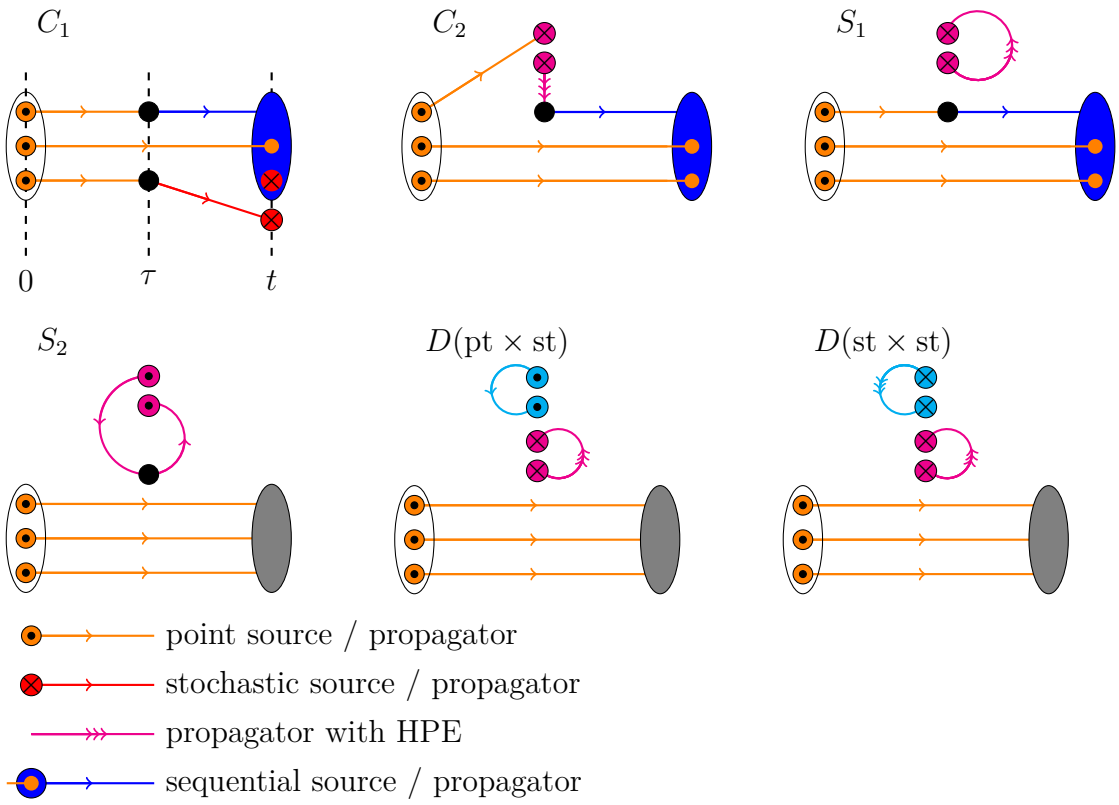

Figure 4.2: Technical sketch of all graphs showing the chosen calculation method for each element. For the D graph we have two versions, first with one fixed point source (center bottom), second with two stochastic loops, which enables volume averaging (right bottom). For the C_1 graph we indicate the time slices of the source, the sink and the insertions.

In the following, we derive explicit expressions for the contractions (4.18), (4.20), (4.21) and (4.22) being evaluated in the simulation. Each graph is calculated on a smeared quark point source $S_x^{\Phi,\vec{p}} = \Phi^{\vec{p}} S_x$ located at position x, where $(S_x)^{ab}_{\alpha\beta}(y) = \delta_{xy}\delta_{\alpha\beta}\delta_{ab}$. We shall discuss each ingredient separately. A technical sketch of all graphs is shown in Figure 4.2.

Smearing: The smearing function $\Phi^{\vec{p}}$ also includes a phase injecting a momentum $b\vec{p}$ to each of the quarks, where $\vec{p}$ corresponds to the proton's momentum. This increases the

overlap of the interpolating operators with the ground state as discussed in section 3.4.1:

$$(\Phi_0^{\vec{p}})_{x,y} = \frac{1}{1+6\epsilon}\left[\delta_{x,y} + \epsilon \sum_{j=1}^{3}\left(\delta_{x+\hat{j},y} U_j^{\mathrm{sm}}(x) e^{ib\vec{p}\hat{j}} + \delta_{y+\hat{j},x} U_j^{\mathrm{sm},\dagger}(y) e^{-ib\vec{p}\hat{j}}\right)\right] , \qquad (4.32)$$

where the parameter ϵ is set to 0.25. For the nucleon it is found that choosing $b = 0.45$ yields maximal overlap with the ground state. The method is known as momentum smearing [96], which is based on the Wuppertal smearing technique [97]. Notice that the smearing function is applied multiple times, i.e. the sources and propagators are smeared by applying $\Phi = \Phi_0^n$. The gauge links U^{sm} appearing in (4.32) are smoothed versions of the original gauge links U. They are obtained by the APE-smearing method [98], where the gauge links are extended by the average over their adjacent spatial staples. This reduces unphysical short-distance fluctuations.
Inverting the Dirac operator (3.41) on the source $S_x^{\Phi,\vec{p}}$, we obtain the source-smeared point-to-all quark propagator $M_x^{\Phi,\vec{p}}(y)$:

$$\mathcal{D} M_x^{\Phi,\vec{p}} = S_x^{\Phi,\vec{p}} \ . \qquad (4.33)$$

From this propagator all contractions contributing to $C_{4\mathrm{pt}}$ and the two point function are constructed.

Stochastic propagators and improvements: For most of the graphs we need knowledge about all-to-all propagation of the quark fields. Obviously, it is not feasible to invert the Dirac equation on the entire lattice. Therefore, we approximate the unit matrix by a stochastic decomposition:

$$\frac{1}{N_{\mathrm{st}}} \sum_{\ell}^{N_{\mathrm{st}}} \eta_t^{(\ell)} \otimes \eta_t^{\dagger(\ell)} \xrightarrow{N_{\mathrm{st}}\to\infty} \mathbb{1}_t \ . \qquad (4.34)$$

The objects $\eta_t^{(\ell)}$ are stochastic noise vectors in space, spin and color and are seeded on timeslice t only, where they can take the values:

$$\left(\eta_t^{(\ell)}\right)_{\alpha a x} = \frac{1}{\sqrt{2}}(\pm 1 \pm i)\ \delta_{x^4,t} \ . \qquad (4.35)$$

The corresponding propagator $\psi_t^{(\ell)}$ obtained by

$$\mathcal{D}\psi_t^{(\ell)} = \eta_t^{(\ell)} \qquad (4.36)$$

contains information for the propagation from any spatial site at time t to any site within the entire lattice.
Considering the l.h.s. in (4.34), the off-diagonal entries belonging to the seeded time slice t represent only stochastic noise terms. Especially the entries near the diagonal

Γ	V^μ	A^μ	$T^{\mu\nu}$
N_{hpe}	3	4	1

Table 4.2: Number of omitted hopping terms in the L_1 contraction.

affect the final quantity due to larger values of the stochastic propagator ψ. In the following, we review a technique for eliminating near-diagonal terms, exploiting ultra-locality of the employed action, for reference see [99]. We rewrite the Dirac operator as $\mathcal{D} = (\mathbb{1} - H)/(2a\kappa)$ and make use of the geometric series to express the propagator. Comparing with (3.41) we identify H with:

$$H[U_\mu] = \kappa H_{\mathrm{W}}[U_\mu](x|y) - 2a^2\kappa c_{\mathrm{SW}} C[U_\mu](x|y) \ . \tag{4.37}$$

If we know that the first N terms are exactly zero in the stochastic limit, we can rewrite:

$$\begin{aligned} \mathcal{D}^{-1} &= 2a\kappa \sum_{n=0}^{\infty} H^n = 2a\kappa \sum_{n=0}^{N-1} H^n + 2a\kappa \sum_{n=N}^{\infty} H^n \\ &= 0 + 2a\kappa \sum_{n=N}^{\infty} H^n = H^N 2a\kappa \sum_{n=0}^{\infty} H^n = H^N \mathcal{D}^{-1} \ . \end{aligned} \tag{4.38}$$

Thus, replacing $\mathcal{D}^{-1}$ by $H^N\mathcal{D}^{-1}$ removes the first N terms in the series. For a propagator connecting two sites being separated by a vector y, we can set $aN(y) = |y_1| + |y_2| + |y_3|$, since the hopping terms connect only nearest neighbors. Taking into account the periodicity of the lattice, the exact definition of $N(y)$ is:

$$N(y) = \sum_{i=1}^{3} \min\left(\frac{|y_i|}{a}, L - \frac{|y_i|}{a}\right) \ . \tag{4.39}$$

We define the correspondingly improved stochastic propagator as:

$$\xi_\tau^{(\ell),N}(y) = H^N \psi_\tau^{(l)}(y) \ . \tag{4.40}$$

This improvement is applicable to the calculation of the C_2 graph, which we will discuss within this section.
Furthermore, we find cancellation of a certain number of low-order terms in the expansion if we take the trace of the product of a quark propagator with a specific Dirac matrix. This is the case for one-current loops, e.g. L_1, see (4.17). The number of terms that can be omitted depends on the type of the Dirac matrix, see table 4.2 [100].

Interpolator kernels: For simplicity we introduce the following short notation concerning the baryon interpolators:

$$\begin{aligned} (E^a)^{bc}_{\beta\gamma} &:= \epsilon^{abc} \left(\Gamma^B\right)_{\beta\gamma} \ , \\ \Pi_{\alpha\beta} &:= \left(P_\pm \Gamma^A\right)_{\alpha\beta} \ , \\ \overline{\Pi}_{\alpha\beta} &:= \left(\Gamma^A P_\pm\right)_{\alpha\beta} \ , \\ \mathcal{E}^{\vec{p}}(x) &:= e^{-i\vec{x}\vec{p}} \ , \end{aligned} \tag{4.41}$$

where Γ^A and Γ^B are given by (4.7) for the proton case, P_+ is defined by (4.8). The baryon annihilation operator kernel, which yields the annihilation operator itself after contracting with the quark fields, can be written as:

$${}_\sigma\mathcal{O}^{abc}_{\alpha\beta\gamma} = \Pi_{\sigma\alpha} \, (E^a)^{bc}_{\beta\gamma} \ . \tag{4.42}$$

This object is used for the calculation of the sequential propagator. In an analogous way we can formulate the baryon creation operator kernel:

$${}_\sigma\overline{\mathcal{O}}^{abc}_{\alpha\beta\gamma} = (E^c)^{ab}_{\alpha\beta} \, \overline{\Pi}_{\gamma\sigma} \ . \tag{4.43}$$

The two point function $C_{2\mathrm{pt}}$: Let us first discuss the Wick contractions for the two point function $C_{2\mathrm{pt}}$ introduced in (4.22). We call the total contribution of all two point contractions $G_{2\mathrm{pt}}$. This object is also needed to construct the four-point contractions S_2 and D, which is explained later in this section.
Combining all quark-antiquark pairs of the same flavor, we find in the case of the proton:

$$\begin{aligned} G^{\vec{p}}_{2\mathrm{pt}}(z') = \Big[& \Pi_{\beta\alpha} \left(\Phi^{\vec{p}} M_z^{\Phi,\vec{p}}\right)^{ab}_{\alpha\beta}(z') \, \mathrm{tr} \left\{ \left(\Phi^{\vec{p}} M_z^{\Phi,\vec{p}}(z') E^b\right)^T E^a \Phi^{\vec{p}} M_z^{\Phi,\vec{p}}(z') \right\} \\ & + \Pi_{\beta\alpha} \left(\Phi^{\vec{p}} M_z^{\Phi,\vec{p}}\right)^{ab}_{\alpha\gamma}(z') \left[\left(\Phi^{\vec{p}} M_z^{\Phi,\vec{p}}(z') E^b\right)^T E^a \Phi^{\vec{p}} M_z^{\Phi,\vec{p}}(z') \right]^{cc}_{\gamma\beta} \Big] \\ & \times \mathcal{E}^{\vec{p}}(z'-z) \ . \end{aligned} \tag{4.44}$$

The two point function is defined as the mean value over all gauge configurations, which is denoted by $\langle . \rangle$. Furthermore, we have to project onto definite momentum $\vec{p}$ by summing over all spatial positions $\vec{z}$, $\vec{z}'$. Note that the momentum phases are included in the definition (4.44). Because of translational invariance it is only necessary to perform the sum at the sink for a fixed source point $\vec{z}$. The two point function can be rewritten as:

$$C^{\vec{p}}_{2\mathrm{pt}}(t) = \left\langle \tilde{G}^{\vec{p}}_{2\mathrm{pt}}(t) \right\rangle \ , \qquad \tilde{G}^{\vec{p}}_{2\mathrm{pt}}(t) = a^3 V \sum_{\vec{z}'} G^{\vec{p}}_{2\mathrm{pt}}(z') \Big|_{(z')^4 = z^4 + t} \ , \tag{4.45}$$

where the factor V compensates the omitted sum over the source position z.

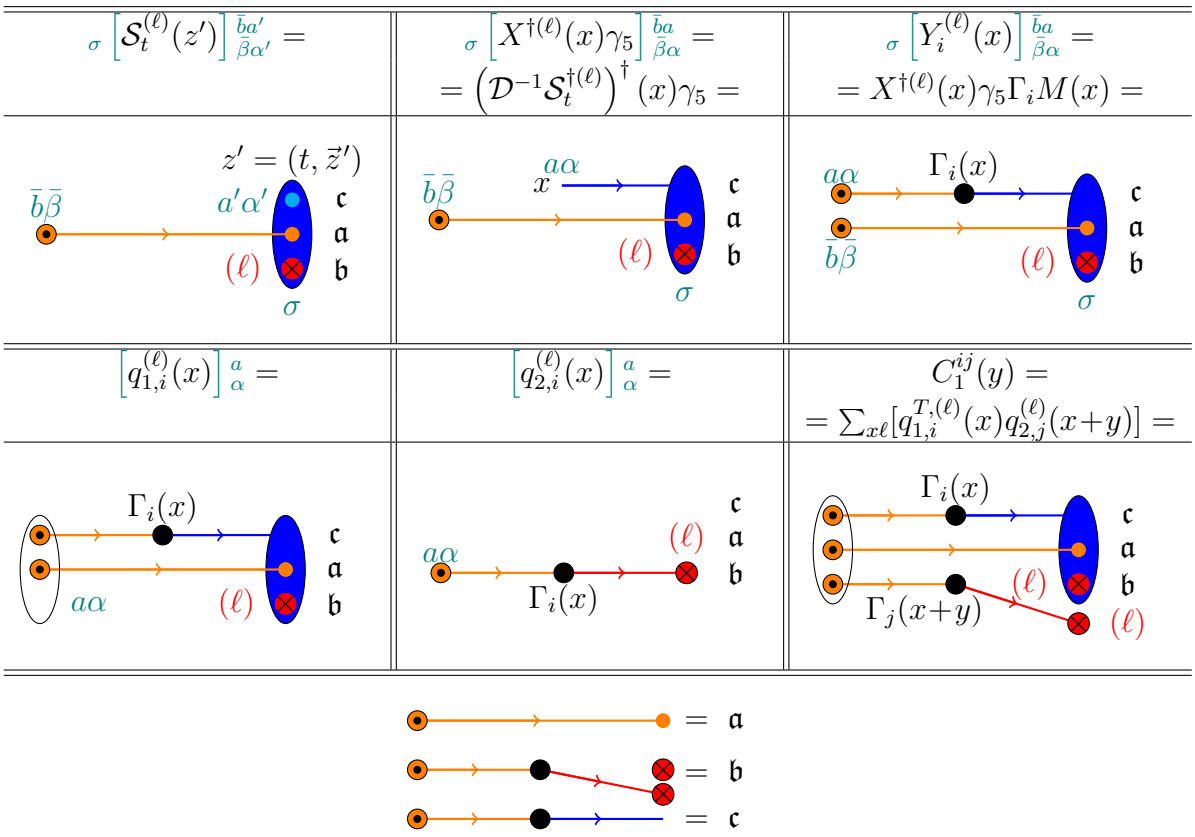

Figure 4.3: Detailed technical sketch of each part entering the C_1 contraction. The symbols have the same meaning as in Figure 4.2. For each piece we also show spinor, color and stochastic indices and spacetime arguments. We also indicate to which of the quark lines $\mathfrak{a}$, $\mathfrak{b}$ or $\mathfrak{c}$ the shown elements belong. The quark lines themselves are defined in the lower panel. Upper panels: Left: The sequential source $\mathcal{S}_t$ at timeslice t, which is a combination of the terms given in (4.48). The sequential source already incorporates parts of each quark line, see (4.47). The light blue dot denotes the open spinor and color indices used for the inversion of the Dirac operator. Center: Sequential propagator $X^\dagger\gamma_5$ after the Hermitian conjugation. Right: The combination of the sequential propagator and the forward propagator M, which is called Y. Center panels: Left: q_1, which is a combination of the contractions (4.52). These are constructed from the quantity Y. The open baryon spinor index σ of the sink does not appear here anymore, since it is contracted with the baryon spinor index of the source. Center: q_2 representing a part of the quark line $\mathfrak{b}$. Right: The complete C_1 graph, which is constructed from $q_{1,i}$ and $q_{2,j}$ (or in some cases $q_{1,j}$ and $q_{2,i}$)

Graph C_1: For C_1-type graphs we have the two operators placed at two different quark lines connecting the baryon operators. For the proton we have contributions for

$$\begin{aligned} &\langle p|\, \mathcal{O}_i^{uu}(x)\ \mathcal{O}_j^{dd}(x+y)\,|p\rangle\ , \\ &\langle p|\, \mathcal{O}_i^{uu}(x)\ \mathcal{O}_j^{uu}(x+y)\,|p\rangle\ , \\ &\langle p|\, \mathcal{O}_i^{du}(x)\ \mathcal{O}_j^{ud}(x+y)\,|p\rangle\ . \end{aligned} \tag{4.46}$$

The basic technical procedure of the calculation is the following: We compute a simple point-to-all forward propagator $M_x^{\Phi,\vec{p}}$ (see (4.33)) at the momentum smeared source. Furthermore, we put a stochastic wall source η_t on the sink at timeslice t, which we use for the calculation of a stochastic propagator ψ_t, which connects one of the currents to the sink. The stochastic source and the forward propagator are then combined to a sequential source, which is used for the calculation of a sequential propagator, which is connected to the second current. For general reference regarding the sequential source technique see [101]. From this procedure we obtain all pieces we need to evaluate the C_1 contributions. Each piece is sketched in Figure 4.3. In Figure 4.3 to Figure 4.6 and the equations (4.47) to (4.52) we shall label the quark lines as follows:

- $\mathfrak{a}$ forward propagator connecting the baryon operators
- $\mathfrak{b}$ quark line with the stochastic source, the stochastic propagator, and one insertion
- $\mathfrak{c}$ quark line with the sequential propagator and the other insertion.

We have the following pieces attached to the sink, where $\bar{.}$ denotes the open source index of the forward propagator and $.'$ the open index used for the inversion:

$$\begin{aligned} &(\Phi^{\vec{p}}\, M_z^{\Phi,\vec{p}})^{a\bar{a}}_{\alpha\bar{\alpha}}(z') \quad (\ \mathfrak{a}\ )\ , \\ &\left(\Phi^{\vec{p}}\gamma_5\eta^{(\ell)}\right)^{a}_{\alpha}(z') \quad (\ \mathfrak{b}\ )\ , \\ &(\gamma_5)^{aa'}_{\alpha\alpha'} \quad (\ \mathfrak{c}\ )\ . \end{aligned} \tag{4.47}$$

As given in the parentheses, the expressions correspond to the different quark lines connected to the sink. Except for the first line, which is exactly the quark line $\mathfrak{a}$ itself, the expressions represent only a part of corresponding quark line. The γ_5 in the second and third line arises from the Hermitian conjugation of the sequential propagator or the stochastic propagator, respectively. There are six possibilities to connect these parts to the sink. These are labeled by the number (n) of the quark in the baryon annihilation operator according to (4.13), where we use the ordering $S_{n(\mathfrak{a})n(\mathfrak{b})n(\mathfrak{c})}$. Considering e.g. in the sequential source S_{213}, quark (1) is part of the quark line with the stochastic propagator (quark line $\mathfrak{b}$), quark (2) belongs to the quark line with the forward propagator (quark line $\mathfrak{a}$) and quark (3) is part of the quark line with the sequential propagator (quark line $\mathfrak{c}$). Explicitly, the six possibilities of sequential sources read:

$$_{\sigma}\left(S_{123}^{\vec{p},(\ell)}\right)^{\bar{b}a'}_{\bar{\beta}\alpha'}(z') := \mathcal{E}^{\vec{p}}(z')\,(\Pi\gamma_5)_{\sigma\alpha'}\left[\left(\Phi^{\vec{p}}\, M_z^{\Phi,\vec{p}}\right)^T(z')\ E^{a'}\Phi^{\vec{p}}\gamma_5\eta^{(\ell)}(z')\right]^{\bar{b}}_{\bar{\beta}}\ ,$$

$$
\begin{aligned}
{}_\sigma\left(S^{\vec{p},(\ell)}_{213}\right)^{\bar{c}a'}_{\bar{\gamma}\alpha'}(z') &:= \mathcal{E}^{\vec{p}}(z')\,(\Pi\gamma_5)_{\sigma\alpha'}\left[\left(\Phi^{\vec{p}}\eta^{(\ell)}\right)^T(z')\gamma_5^T E^{a'}\Phi^{\vec{p}}M_z^{\Phi,\vec{p}}(z')\right]^{\bar{c}}_{\bar{\gamma}}\ ,\\
{}_\sigma\left(S^{\vec{p},(\ell)}_{231}\right)^{\bar{c}b'}_{\bar{\gamma}\beta'}(z') &:= \mathcal{E}^{\vec{p}}(z')\left(\Pi\Phi^{\vec{p}}\gamma_5\eta^{(\ell)}(z')\right)^a_\sigma\left[\gamma_5^T E^a\Phi^{\vec{p}}M_z^{\Phi,\vec{p}}(z')\right]^{b'\bar{c}}_{\beta'\bar{\gamma}}\ ,\\
{}_\sigma\left(S^{\vec{p},(\ell)}_{132}\right)^{\bar{b}c'}_{\bar{\beta}\gamma'}(z') &:= \mathcal{E}^{\vec{p}}(z')\left(\Pi\Phi^{\vec{p}}\gamma_5\eta^{(\ell)}(z')\right)^a_\sigma\left[\left(\Phi^{\vec{p}}M_z^{\Phi,\vec{p}}\right)^T(z')\ E^a\gamma_5\right]^{\bar{b}c'}_{\bar{\beta}\gamma'}\ ,\\
{}_\sigma\left(S^{\vec{p},(\ell)}_{312}\right)^{\bar{a}c'}_{\bar{\alpha}\gamma'}(z') &:= \mathcal{E}^{\vec{p}}(z')\left(\Pi\Phi^{\vec{p}}M_z^{\Phi,\vec{p}}(z')\right)^{a\bar{a}}_{\sigma\bar{\alpha}}\left[\left(\Phi^{\vec{p}}\eta^{(\ell)}\right)^T(z')\gamma_5^T E^a\gamma_5\right]^{c'}_{\gamma'}\ ,\\
{}_\sigma\left(S^{\vec{p},(\ell)}_{321}\right)^{\bar{a}b'}_{\bar{\alpha}\beta'}(z') &:= \mathcal{E}^{\vec{p}}(z')\left(\Pi\Phi^{\vec{p}}M_z^{\Phi,\vec{p}}(z')\right)^{a\bar{a}}_{\sigma\bar{\alpha}}\left[\gamma_5^T E^a\Phi^{\vec{p}}\gamma_5\eta^{(\ell)}(z')\right]^{b'}_{\beta'}\ .
\end{aligned}
\tag{4.48}
$$

The sequential sources appearing in a sum of contractions can be combined if $n(\mathfrak{c})$ (the last integer index) is the same in each expression. The sequential source to be inverted is called $\mathcal{S}$ and can be either one of the sequential sources (4.48) or a combination of these. Furthermore, we define $\mathcal{S}_t$ as

$$
\mathcal{S}_t^{\vec{p},(\ell)}(z') = \mathcal{S}^{\vec{p},(\ell)}(z')\delta_{z'_4,t}\ , \tag{4.49}
$$

i.e. the sequential source seeded at timeslice t only. To this source we apply again momentum smearing $\Phi^{\vec{p}}$. Inverting on this source, we obtain the sequential propagator $X_t^{\Phi,\vec{p},(\ell)}(y)$. Notice that this is done by solving on the Hermitian conjugate of the source, since we again have to take the Hermitian conjugate of the solution in the complete correlation function:

$$
\mathcal{D}X_t^{\Phi,\vec{p},(\ell)} = \Phi^{\vec{p}}\mathcal{S}_t^{\dagger,\vec{p},(\ell)} \tag{4.50}
$$

For a graphical representation of $\mathcal{S}_t$ and X we refer to Figure 4.3. Moreover, we define the expression Y, which incorporates the two quark lines $\mathfrak{a}$ and $\mathfrak{c}$ (see Figure 4.3):

$$
Y_{t,j}^{\vec{p},(\ell)}(y) := X_t^{\dagger,\Phi,\vec{p},(\ell)}(y)\gamma_5\Gamma_j M_z^{\Phi,\vec{p}}(y)\ , \tag{4.51}
$$

where X is the sequential propagator, obtained from the inversion on $\mathcal{S}_t$. The Hermitian conjugation of X together with the γ_5 completes the transformation of the propagator on the $\mathfrak{c}$ quark line to a forward propagator. The sequential propagator implicitly contains the sum over the sink position $\vec{z}'$. Notice that the sequential source and the corresponding propagator and, subsequently, Y carry the baryon spinor index σ appearing in the baryon sink. To construct the C_1 graph we contract the expression Y with the source, leaving one spinor-color index open, which will be connected to the stochastic part. Again there are in general six possibilities, which are denoted in the same manner as the sequential sources before, but this time the integer indices refer to the quark fields in the baryon source, i.e. $(\bar{1})$, $(\bar{2})$ and $(\bar{3})$ instead of (1), (2) and (3):

$$
\left(\overline{S}^{\vec{p},(\ell)}_{123,t,j}\right)^b_\beta(y) := \mathcal{E}^{-\vec{p}}(z)\sum_\sigma\left[{}_\sigma Y^{T,\vec{p},(\ell)}_{t,j}(z)E^c\right]^{cb}_{\gamma\beta}\overline{\Pi}_{\gamma\sigma}\ ,
$$

$$
\begin{aligned}
\left(\overline{S}^{\vec{p},(\ell)}_{213,t,j}\right)^{a}_{\alpha}(y) &:= \mathcal{E}^{-\vec{p}}(z)\sum_{\sigma}\left[E^{c}{}_{\sigma}Y^{\vec{p},(\ell)}_{t,j}(z)\right]^{ac}_{\alpha\gamma}\overline{\Pi}_{\gamma\sigma}\ ,\\
\left(\overline{S}^{\vec{p},(\ell)}_{231,t,j}\right)^{c}_{\gamma}(y) &:= \mathcal{E}^{-\vec{p}}(z)\sum_{\sigma}\mathrm{tr}\left\{{}_{\sigma}Y^{\vec{p},(\ell)}_{t,j}(z)E^{c}\right\}\overline{\Pi}_{\gamma\sigma}\ ,\\
\left(\overline{S}^{\vec{p},(\ell)}_{132,t,j}\right)^{c}_{\gamma}(y) &:= \mathcal{E}^{-\vec{p}}(z)\sum_{\sigma}\mathrm{tr}\left\{E^{c}{}_{\sigma}Y^{T,\vec{p},(\ell)}_{t,j}(z)\right\}\overline{\Pi}_{\gamma\sigma}\ ,\\
\left(\overline{S}^{\vec{p},(\ell)}_{312,t,j}\right)^{a}_{\alpha}(y) &:= \mathcal{E}^{-\vec{p}}(z)\sum_{\sigma}\left[E^{c}{}_{\sigma}Y^{T,\vec{p},(\ell)}_{t,j}(z)\right]^{ac}_{\alpha\gamma}\overline{\Pi}_{\gamma\sigma}\ ,\\
\left(\overline{S}^{\vec{p},(\ell)}_{321,t,j}\right)^{b}_{\beta}(y) &:= \mathcal{E}^{-\vec{p}}(z)\sum_{\sigma}\left[{}_{\sigma}Y^{\vec{p},(\ell)}_{t,j}(z)E^{c}\right]^{cb}_{\gamma\beta}\overline{\Pi}_{\gamma\sigma}\ .
\end{aligned}
\tag{4.52}
$$

The spin index σ is contracted with the baryon spinor index of the baryon source, which is indicated by the sum over σ in (4.52).
We will now write explicitly the expressions for the three aforementioned matrix elements in terms of the previously discussed quantities. We start with $\langle p|\,\mathcal{O}^{uu}_{i}(0)\mathcal{O}^{dd}_{j}(y)\,|p\rangle$. The contributions are depicted in Figure 4.4. In the construction of the required se-

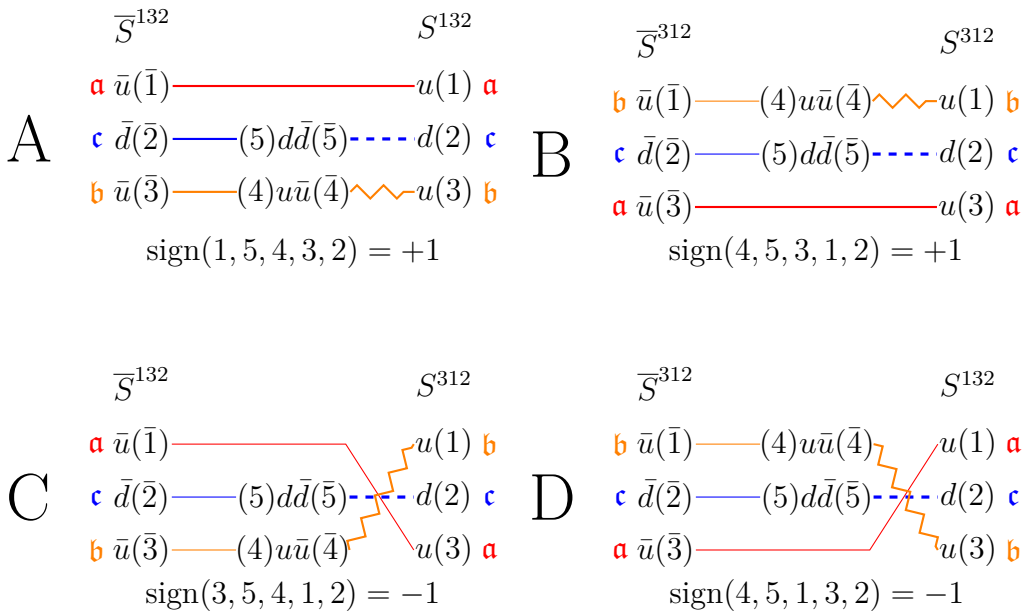

Figure 4.4: Contributions to $\langle p|\,\mathcal{O}^{uu}_{i}(0)\mathcal{O}^{dd}_{j}(y)\,|p\rangle$ with C_1 topology. The forward propagator M_z is depicted by a simple line, the stochastic propagator ψ by a zigzag line and the sequential propagator X (without the incorporated forward propagator and the stochastic source) is represented by a dashed line. The colors indicate the quark lines: red corresponds to $\mathfrak{a}$, orange to $\mathfrak{b}$ and blue to $\mathfrak{c}$. The combination of the quark lines with the numbers (1), (2), (3) at the sink or $(\bar{1})$, $(\bar{2})$, $(\bar{3})$ at the source determines the sequential source type $S_{n(\mathfrak{a})n(\mathfrak{b})n(\mathfrak{c})}$ (see (4.48)) or the contraction $\overline{S}_{n(\mathfrak{a})n(\mathfrak{b})n(\mathfrak{c})}$ (see (4.52)), respectively, which is also shown for the specific cases.

quential source $\mathcal{S}$ we are able to combine A with C and B with D, which yields in both cases up to a global sign:

$$\mathcal{S}^{\vec{p},(\ell)}(z') = S_{132}^{\vec{p},(\ell)}(z') - S_{312}^{\vec{p},(\ell)}(z') \ . \tag{4.53}$$

Relative signs, which are also indicated in Figure 4.4, correspond to the permutation sign of Wick's theorem (3.65). Using the combination (4.53) in (4.49), (4.50) and (4.51) yields the quantity Y for the given flavor combination. Contracting Y with the baryon source according to (4.52) gives a quantity that completely represents the quark lines $\mathfrak{a}$ and $\mathfrak{c}$, see Figure 4.3. In the case of $C_{1,uudd}$ we need the contractions $\overline{S}_{132}$ (A,C) and $\overline{S}_{312}$ (B,D), which can be read off in Figure 4.4. Since the stochastic line $\mathfrak{b}$ is always connected with the insertion operator $\bar{d}\Gamma_j d$, we can also combine the two expressions before doing the correlation:

$$q_{1,t,j}^{\vec{p},(\ell)}(y) = \overline{S}_{132,t,j}^{\vec{p},(\ell)}(y) - \overline{S}_{312,t,j}^{\vec{p},(\ell)}(y) \ . \tag{4.54}$$

The contribution from the stochastic quark line $\mathfrak{b}$ reads:

$$\left(q_{2,t,i}^{\vec{p},(\ell)}\right)_{\alpha}^{a}(y) := \left[\psi_t^{\dagger,(\ell)}(y)\gamma_5\Gamma_i M_z^{\Phi,\vec{p}}(y)\right]_{\alpha}^{a} \ , \tag{4.55}$$

where the stochastic propagator $\psi_t^{(\ell)}$ is obtained from an inversion on $\eta^{(\ell)}(z')\delta_{z'^4,t}$, see (4.36). The total C_1-contribution is obtained by performing the spatial correlation of q_1 and q_2:

$$C_{1,uudd}^{ij,\vec{p},(\ell)}(\vec{y},t,\tau) = \frac{a^3}{N_{\mathrm{st}}}\sum_{\vec{x}}\sum_{\ell}^{N_{\mathrm{st}}}\left\langle\left[q_{2,t,i}^{T,\vec{p},(\ell)}(x)q_{1,t,j}^{\vec{p},(\ell)}(x+y)\right]\right\rangle\Big|_{x^4=\tau,y^4=0} \ . \tag{4.56}$$

The [.]-notation without indices indicates a closed spinor-color structure. In the expression above we exploit translational invariance to perform a volume average, i.e. instead of evaluating the first insertion at $\vec{0}$ and the second insertion at $\vec{y}$, we consistently sum over all spatial positions, which is represented by the sum over $\vec{x}$.
For the combination $\mathcal{O}^{uu}\mathcal{O}^{uu}$ we read off the sequential sources from Figure 4.5. For this matrix element we only need S^{213}, which we use for the sequential propagator X. From X we again create Y according to (4.51), which is then inserted in the required contractions (4.52). We are able to combine A with C and B with D before doing the spatial correlation, since each insertion is connected to the same quark line within these pairs. In total we have:

$$\begin{aligned}
q_{1,AC,t,j}^{\vec{p},(\ell)}(y) &= \overline{S}_{213,t,j}^{\vec{p},(\ell)}(y) - \overline{S}_{231,j}^{\vec{p},(\ell)}(y) \ , \\
q_{1,BD,t,i}^{\vec{p},(\ell)}(y) &= -\overline{S}_{231,t,i}^{\vec{p},(\ell)}(y) + \overline{S}_{213,i}^{\vec{p},(\ell)}(y) \ , \\
q_{2,AC,t,i}^{\vec{p},(\ell)}(x) &= \psi_t^{\dagger,(\ell)}(x)\gamma_5\Gamma_i M_z^{\Phi,\vec{p}}(x) \ , \\
q_{2,BD,t,j}^{\vec{p},(\ell)}(x) &= \psi_t^{\dagger,(\ell)}(x)\gamma_5\Gamma_j M_z^{\Phi,\vec{p}}(x) \ .
\end{aligned} \tag{4.57}$$

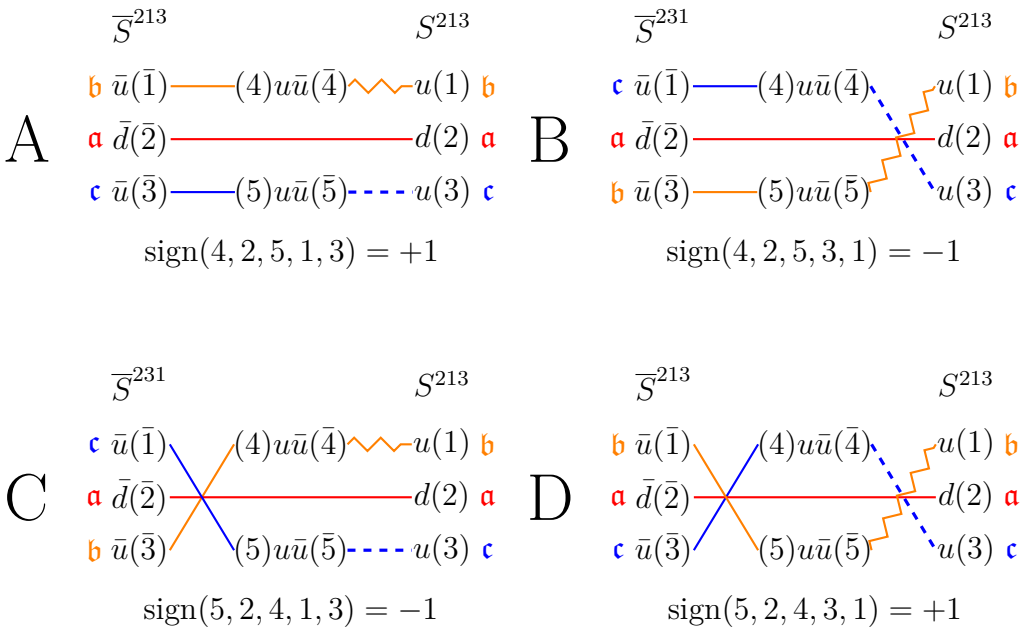

Figure 4.5: Same as Figure 4.4 showing the contributions to $\langle p|\, \mathcal{O}_i^{uu}(0)\mathcal{O}_j^{uu}(y)\,|p\rangle$ with C_1 topology.

With these expressions the total contribution reads:

$$C^{ij,\vec{p},(\ell)}_{1,uuuu}(\vec{y},t,\tau) = \frac{a^3}{N_{\mathrm{st}}}\sum_{\vec{x}}\sum_{\ell}^{N_{\mathrm{st}}}\Big\langle\Big[q^{T,\vec{p},(\ell)}_{2,AC,t,i}(x)\; q^{\vec{p},(\ell)}_{1,AC,t,j}(x+y)\Big] + \Big[q^{T,\vec{p},(\ell)}_{1,BD,t,i}(x)\; q^{\vec{p},(\ell)}_{2,BD,t,j}(x+y)\Big]\Big\rangle\Big|_{x^4=\tau,y^4=0}\ . \tag{4.58}$$

Finally, we discuss the combination $\mathcal{O}^{du}\mathcal{O}^{ud}$, which is not investigated in this thesis, but planned for future work. This case works similar to that of $\mathcal{O}^{uu}\mathcal{O}^{dd}$: From the contributions depicted in Figure 4.6 we combine A with B and C with D, which yields for both combinations the same sequential source (notice that this is exactly the same source as for the $\mathcal{O}^{uu}\mathcal{O}^{dd}$ case):

$$\mathcal{S}^{\vec{p},(\ell)}(y) = S^{\vec{p},(\ell)}_{132}(y) - S^{\vec{p},(\ell)}_{312}(y)\ . \tag{4.59}$$

Subsequently, we proceed like for the flavor combinations we discussed before. The stochastic line is always connected to Γ_j, so we can again combine the obtained terms

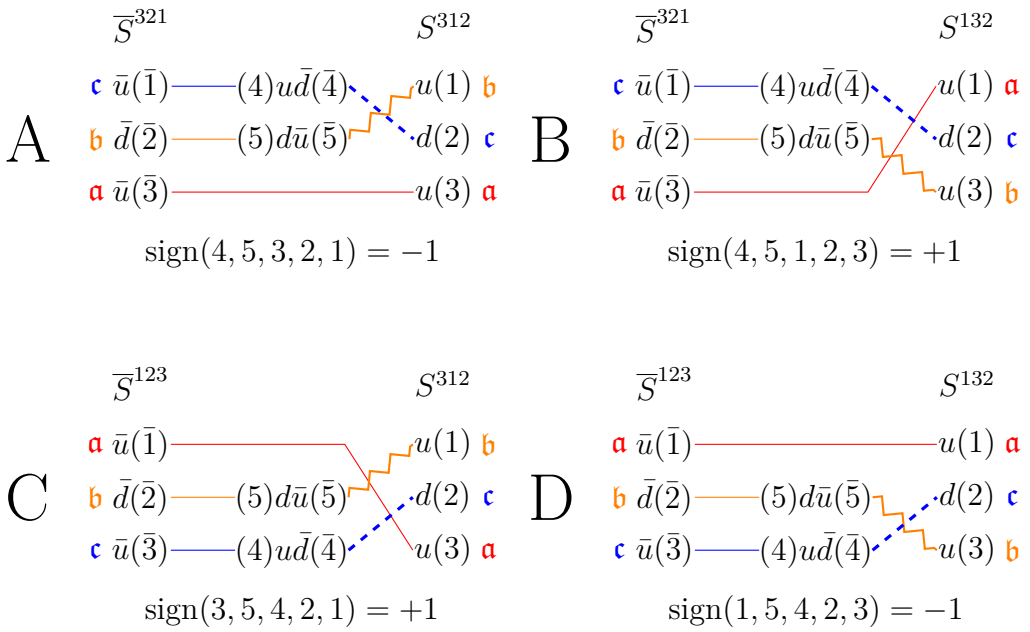

Figure 4.6: Same as Figure 4.4 showing the contributions to $\langle p|\, \mathcal{O}_i^{du}(0)\mathcal{O}_j^{ud}(y)\,|p\rangle = \langle p|\, \mathcal{O}_j^{ud}(0)\mathcal{O}_i^{du}(-y)\,|p\rangle$ with C_1 topology

before doing the correlation:

$$\begin{aligned} q_{1,t,i}^{\vec{p},(\ell)}(y) &= \overline{S}_{321,t,i}^{\vec{p},(\ell)}(y) - \overline{S}_{123,t,i}^{\vec{p},(\ell)}(y)\ , \\ q_{2,t,j}^{\vec{p},(\ell)}(x) &:= \psi_t^{\dagger,(\ell)}(x)\gamma_5\Gamma_j M_z^{\Phi,\vec{p}}(x)\ , \\ C_1^{ij,duud}(\vec{y},t,\tau) &= \frac{a^3}{N_{\mathrm{st}}}\sum_{\vec{x}}\sum_{\ell}^{N_{\mathrm{st}}}\left\langle\left[q_{2,t,j}^{T,\vec{p},(\ell)}(x)q_{1,t,i}^{\vec{p},(\ell)}(x+y)\right]\right\rangle\Big|_{x^4=\tau,y^4=0}\ . \end{aligned} \tag{4.60}$$

For each momentum and each flavor combination we discussed so far we require $12+49N$ inversions, where N is the number of stochastic sources being used. These numbers include the inversion of the spinor-color explicit forward propagator $M_z^{\Phi,\vec{p}}$, which requires 12 inversions, and the sequential and stochastic propagator. For the sequential propagator $X_t^{\Phi,\vec{p},(\ell)}$ we need to invert $12\times 4 = 48$ times, i.e. for each spinor and color index value at the source and for each value of the open fermion spinor index at the sink. However, this is still requires much less inversions than spinor-color explicit all-to-all propagators ($48 \ll 12L^3$). The stochastic propagator $\psi_t^{(\ell)}$ requires the inversion of only one column.

Loops L_1 and L_2: Before we discuss the remaining graphs, we have to consider the loops L_1 and L_2 defined in (4.17), which are needed for the S_1, S_2 and D contraction. For the first loop type L_1 we implement two solutions, where for the first one we employ stochastic sources, and for the second one we use a point source at a fixed position.

For L_1 we use the same type of stochastic sources as for the C_1 graph but at time slice τ. The appearance of additional fluctuations introduced by the usage of stochastic noise vectors may be reduced by implicitly removing hopping terms of the Dirac operator, as we discussed earlier in this section. In total the loop can be written as:

$$L^j_{1,\mathrm{st}}(\vec{y},\tau) := \frac{1}{N_{\mathrm{st}}} \sum_{\ell}^{N_{\mathrm{st}}} \left[\eta^{\dagger(\ell)}_{\tau}(y)\Gamma_j \xi^{(\ell),N}_{\tau}(y)\right]\Big|_{y^4=\tau} , \tag{4.61}$$

where N depends on the Dirac structure Γ, see table 4.2. Another possibility is to calculate the loop L_1 directly on a point source, which avoids the introduction of stochastic noise. A disadvantage is that for each loop position we are interested in the calculation has to be repeated. This version we shall only apply in the case of the D graph:

$$L^j_{1,\mathrm{pt}}(\vec{y},\tau) := \mathrm{tr}\left\{\Gamma_j M_y(y)\right\}|_{y^4=\tau} \ . \tag{4.62}$$

Sometimes we will use the volume average of the loop expressions. For this purpose we introduce the notation

$$\left\langle\left\langle L^j_1(\tau)\right\rangle\right\rangle := \frac{1}{V}\sum_{\vec{y}} \left\langle L^j_1(\vec{y},\tau)\right\rangle \ . \tag{4.63}$$

The second kind of loops L_2 contributes in the case of the S_2 graph. Its basic structure contains two spatially separated insertions being connected by two propagators. Using stochastic noise vectors is not feasible in this case. Thus, we will evaluate the loop employing point-to-all propagators only. Specifically, that is:

$$L^{ij}_2(\vec{y},\tau) = \mathrm{tr}\left\{\gamma_5 M^{\dagger}_x(x+y)\gamma_5\Gamma_i M_x(x+y)\Gamma_j\right\}\Big|_{x^4=\tau,y^4=0} \ , \tag{4.64}$$

where we may average over several positions $\vec{x}$ to improve the signal.

Graphs C_2 and S_1: The two contractions C_2 and S_1 defined in (4.20) are both constructed using the sequential source method, where we reuse the sources that have been employed for usual proton three point functions. These are already provided by [102]. For our purposes we need the following sources[1]:

$$\begin{aligned}\left(S^{\vec{p}}_{3\mathrm{pt},u}\right)^{ab}_{\alpha\beta}(z') = {}& \mathcal{E}^{\vec{p}}(z')\left[\Pi\Phi^{\vec{p}} M^{\Phi,\vec{p}}_z(z') E^a \left(E^b \Phi^{\vec{p}} M_z(z')^{\Phi,\vec{p}}\right)^T\right]^{cc}_{\alpha\beta} \\ & + \mathcal{E}^{\vec{p}}(z')\Pi_{\alpha\beta}\,\mathrm{tr}\left\{\Phi^{\vec{p}} M^{\Phi,\vec{p}}_z(z') E^a \left(E^b \Phi^{\vec{p}} M^{\Phi,\vec{p}}_z(z')\right)^T\right\} \\ & + \mathcal{E}^{\vec{p}}(z')\left[\left(E^b \Phi^{\vec{p}} M^{\Phi,\vec{p}}_z(z') E^a\right)^T \Phi^{\vec{p}} M^{\Phi,\vec{p}}_z(z')\Pi\right]^{cc}_{\alpha\beta}\end{aligned} \tag{4.65}$$

[1] In contrast to the sequential source (4.48) used for the C_1 contraction, the three-point sources $S^{\vec{p}}_{3\mathrm{pt}}$ are defined without γ_5, instead, it is re-included in (4.66)

$$+ \mathcal{E}^{\vec{p}}(z') \left(\Phi^{\vec{p}} M_z^{\Phi,\vec{p}}(z')\Pi\right)^{cd}_{\gamma\gamma} \left[\left(E^b \Phi^{\vec{p}} M_z^{\Phi,\vec{p}}(z') E^a\right)^T\right]^{dc}_{\alpha\beta} ,$$

$$\left(S^{\vec{p}}_{3\mathrm{pt},d}\right)^{ab}_{\alpha\beta}(z') = \mathcal{E}^{\vec{p}}(z') \left(\Phi^{\vec{p}} M_z^{\Phi,\vec{p}}(z')\Pi\right)^{cd}_{\gamma\gamma} \left[\left(E^b \Phi^{\vec{p}} M_z^{\Phi,\vec{p}}(z') E^a\right)^T\right]^{dc}_{\alpha\beta}$$
$$- \mathcal{E}^{\vec{p}}(z') \left(E^b \Phi^{\vec{p}} M_z^{\Phi,\vec{p}}(z')\right)^{cd}_{\beta\gamma} \left(\Pi \Phi^{\vec{p}} M_z^{\Phi,\vec{p}}(z') E^a\right)^{cd}_{\gamma\alpha} .$$

The corresponding sequential propagator X_t is then obtained by:

$$\mathcal{D} X^{\Phi,\vec{p}}_{t,3\mathrm{pt}} = \Phi^{\vec{p}} \gamma_5 S^{\dagger,\vec{p}}_{t,3\mathrm{pt}} , \tag{4.66}$$

where again

$$S^{\vec{p}}_{t,3\mathrm{pt}}(z') = S^{\vec{p}}_{3\mathrm{pt}}(z') \; \delta_{z'^4,t} . \tag{4.67}$$

In the case of the C_2 graph the corresponding sequential solution has to be contracted with an additional propagator connecting the two inserted operators. This propagator is obtained by an inversion on a stochastic source. As we already discussed, we are able to reduce noise by means of the hopping parameter expansion (HPE), see (4.39). In total we can write the C_2 graph as:

$$\begin{aligned} C_2^{ij,\vec{p}}(\vec{y},t,\tau) = \frac{a^3}{N_{\mathrm{st}}} \mathcal{E}^{-\vec{p}}(z) \sum_{\ell}^{N_{\mathrm{st}}} \sum_{\vec{x}} \Big\langle \Big[X^{\dagger,\Phi,\vec{p}}_{t,3\mathrm{pt}}(\vec{x},\tau) \gamma_5 \Gamma_i \xi^{(\ell),n(\vec{y})}_{\tau}(\vec{x},\tau) \Big] \\ \times \Big[\eta^{\dagger(\ell)}(\vec{x}+\vec{y},\tau) \Gamma_j M_z^{\Phi,\vec{p}}(\vec{x}+\vec{y},\tau) \Big] \Big\rangle \Big|_{z^4=0} . \end{aligned} \tag{4.68}$$

In order to give an expression for the S_1 graph, we define the three point contraction as:

$$G^{i,\vec{p}}_{3\mathrm{pt}}(\vec{x},\tau,t) = \frac{1}{N_{\mathrm{st}}} \mathcal{E}^{-\vec{p}}(z) \sum_{\ell}^{N_{\mathrm{st}}} \Big[X^{\dagger,\Phi,\vec{p}}_{t,3\mathrm{pt}}(\vec{x},\tau) \gamma_5 \Gamma_i M_z^{\Phi,\vec{p}}(\vec{x},\tau) \Big] \Big|_{z^4=0} . \tag{4.69}$$

The contraction S_1 itself is obtained by a spatial correlation of the function $G_{3\mathrm{pt}}$ with the loop L_1 introduced above. Notice that for operator combinations having the same quantum numbers as the vacuum, each of the two disconnected parts may have contributions arising from overlap with the vacuum. These contributions we have to subtract. In total we have:

$$\begin{aligned} S_1^{ij,\vec{p}}(\vec{y},t,\tau) = -a^3 \sum_{\vec{x}} \langle G^{i,\vec{p}}_{3\mathrm{pt}}(\vec{x},\tau,t) L_1^j(\vec{x}+\vec{y},\tau) \rangle \\ + a^3 \sum_{\vec{x}} \langle G^{i,\vec{p}}_{3\mathrm{pt}}(\vec{x},\tau,t) \rangle \langle \langle L_1^j(\tau) \rangle \rangle . \end{aligned} \tag{4.70}$$

Graphs S_2 and D: The remaining two graphs are composed of a two point contraction correlated with one L_2 loop or two spatially separated L_1 loops, respectively. Again, we have to consider vacuum contributions, which have to be subtracted. Since the spatial

id	β	a[fm]	$L^3 \times T$	$\kappa_{l/s}$	$m_{\pi/K}$[MeV]	$m_\pi La$	conf.
H102	3.4	0.0856	$32^3 \times 96$	0.136865	355	4.9	2037
				0.136549339	441		

Table 4.3: Details of the CLS ensemble used for our simulation. The simulations include 990 configurations.

	$\vec{p}$	C_1	C_2	S_1(st)	S_2(pt)	D(st⊗st)	D(st⊗pt)	3pt	2pt
$N_{\text{nucl-src}}$	$= \vec{0}$	1	2	-	-	-	-	4	25
	$\neq \vec{0}$	1	1	-	-	-	-	1	21
$N_{\text{stoch/ins}}$	all	2	96	120	240	$4(60 \otimes 60)$	$2(120 \otimes 120)$	-	-
vol. average	all	y	y	y	n	y	n	y	n

Table 4.4: Overview of the statistics entering the simulations. $N_{\text{nucl-src}}$ describes the number of proton source positions being used for each graph. $N_{\text{stoch/ins}}$ corresponds to the size of the set of stochastic noise vectors. In the last line we list whether volume averaging is possible.

position of the L_2 loop is fixed by definition, we are not able to perform a volume average like in the previous cases:

$$S_2^{ij,\vec{p}}(\vec{y},t,\tau) = -\langle \tilde{G}^{\vec{p}}_{\text{2pt}}(t) L_2^{ij}(\vec{y},\tau)\rangle + \langle \tilde{G}^{\vec{p}}_{\text{2pt}}(t)\rangle\langle L_2^{ij}(\vec{y},\tau)\rangle \ . \tag{4.71}$$

The D graph is evaluated in two different manners, first, using two stochastic loops $L_{1,\text{st}}$, which enables us to perform a volume average, and second, with one loop being evaluated using a point source at fixed position. For brevity, we give here only the expression for the first version, the second expression looks completely analogue, where the second stochastic loop has to be replaced by a point source loop. As a consequence, the sum incorporating the volume average has to be dropped:

$$\begin{aligned} D^{ij,\vec{p}}(\vec{y},t,\tau) = a^3 \sum_{\vec{x}} \Big\{ & \Big\langle \tilde{G}^{\vec{p}}_{\text{2pt}}(t) L^i_{1,\text{st}}(\vec{x},\tau) L^j_{1,\text{st}}(\vec{x}+\vec{y},\tau)\Big\rangle \\ & - \Big\langle \tilde{G}^{\vec{p}}_{\text{2pt}}(t)\Big\rangle \Big\langle L^i_{1,\text{st}}(\vec{x},\tau) L^j_{1,\text{st}}(\tau)\Big\rangle \\ & - \Big\langle \tilde{G}^{\vec{p}}_{\text{2pt}}(t) L^i_{1,\text{st}}(\vec{x},\tau)\Big\rangle \Big\langle \Big\langle L^j_{1,\text{st}}(\tau)\Big\rangle\Big\rangle \\ & - \Big\langle \tilde{G}^{\vec{p}}_{\text{2pt}}(t) L^j_{1,\text{st}}(\vec{x},\tau)\Big\rangle \Big\langle \Big\langle L^i_{1,\text{st}}(\tau)\Big\rangle\Big\rangle \Big\} \\ & + 2 \Big\langle \tilde{G}^{\vec{p}}_{\text{2pt}}(t)\Big\rangle \Big\langle \Big\langle L^i_{1,\text{st}}(\tau)\Big\rangle\Big\rangle \Big\langle \Big\langle L^j_{1,\text{st}}(\tau)\Big\rangle\Big\rangle \ . \end{aligned} \tag{4.72}$$

4.3.2 Lattice setup

We now discuss the details of the setup that is used for our simulations. The employed ensemble has been generated by the CLS collaboration [76] with $n_f = 2 + 1$ non-perturbatively improved Sheikholeslami-Wohlert fermions and the tree level improved Lüscher-Weisz action, see (3.44). The collaboration has generated a whole set of ensembles following certain trajectories regarding the lattice parameters. Repeating the present calculation on more ensembles corresponding to one trajectory would allow to extrapolate to the physical point, which is not intended in our analysis. For this pilot study we start with the ensemble H102, a $32^3 \times 96$ ensemble with open boundary conditions in time and pseudoscalar masses $m_\pi = 355$ MeV and $m_K = 441$ MeV. The lattice spacing is $a = 0.0856$ fm corresponding to $\beta = 3.4$. More details can be found in table 4.3.
For our purpose it is important to cover a wide range of proton momenta. The simulations have been performed for momenta $\vec{p} = -2\pi\vec{P}/(La)$ with $\vec{P} = (0,0,0)$, $(1,1,1)$, $(2,2,2)$, $(-2,-2,2)$, $(-2,2,-2)$, $(2,-2,-2)$, corresponding to a largest squared momentum of $\vec{p}^2 = 2.47\ \mathrm{GeV}^2$.
Since the ensemble has open boundary conditions, we place the proton source at $t_{\mathrm{src}} = T/2 = 48a$ at random spatial position. As source-sink time separation we choose $t = t_{\mathrm{snk}} - t_{\mathrm{src}} = 12a$ for the case where the proton momentum is zero and $t = 10a$ for all other momenta. The C_1 graph is evaluated for all possible intermediate insertion times $0 < \tau < t$, whereas all other contractions are calculated for insertion time $\tau = 6a$ ($\vec{p} = \vec{0}$) or $\tau = 5a$ ($\vec{p} \neq \vec{0}$), respectively. The disconnected parts $\langle L_2(\tau)\rangle$ and $\langle L_1(\tau)L_1(\tau)\rangle$ do not depend on the proton momentum and are averaged over both insertion times to increase statistics. Since we use a different source-sink separation for $\vec{p} = \vec{0}$ and $\vec{p} \neq \vec{0}$, the average time of the insertion is slightly off-center between source and sink, which is fine as long as there are no significant excited state contributions.
To increase statistics, the calculations are performed for multiple proton source positions on each configuration. An overview of the corresponding numbers can be found in table 4.4. Therein we also summarize the numbers of stochastic noise vectors being used for each contraction. As described earlier, the propagators are momentum smeared (see (4.32)) at the proton source and sink, where we apply 250 smearing iterations.
In this simulation we evaluate each graph for each momentum and flavor combination contributing to proton-proton matrix elements, but we omit the C_1 graph for flavor changing operators. This is left for future work.

4.3.3 Computational details

Each of the expressions derived in section 4.3.1 is evaluated in the framework of the Chroma software stack [102]. The existing library has been extended accordingly. For the inversions of the Wilson-Dirac operator, which yield the required propagators, we use the multi-grid algorithm [103–106], which has been adapted to the used architecture. The simulations are performed on the KNL cluster QPACE 3 [107].
Each quantity is calculated for 990 gauge configurations. In order to reduce effects

of autocorrelations between the gauge configurations, we employ the binning method, where each sample is calculated from 10 configurations. From these we create 99 Jackknife samples, which are used to treat error propagation consistently within subsequent analyses. For a brief summary of the method, see section A.5.

4.4 Results and data quality

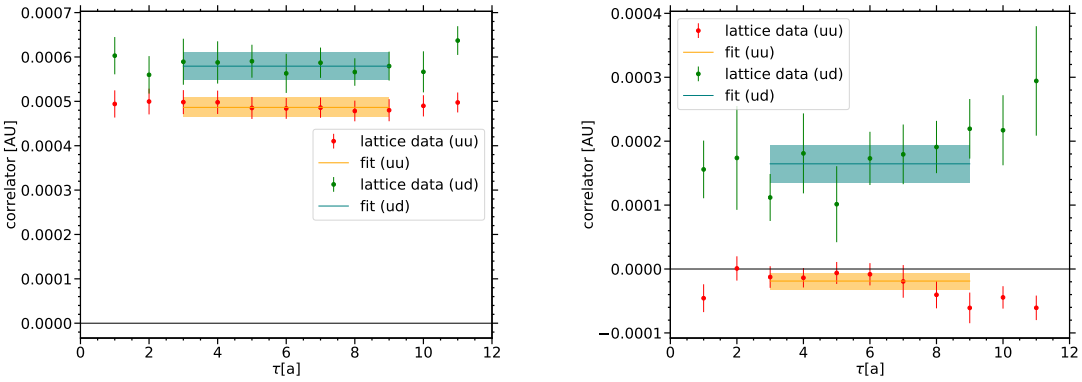

(a) τ-fit at $\vec{y} = (-3, 4, 3)a$ for $\langle V^0 V^0 \rangle$ (b) τ-fit at $\vec{y} = (-3, 4, 3)a$ for $\langle A^0 A^0 \rangle$

Figure 4.7: Dependence of C_1^{uuuu} (red) and C_1^{uudd} (green) on the insertion time τ for operator insertions $V^0 V^0$ (a) and $A^0 A^0$ (b) and the operator separation $y = (-3, 4, 3)$. We also show the plateau fit, from which the final value of C_1 for the given operator distance is determined.

We conclude this chapter with first results concerning the bare two-current matrix elements. We restrict ourselves to the current combinations $V^4 V^4$ and $A^4 A^4$ and the proton momentum $\vec{p} = \vec{0}$. We give an overview of all contributing contractions for each matrix element.
As described earlier, the C_1 graph is calculated for several insertion time slices. The final result, which depends on the operator distance only, is obtained by a fit over a region where excited states are assumed to be suppressed, i.e. the time difference between the insertions and the source or the sink is sufficiently large. Figure 4.7 shows the dependence on the insertion time τ for the possible flavor combinations in the vector-vector and axial-axial case. The spatial insertion operator separation is $\vec{y} = (-3, 4, 3)a$. In the vector-vector case we can observe a flat platteau in the whole plot region. Excited states can be assumed to be under control in that case. The signal turns out to be less smooth in the axial-axial channel. Nevertheless, within the statistical error we cannot definitely observe a curvature indicating excited states.
The plots also indicate mean value and error band of the constant fit over τ in the corresponding region, which we have chosen to be $\tau \in [3a, 9a]$. This fit result determines the value of $C_1(\vec{y})$ for each separation $\vec{y}$. As mentioned earlier, the contractions C_2, S_1, S_2 and D have been calculated for $\tau = t/2$ only, which is $\tau = 12a$ for $\vec{p} = \vec{0}$.

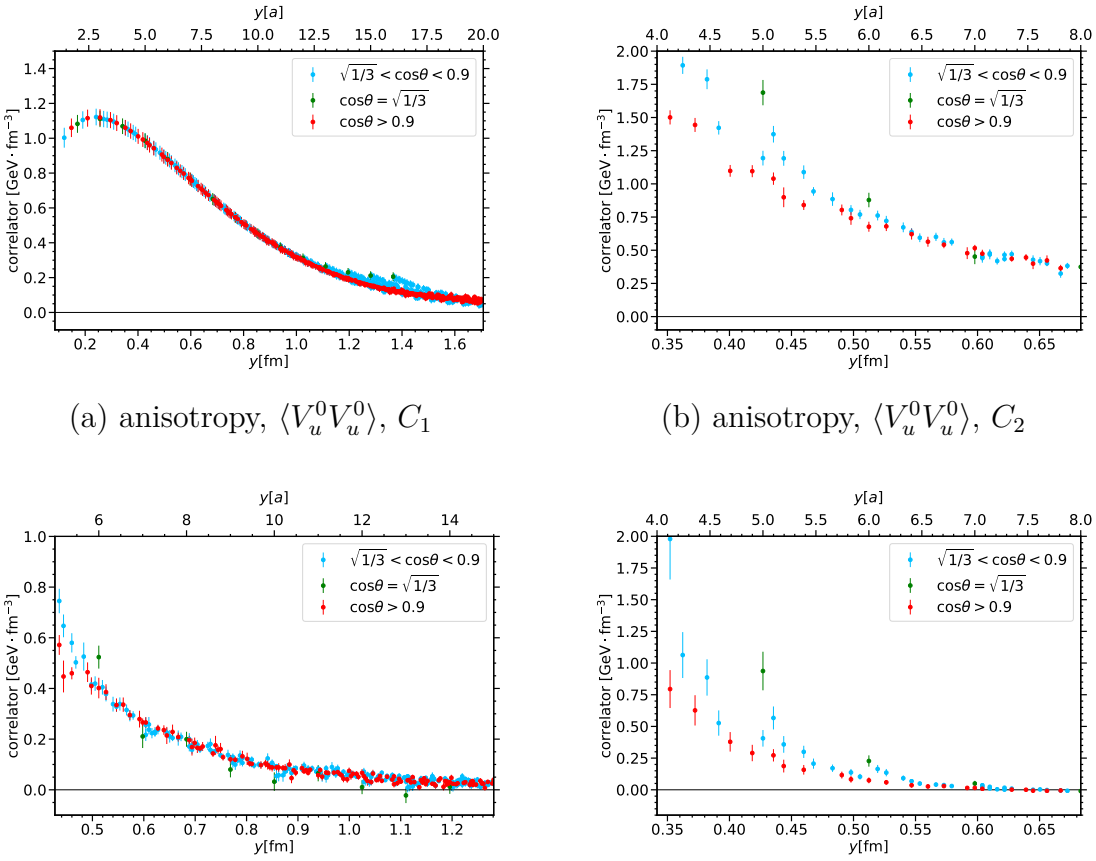

(a) anisotropy, $\langle V_u^0 V_u^0 \rangle$, C_1

(b) anisotropy, $\langle V_u^0 V_u^0 \rangle$, C_2

(c) anisotropy, $\langle V_d^0 V_d^0 \rangle$, C_2

(d) anisotropy, $\langle V_q^0 V_q^0 \rangle$, S_2

Figure 4.8: Visualization of different kinds of anisotropy effects appearing in the 4pt data, where we distinguish between different ranges of the angle θ between $\vec{y}$ and the neighboring diagonal. Here we show the data for the VV channel for the C_1 graph for flavor uu (a), as well as the C_2 graph for uu (b) and dd (c), and the S_2 graph (d).

From now on we concentrate on the $\vec{y}$-dependence of the contractions. In the case of zero momentum, the considered matrix elements are rotational invariant in the continuum, i.e. they only depend on $y = |\vec{y}|$ (for remarks on the notation of the distance, see (A.15)). On the lattice this symmetry is broken, leading to artifacts in the observed signal. Each contraction may be affected by that in various manners.
A source of anisotropy is the finite extension of the lattice combined with periodic boundary conditions. As a consequence, the resulting signal appears to be modified by mirror charges w.r.t. to the lattice boundary planes. The overlap is stronger for current separations parallel to the axes, since mirror charges lie closer together in this case. In panel (a) of Figure 4.8 we show the data of C_1^{uuuu} for the VV channel, where we distinguish the points w.r.t. to the angle θ between the corresponding separation vector $\vec{y}$ and the neighboring diagonal. We observe that for separations along a lattice

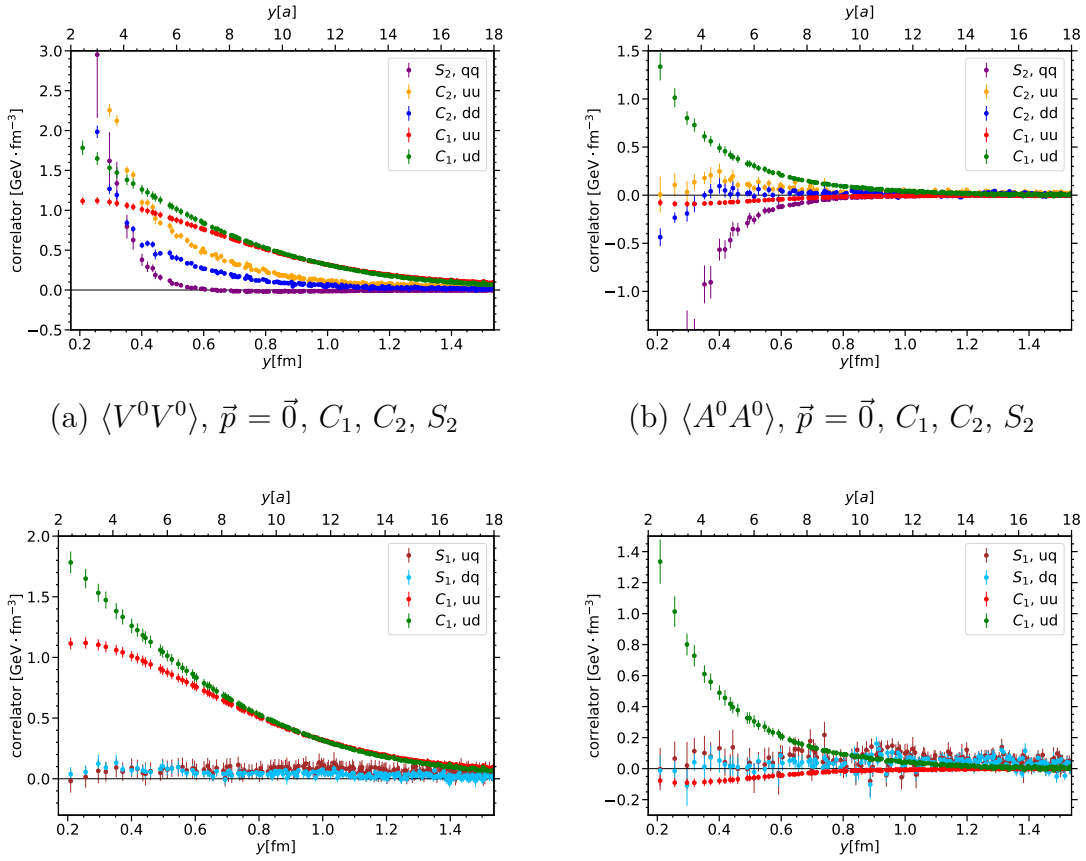

(a) $\langle V^0 V^0 \rangle$, $\vec{p} = \vec{0}$, C_1, C_2, S_2

(b) $\langle A^0 A^0 \rangle$, $\vec{p} = \vec{0}$, C_1, C_2, S_2

(c) $\langle V^0 V^0 \rangle$, $\vec{p} = \vec{0}$, C_1, S_1

(d) $\langle A^0 A^0 \rangle$, $\vec{p} = \vec{0}$, C_1, S_1

Figure 4.9: Results for two-current matrix elements for the insertions V^4V^4 (a,c) and A^4A^4 (b,d) in dependence of the operator distance y for $\vec{p} = \vec{0}$. The data is compared for the graphs C_1, C_2 and S_2 (a,b), as well as C_1 and S_1 (c,d) for a specific flavor combination. q can be both, an up or a down quark.

axis ($\cos\theta = 1/\sqrt{3}$) the values for the correlator are significantly different from those obtained for separations close to a lattice diagonal ($\cos\theta > 0.9$).
Another anisotropy effect can be seen in those contractions where the two currents are directly connected by a quark propagator. This is originating from the fact that the Wilson propagator itself shows some anisotropic behavior, which has been studied in detail in [108]. In the present study this concerns the contractions C_2 and S_2. These effects are visualized in Figure 4.8 (b-d), where we again compare the data points for lattice sites in the vicinity of a diagonal (red) with the other data points (blue and green, where green points are those on the axes).
On the basis of this discussion we decide for subsequent analysis steps to take into

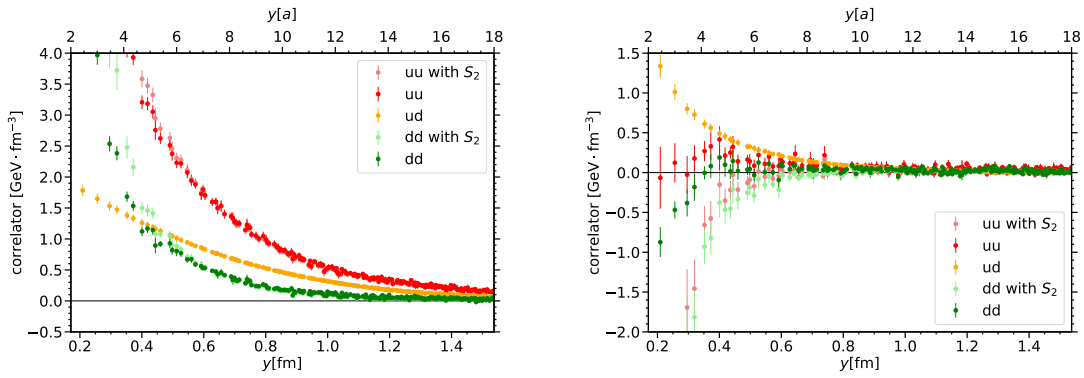

(a) $\langle V^0 V^0 \rangle, \vec{p} = \vec{0}$ (b) $\langle A^0 A^0 \rangle, \vec{p} = \vec{0}$

Figure 4.10: Physical sums of contractions for a specific flavor combination according to (4.28). This is shown for the insertions V^4V^4 (a) and A^4A^4 (b) in dependence of the operator distance y. The data includes the graphs C_1, C_2 and S_2.

account only data points at positions $\vec{y}$ that fulfill the condition

$$\cos(\theta(\vec{y})) > 0.9 \ . \tag{4.73}$$

This cut has been used e.g. in [109] in order to remove the lattice propagator anisotropies. In the cases where we have a slowly decreasing signal at large distances, this cut will also remove the effects caused by mirror charges, which we have discussed before. The final results for the contractions C_1, C_2, S_1 and S_2 for different flavor combinations is plotted in Figure 4.9 for the considered channels V^4V^4 and A^4A^4. The D graph is not shown, since it has been found that the spatial correlation of two loops L_1 does not yield a clear signal at the current level of statistics. This is the case for both evaluation methods we introduced in section 4.3.1. Although we expect this contraction to give at most a small contribution, this part of our analysis is a source of non-negligible uncertainties. For all other contractions we find clear signals, which are dominated by the connected contractions C_1 and C_2 in the channel V^4V^4. The latter is mostly relevant at smaller insertion distances. The two disconnected contributions S_1 and S_2 are compatible with zero for large $\vec{y}$. While this is also the case for S_1 in the short distance region, we observe a steep increase of the signal for the S_2 contraction. The situation is different, when considering the two axial vector currents, where one can observe a suppression of the C_2 signal and the flavor combination uu.
We finally show some results on physical matrix elements, i.e. the sum of contractions needed to obtain a matrix element of operators with definite quark flavor. These have already been listed in (4.28). The combinations are built taking into account the data for the graphs C_1, C_2 and S_2, since these contractions yield large contributions, whereas the signal of S_1 is consistent with zero. The corresponding data are shown in Figure 4.10, again for the two operator combinations V^4V^4 and A^4A^4. As we will discover in the following chapter the S_2 contribution breaks Lorentz symmetry at small

distances. Therefore, results containing S_2 data should be interpreted with great care in regions where y is small. In Figure 4.10 we plot the physical matrix elements having a S_2 contribution, i.e. uu and dd, with the S_2 data added (light colors), as well as the result without the S_2 contribution. For $\langle V^0 V^0 \rangle$ adding S_2 visibly enhances the signal. This is more drastic in the case of $\langle A^0 A^0 \rangle$, where without the S_2 contribution the signal is close to zero.
For ud we observe a clear signal for both matrix elements. In the case of $\langle V^0 V^0 \rangle$ we find also a large contribution of uu, which is steeply increasing at small current distances. The same holds for dd, where the signal is very small for larger y. In the case of $\langle A^0 A^0 \rangle$ uu and dd contributions are relatively large at small y if one takes into account the S_2 data. Otherwise, the values are small compared to ud.
At this point we want to mention that $\langle V^0 V^0 \rangle$ has already been calculated for the proton in quenched simulations in the past [88–91]. The first simulations including $n_f = 2$ dynamical fermions have been performed in [92, 93]. In the latter a maximal lattice extension of $24^3 \times 40$ with lattice spacing $a = 0.077$ fm and parameters corresponding to a pion mass $m_\pi \geq 384$ MeV have been employed, using around 200 gauge configurations. These studies take into account only one contraction, which corresponds to our C_1-graph for flavor ud. The results obtained therein show a slightly steeper decay of the signal with increasing distance. This can be explained with the different pion mass.

5 Mellin moments of DPDs

The results we obtained from the lattice in the previous chapter provide access to quantities related to DPDs. In particular, we are able to resolve their dependence on the transverse quark distance. As we shall explain in the following, the two-current matrix elements can be parameterized in terms of invariant functions, which correspond to Mellin moments of DPDs for certain combinations of quark polarizations. Furthermore, we are able to study the quark flavor dependence by considering the physical sums of lattice contractions (4.28). The relative size of polarization effects for DPDs in the nucleon for a specific quark flavor combination has been investigated in the context quark models [33, 36].

5.1 Relation to two-current correlations

As we have seen in section 2.4, the definition of a collinear DPD involves a hadronic matrix element of two light cone operators. Since our calculations on the lattice are performed in Euclidean spacetime, these matrix elements cannot be computed directly, because we are not able to access physical time. A common way around this issue is to consider not the distribution function itself, but its moments w.r.t. the momentum fractions it depends on. This is frequently used for calculations of PDFs or GPDs. The same is carried out for DPDs $F_{ab}(x_1, x_2, \zeta, \boldsymbol{y})$ in this work, where we take into account the non-forward case $\zeta \neq 0$. We generally define the (n, m)-th Mellin moment as:

$$M_{ab}^{(n,m)}(\zeta, \boldsymbol{y}) = \int_{-1}^{1} \mathrm{d}x_1 \; x_1^{n-1} \int_{-1}^{1} \mathrm{d}x_2 \; x_2^{m-1} F_{ab}(x_1, x_2, \zeta, \boldsymbol{y}) \; . \tag{5.1}$$

Applying this integral to the expression (2.50) and performing $n-1$ or $m-1$ partial integration steps in the x_1 or x_2 integral, respectively, the corresponding Fourier coefficient will fix the light cone distance within the quark bilinears to zero. Hence, the resulting matrix elements only contain local operators being separated by a vector y:

$$\begin{aligned} M_{ab}^{(n,m)}(\zeta, \boldsymbol{y}) &= (p^+)^{1-n-m} \sum_{\lambda} \int \mathrm{d}y^- e^{-i\zeta p^+ y^-} \; \langle p, \lambda | \, \mathcal{O}_a^{n-1}(y) \; \mathcal{O}_b^{m-1}(0) \, | p, \lambda \rangle \Big|_{y^+=0} \\ &= 2(p^+)^{1-n-m} \int \mathrm{d}y^- e^{-i\zeta p^+ y^-} \; \mathcal{M}_{ba}^{(n-1,m-1)}(p, y) \Big|_{y^+=0} \; , \end{aligned} \tag{5.2}$$

with the local operators being defined as:

$$\mathcal{O}_a^n(y) := \bar{q}^{(f_a)}(y) \; \Gamma_a \left(i \overleftrightarrow{D}^+ \right)^n q^{(f_a)}(y) \; . \tag{5.3}$$

Notice that for $(n, m) = (1, 1)$ the matrix elements in (5.2) can be identified with those defined in (4.1)[1]

$$\begin{aligned}
\mathcal{M}^{++}_{VV,qq'} &= 4\mathcal{M}_{qq'} \ , & \mathcal{M}^{++}_{AA,qq'} &= 4\mathcal{M}_{\Delta q\Delta q'} \ , \\
\mathcal{M}^{j++}_{TV,qq'} &= 4\mathcal{M}^{j}_{\delta qq'} \ , & \mathcal{M}^{+j+}_{VT,qq'} &= 4\mathcal{M}^{j}_{q\delta q'} \ , \\
\mathcal{M}^{j+l+}_{TT,qq'} &= 4\mathcal{M}^{jl}_{\delta q\delta q'} \ .
\end{aligned} \tag{5.4}$$

The factors 4 on the r.h.s. of each equation in (5.4) arises from the relative factor 2 between the operator definitions (2.29) and (3.68), respectively. Still the r.h.s. of (5.2) cannot be computed directly on the lattice because of the non-vanishing light like distance y^-. In order to avoid this problem, we exploit Lorentz symmetry of the appearing matrix elements. Depending on the Dirac structure and the number of derivatives, each matrix element carries a certain number of Lorentz indices. On the other hand, there are at most two Lorentz vectors the quantities in (5.2) depend on, namely y and p. Thus, we are able to decompose the local matrix elements in terms of these vectors and invariant functions.
At the moment, we only consider operators that do not contain derivatives, i.e. we focus on the first Mellin moment in each momentum fraction. At leading twist we have to take into account three types of operators, namely V^μ, A^μ and $T^{\mu\nu}$. Furthermore, we subtract trace contributions where these are not relevant, which will reduce the complexity of our calculations. For the channels we are interested in, we write the following decompositions, which have been formulated in [46]:

$$\begin{aligned}
\mathcal{M}^{\mu\nu}_{VV,qq'} - \frac{1}{4}g^{\mu\nu}\,\mathrm{tr}\,\{\mathcal{M}_{VV,qq'}\} &= u^{\mu\nu}_{VV,A}A_{q'q} + u^{\mu\nu}_{VV,B}m^2B_{q'q} + u^{\mu\nu}_{VV,C}m^4C_{q'q} \ , \\
\mathcal{M}^{\mu\nu\rho}_{TV,qq'} + \frac{2}{3}g_{\lambda\sigma}g^{\rho[\mu}\mathcal{M}^{\nu]\lambda\sigma}_{TV,qq'} &= u^{\mu\nu\rho}_{TV,A}mA_{q'\delta q} + u^{\mu\nu\rho}_{TV,B}m^3B_{q'\delta q} \ , \\
\frac{1}{2}\left[\mathcal{M}^{\mu\nu\rho\sigma}_{TT,qq'} + \mathcal{M}^{\rho\sigma\mu\nu}_{TT,qq'}\right] &= u^{\mu\nu\rho\sigma}_{TT,A}A_{\delta q'\delta q} + u^{\mu\nu\rho\sigma}_{TT,B}m^2B_{\delta q'\delta q} + u^{\mu\nu\rho\sigma}_{TT,C}m^2C_{\delta q'\delta q} \\
&\quad + u^{\mu\nu\rho\sigma}_{TT,D}m^4D_{\delta q'\delta q} + u^{\mu\nu\rho\sigma}_{TT,E}m^2E_{\delta q'\delta q} \ ,
\end{aligned} \tag{5.5}$$

where we absorbed tensor expressions involving y^μ, p^μ and $g^{\mu\nu}$ into the Lorentz covariant variables u, which are listed in section A.3. The decomposition for $\mathcal{M}^{\mu\nu}_{AA,qq'}$ is exactly the same as for $\mathcal{M}^{\mu\nu}_{VV,qq'}$, which introduces the invariant functions $A_{\Delta q'\Delta q}$, $B_{\Delta q'\Delta q}$ and $C_{\Delta q'\Delta q}$. A decomposition of $\mathcal{M}^{\mu\nu\rho}_{TV,qq'}$ is achieved by interchanging the indices ρ and $\mu\nu$ on the l.h.s. . The functions A, B, etc are Lorentz scalars, i.e. they depend only on the Lorentz scalars py and y^2. If we consider only components contributing to leading

[1] In contrast to the definition in (4.1) we write flavor indices as subscript to avoid confusions with the Lorentz index notation.

twist, we find that the expression (5.5) gives:

$$\begin{aligned}
\mathcal{M}^{++}_{VV,qq'}(p,y) &= 2(p^+)^2 A_{q'q}(py,y^2)\ , \\
\mathcal{M}^{++}_{AA,qq'}(p,y) &= 2(p^+)^2 A_{\Delta q'\Delta q}(py,y^2)\ , \\
\mathcal{M}^{j++}_{TV,qq'}(p,y) &= 2(p^+)^2 y^j m A_{q'\delta q}(py,y^2)\ , \\
\mathcal{M}^{+j+}_{VT,qq'}(p,y) &= 2(p^+)^2 y^j m A_{\delta q' q}(py,y^2)\ , \\
\mathcal{M}^{j+l+}_{TT,qq'}(p,y) &= 2(p^+)^2 \left[\delta^{jl} A_{\delta q'\delta q}(py,y^2) - (2y^j y^l + \delta^{jl} y^2) m^2 B_{\delta q'\delta q}(py,y^2)\right]\ ,
\end{aligned} \tag{5.6}$$

i.e. there are six[2] independent functions contributing to twist-2 matrix elements. These functions are referred to as twist-2 functions in the following. Following the nomenclature of [46] the functions $A_{\Delta q\Delta q'}$ and $A_{\delta q\delta q'}$ are called "spin-spin-correlations", whereas $A_{q\delta q'}$, $A_{\delta qq'}$ and $B_{\delta q\delta q'}$ are named "spin-orbit-correlations".
Comparing with the decompositions of collinear DPDs (2.57) in terms of $f(x_1,x_2,\zeta,y^2)$, we can identify exactly the same coefficients as in (5.6) if we apply a rotation of the transverse polarization by 90°. This is necessary, since the twist-2 operator that corresponds to transverse polarization, see (2.29), includes an extra γ_5 compared to the lattice operators (3.68). The γ_5 is removed by the aforementioned rotation, which follows from the identity $i\sigma^{j+}\gamma_5 = \epsilon^{jk}\sigma^{k+}$.
Integrating over the momentum fractions and plugging in the relation (5.2), we find e.g. for the case of V^+V^+:

$$\begin{aligned}
\int \mathrm{d}x_1 \int \mathrm{d}x_2\ f_{qq'}(x_1,x_2,\zeta,y^2) &= \int \mathrm{d}x_1 \int \mathrm{d}x_2\ F_{qq'}(x_1,x_2,\zeta,\boldsymbol{y}) \\
&= (2p^+)^{-1} \int \mathrm{d}y^- e^{-i\zeta p^+ y^-}\ \mathcal{M}^{++}_{VV,q'q}(p,y)\Big|_{y^+=0} \\
&= p^+ \int \mathrm{d}y^- e^{-i\zeta p^+ y^-} A_{qq'}(py,y^2) \\
&= \int \mathrm{d}(py)\ e^{-i\zeta py} A_{qq'}(py,y^2)\ .
\end{aligned} \tag{5.7}$$

The last step is possible, because in the frame we are working in we have $y^+ = 0$ and $\boldsymbol{p} = \boldsymbol{0}$. Therefore, it holds that $py = p^+y^-$ and $\boldsymbol{y}^2 = -y^2$. The same line of arguments applies for the remaining channels we are interested in. In total, we obtain a relation connecting DPD Mellin Moments and the twist-2 functions A_{ab} and $B_{\delta q\delta q'}$:

$$\begin{aligned}
I_{ab}(\zeta,y^2) &= \int \mathrm{d}(py)\ e^{-i\zeta py} A_{ab}(py,y^2)\ , \\
I^t_{\delta q\delta q'}(\zeta,y^2) &= \int \mathrm{d}(py)\ e^{-i\zeta py} B_{\delta q\delta q'}(py,y^2)\ ,
\end{aligned} \tag{5.8}$$

[2] if the two quark flavors are equal, there are only five independent twist-2 functions, since $A_{q\delta q}$ and $A_{\delta qq}$ are related by exchanging the quark operators.

where in analogy to (5.1) $I_{ab}(\zeta, y^2)$ is the $(1,1)$-moment of $f_{ab}(x_1, x_2, \zeta, y^2)$:

$$\begin{aligned} I_{ab}(\zeta, y^2) &= \int \mathrm{d}x_1 \int \mathrm{d}x_2 \; f_{ab}(x_1, x_2, \zeta, y^2) \;, \\ I^t_{\delta q \delta q'}(\zeta, y^2) &= \int \mathrm{d}x_1 \int \mathrm{d}x_2 \; f^t_{\delta q \delta q'}(x_1, x_2, \zeta, y^2) \;. \end{aligned} \tag{5.9}$$

The twist-2 functions A_{ab} and $B_{\delta q \delta q'}$ can be extracted from our lattice data we presented in chapter 4 if the conditions

$$y^2 < 0 \;, \qquad (py)^2 \leq \vec{p}^2 \vec{y}^2 \tag{5.10}$$

are fulfilled, which is a consequence of Euclidean spacetime. Furthermore, the region in the (py, y^2)-plane is bounded by the lattice extension and the highest momentum. Thus, in order to evaluate the integral over py, it is necessary to employ some suitable model fitting the data. We shall discuss this in detail in section 5.3.

5.2 Twist-2 functions

In the following, we show the lattice data for the twist-2 functions introduced in the previous section and discuss some physical implications. Furthermore, we calculate the moment of ζ^2 of the corresponding Mellin moments. The obtained results motivate the model used for fitting the twist-2 functions.
The twist-2 functions A_{ab} and $B_{\delta q \delta q'}$ are obtained by solving the overdetermined equation system introduced by the decompositions (5.5), where the r.h.s. is represented by the lattice data we have already shown in section 4.4. We solve this system of equations for each possible combination of the Lorentz invariants y^2 and py by χ^2 minimization. The exact method we used is summarized in section A.6.2.

5.2.1 Data quality and artifacts

Before we present results of physical relevance, we again discuss the data quality and effects of discrete and finite spacetime. For the moment we consider each contraction and each momentum separately. We use the notation $y = |\vec{y}|$ and $p = |\vec{p}|$, see (A.15). As for the two-current matrix elements, we recognize the saw-tooth pattern caused by mirror charges, when approaching current distances close to the lattice boundary. As an example we show the data of the C_1 contraction for A_{ud} for $\vec{p} = (0,0,0)$ $(py = 0)$, as well as $\vec{p} = -(1,1,1)2\pi/(La)$ at $py = 1.6$. This is plotted in Figure 5.1 panel (a) and (b), respectively, where we separated the data according to the angle θ of the distance vector $\vec{y}$ to the lattice diagonal of the corresponding octant. These artifacts are especially prominent in the data of the C_1 contraction, also for $\vec{p} \neq \vec{0}$. Similar patterns can be seen in the C_1 data of the twist-2 functions that are not shown in the plots. Furthermore, we observe an anisotropy pattern for each region in y for the twist-2 function

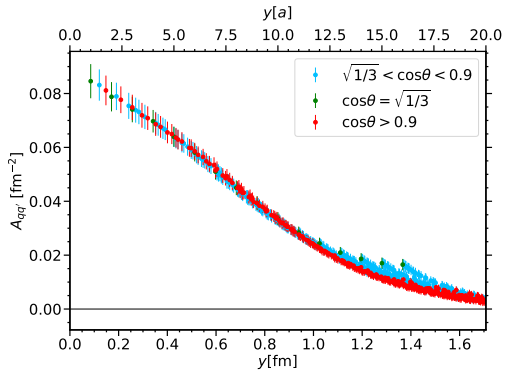

(a) anisotropy, A_{ud}, C_1, $\vec{p} = \vec{0}$, $py = 0$

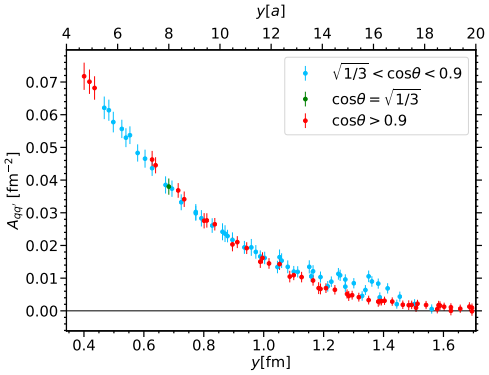

(b) anisotropy, A_{uu}, C_1, $\vec{p} = -(1,1,1)2\pi/(La)$, $py = 1.6$

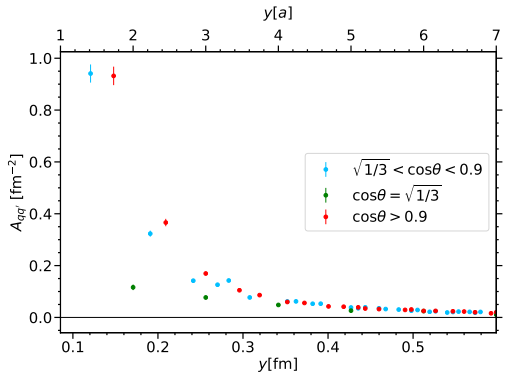

(c) anisotropy, A_{uu}, C_2, $\vec{p} = \vec{0}$, $py = 0$

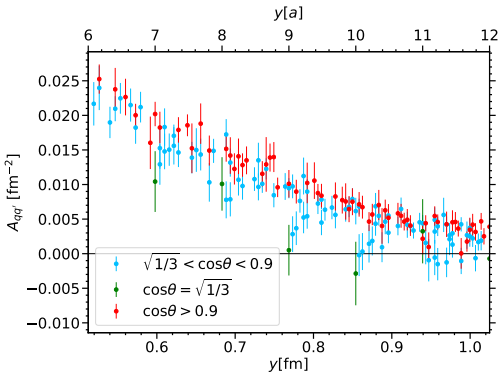

(d) anisotropy, A_{uu}, C_2, $\vec{p} = \vec{0}$, $py = 0$

Figure 5.1: Data for $A_{qq'}$ as function of the operator distance $\vec{y}$, where we distinguish between different ranges of the angle θ between $\vec{y}$ and the neighboring diagonal.

$B_{\delta q \delta q'}$, where the data for $\vec{p} = \vec{0}$ along the lattice axes appears to be significantly larger than the data along the diagonals. This pattern vanishes at non-zero momentum, where the data seems to be consistent with the data close to the diagonals for $\vec{p} = \vec{0}$, which is shown in Figure 5.2.

The second kind of discretization effects, which has been already found for the matrix elements itself, is the anisotropy of the lattice propagator, which is extreme if the current distance is small. These effects are present in the data of contractions where the two operators are directly connected by a quark propagator, i.e. C_2 and S_2. Figure 5.1, panels (c) and (d), shows the data for C_2 and A_{uu} at zero momentum for two different regions in $\vec{y}$. For the remaining twist-2 functions similar effects are observed.

In Figure 5.5 we present the results for each possible contribution separately, where we consider the functions $A_{qq'}$ and $A_{\delta qq'}$ and $\vec{p} = \vec{0}$. We multiply the data of the contractions C_2 and S_1 by a factor two, since in physical sums these graphs appear twice. Again

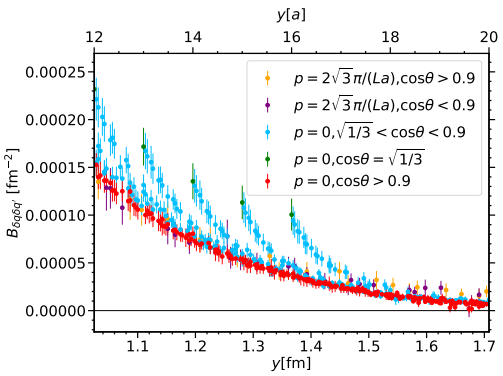

(a) anisotropy, $B_{\delta u \delta d}$, C_1, $py = 0$

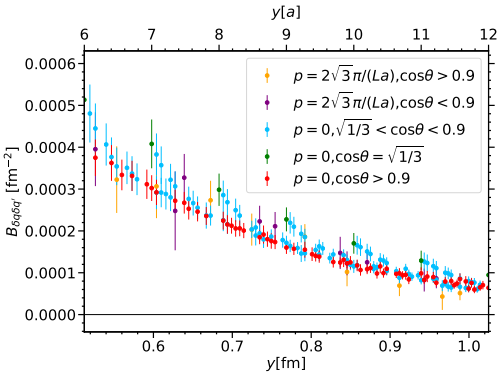

(b) anisotropy, $B_{\delta u \delta u}$, C_1, $py = 0$

Figure 5.2: Anisotropy effects being observed for $B_{\delta q \delta q'}$. We compare the data for different momenta and directions w.r.t. to the diagonals.

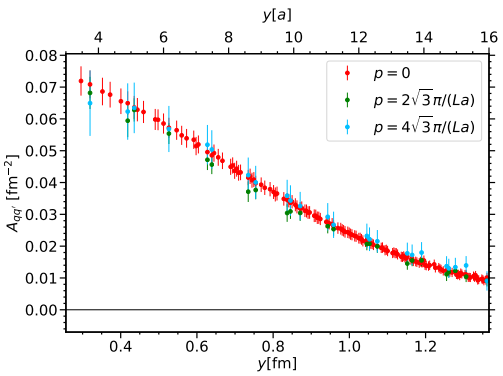

(a) Lorentz invariance, A_{ud}, C_1, $py = 0$

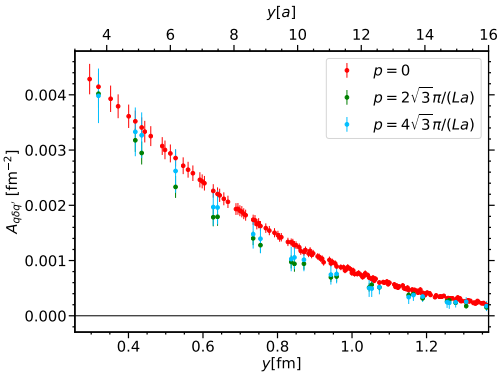

(b) Lorentz invariance, $A_{\delta du}$, C_1, $py = 0$

Figure 5.3: Comparison of the twist-2 functions obtained from projections which separately take into account data for $p = 0$ (red), $p = 2\sqrt{3}\pi/(La)$ (green) and $p = 4\sqrt{3}\pi/(La)$ (blue)

we observe dominance of the connected diagrams. In both cases C_1 is slowly decreasing with increasing distance. C_2 is observed to be large mainly for small y. S_2 is close to zero for large y, but steeply increases, once the distance is smaller than $6a$. The data of S_1 (panels (c) and (d)) is consistent with zero in the most cases. For $A_{qq'}$ there is a significant offset, which is small compared to the connected diagrams.
A useful consistency check is the comparison of the data for the twist-2 functions corresponding to different momenta p. Figure 5.3 shows the situation for C_1 for the functions $A_{qq'}$ (a) and $A_{\delta qq'}$ (b). While for $A_{qq'}$ Lorentz invariance is present within the errors, there are slight discrepancies in the case of $A_{\delta qq'}$. A reason of this might be a larger sensitivity to excited states in this channel combined with the usage of different source-

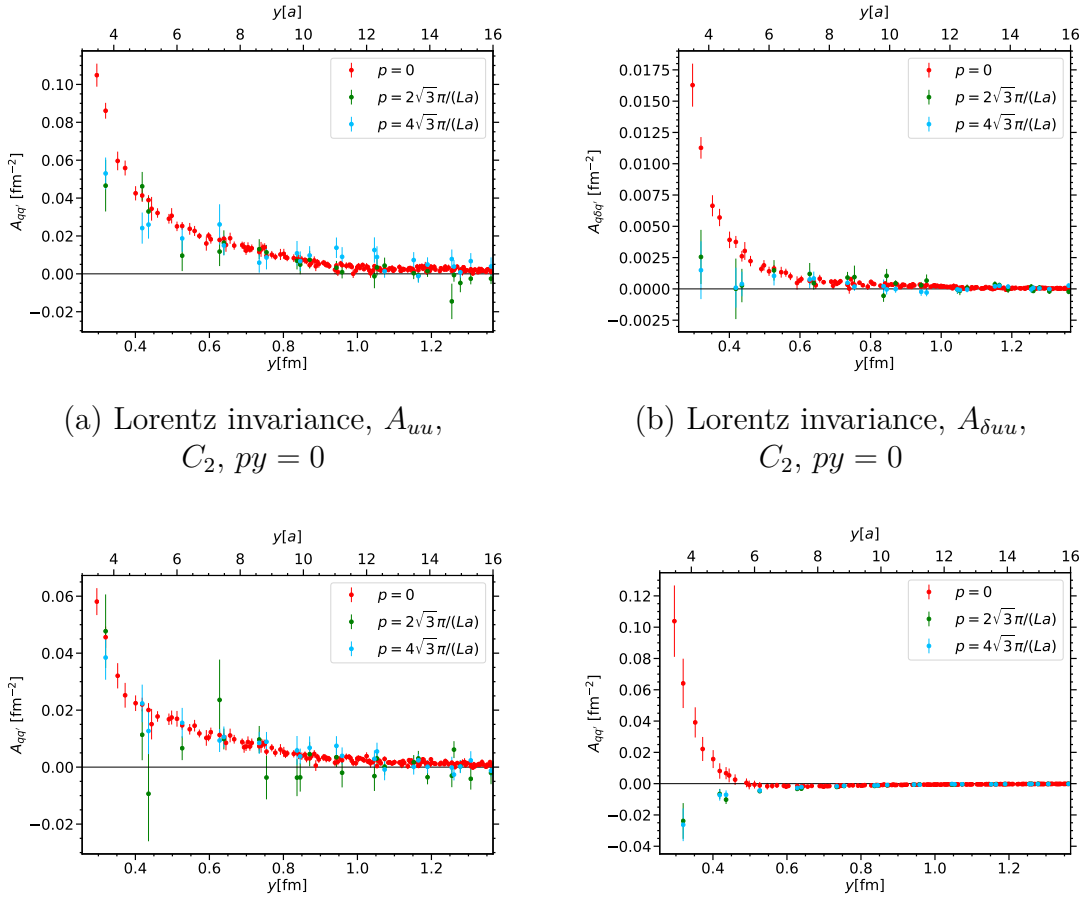

(a) Lorentz invariance, A_{uu}, C_2, $py = 0$

(b) Lorentz invariance, $A_{\delta uu}$, C_2, $py = 0$

(c) Lorentz invariance, A_{dd}, C_2, $py = 0$

(d) Lorentz invariance, A_{qq}, S_2, $py = 0$

Figure 5.4: Same as Figure 5.3 for the C_2 contribution to A_{uu} (a), $A_{\delta uu}$ (b) and A_{dd} (c), as well as the S_2 signal for A_{qq} (d).

sink separations for $\vec{p} = \vec{0}$ and $\vec{p} \neq \vec{0}$, respectively.
The situation is more complicated for other non-negligible contributions. For C_2 the signals for different momenta are consistent within the errors at almost each distance y, except for the region $y < 5a$, which can be observed for both, $A_{qq'}$ and $A_{\delta qq'}$, see Figure 5.4 (a) and (b), respectively. Discrepancies become large if $y < 4a$. The signal for A_{dd} (c) seems to be less affected. This is even worse for S_2, where the signals clearly differ in sign for $y < 6a$, i.e. the region where the order of magnitude becomes comparable to that of the other graphs. For that reason we will not take into account S_2 in physical sums, but keep in mind that there remains an uncertainty for $y < 6a$.
In the following, we consider combinations corresponding to definite quark flavors in the operators. We take into account only C_1 and C_2 contributions. Furthermore, we restrict ourselves on distances $y > 4a$, i.e. to a region where we observe a reasonable consistence

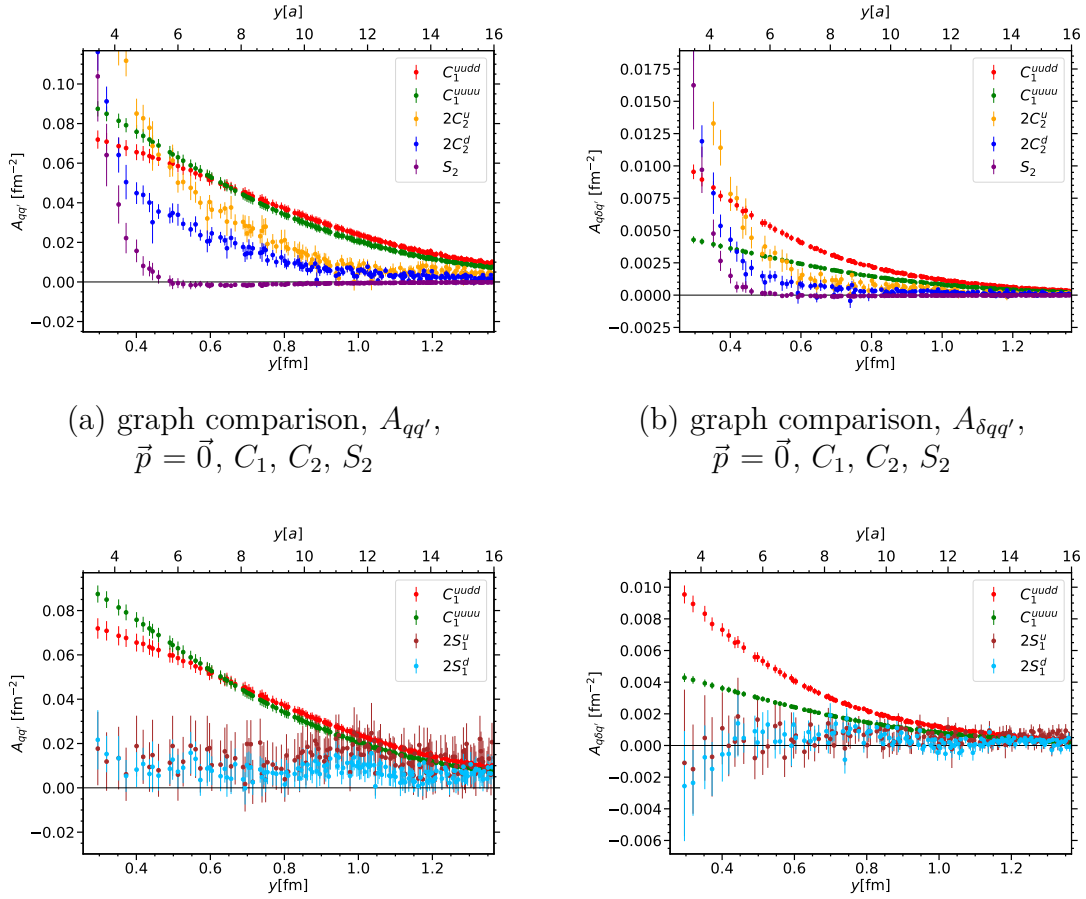

(a) graph comparison, $A_{qq'}$, $\vec{p} = \vec{0}$, C_1, C_2, S_2

(b) graph comparison, $A_{\delta qq'}$, $\vec{p} = \vec{0}$, C_1, C_2, S_2

(c) graph comparison, $A_{qq'}$, $\vec{p} = \vec{0}$, C_1, S_1

(d) graph comparison, $A_{\delta qq'}$, $\vec{p} = \vec{0}$, C_1, S_1

Figure 5.5: Contributions of each graph to the twist-2 functions $A_{qq'}$ (a,c) and $A_{\delta qq'}$ (b,d). The panels at the top show the comparison between the graphs C_1, C_2 and S_2, whereas in the panels at the bottom we compare C_1 with S_1.

with Lorentz invariance for the considered graphs. In order to reduce the contribution of discretization artifacts and finite volume effects discussed before, we apply the cut in the direction of the distance vector $\vec{y}$ according to (4.73).

5.2.2 Physical results for $py = 0$

In the following, we present results for the twist-2 functions for given flavor combinations. As previously discussed, we take into account the contractions C_1 and C_2 and consider current distance vectors for which $4a \geq y \geq La$ and $\cos\theta \geq 0.9$. The twist-2 functions are obtained by solving the system of equations given by the corresponding expression in (5.5), using the data for each available momentum. The flavor specific

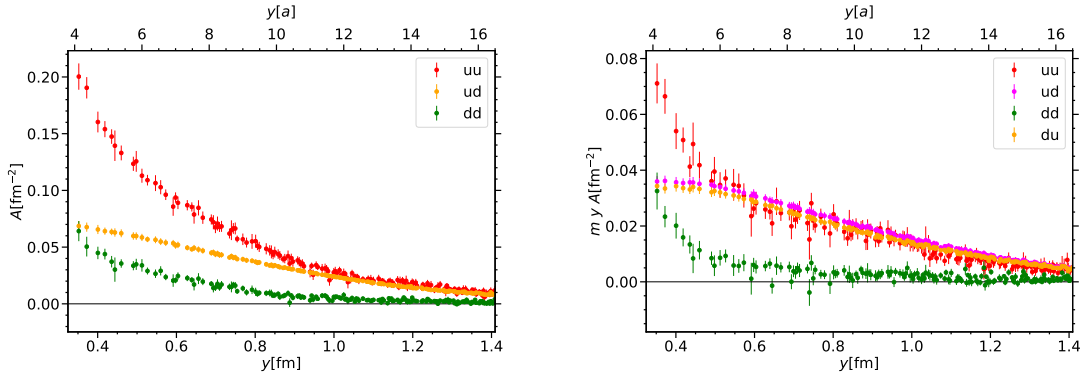

(a) flavor comparison, $A_{qq'}$, $py = 0$ (a) flavor comparison, $A_{\delta qq'}$, $py = 0$

Figure 5.6: Comparison between the flavor combinations uu, ud and dd for the twist-2 functions $A_{qq'}$ (a) and $A_{\delta qq'}$ (b) for $py = 0$.

contractions are given by (4.28). For the moment we take $py = 0$ in order to analyze the y^2-dependence.
Figure 5.6 shows the twist-2 functions for all flavor combinations, considering $A_{qq'}$ and $A_{\delta qq'}$, which correspond to two unpolarized quarks in the first case and in the second case to the first quark being unpolarized while the second has transverse polarization. According to the corresponding prefactor in the decomposition (5.5), $A_{\delta qq'}$ is weighted by the factor my, which allows a consistent comparison to other twist-2 functions. In the two observed cases we find signals of the same order of magnitude for uu and ud in the region, where the separation y is large. The dd data is suppressed in this region. Going to smaller distances, the signal increases for uu and dd. As a consequence the dd contribution becomes as large as the ud signal.
Let us now take a look at the polarization dependence. In Figure 5.7 we compare for definite flavor the data for different channels being related to the quark polarization. Polarization effects are visible in all cases. They are most prominent in the ud case, also for larger separations. The spin-orbit correlations $A_{\delta du}$ and $A_{\delta ud}$ yield the largest polarized contributions. In the case of two polarized quarks we observe a relatively small but clearly non-vanishing signal. Polarization effects are suppressed for uu and dd, except for the spin-orbit correlations $A_{\delta uu}$ and $A_{\delta dd}$. In the case of dd they are at least observable for small y.
At this point we want to compare the previously shown results to those for ud in the π^+, which have been obtained in [46]. In this case the situation is quite similar to the nucleon case. A difference is the opposite sign in all shown channels, which is a consequence of the fact that we have a $\bar{d}$-quark instead of a d-quark in the π^+. The results for the π^+ are also shown in Figure 5.7 (d).

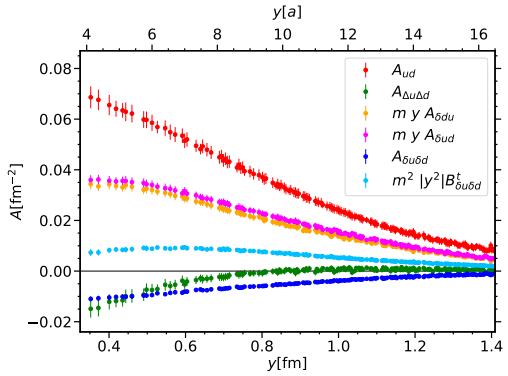

(a) polarization dependence, ud, $py = 0$

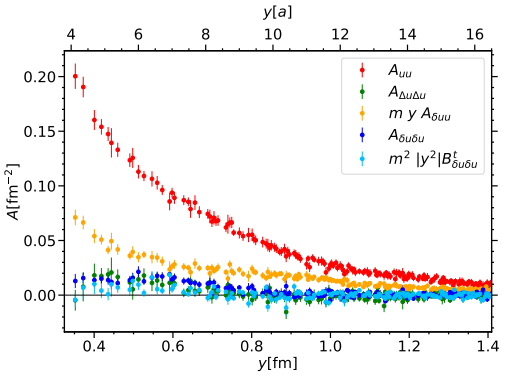

(b) polarization dependence, uu, $py = 0$

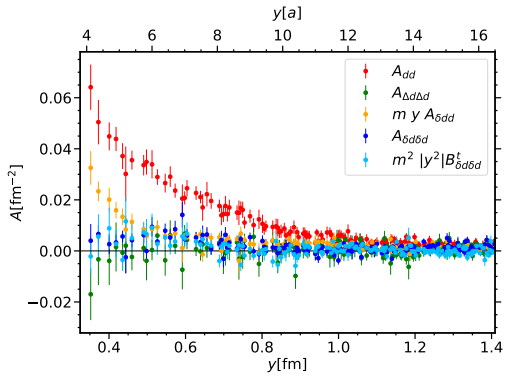

(c) polarization dependence, dd, $py = 0$

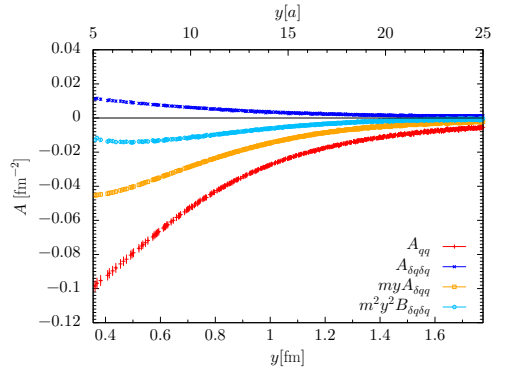

(d) polarization dependence, ud in π^+, $py = 0$

Figure 5.7: Twist-2 functions for different channels corresponding to a certain quark polarization. The data is shown for flavor combinations ud (a), uu (b) and dd (c) in the nucleon at $py = 0$. We also show the analogue results obtained for ud in the pion (d) [46].

5.2.3 Modeling the y^2-dependence

For further analyses it is advantageous to find a model which sufficiently describes the dependence of the twist-2 functions on y^2. Figure 5.8 shows again the y-dependence of the data for A_{ud}, A_{uu}, $A_{\delta du}$ and $A_{\delta uu}$, respectively. This is plotted using a logarithmic scale, which emphasizes the double exponential shapes of the data in most of the cases. However, a pure double exponential description is not sufficient in some cases, which is why we take the more general fit ansatz:

$$A(py = 0, y^2) = (\eta_1 y)^\delta A_1 e^{-\eta_1 (y - y_0)} + (\eta_2 y)^\delta A_2 e^{-\eta_2 (y - y_0)} \ . \tag{5.11}$$

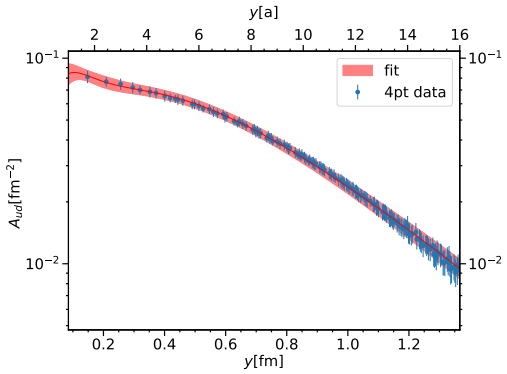

(a) double-exponential fit on $A_{ud}(py = 0, y^2)$

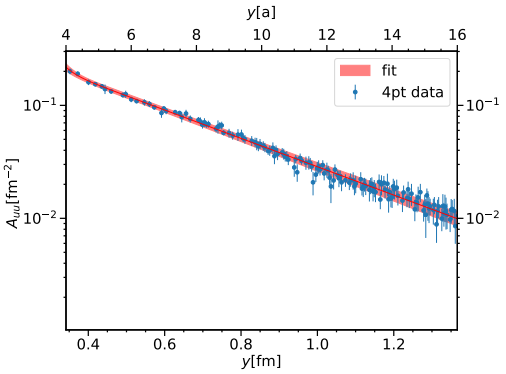

(b) double-exponential fit on $A_{uu}(py = 0, y^2)$

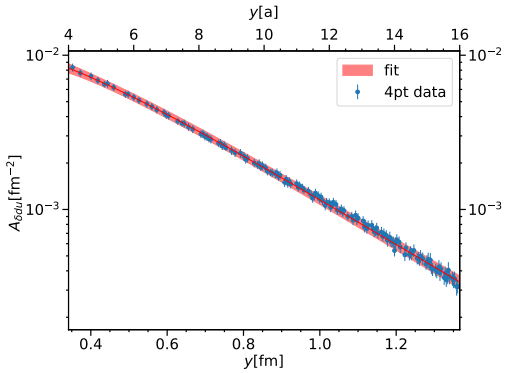

(c) double-exponential fit on $A_{\delta du}(py = 0, y^2)$

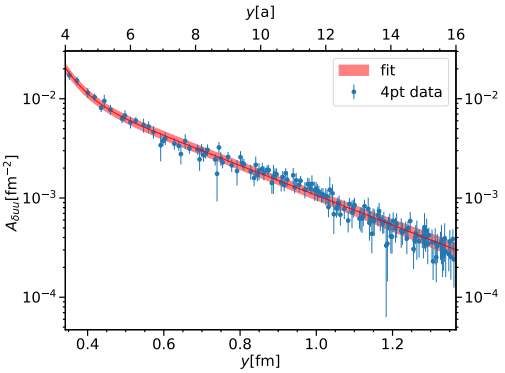

(d) double-exponential fit on $A_{\delta uu}(py = 0, y^2)$

Figure 5.8: Twist-2 functions and the corresponding fit to the double exponential for A_{ud} (a), A_{uu} (b), $A_{\delta du}$ and $A_{\delta uu}$ (d). Each plot has a logarithmic scale at the vertical axis.

The exponent δ enters the fit not as a free parameter, but is fixed to a certain value. For A_{ud} and $A_{\delta u \delta d}$ (the latter is not shown in the plots) it turns out that $\delta = 1.2$ is a suitable choice, whereas in all other channels $\delta = 0$, i.e. the pure double exponential, is sufficient. Since most of the fits are not sensitive to the region $y \approx 0$, where the exponential is equal to one, which leads to large errors of A_i, we introduce a shift $y_0 = 4a$ in the distance. The fits are performed in three stages: In the first one we fit only the parameters A_1 and η_1, taking into account the data for large y, where a single exponential term sufficiently describes the shape. Depending on the polarization and flavor this holds for $y > y_{\text{min}} > 5a$. In the second stage we fit the region $3a \leq y \leq 16a$ taking into account the parameters A_2 and η_2, while the parameters A_1 and η_1 are fixed to the values obtained in the first stage. In the final stage every parameter is left free,

channel	fit range	δ	$y_0[a]$
A_{ud}	$[1a, 16a]$	1.2	4
A_{dd}	$[3.5a, 16a]$	0	4
$A_{\Delta d \Delta d}$	$[3.5a, 15a]$	0	4
$A_{\delta u \delta d}$	$[3a, 16a]$	1.2	4
$A_{\delta d \delta d}$	$[3.5a, 15a]$	0	4
$B_{\delta d \delta d}$	$[4a, 15a]$	0	4
else	$[4a, 16a]$	0	4

Table 5.1: Summary of the intervals in y for each twist-2 function, where the corresponding final fit has been performed. Furthermore, we list the fixed parameters δ and y_0

where as starting value the results from the last stages are taken. Therein, we mainly take into account the range $4a \leq y \leq 16a$. In some cases we take smaller values of the lower boundaries in order to obtain a stable fit result. In each of these cases we checked that the corresponding data is not significantly affected by anisotropy effects or issues regarding Lorentz invariance as discussed in section 5.2.2. The ranges used for each fit, as well as the parameters δ and y_0, are summarized in table 5.1. All fits are performed taking into account only the diagonal part of the covariance matrix for stability reasons. In Figure 5.8 we plot also the curves resulting from the final fit stage. The corresponding values for the fit parameters are summarized in table 5.2.

5.2.4 py-dependence and moments in ζ^2

So far we considered the twist-2 functions at $py = 0$. According to (5.8) the dependence on py contains crucial information, since it is the Fourier conjugate variable to the non-forward parameter ζ. Being restricted by the lattice volume and the highest proton momentum, we are not able to explore the complete region in py. In our simulations the highest 3-momentum is $p = 2\pi\sqrt{12}/(La)$ and the largest distance $y = La\sqrt{3/4}$. Therefore, an explicit boundary for py is given by

$$|py| \leq \frac{2\pi\ \sqrt{12}y}{La} \leq 6\pi \approx 18.85\ . \tag{5.12}$$

Hence, in order to evaluate the Fourier transform, it is necessary to find a model describing the py dependence appropriately. In (2.53) we already gave constraints for the support region of skewed DPDs in the (x_1, x_2, ζ)-space, in particular $-1 \leq \zeta \leq 1$. Furthermore, it was pointed out in (2.58) that DPDs have to be even functions in ζ. Within this background, we start building the model in momentum space by approximating the

channel	$A_1[\mathrm{fm}^{-2}]$	$\eta_1[\mathrm{fm}^{-1}]$	$A_2[\mathrm{fm}^{-2}]$	$\eta_2[\mathrm{fm}^{-1}]$	χ^2/dof
A_{uu}	0.026(17)	39(20)	0.1920(99)	2.89(15)	0.37
A_{ud}	0.00037(35)	17.5(3.1)	0.0530(28)	3.52(12)	0.07
A_{dd}	0.010(12)	46(47)	0.0573(64)	3.66(36)	0.48
$A_{\Delta u\Delta u}$	−0.62(57)	13.7(3.8)	0.61(58)	12.3(2.3)	0.63
$A_{\Delta u\Delta d}$	−0.0190(39)	4.86(46)	0.0026(24)	1.30(73)	0.30
$A_{\Delta d\Delta d}$	−0.029(61)	14(15)	0.010(61)	4.6(8.2)	0.61
$A_{\delta uu}$	0.0208(46)	21.8(6.9)	0.0211(31)	3.45(25)	0.49
$A_{\delta du}$	−0.0059(27)	6.80(37)	0.0228(23)	3.40(15)	0.20
$A_{\delta ud}$	−0.0085(27)	6.85(23)	0.0258(26)	3.43(16)	0.25
$A_{\delta dd}$	0.0144(36)	17.7(7.7)	0.0036(26)	3.6(1.1)	0.64
$A_{\delta u\delta u}$	−0.193(99)	9.5(1.3)	0.196(98)	7.5(1.3)	0.74
$A_{\delta u\delta d}$	−0.000033(88)	21(13)	−0.00835(65)	3.57(24)	0.16
$A_{\delta d\delta d}$	−0.0027(82)	18(35)	0.0073(81)	3.0(2.3)	1.01
$B_{\delta u\delta u}$	−0.72(99)	15.8(2.9)	0.72(99)	15.7(3.0)	1.01
$B_{\delta u\delta d}$	−0.00074(71)	7.9(2.1)	0.00253(56)	4.13(23)	0.07
$B_{\delta d\delta d}$	0.73(41)	16.9(1.5)	−0.73(41)	17.0(1.5)	0.72

Table 5.2: Parameters of the double exponential obtained from a fit on the twist-2 functions for each channel. We also list the corresponding χ^2/dof in the right column.

DPD Mellin moments by an even polynomial in ζ for $|\zeta| \leq 1$:

$$I(\zeta, y^2) = \pi \sum_{n=0}^{N} a_n(y^2)\ \zeta^{2n}\ \Theta(1-\zeta^2)\ . \tag{5.13}$$

Expressions for the twist-2 functions can be obtained by executing the inverse Fourier transform, which yields:

$$A(py, y^2) = \sum_{n=0}^{N} a_n(y^2) h_n(py)\ , \tag{5.14}$$

where each of the h_n corresponds to a term in the polynomial in momentum space. They can be defined as:

$$h_n(x) := \frac{1}{2}\int_{-1}^{1} \mathrm{d}\zeta e^{ix\zeta}\zeta^{2n} = \sin(x)s_n(x) + \cos(x)c_n(x)\ , \tag{5.15}$$

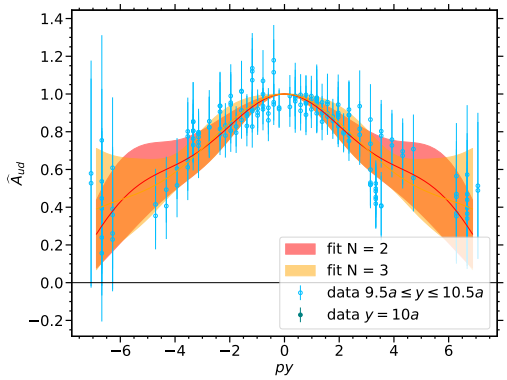

(a) local fit on $\widehat{A}_{ud}$ at $y = 10a$

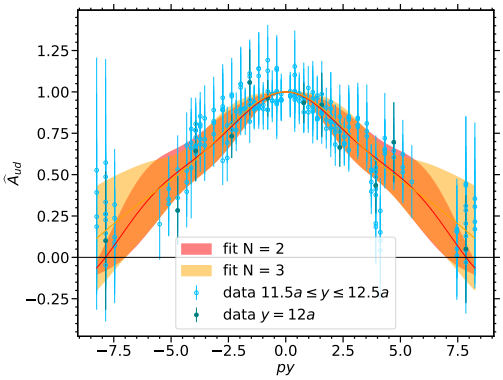

(b) local fit on $\widehat{A}_{ud}$ at $y = 12a$

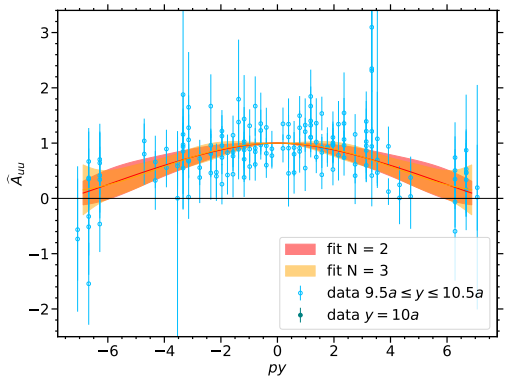

(c) local fit on $\widehat{A}_{uu}$ at $y = 10a$

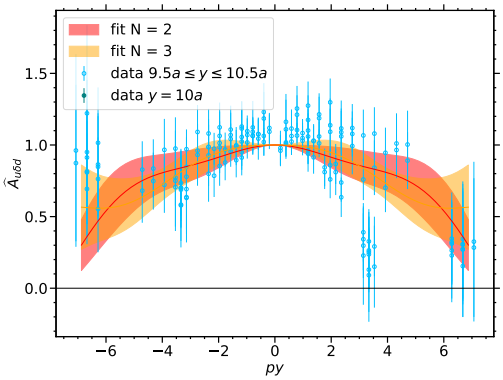

(d) local fit on $\widehat{A}_{\delta du}$ at $y = 10a$

Figure 5.9: The py-dependence of the twist-2 functions, where we show the data within a band around a specific distance ($y \pm 0.5a$). In each plot we present the curves resulting from a fit of these data points on the h_n series, taking into account $N = 2, 3$ non-trivial terms. In the panels (a) and (b) we plot this for A_{ud} for the distance $10a$ and $12a$, respectively. Furthermore, we show the same for the distance $10a$ for A_{uu} (c) and $A_{\delta du}$ (d).

with

$$
\begin{aligned}
s_n(x) &= \sum_{m=0}^{n} \frac{(2n)!(-1)^m}{(2n-2m)!x^{1+2m}} \ , \\
c_n(x) &= \sum_{m=0}^{n-1} \frac{(2n)!(-1)^m}{(2n-2m-1)!x^{2+2m}} \ .
\end{aligned}
\tag{5.16}
$$

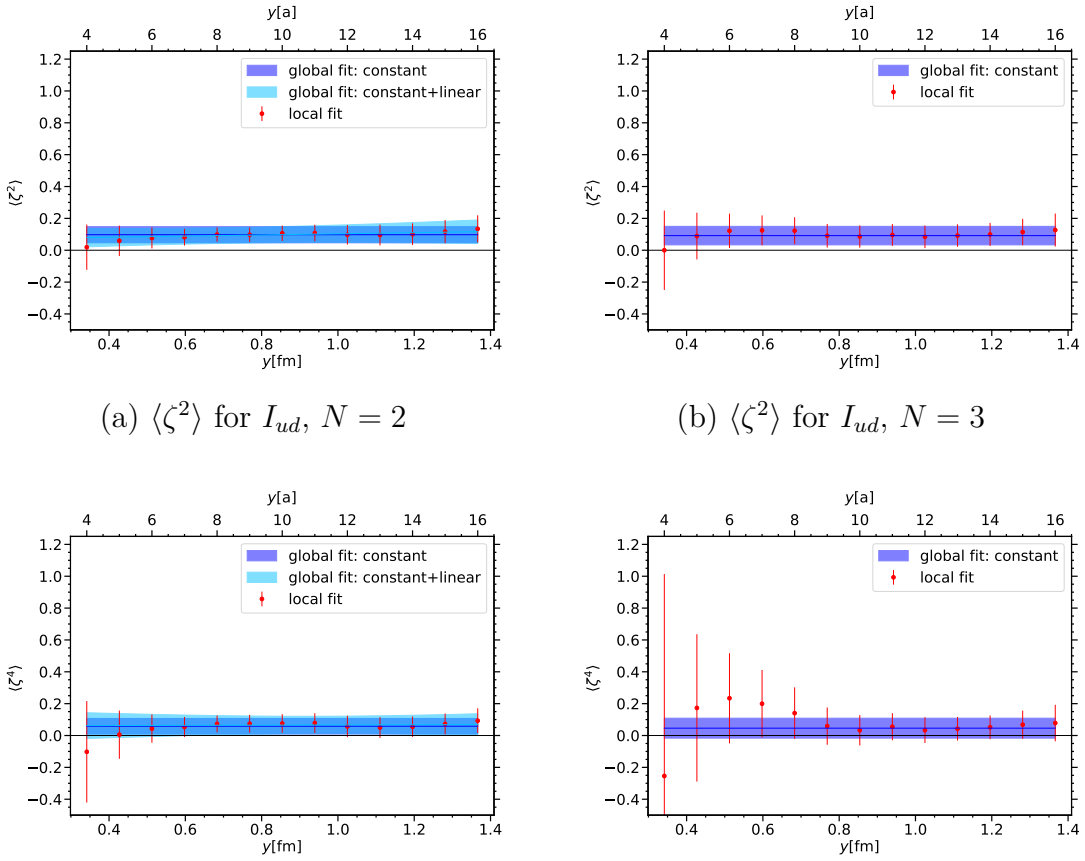

(a) $\langle\zeta^2\rangle$ for I_{ud}, $N = 2$

(b) $\langle\zeta^2\rangle$ for I_{ud}, $N = 3$

(c) $\langle\zeta^4\rangle$ for I_{ud}, $N = 2$

(d) $\langle\zeta^4\rangle$ for I_{ud}, $N = 3$

Figure 5.10: Moments of ζ in I_{ud} obtained from a fit on the corresponding twist-2 function data using $N = 2$ (left) or $N = 3$ (right) non-trivial terms in the h_n series. (a) and (b) show this for the second moment, whereas in (c) and (d) the fourth moment is plotted. Each panel shows the local fits (red), where only data within the band $y \pm 0.5a$ are taken into account, as well as global fits using the fit ansatz (5.25) for $K = 0$ (dark blue) and $K = 1$ (light blue).

Further properties of the functions $h_n(x)$ are listed in section A.4. To determine the coefficients $a_n(y^2)$ of this ansatz we consider the normalized twist-2 functions $\widehat{A}(py, y^2)$:

$$\widehat{A}(py, y^2) := \frac{A(py, y^2)}{A(0, y^2)} = \sum_{n=0}^{N} \hat{a}_n(y^2)\ h_n(py)\ , \tag{5.17}$$

with the normalized coefficient $\hat{a}_n$, which is defined by:

$$\hat{a}_n(y^2) = \frac{a_n(y^2)}{A(0, y^2)}\ . \tag{5.18}$$

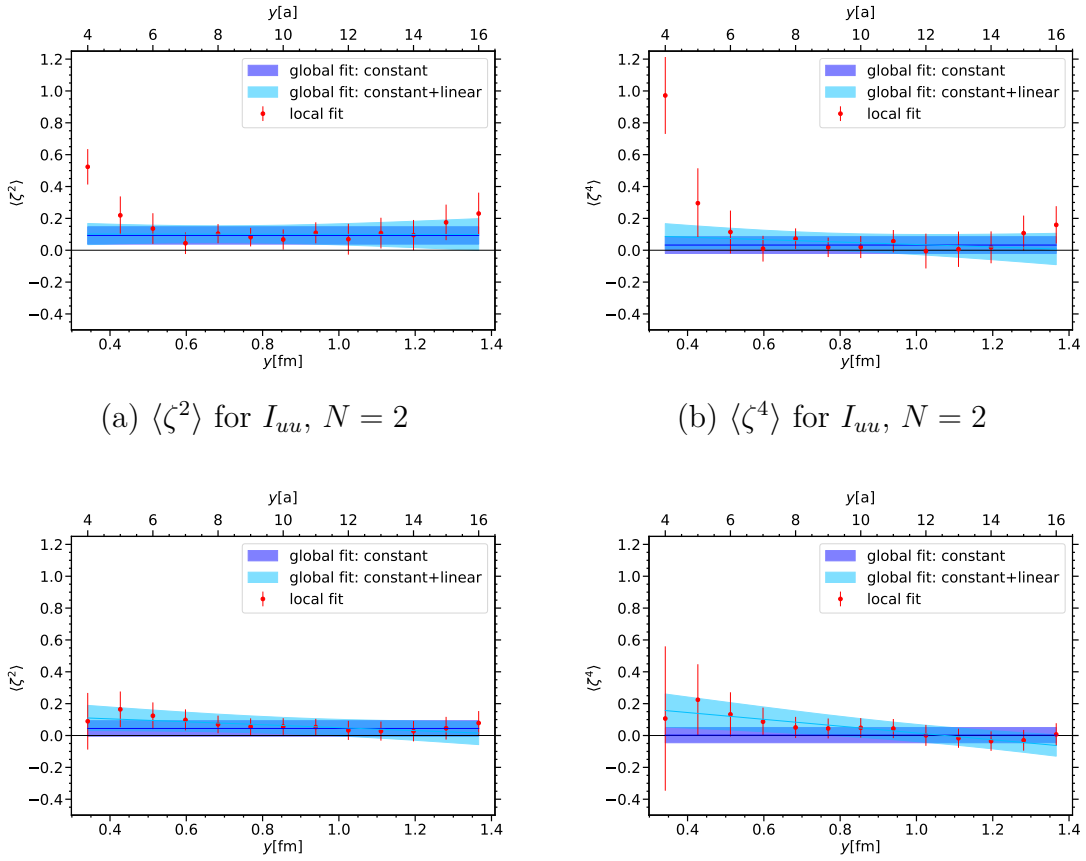

(a) $\langle\zeta^2\rangle$ for I_{uu}, $N = 2$

(b) $\langle\zeta^4\rangle$ for I_{uu}, $N = 2$

(c) $\langle\zeta^2\rangle$ for $I_{\delta du}$, $N = 2$

(d) $\langle\zeta^4\rangle$ for $I_{\delta du}$, $N = 2$

Figure 5.11: Same as Figure 5.10 for $N = 2$. This is shown for the second (left) and fourth (right) moment of ζ in I_{uu} (a) or (c) and $I_{\delta du}$ (b) or (d), respectively

In py-space the coefficients $\hat{a}_n$ have no direct meaning. However, we can define a linear transform to express the series in terms of $2m$-th derivative in py at $py = 0$. Here we exploit the relation between the $2m$-th derivative of h_n and h_{n+m}, see (A.33):

$$(-1)^m \left.\frac{\partial^{2m}\widehat{A}(py, y^2)}{\partial(py)^{2m}}\right|_{py=0} = \sum_{n=0}^{N} \hat{a}_n(y^2) h_{n+m}(0) = \sum_{n=0}^{N} T_{mn}\hat{a}_n(y^2) \ , \tag{5.19}$$

where the transformation matrix T reads:

$$T_{mn} := h_{n+m}(0) = \frac{1}{1 + 2(n+m)} \ . \tag{5.20}$$

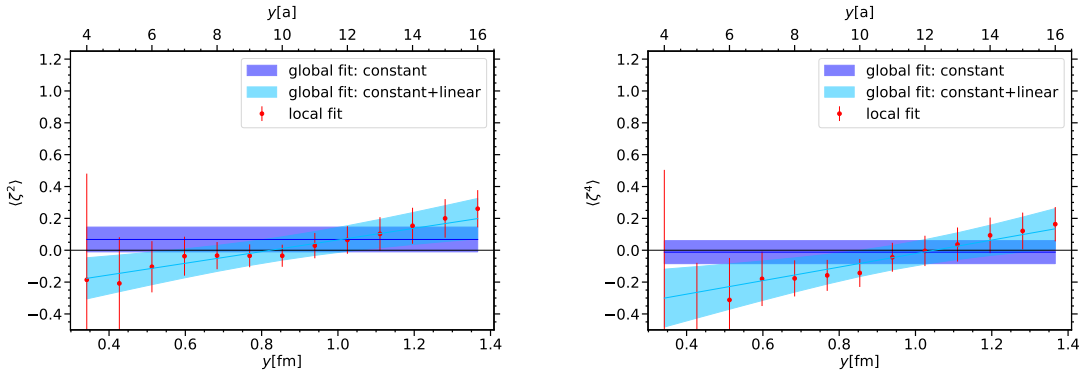

(a) $\langle\zeta^2\rangle$ for $I^t_{\delta u\delta d}$, $N = 2$ (b) $\langle\zeta^4\rangle$ for $I^t_{\delta u\delta d}$, $N = 2$

Figure 5.12: Same as Figure 5.10 for $N = 2$ and $I^t_{\delta u\delta d}$. This is shown for the second (left) and fourth (right) moment of ζ, respectively

The derivatives (5.19) are directly related to moments of ζ of the non-forward DPD Mellin moments $I(\zeta, y^2)$:

$$\langle\zeta^{2m}\rangle(y^2) := \frac{\int_{-1}^{1} \mathrm{d}\zeta\ \zeta^{2m} I(\zeta, y^2)}{\int_{-1}^{1} \mathrm{d}\zeta\ I(\zeta, y^2)} = (-1)^m\ \frac{\partial^{2m} \widehat{A}(py, y^2)}{\partial(py)^{2m}}\bigg|_{py=0} . \tag{5.21}$$

The last equality in (5.21) is obtained by considering $\int_{-1}^{1} \mathrm{d}\zeta\ e^{i\zeta py}\zeta^{2m} I(\zeta, y^2)$ at $py = 0$ instead of the integral in the denominator. Subsequently, ζ^{2m} is replaced by the $2m$-th derivative in py via partial integration. $\widehat{A}$ can be expressed as:

$$\widehat{A}(py, y^2) = \sum_{n,m=0}^{N} \left(T^{-1}\right)_{nm} h_n(py) \langle\zeta^{2m}\rangle(y^2) , \tag{5.22}$$

i.e. the py dependence is parameterized by the moments in ζ, such that $\hat{a}$ can be written as:

$$\hat{a}_n(y^2) = \sum_{m=0}^{N} \left(T^{-1}\right)_{nm} \langle\zeta^{2m}\rangle(y^2) . \tag{5.23}$$

Notice that the first non-trivial moment is the second one, since $\widehat{A}(py = 0, y^2) \equiv 1$ by definition.

We use the expression (5.22) as ansatz to fit the py-dependence. This is carried out for selected distances y_0. For each distance we take into account all data points within the region $y_0 - 0.5a \leq y \leq y_0 + 0.5a$, assuming that changes of the data within this region are negligible. Moreover, the fits are performed taking $N = 2, 3$ non-trivial terms in the h_n series. Since the fit ansatz (5.22) is linear in the fit parameters $\langle\zeta^{2m}\rangle$, it is possible to perform the fit by directly solving the corresponding overdetermined

system of equations, see section A.6.2. Like for the double-exponential fits we previously discussed, only diagonal entries of the covariance matrix are taken into account. The resulting curves in the py-plane for selected y are plotted in Figure 5.9, where we show as examples fits for A_{uu} and A_{ud} and $A_{\delta du}$. For each value of N the corresponding fit yields a reasonable description of the data. However, it is observed that for large values of N the fit becomes sensitive to fluctuations at large py, see e.g. (a) and (d). This increases the statistical error of the final result and might be a first indication of overfitting.
Difficulties are encountered if the signal is very small or comparable with zero, such that the data is dominated by fluctuations. In particular, this affects the data for uu and dd if we consider channels where both quarks are polarized. Therefore, a reliable determination of the Mellin moments or their moments in ζ^2 is not feasible for $A_{\Delta q\Delta q'}$, $B_{\delta u\delta u}$ and the polarized channels for flavor dd. In the physical discussion in section 5.4 these "bad" channels will not be considered for this reason.
From the fits we directly obtain the values of $\langle\zeta^{2n}\rangle$ for the corresponding DPD Mellin moments. We show their y-dependence for some selected channels in Figure 5.10 and Figure 5.11. It is observed that the moments of ζ are very small ($\langle\zeta^{2n}\rangle < 0.25$) and in almost all cases are sufficiently described by a linear function in y. In most channels the moments do not depend on y at all. An exception is found for uu at small y, where the data tends to increase. We want to remind ourselves that in this region deviations from Lorentz invariance have been found in the data of the corresponding twist-2 functions, which might skew the py-dependence and therefore cause these effects. The results that are not shown in the plots look similar. In the case of $A_{\delta u\delta u}$ we observe very large error bands.
The behavior of the moments in ζ is quite different than for the pion, where the moments have been found to be significantly larger, clearly showing a linear dependence on y [46].

5.3 Extraction of Mellin moments

So far we have investigated separately the dependence on y^2 and, for each distance, on py. Building on these results we shall now construct a combined model to describe the twist-2 functions.

5.3.1 The model

The dependence on y has been found to be consistent with a double exponential. Furthermore, from symmetry arguments and constraints on the support region of the skewed DPDs we established an ansatz in terms of the functions h_n, which describes the py-dependence of the twist-2 functions very well. From the results for the moments in ζ obtained in the last section we can conclude that for the most cases these are nearly constant with increasing distance y. Some channels require an extra linear term in y,

which is also included in our global fit ansatz:

$$\langle\zeta^{2m}\rangle(y^2) = \sum_{k=0}^{K=1} c_{mk}(y)^k \ , \tag{5.24}$$

where $c_{00} \equiv 1$ and $c_{01} \equiv 0$, since $\widehat{A}(py = 0, y^2) \equiv 1$ by definition. Here and in the following we denote $(y)^k = \sqrt{-y^\mu y_\mu}^k$, see also (A.16). The complete ansatz reads:

$$A(py, y^2) = \sum_{i=1,2} A_i e^{-\eta_i(y-y_0)} \sum_{n,m=0}^{N} \sum_{k=0}^{K} \left(T^{-1}\right)_{nm} c_{mk} \ (y)^{k+\delta} \ \eta_i^\delta \ h_n(py) \ . \tag{5.25}$$

In the following section, we discuss the corresponding fits and show results for the parameters c_{mk} being obtained from a global fit.

5.3.2 Results

	N	K	c_{10}	$c_{11}[\mathrm{fm}^{-1}]$	c_{20}	$c_{21}[\mathrm{fm}^{-1}]$	c_{30}	χ^2/dof
A_{uu}	2	0	0.093(55)	-	0.032(53)	-	-	0.96
		1	0.102(98)	−0.00(12)	0.11(12)	−0.08(14)	-	0.95
	3	0	0.104(66)	-	0.056(76)	-	0.059(88)	0.96
A_{ud}	2	0	0.097(51)	-	0.058(49)	-	-	0.47
		1	0.067(77)	0.036(84)	0.06(11)	0.006(97)	-	0.46
	3	0	0.092(58)	-	0.046(63)	-	0.038(69)	0.46
A_{dd}	2	0	−0.029(99)	-	−0.13(12)	-	-	0.93
		1	−0.03(27)	0.02(34)	−0.03(34)	−0.10(42)	-	0.93
	3	0	0.05(10)	-	0.03(13)	-	0.10(17)	0.92

Table 5.3: Summary of the fit results for the parameters c_{mk}. The results for each fit are listed for $A_{qq'}$ considering all flavor combinations uu, ud and dd. We have taken into account $(N, K) = (2, 0), (2, 1), (3, 0)$.

For each channel and flavor combination we perform a global fit on the corresponding twist-2 function data, using the ansatz (5.25). For the parameters describing the double exponential we reuse the results obtained in section 5.2.3, see table 5.2. These are also employed to obtain the normalized twist-2 functions $\widehat{A}$.
The fit technique is the same as for the local fits we presented before. We take into account each data point for which $4a < y < 16a$. Notice that there is linearly increasing number of data points for increasing y, which is why the region of large quark distances might be overrepresented in the determination of the y-dependence.
We perform three different fits: Two fits assuming only a constant value of the ζ moments for all distances. Here we consider $N = 2, 3$ non-trivial terms in the h_n series. Furthermore, we make an additional fit allowing also a linear term in y, where we choose

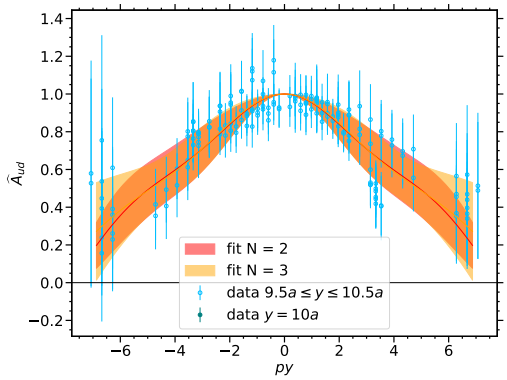

(a) global fit on $\widehat{A}_{ud}$ at $y = 10a$, $K = 0$

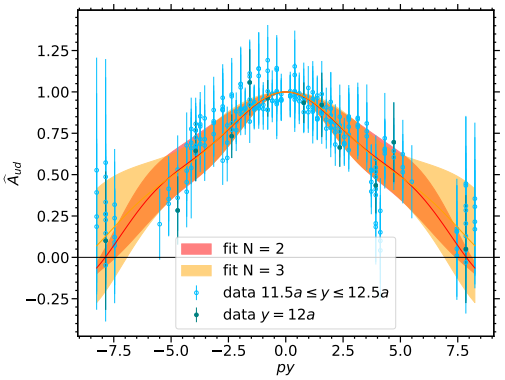

(b) global fit on $\widehat{A}_{ud}$ at $y = 12a$, $K = 0$

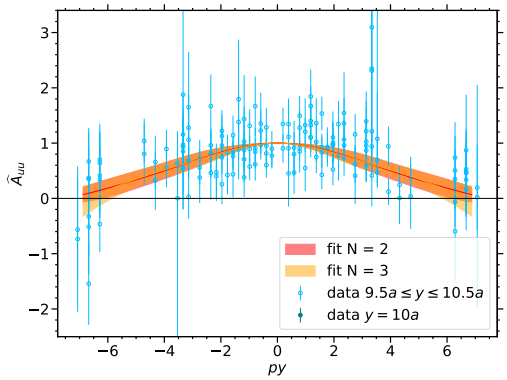

(c) global fit on $\widehat{A}_{uu}$ at $y = 10a$, $K = 0$

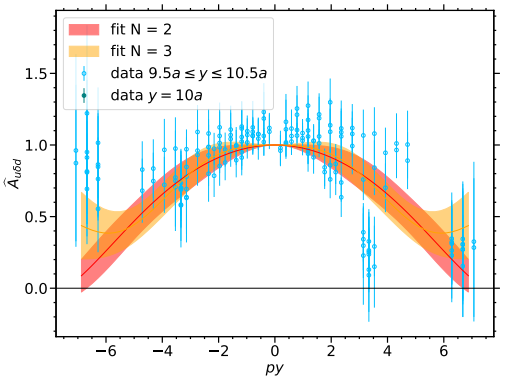

(d) global fit on $\widehat{A}_{\delta du}$ at $y = 10a$, $K = 0$

Figure 5.13: Same as Figure 5.9, but here we show slices of the global fit, where the ansatz (5.14) with $K = 0$ has been used.

$N = 2$. $N = 3$ is not considered in this case, since this ansatz has been found to overfit the data.
The results for the fit parameters c_{mk} are shown in table 5.3 to table 5.7. Furthermore, we show for some selected channels the resulting curves in the py-plane for specific y in Figure 5.13. The values of the moments in ζ depending on y can be found in comparison to the corresponding results from the local fits in Figure 5.10 and Figure 5.11. It is often the case that the linear curve only weakly differs from that of the constant fit. In few cases, taking into account the linear term yields better congruence with the data. An example is given in Figure 5.12, which shows the local and global fits for $I^t_{\delta u \delta d}$. Here the global fit with $K = 1$ seems to yield a better overlap with the data points, the corresponding value for χ^2/dof is barely smaller compared to that for $K = 0$. The corresponding fit to a constant still covers the data points within the error bars. In the case of all other channels than $I^t_{\delta u \delta d}$ the linear term turns out to be less important or completely unnecessary. The results for $K = 1$ have to be treated carefully: The

	N	K	c_{10}	$c_{11}[\mathrm{fm}^{-1}]$	c_{20}	$c_{21}[\mathrm{fm}^{-1}]$	c_{30}	χ^2/dof
$A_{\Delta u\Delta u}$	2	0	$-0.36(87)$	-	$-0.8(1.3)$	-	-	0.24
		1	$-0.3(3.2)$	0.4(6.8)	1.6(4.6)	$-3.6(9.2)$	-	0.24
	3	0	0.21(90)	-	0.9(1.7)	-	2.4(3.3)	0.24
$A_{\Delta u\Delta d}$	2	0	0.15(42)	-	0.07(62)	-	-	0.17
		1	0.26(96)	$-0.2(1.5)$	0.2(1.2)	$-0.2(1.5)$	-	0.17
	3	0	0.09(49)	-	$-0.10(84)$	-	$-0.2(1.2)$	0.17
$A_{\Delta d\Delta d}$	2	0	0.4(1.3)	-	0.2(1.5)	-	-	0.12
		1	1.3(2.6)	$-1.4(5.1)$	1.7(4.0)	$-2.0(6.4)$	-	0.12
	3	0	0.6(1.2)	-	0.7(2.0)	-	0.8(3.0)	0.12

Table 5.4: Same as table 5.3, but for the twist-2 function $A_{\Delta q\Delta q'}$.

	N	K	c_{10}	$c_{11}[\mathrm{fm}^{-1}]$	c_{20}	$c_{21}[\mathrm{fm}^{-1}]$	c_{30}	χ^2/dof
$A_{\delta uu}$	2	0	0.126(82)	-	0.080(84)	-	-	0.98
		1	$-0.14(24)$	0.29(24)	$-0.25(31)$	0.36(31)	-	0.97
	3	0	0.137(85)	-	0.102(97)	-	0.11(11)	0.98
$A_{\delta du}$	2	0	0.044(49)	-	0.002(48)	-	-	1.02
		1	0.14(11)	$-0.09(11)$	0.23(14)	$-0.21(13)$	-	0.95
	3	0	0.017(54)	-	$-0.056(60)$	-	$-0.086(67)$	0.91
$A_{\delta ud}$	2	0	0.106(49)	-	0.048(49)	-	-	1.06
		1	0.013(99)	0.099(96)	$-0.02(11)$	0.077(99)	-	1.03
	3	0	0.123(54)	-	0.085(60)	-	0.095(66)	1.01
$A_{\delta dd}$	2	0	$-0.36(26)$	-	$-0.51(28)$	-	-	0.76
		1	$-0.70(61)$	0.49(67)	$-0.52(83)$	0.15(85)	-	0.75
	3	0	$-0.31(31)$	-	$-0.42(42)$	-	$-0.38(53)$	0.76

Table 5.5: Same as table 5.3, but for the twist-2 function $A_{\delta qq'}$.

obtained values of the moments are close to zero, so that the linear term often causes negative values in a wide range of y. This is e.g. the case for $\langle\zeta^2\rangle$ or $\langle\zeta^4\rangle$ in $I^t_{\delta u\delta d}$ in the region $y < 0.8$ fm or $y < 1.1$ fm, respectively, see Figure 5.12. However, negative values for even moments of ζ are mathematically not allowed.
Finally, we are able to calculate the DPD Mellin moments from the parameters A_i, η_i and c_{mk}. Combining (5.11), (5.18), (5.23) and the ansatz for $I(\zeta, y^2)$ (5.13) we find

$$I_{qq'}(\zeta, y^2) = \pi \sum_{i=1,2} A_i e^{-\eta_i(y-y_0)} \sum_{n,m=0}^{N} \sum_{k=0}^{K} \zeta^{2n} \left(T^{-1}\right)_{nm} c_{mk}\ (y)^{k+\delta}\ \eta_i^{\delta}\ \Theta(1-\zeta^2)\ . \quad (5.26)$$

Since the results naturally have a strong model dependence, a useful check of the reliability is the comparison of the results obtained from different models. The results for

	N	K	c_{10}	$c_{11}[\mathrm{fm}^{-1}]$	c_{20}	$c_{21}[\mathrm{fm}^{-1}]$	c_{30}	χ^2/dof
$A_{\delta u\delta u}$	2	0	0.18(29)	-	0.37(33)	-	-	0.58
		1	−0.2(1.1)	0.6(1.7)	0.2(1.5)	0.4(2.2)	-	0.58
	3	0	0.45(38)	-	1.01(68)	-	1.5(1.0)	0.58
$A_{\delta u\delta d}$	2	0	0.057(87)	-	0.024(95)	-	-	0.80
		1	0.04(19)	0.01(21)	−0.15(22)	0.15(22)	-	0.78
	3	0	0.085(93)	-	0.08(11)	-	0.12(13)	0.78
$A_{\delta d\delta d}$	2	0	0.38(49)	-	0.35(56)	-	-	0.47
		1	−0.1(1.5)	0.7(1.8)	0.1(1.9)	0.4(2.2)	-	0.47
	3	0	0.69(62)	-	0.96(95)	-	1.2(1.3)	0.46

Table 5.6: Same as table 5.3, but for the twist-2 function $A_{\delta q\delta q'}$.

	N	K	c_{10}	$c_{11}[\mathrm{fm}^{-1}]$	c_{20}	$c_{21}[\mathrm{fm}^{-1}]$	c_{30}	χ^2/dof
$B_{\delta u\delta u}$	2	0	0.5(1.0)	-	0.5(1.5)	-	-	0.25
		1	5.2(4.4)	−7.7(7.8)	11.4(8.1)	−18(14)	-	0.25
	3	0	1.6(1.3)	-	3.9(2.6)	-	6.9(4.6)	0.25
$B_{\delta u\delta d}$	2	0	0.068(78)	-	−0.012(72)	-	-	0.71
		1	−0.30(19)	0.37(20)	−0.45(27)	0.42(26)	-	0.66
	3	0	0.080(92)	-	0.01(10)	-	0.01(12)	0.70
$B_{\delta d\delta d}$	2	0	−0.4(1.3)	-	−0.7(2.0)	-	-	0.20
		1	6(12)	−11(23)	13(20)	−23(35)	-	0.20
	3	0	1.3(1.6)	-	4.3(5.4)	-	9(11)	0.20

Table 5.7: Same as table 5.3, but for the twist-2 function $B_{\delta q\delta q'}$.

selected polarizations and flavor combinations are shown in Figure 5.14 for the three different fits at $\zeta = 0$. In the shown cases one can observe a reasonable agreement between the resulting curves within the error bands. Small deviations can be seen e.g. in the results for I_{uu}, see panel (c). In all cases, except for the "bad" channels, which we figured out in section 5.2.4, we observe a similar agreement of the curves or deviations which are at most of the relative size observed for I_{uu}. In particular, we find congruence of the curves in channels where the moments of ζ seemed to require $K \neq 0$, as it was the case for $I^t_{\delta u\delta d}$. The corresponding results are plotted in panel (b) of Figure 5.14.
For the physical discussion in the following section we mainly consider the results obtained for $N = 2$ and $K = 0$. As previously discussed, a constant y-dependence of the ζ-moments sufficiently describes the data and, moreover, the results for other choices of N and K agree within the error bands.

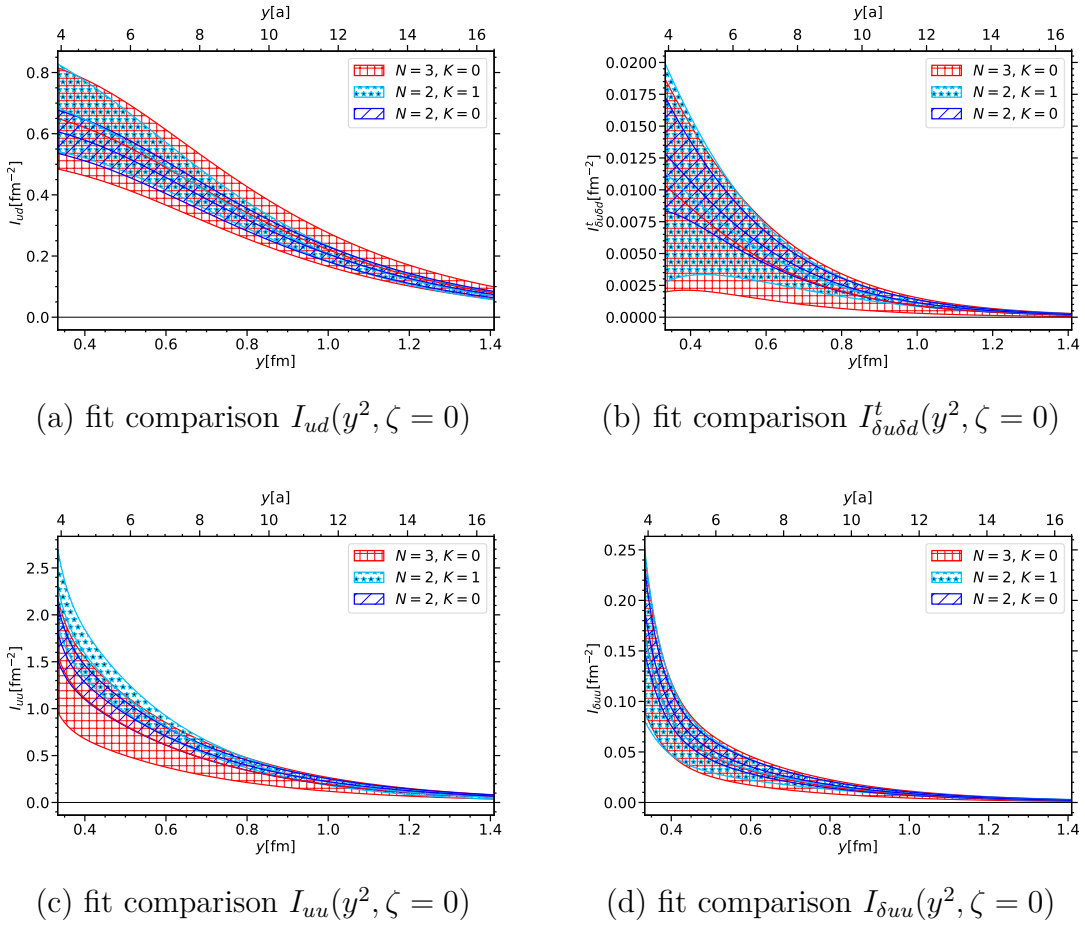

(a) fit comparison $I_{ud}(y^2, \zeta = 0)$

(b) fit comparison $I^t_{\delta u\delta d}(y^2, \zeta = 0)$

(c) fit comparison $I_{uu}(y^2, \zeta = 0)$

(d) fit comparison $I_{\delta uu}(y^2, \zeta = 0)$

Figure 5.14: Comparison of results for DPD Mellin moments obtained from the fits with $(N, K) = (2, 0), (2, 1), (3, 0)$ for selected channels.

5.4 Discussion

The first aspect of physical relevance we want to look at is the dependence on the quark flavor. The corresponding results for $\zeta = 0$, i.e. the forward case, which is relevant for the DPS cross section, is shown in Figure 5.15 for the moments $I_{qq'}$ and $I_{\delta qq'}$. Again we see dominance of uu and ud for large transverse current separations. At small y the curves of uu and dd show a steeper increase than the ud curve.
An interesting observation is the fundamentally different behavior of the curves for different flavor combinations, e.g. I_{uu} and I_{ud}. Naive factorization hypotheses, like the pocket formula, require functions encoding the transverse structure of parton correlations to be universal, i.e. flavor independent. This is in contradiction to our results.
We discuss next the dependence on the quark polarization for a given flavor combination. The corresponding results are plotted in Figure 5.16, where we also show again the data of the twist-2 functions at $py = 0$. The results for the twist-2 functions, as well as

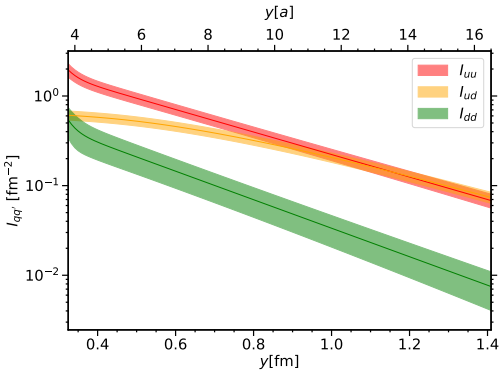

(a) flavor comparison, $I_{qq'}(y^2, \zeta = 0)$, $N = 2$, $K = 0$

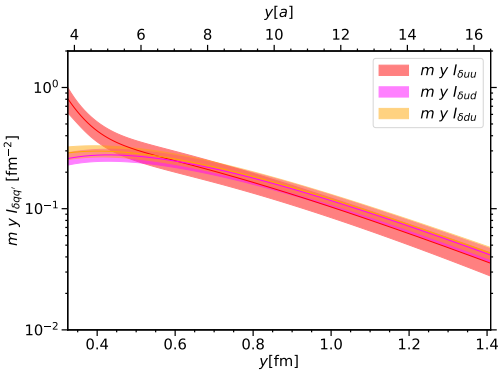

(b) flavor comparison, $I_{\delta qq'}(y^2, \zeta = 0)$, $N = 2$, $K = 0$

Figure 5.15: Comparison between different flavor combinations for the DPD Mellin moments $I_{qq'}$ (a) and $I_{\delta qq'}$ (b) for $\zeta = 0$. In the latter dd is not shown due to the fit quality. In order to emphasize the different behavior for each quark flavor, we use a logarithmic scale at the vertical axis.

the corresponding Mellin moments, show clear polarization effects for ud. In particular, $I_{\delta ud}$ and $I_{\delta du}$ are quite large. These results are very similar to those obtained for the pion in [46], which are shown in Figure 5.17. For uu the result for moments involving at least one polarized quark is observed to be relatively small compared to the curve for unpolarized quarks.
As already mentioned, we do not show the Mellin moments for two longitudinally polarized quarks, since a reliable determination was not possible. However, the size of the corresponding twist-2 functions is much smaller than those obtained for the other polarizations. This might indicate that the Mellin moments themselves are also small.
In section 2.1 we gave a $SU(2) \times SU(3)$-symmetric expression for the spin-flavor part of the proton wave function (2.5). From this, relations for the ratios of DPDs and the corresponding Mellin moments can be derived. In particular, one finds for spin-spin correlations:

$$\begin{aligned} \frac{f_{\Delta u \Delta u}}{f_{uu}} &= \frac{1}{3}\,, & \frac{f_{\Delta u \Delta d}}{f_{ud}} &= -\frac{2}{3}\,, \\ \frac{f_{\delta u \delta u}}{f_{uu}} &= \frac{1}{3}\,, & \frac{f_{\delta u \delta d}}{f_{ud}} &= -\frac{2}{3}\,. \end{aligned} \tag{5.27}$$

In general the results we obtained for spin-spin correlations, and, as far as available, for the corresponding Mellin moments, are relatively small compared to the unpolarized channels. For quark flavor ud the factor $-2/3$ is neither realized in the twist-2 functions nor in the Mellin moments. Merely the negative sign in the spin-spin correlations can be observed. Moreover, $A_{\Delta u \Delta d}$ and $A_{\delta u \delta d}$ are not equal as predicted by (5.27). Considering flavor uu, we also observe a very small signal for the spin-spin correlations $A_{\Delta u \Delta u}$ and

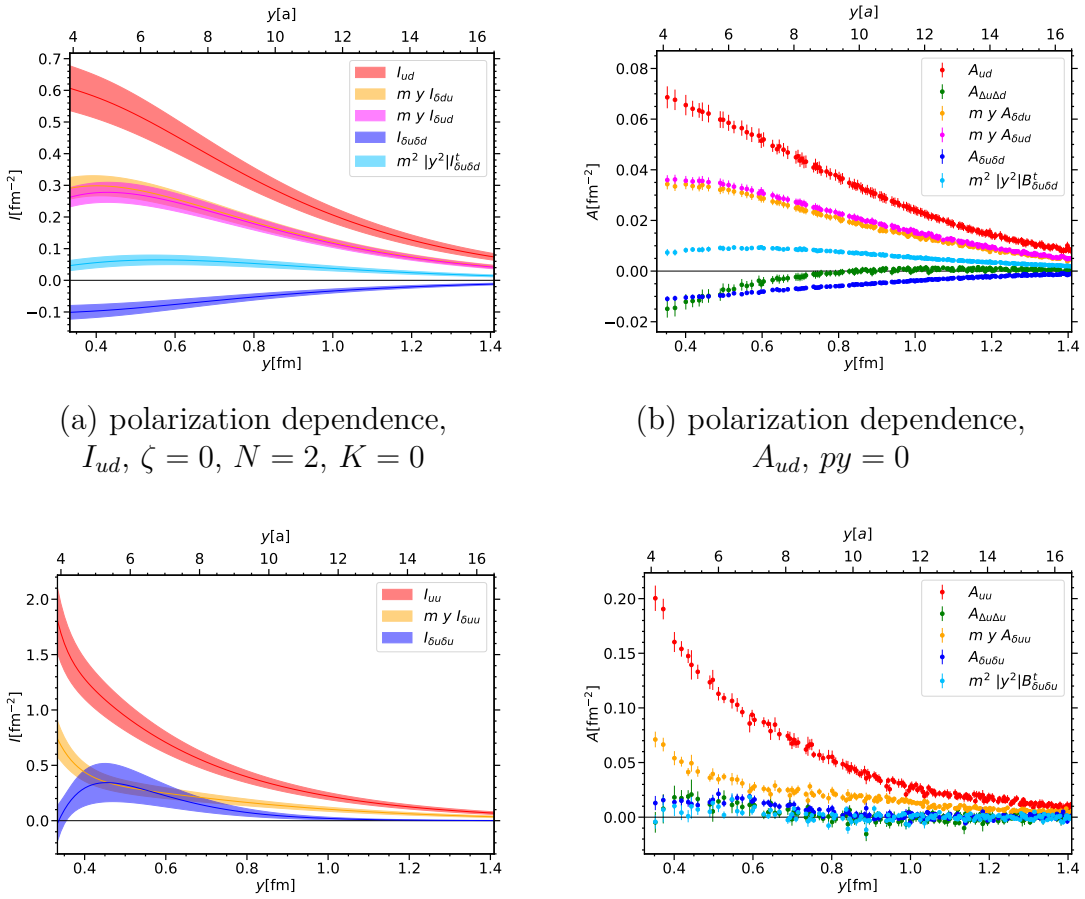

(a) polarization dependence, I_{ud}, $\zeta = 0$, $N = 2$, $K = 0$

(b) polarization dependence, A_{ud}, $py = 0$

(c) polarization dependence, I_{uu}, $\zeta = 0$, $N = 2$, $K = 0$

(d) polarization dependence, A_{uu}, $py = 0$

Figure 5.16: DPD Mellin moments for different quark polarizations. The data is shown for flavor combinations ud (a) and uu (c) at $\zeta = 0$ for $N = 2$ and $K = 0$. Panels (b) and (d) show again the corresponding twist-2 functions.

$A_{\delta u \delta u}$, which is barely above zero. The factor 1/3 given by (5.27) is generally not observed, however the size of $I_{\delta u \delta u}/I_{uu}$ in the region $y \approx 6a$ might coincide with 1/3. The results we obtained for ud in the nucleon are very similar to those which have been found for the corresponding channels in the pion, which is plotted in Figure 5.17 [46].

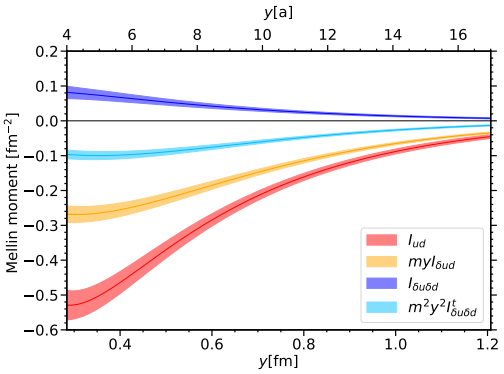

(a) polarization dependence, A_{ud} in π^+, $\zeta = 0$, $N = 1$, $K = 1$

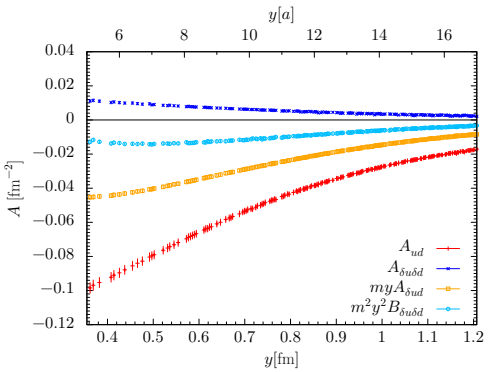

(b) polarization dependence, I_{ud} in π^+, $py = 0$

Figure 5.17: Same as Figure 5.16 for ud in the pion π^+ obtained in [46]

5.5 The number sum rule for DPDs

We want to conclude the analysis regarding DPD Mellin moments by investigating the consistency with the DPD number sum rule (2.62). We consider the DPD for one u-quark and one d-quark in a proton, where $N_u N_d = 2$. In contrast to (2.62) the leading splitting contribution is of order $\mathcal{O}(\alpha_s^2(\mu))$, since the two quark flavors are different. After integrating over the two momentum fractions, the sum rule becomes:

$$\int_{-1}^{1} \mathrm{d}x_1 \int_{-1}^{1} \mathrm{d}x_2 \int_{b_0/\mu} \mathrm{d}^2\boldsymbol{y}\; F_{ud}(x_1, x_2, \boldsymbol{y}; \mu) = 2 + \mathcal{O}(\alpha_s^2(\mu)) + \mathcal{O}((b_0\Lambda/\mu)^2)\ . \tag{5.28}$$

Notice that the l.h.s. of (5.28) is equivalent to an integral over $\boldsymbol{y}$ on the l.h.s. of (5.8). Hence, we can formulate the sum rule in terms of the twist-2 functions we have already calculated. Up to the corrections in α_s^2 and $(b_0\Lambda/\mu)^2$ this is:

$$\int_{b_0/\mu} \mathrm{d}^2\boldsymbol{y} \int \mathrm{d}(py)\; A_{ud}(py, y^2) = 2\ . \tag{5.29}$$

In the following, we use again the short notation $y = |\boldsymbol{y}|$. Using the ansatz (5.25) the py-integral on the l.h.s. of (5.29) turns into:

$$\begin{aligned} \int \mathrm{d}(py)\; A_{ud}(py, y^2) &= \pi \sum_{i,n,k} A_i\; e^{-\eta_i(y-y_0)}\; \left(T^{-1}c\right)_{nk}\; (y)^{k+\delta}\eta_i^\delta \int \frac{\mathrm{d}(py)}{\pi} h_n(py) \\ &= \pi \sum_{i,k} A_i\; e^{-\eta_i(y-y_0)}\; \left(T^{-1}c\right)_{0k}\; (y)^{k+\delta}\eta_i^\delta\ . \end{aligned} \tag{5.30}$$

The integration over py translates the h_n back into their Fourier transform at $\zeta = 0$, which is non-zero, only if $n = 0$. Therefore, in the last line of (5.30) only the first term in the n-series remains. Using the expression above and polar coordinates, the

$\boldsymbol{y}$-integral in the l.h.s of (5.29) becomes:

$$\begin{aligned} &2\pi^2 \sum_{i,k} A_i \; e^{\eta_i y_0} \; \left(T^{-1}c\right)_{0k} \eta_i^{\delta} \int_{b_0/\mu}^{\infty} \mathrm{d}y \; e^{-\eta_i y} (y)^{k+1+\delta} \\ &= 2\pi^2 \sum_{i,k} \frac{A_i \; e^{\eta_i y_0} \; (T^{-1}c)_{0k}}{\eta_i^{k+2}} \Gamma(2+k+\delta, \eta_i b_0/\mu) \; . \end{aligned} \tag{5.31}$$

In the present study, where we work at a renormalization scale $\mu = 2$ GeV, the cutoff has the explicit value $b_0/\mu = 0.11$ fm. Putting everything together, the sum rule in terms of the fit parameters reads:

$$2\pi^2 \sum_{i,k,m} \left(T^{-1}\right)_{0j} \frac{A_i \; e^{\eta_i y_0} \; c_{mk}}{\eta_i^{k+2}} \Gamma(2+k+\delta, \eta_i b_0/\mu) \stackrel{!}{=} 2 \; . \tag{5.32}$$

We perform the calculation of (5.32) for each fit we have presented in section 5.3. The corresponding numbers are summarized in table 5.8. For each fit, we obtain numbers

N	K	χ^2/dof	integral
2	0	0.47	1.93(23)
3	0	0.46	2.07(51)
2	1	0.46	1.98(24)

Table 5.8: The values of (5.32) which are calculated using the fit parameters resulting from fits for $(N, K) = (2, 0), (3, 0), (2, 1)$. We also list the corresponding χ^2/dof again.

close to the value predicted by the sum rule, where the absolute deviation of the mean value is at most 0.07. The statistical error is 12% to 25%, i.e. larger than the systematic error introduced by the choice of the model. In order to estimate the sensitivity to extrapolations in y, we vary the integration boundaries: Increasing the lower boundary to $2b_0/\mu$ decreases the results by 5% w.r.t. to the values given in table 5.8. Decreasing the upper boundary to $16a = 1.37$ fm yields values that are at most 16% smaller. Hence, the uncertainty from the extrapolation in y can be thought of having roughly the same relative size as the statistical error.

6 Factorization of two-current correlations

Two-current matrix elements and thus DPDs contain important information of correlations between quarks in a hadron, which influences the signal in DPS events. Concerning the cross section, quark correlations are often taken into account in a simplified manner or completely neglected, since they are hard to determine theoretically or in experiment. As an example we refer again to the pocket formula (1.3), which we already discussed in chapter 1. These factorization assumptions are known to fail in quark model calculations, in particular for the case of polarized quarks [34, 36, 37].
In the following, we want to investigate the strength of quark-quark correlations obtained from our lattice calculations. In order to do so, we compare our results for the two-current correlations and the corresponding twist-2 functions to their factorized analogue. The corresponding expressions are derived by inserting a complete set of states and assuming that only the nucleon state contributes. We obtain a convolution of nucleon form factors (FFs), which are also obtained by lattice calculations. Details on the corresponding simulations can be found in [110].
Analogue investigations have been made in the past for the pion [45, 46], where visible discrepancies have been found. Similar results have been obtained in recent quark model studies [111].

6.1 Factorization approaches

Within this work, we want to investigate two quantities involving two currents, first, the correlation function of local currents in an unpolarized proton, which has been evaluated in chapter 4, and second, the unpolarized proton matrix element of two light cone currents. As we have discussed in chapter 5, the latter is related to Mellin moments of (skewed) DPDs and furthermore to the twist-2 functions we have calculated.

6.1.1 Factorization of skewed DPDs

For this kind of factorization we consider the matrix element appearing in (2.50) and insert a complete set of states between the two currents. If the resulting expression is

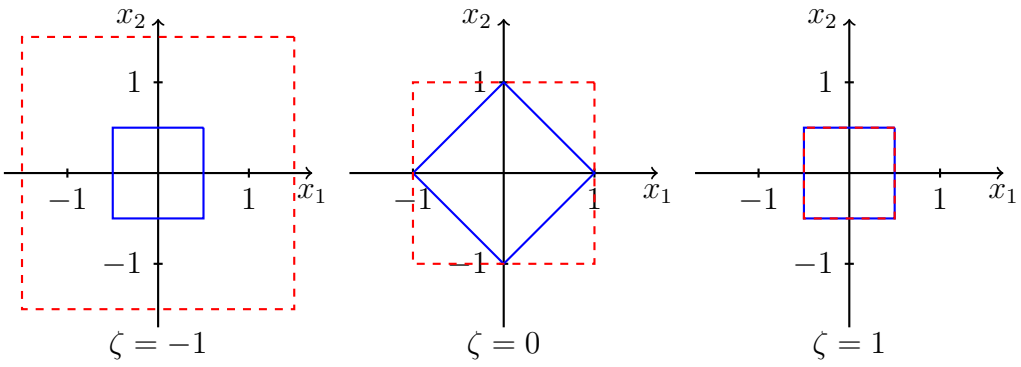

Figure 6.1: Support regions in the (x_1, x_2)-plane for different values of ζ of the DPD $F(x_1, x_2, \zeta, \boldsymbol{y})$ (blue line) compared to that of the factorized expression on the r.h.s. of (6.4) (red dashed line).

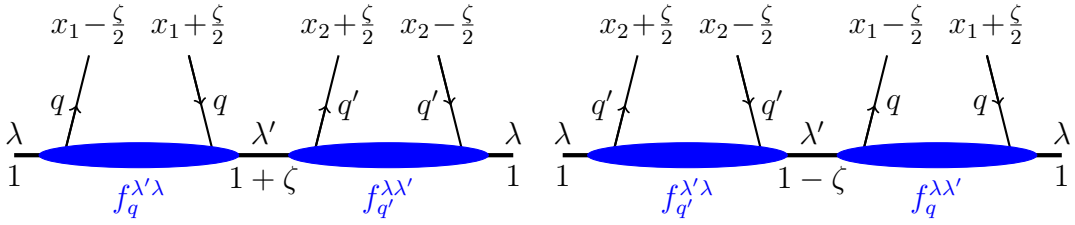

Figure 6.2: Visualization of the factorization of the DPD $F_{qq'}$ in terms of the GPD matrix elements $f^{\lambda\lambda'}$. The r.h.s. represents the expression obtained after the insertion of a complete set of states in the matrix element $\langle p, \lambda | \, \mathcal{O}_q \mathcal{O}_{q'} \, | p, \lambda \rangle$, which will be used if $\zeta \geq 0$. For $\zeta \leq 0$ we employ the analogue expression obtained from a factorized matrix element where the operators have been commuted. This is shown on the l.h.s.

dominated by nucleon states, we can write:

$$\begin{aligned} &\sum_{\lambda} \langle p, \lambda | \, \mathcal{O}_a(z_1, y) \; \mathcal{O}_b(z_2, 0) \, | p, \lambda \rangle \approx \\ &\approx \sum_{\lambda, \lambda'} \int \frac{\mathrm{d}p'^{+} \mathrm{d}^2 \boldsymbol{p}'}{2p'^{+}(2\pi)^3} e^{-iy(p'-p)} \, \langle p, \lambda | \, \mathcal{O}_a(z_1, 0) \, | p', \lambda' \rangle \, \langle p', \lambda' | \, \mathcal{O}_b(z_2, 0) \, | p, \lambda \rangle \; . \end{aligned} \tag{6.1}$$

Considering the DPD in momentum space (2.51), we have to integrate over $\boldsymbol{y}$ and y^-. A subsequent integration over p' leads to the following assignment:

$$p'^{+} = (1 - \zeta) p^{+} \; , \qquad \boldsymbol{p}' = \boldsymbol{p} - \boldsymbol{r} \; . \tag{6.2}$$

In order to express everything on the r.h.s. in terms of GPD matrix elements $f^{\lambda\lambda'}(\bar{x},\xi,\boldsymbol{r})$, we identify for $\boldsymbol{p}=\boldsymbol{0}$:

$$\begin{aligned} \bar{x}_i &= \frac{x_i}{1-\frac{\zeta}{2}} \ , & \xi &= \frac{\zeta}{\zeta-2} \ , \\ t(\zeta,\boldsymbol{r}^2) &:= -\frac{\zeta^2 m^2+\boldsymbol{r}^2}{1-\zeta} \ , & -\boldsymbol{p}' &= \boldsymbol{r} \ . \end{aligned} \tag{6.3}$$

Replacing the matrix element in (2.50) by our ansatz (6.1) and using the variables (6.3), we find for the DPD in momentum space (2.51):

$$\begin{aligned} F_{ab}(x_1,x_2,\zeta,\boldsymbol{r}^2) &\approx \frac{1}{2(1-\zeta)}\left[\prod_{i=1,2}\int\frac{\mathrm{d}z_i^-}{2\pi}e^{ix_i p^+ z_i^-}\right] \\ &\times\sum_{\lambda\lambda'}\langle p,\lambda|\,\mathcal{O}_a(z_1,0)\,|(1-\zeta)p^+,\boldsymbol{p}-\boldsymbol{r},\lambda'\rangle\,\langle(1-\zeta)p^+,\boldsymbol{p}-\boldsymbol{r},\lambda'|\,\mathcal{O}_b(z_2,0)\,|p,\lambda\rangle \\ &= \frac{1}{2(1-\zeta)}\sum_{\lambda\lambda'}f_a^{\lambda\lambda'}(\bar{x}_1,\xi,\boldsymbol{r})f_b^{\lambda'\lambda}(\bar{x}_2,-\xi,-\boldsymbol{r}) \ . \end{aligned} \tag{6.4}$$

Within this context we want to analyze the DPDs $F_{qq'}$ and $F_{\Delta q\Delta q'}$. Using the decomposition (2.44) with (2.45), one finds for the sum in the last line of (6.4)

$$\begin{aligned} \frac{1}{2}\sum_{\lambda\lambda'}f_q^{\lambda\lambda'}(x_1,\xi,\boldsymbol{r})f_{q'}^{\lambda'\lambda}(x_2,-\xi,-\boldsymbol{r}) &= (1-\xi^2)H_q(x_1,\xi,t)H_{q'}(x_2,-\xi,t) \\ &- \xi^2 H_q(x_1,\xi,t)E_{q'}(x_2,-\xi,t) - \xi^2 E_q(x_1,\xi,t)H_{q'}(x_2,-\xi,t) \\ &+ \left(\frac{\xi^4}{1-\xi^2}+\frac{1-\xi}{1+\xi}\frac{\boldsymbol{r}^2}{4m^2}\right)E_q(x_1,\xi,t)E_{q'}(x_2,-\xi,t) \ , \\ \frac{1}{2}\sum_{\lambda\lambda'}f_{\Delta q}^{\lambda\lambda'}(x_1,\xi,\boldsymbol{r})f_{\Delta q'}^{\lambda'\lambda}(x_2,-\xi,-\boldsymbol{r}) &= (1-\xi^2)\tilde{H}_q(x_1,\xi,t)\tilde{H}_{q'}(x_2,-\xi,t) \\ &- \xi^2\tilde{H}_q(x_1,\xi,t)\tilde{E}_{q'}(x_2,-\xi,t) - \xi^2\tilde{E}_q(x_1,\xi,t)\tilde{H}_{q'}(x_2,-\xi,t) \\ &+ \left(\frac{\xi^4}{1-\xi^2}+\frac{1-\xi}{1+\xi}\xi^2\frac{\boldsymbol{r}^2}{4m^2}\right)\tilde{E}_q(x_1,\xi,t)\tilde{E}_{q'}(x_2,-\xi,t) \ . \end{aligned} \tag{6.5}$$

Before we continue we have to discuss the following issue: The support regions in the (x_1,x_2)-plane are not identical on both sides of the equation. On the r.h.s. the support region is given by $-1+\zeta/2 \le x_i \le 1-\zeta/2$, which exceeds the constraints given by (2.53) in almost every case, see Figure 6.1. The only exception is found for $\zeta=1$. The mismatch is even larger for $\zeta<0$. Hence, we consider the factorization assumption to be suitable only for $\zeta\ge 0$. However, we are able to derive an alternative factorized expression by commuting the two operators on the l.h.s. of (6.1). Performing the same steps again, we arrive at a similar formula as (6.4), where ζ has been replaced by $-\zeta$

on the r.h.s.

$$F_{ab}(x_1, x_2, \zeta, \boldsymbol{r}^2) \approx \frac{1}{2(1+\zeta)} \sum_{\lambda\lambda'} f_b^{\lambda\lambda'}(\bar{x}_2', \xi', \boldsymbol{r}) f_a^{\lambda'\lambda}(\bar{x}_1', -\xi', -\boldsymbol{r}) \ , \\ \xi' = \frac{\zeta}{2+\zeta} \ , \qquad \bar{x}_i' = \frac{x_i}{1+\frac{\zeta}{2}} \ . \tag{6.6}$$

In the following, we will consider (6.4) if $\zeta \geq 0$ and (6.6) if $\zeta \leq 0$. Taking Mellin moments on both sides we obtain for $\zeta \geq 0$:

$$I_{ab}(\zeta, \boldsymbol{r}^2) = \frac{(1-\frac{\zeta}{2})^2}{2(1-\zeta)} \int \mathrm{d}x_1 \int \mathrm{d}x_2 \sum_{\lambda\lambda'} \ f_a^{\lambda\lambda'}(x_1, \xi, \boldsymbol{r}) f_b^{\lambda'\lambda}(x_2, -\xi, -\boldsymbol{r}) \ . \tag{6.7}$$

After a Fourier transform we find through the relation (5.8)

$$\int \mathrm{d}(py) e^{-i\zeta py} A_{ab}(py, y^2) = \int \frac{\mathrm{d}^2\boldsymbol{r}}{(2\pi)^2} e^{-i\boldsymbol{r}\boldsymbol{y}} I_{ab}(\zeta, \boldsymbol{r}^2) \ , \tag{6.8}$$

with the twist-2 function $A_{ab}(py, y^2)$ defined in (5.5), which we calculated on the lattice. By inverting the Fourier transform on the l.h.s. we are able to express the twist-2 function A_{ab} for $py = 0$ in terms of the factorized DPD Mellin moment (6.7). Again, we define $y = |\boldsymbol{y}|$ and $r = |\boldsymbol{r}|$:

$$A_{ab}(py = 0, y^2) =: A_{ab}(y^2) = \frac{1}{4\pi^2} \int_{-1}^{1} \mathrm{d}\zeta \int \mathrm{d}r \ r \ J_0(yr) \ I_{ab}(\zeta, \boldsymbol{r}^2) \ . \tag{6.9}$$

Combining everything, the first test can be formulated as:

$$A_{ab}(y^2) \stackrel{?}{=} \frac{1}{4\pi^2} \int_0^1 \mathrm{d}\zeta \frac{(1-\frac{\zeta}{2})^2}{2(1-\zeta)} \int \mathrm{d}r \ r \ J_0(yr) \sum_{\lambda\lambda'} \int \mathrm{d}x_1 \ \int \mathrm{d}x_2 \\ \times \left[f_a^{\lambda\lambda'}(x_1, \xi, t, \boldsymbol{r}) f_b^{\lambda'\lambda}(x_2, -\xi, t, -\boldsymbol{r}) + f_b^{\lambda\lambda'}(x_2, \xi, t, \boldsymbol{r}) f_a^{\lambda'\lambda}(x_1, -\xi, t, -\boldsymbol{r}) \right] \ , \tag{6.10}$$

where the second term in the last line of (6.10) represents the contribution for $\zeta < 0$. For the cases $A_{qq'}$ and $A_{\Delta q \Delta q'}$ we can now give an explicit formulation of the factorization

test. Starting from (6.10) and inserting the spin sum (6.5), we find:

$$\begin{aligned}
A_{qq'}(y^2) &\stackrel{?}{=} \frac{1}{2\pi^2}\int_0^1 \mathrm{d}\zeta \frac{(1-\frac{\zeta}{2})^2}{1-\zeta}\int \mathrm{d}r\ r\ J_0(yr)\times \\
&\times\Bigg[Z_1(\zeta)F_1^q(t)F_1^{q'}(t) - Z_2(\zeta)\left(F_1^q(t)F_2^{q'}(t)+F_1^{q'}(t)F_2^q(t)\right) \\
&\quad + \left(Z_3(\zeta)+Z_4(\zeta)\frac{\boldsymbol{r}^2}{4m^2}\right)F_2^q(t)F_2^{q'}(t)\Bigg]\ , \\
A_{\Delta q\Delta q'}(y^2) &\stackrel{?}{=} \frac{1}{2\pi^2}\int_0^1 \mathrm{d}\zeta \frac{(1-\frac{\zeta}{2})^2}{1-\zeta}\int \mathrm{d}r\ r\ J_0(yr)\times \\
&\times\Bigg[Z_1(\zeta)g_A^q(t)g_A^{q'}(t) - Z_2(\zeta)\left(g_A^q(t)g_P^{q'}(t)+g_A^{q'}(t)g_P^q(t)\right) \\
&\quad + \left(Z_3(\zeta)+Z_5(\zeta)\frac{\boldsymbol{r}^2}{4m^2}\right)g_P^q(t)g_P^{q'}(t)\Bigg]\ ,
\end{aligned} \tag{6.11}$$

with

$$\begin{aligned}
Z_1(\zeta) &:= 1-Z_2(\zeta)\ , & Z_2(\zeta) &:= \frac{\zeta^2}{(2-\zeta)^2}\ , & Z_3(\zeta) &:= \frac{(Z_2(\zeta))^2}{Z_1(\zeta)}\ , \\
Z_4(\zeta) &:= \frac{1}{1-\zeta}\ , & Z_5(\zeta) &:= Z_2(\zeta)Z_4(\zeta)\ ,
\end{aligned} \tag{6.12}$$

and the nucleon form factors F_1, F_2, g_A and g_P defined by (2.43), which are identified with the first Mellin moments of H, E, $\tilde{H}$ and $\tilde{E}$ by (2.46).
For the case $\zeta = 0$ the expressions in (6.5) have already been derived in [55], see equations (4.48) and (4.49) therein.

6.1.2 Factorization of local matrix elements

The second possibility is to insert the complete set of states in a local matrix element:

$$\mathcal{M}^{ij}_{qq'}(p,y) \approx \frac{1}{2}\sum_{\lambda\lambda'}\int \frac{\mathrm{d}^3\vec{r}}{(2\pi)^3 2E_{\vec{r}}} e^{i\vec{y}(\vec{r}-\vec{p})}\,\langle p,\lambda|\,\mathcal{O}_i^q(0)\,|r,\lambda'\rangle\,\langle r,\lambda'|\,\mathcal{O}_j^{q'}(0)\,|p,\lambda\rangle\ , \tag{6.13}$$

with $E_{\vec{r}} = \sqrt{m^2+\vec{r}^2}$. The one-current matrix elements appearing in the expression above can be decomposed in terms of spinors. The decomposition depends on the specific insertion type, see (2.43):

$$\langle p,\lambda|\,\mathcal{O}_i^q(0)\,|r,\lambda'\rangle = \bar{u}^\lambda(p)\mathcal{J}[\mathcal{O}_i]u^{\lambda'}(r)\ . \tag{6.14}$$

Exploiting the completeness of the spinor solutions (2.8), the factorized matrix element reads (again we have to consider $y^0 = 0$):

$$\begin{aligned}\mathcal{M}^{ij}_{qq'}(p,y) &\approx \frac{1}{4}\int \frac{\mathrm{d}^3\vec{r}}{(2\pi)^3 E_{\vec{r}}} e^{i\vec{y}(\vec{r}-\vec{p})}\,\mathrm{tr}\left\{(\not{p}-m)\mathcal{J}[\mathcal{O}^q_i](\not{r}-m)\mathcal{J}[\mathcal{O}^{q'}_j]\right\} \\ &=: \frac{1}{4}\int \frac{\mathrm{d}^3\vec{r}}{(2\pi)^3 E_{\vec{r}}} e^{i\vec{y}(\vec{r}-\vec{p})}\mathcal{J}^{ij}_{qq'}(p,r)\ ,\end{aligned} \tag{6.15}$$

Let us now consider the case, where $\vec{p} = \vec{0}$ and each appearing Lorentz index is set to zero. In this case all expressions have to be rotational invariant, which implies:

$$\mathcal{M}^{ij}_{qq'}(p,y) \to \mathcal{M}^{ij}_{qq'}(\vec{y}^2)\ , \quad \mathcal{J}^{ij}_{qq'}(p,r) \to \mathcal{J}^{ij}_{qq'}(\vec{r}^2)\ . \tag{6.16}$$

This enables us to execute the angular parts of the $\vec{r}$ integral in (6.15). In the following we denote $y = |\vec{y}|$ and $r = |\vec{r}|$:

$$\mathcal{M}^{ij}_{qq'}(\vec{y}^2) \approx \frac{1}{8\pi^2}\int \mathrm{d}r \frac{r\sin(yr)}{E_r y}\mathcal{J}^{ij}_{qq'}(\vec{r}^2)\ . \tag{6.17}$$

Again we give some explicit formulae for the vector and the axial vector case. The corresponding spinor decompositions are given in (2.40), where $t = (p-r)^\mu(p-r)_\mu$. Calculating the trace in (6.15), one finds for $\mathcal{J}^{\mu\nu}_{VV/AA}(p,r)$:

$$\begin{aligned}\mathcal{J}^{\mu\nu}_{VV,qq'}(p,r) &= 4F^q_1(t)F^{q'}_1(t)\left[g^{\mu\nu}\left(m^2 - p^\rho r_\rho\right) + 2p^{\{\mu}r^{\nu\}}\right] \\ &\quad + F^{\{q}_1(t)F^{q'\}}_2(t)\left[2(p-r)^\mu(p-r)^\nu - 4g^{\mu\nu}\left(m^2 - p^\rho r_\rho\right)\right]\ , \\ \mathcal{J}^{\mu\nu}_{AA,qq'}(p,r) &= 4g^q_A(t)g^{q'}_A(t)\left[-g^{\mu\nu}\left(m^2 + p^\rho r_\rho\right) + 2p^{\{\mu}r^{\nu\}}\right] \\ &\quad + 4g^{\{q}_A(t)g^{q'\}}_P(t)(p-r)^\mu(p-r)^\nu \\ &\quad - g^q_P(t)g^{q'}_P(t)\frac{m^2 - p^\rho r_\rho}{m^2}(p-r)^\mu(p-r)^\nu\ .\end{aligned} \tag{6.18}$$

For the case of $\vec{p} = \vec{0}, \mu = 0, \nu = 0$ we have ($t_0 = 2m^2 - 2mE_r$):

$$\begin{aligned}\mathcal{J}^{00}_{VV,qq'}(\vec{r}^2) &= 4F^q_1(t_0)F^{q'}_1(t_0)\left(m^2 + mE_r\right) + F^{\{q}_1(t_0)F^{q'\}}_2(t_0)\ \vec{r}^2\ , \\ \mathcal{J}^{00}_{AA,qq'}(\vec{r}^2) &= 4g^q_A(t_0)g^{q'}_A(t_0)\left(mE_r - m^2\right) + 4g^{\{q}_A(t_0)g^{q'\}}_P(t_0)\,(m-E_r)^2 \\ &\quad - g^q_P(t_0)g^{q'}_P(t_0)\frac{(m-E_r)^3}{m}\ .\end{aligned} \tag{6.19}$$

6.2 The nucleon form factor

To evaluate the convolutions to be compared with our results for two-current matrix elements, we need to know the nucleon form factors F_1, F_2, g_A and g_P appearing in (6.11)

and (6.19). These have been obtained in another simulation, taking into account excited state contributions and considering effects of pion resonances in the axial vector channel, which are modeled using χPT. The calculations shall be sketched in the following, more details are given in [110]. The form factor data used in the following has been provided by [112]. The dependence on the virtuality $t = \Delta^2$ will be discussed afterwards.

6.2.1 Lattice calculations

We consider (3.63) and replace the matrix element by the decompositions (2.43), which yields a relation between the ratio of correlation functions and the form factors F_1 and F_2 or g_A and g_P, respectively. The correlator in the numerator is given by a three point function. In contrast to (4.12) we consider different momenta at the source and the sink:

$$C_{3\mathrm{pt}}^{i,\vec{p},\vec{p}'}(t,\tau) := a^6 \sum_{\vec{x},\vec{z}} e^{-i\vec{p}\vec{x}} e^{i\vec{p}'\vec{z}} \left\langle \mathrm{tr}\left\{ P_+ \mathcal{P}(\vec{x},t)\ \mathcal{O}_i(\vec{0},\tau)\ \overline{\mathcal{P}}(\vec{z},0) \right\} \right\rangle \ , \tag{6.20}$$

where the interpolators $\mathcal{P}(\vec{x},t)$, $\overline{\mathcal{P}}(\vec{z},t)$ and the insertion operators $\mathcal{O}_i(\vec{y},\tau)$ are the same as in (4.12). Using the completeness relation (2.8) of the Dirac spinors and considering only ground state contributions, we find:

$$2E \frac{C_{3\mathrm{pt}}^{\vec{p}',\vec{p}}(t,\tau)}{C_{2\mathrm{pt}}^{\vec{p}'}(t)} = \frac{e^{-(E-E')\tau}\sqrt{Z}\,\mathrm{tr}\left\{P_+(\not{p}'+m)\mathcal{J}[\mathcal{O}_i](\not{p}+m)\right\}}{2\sqrt{Z'}(E'+m)} \ , \tag{6.21}$$

where Z and Z' are the normalization factors of the interpolator overlap terms, which do not cancel as in (4.10), since initial and final states differ ($\vec{p} \neq \vec{p}'$). They are determined from fits on the two-point function $C_{2\mathrm{pt}}^{\vec{p}}$. E and E' denote the energies corresponding to the momenta $\vec{p}$ and $\vec{p}'$, respectively. As mentioned before, the calculations regarding the FFs also include excited state contributions, i.e. in contrast to (6.21) the following relation has been used:

$$\begin{aligned} 2E \frac{C_{3\mathrm{pt}}^{\vec{p}',\vec{p}}(t,\tau)}{C_{2\mathrm{pt}}^{\vec{p}'}(t)} = \frac{e^{-(E-E')\tau}\sqrt{Z}}{2\sqrt{Z'}(E'+m)\left(1+Ae^{-\Delta E' t}\right)} \Big[& \mathrm{tr}\left\{P_+(\not{p}'+m)\mathcal{J}[\mathcal{O}_i](\not{p}+m)\right\} \\ & \times \left(1 + B_{10}e^{-\Delta E'(t-\tau)} + B_{01}e^{-\Delta E\tau} + B_{11}e^{-\Delta E'(t-\tau)}e^{-\Delta E\tau}\right) \\ & + \text{pion resonances} \Big] \ . \end{aligned} \tag{6.22}$$

The coefficients A, B_{10}, B_{01} and B_{11} describe the overlap with the first excited state. Furthermore, resonances with the pion are considered. The latter are only taken into account for the axial vector channel, since they are very strong in this case. Inserting the corresponding decomposition $\mathcal{J}[V^\mu]$ or $\mathcal{J}[A^\mu]$ relates the FFs to the ratio on the l.h.s. . They can be extracted by solving the given system of equations.
There are two Wick contractions to be considered, a connected one and a disconnected

one. Using the notation introduced in section 4.2, these are:

$$\begin{aligned} &a^3 \sum_{\vec{x}} \left\langle G_{\mathrm{3pt}}^{i,\vec{p},\vec{p}'}(\vec{x},t,\tau) \right\rangle \ , \\ &a^3 \sum_{\vec{x}} \left\langle G_{\mathrm{2pt}}^{\vec{p},\vec{p}'}(t) L_1^i(\vec{x},\tau) \right\rangle - \left\langle G_{\mathrm{2pt}}^{\vec{p},\vec{p}'}(t) \right\rangle \left\langle \left\langle L_1^i(\tau) \right\rangle \right\rangle \ . \end{aligned} \tag{6.23}$$

The calculation was performed for the connected contraction only, i.e. effects arising from the disconnected part are not contained in the FF data. $G_{\mathrm{3pt}}^{i,\vec{p},\vec{p}'}(t,\tau)$ is evaluated using the sequential source technique, which has been already described in section 4.2. Notice that only conventional Wuppertal smearing was used, i.e. the source and the sink are not boosted. The calculations are again for the H102 ensemble, including four different source-sink separations, which is necessary to control the excited state contributions. The final state momentum is fixed to $\vec{p}' = \vec{0}$.
The ground state of the matrix element for a given momentum transfer $\vec{\Delta} = -\vec{p}$ is extracted from a simultaneous fit on the parameterization (6.22), including the data for different source-sink separations. The calculations take into account momenta up to $\vec{p}^{\,2} = 5(2\pi/La)^2 \approx 1.029\ \mathrm{GeV}^2$.

6.2.2 Properties

form factor	$F(0)$	$M^2[\mathrm{GeV}^2]$	p(fixed)	χ^2/dof
F_1^u	1.977(12)	1.063(19)	2	1.09
	1.936(11)	1.747(29)	3	1.79
F_2^u	1.764(38)	0.982(44)	2	1.63
	1.711(34)	1.674(68)	3	0.52
F_1^d	1.0421(70)	0.766(13)	2	7.15
	1.0035(60)	1.300(19)	3	2.06
	0.9860(57)	1.837(26)	4	0.94
F_2^d	−1.744(23)	0.834(19)	2	2.51
	−1.658(20)	1.456(29)	3	1.30

Table 6.1: Values of $F(0)$ and M^2 for the vector FFs obtained from a fit on the ansatz (6.24). We also show the values of the corresponding χ^2, where the complete covariance matrix is taken into account.

From the relation (6.22) one obtains the values for the FFs for a specific momentum transfer or virtuality $t = -\vec{\Delta}^{\,2}$. To perform the convolutions (6.11) and (6.19) it is necessary to employ some model describing the t-dependence of the form factors. A

form factor	$F(0)$	M^2[GeV^2]	p(fixed)	χ^2/dof
g_A^u	0.8999(82)	1.971(64)	2	1.61
	0.8920(78)	3.161(97)	3	0.82
g_P^u	29.84(94)	0.327(11)	2	0.30
	24.73(62)	0.688(17)	3	1.03
g_A^d	−0.2930(41)	1.800(81)	2	1.05
	−0.2896(39)	2.90(12)	3	0.93
g_P^d	−9.62(77)	0.305(27)	2	0.13
	−7.88(49)	0.638(44)	3	0.60

Table 6.2: Same as table 6.1 for the axial vector fFFs.

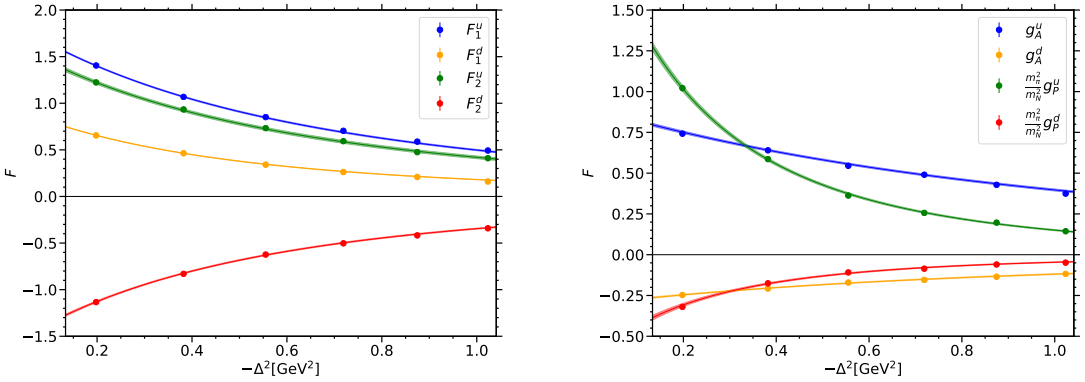

(a) vector form factor fit, $p = 3$ (b) axial vector form factor fit, $p = 3$

Figure 6.3: Data points of the FFs plotted against $\vec{\Delta}^2 = -\Delta^2$ and the corresponding curves obtained by a fit on the ansatz (6.24), using $p = 3$. Panel (a) shows the results for the vector channel, whereas (b) shows those of the axial vector FFs.

commonly used parameterization is given by a dipole or, more generally, a p-pole:

$$F(t) = \frac{F(0)}{\left(1 - \frac{t}{M^2}\right)^p} \,. \tag{6.24}$$

This ansatz could be motivated by the asymptotic behavior, where one obtains for g_A and g_P in the baryonic case $p = 2$ and $p = 3$, respectively [113]. Furthermore, from counting rules we find $p = 2$ for F_1 [114].
The parameters $F(0)$ and M^2 have to be obtained from a fit to the FF data with $0.205\ \text{GeV}^2 \leq \vec{\Delta}^2 \leq 1.029\ \text{GeV}^2$. We perform two sets of fits for two different exponents p in order to estimate the model dependence of the final convolution results. Explicitly, we take $p = 2$ and $p = 3$. Within the fits we employ the full covariance matrix, see Appendix section A.6. The corresponding results for the fit parameters and the values

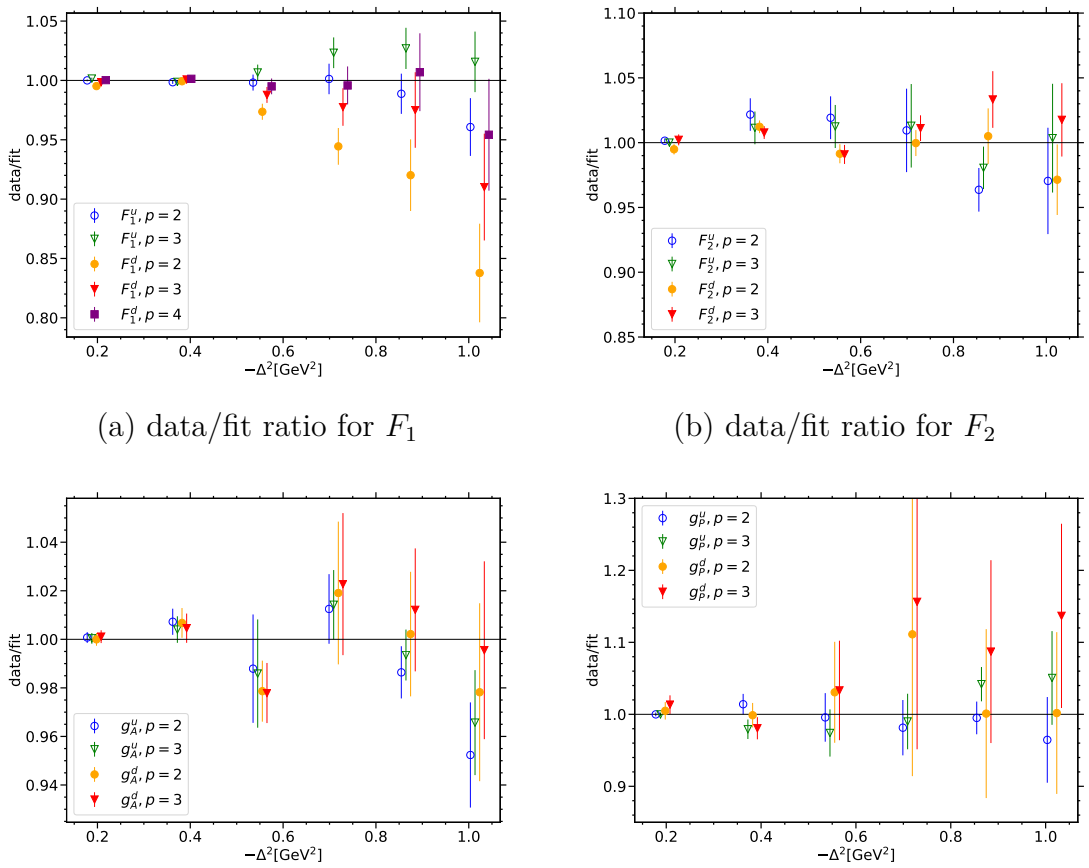

(a) data/fit ratio for F_1

(b) data/fit ratio for F_2

(c) data/fit ratio for g_A

(d) data/fit ratio for g_P

Figure 6.4: Ratio of the FF data and the corresponding fit, which is compared for different values of p. Again we show the Δ^2 dependence, where we employ small offsets for the different data points for better distinguishability. The results are shown for F_1 (a), F_2 (b), g_A (c) and g_P (d), each panel shows the results for both quark flavors.

of χ^2 are summarized in table 6.1 for $F_{1,2}$ and table 6.2 for $g_{A,P}$. The resulting values for $F_1^{u,d}$ are close to 2 or 1, respectively, which is consistent with charge conservation. In Figure 6.3 we show the data points for each form factor, compared to the corresponding curve resulting from fits with $p = 3$.
In Figure 6.4 we plot the ratio of the data points and the corresponding fits for different values of p. Most of the ratios are consistent with 1, indicating that the corresponding fit describes the data reasonably. One exception we want to point out here is the fit for F_1^d for $p = 2$, which does not yield a satisfying description of the FF data. Hence, for F_1^d we perform an alternative fit using $p = 4$, which yields a more consistent result. The corresponding data/fit ratio is also shown in Figure 6.4 (a), the resulting values of the fit parameters and the χ^2/dof is given in table 6.2. In the following, we discard the fit for F_1^d with $p = 2$ and instead use the corresponding results for $p = 4$.

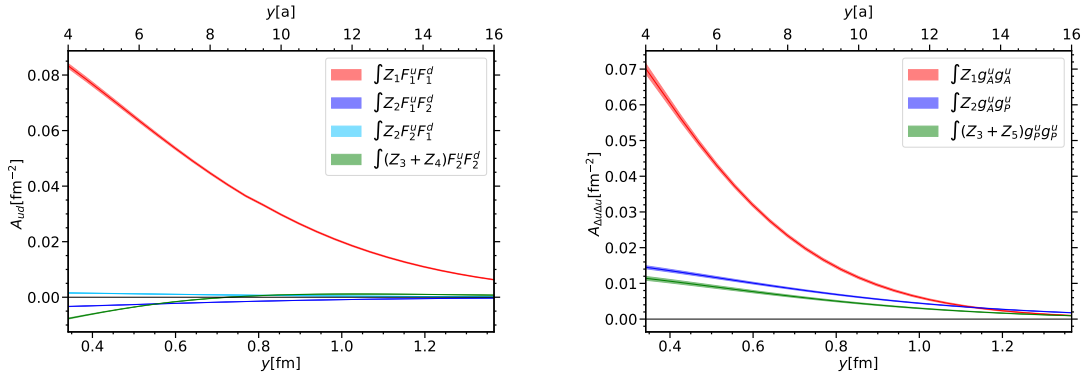

(a) convolution terms A_{ud}, $p = 3$

(b) convolution terms $A_{\Delta u \Delta u}$, $p = 3$

Figure 6.5: Comparison between the different terms within the square brackets in (6.11), which contribute to the factorized expression of A_{ud} (a) and $A_{\Delta u \Delta u}$ (b).

6.3 Convolution results

We use the results of the form factor fits described in the previous section to perform the convolutions (6.11) and (6.19). This is repeated for each possible combination of fit ansätze w.r.t. to the value of the pole p. Considering $p = 3, 4$ in the case of F_1^d and $p = 2, 3$ in all other cases, we have 16 possibilities for the convolution in the case of ud, whereas there are only 4 combinations for uu and dd. The integrals involved by the convolutions are solved numerically. For the two-dimensional integration in (6.11) we used the Vegas algorithm of the Cuba integration library [115]. The integral appearing in (6.19) was performed employing the corresponding routine of the GSL [116].
The results for the factorization of light cone matrix elements according to (6.11) are shown in Figure 6.5 for A_{ud} and $A_{\Delta u \Delta u}$, where we compare the different terms contributing to the factorized expression. We observe that the most relevant contribution is obtained by the integral over $Z_1(\zeta) F_1(t) F_2(t)$ or $Z_1(\zeta) g_A(t) g_A(t)$, respectively. The remaining terms are suppressed, but are still important to decide whether the convolution result agrees with the four-point data. A similar hierarchy of the convolution terms can be observed for the flavor combinations that are not shown.
In Figure 6.6 we compare the total factorized expression with the data of the corresponding twist-2 function, which we have presented in chapter 5. This is shown for A_{ud}, where we take into account several combinations of FF parameterizations which have been used as fit ansatz. Figure 6.7 shows the same for A_{uu} and A_{dd}, in Figure 6.8 results for $A_{\Delta q \Delta q'}$ are presented.
In general, we find that varying the exponent in the fit ansatz (6.24) does not change the result within the statistical error. This indicates a weak dependence of the convolution on the exact functional form of the nucleon FF. The data for $A_{qq'}$ have roughly the same size as the corresponding convolution. This holds for all flavor combinations, see Figure 6.6 and Figure 6.7. However, one can observe deviations for each distance y by

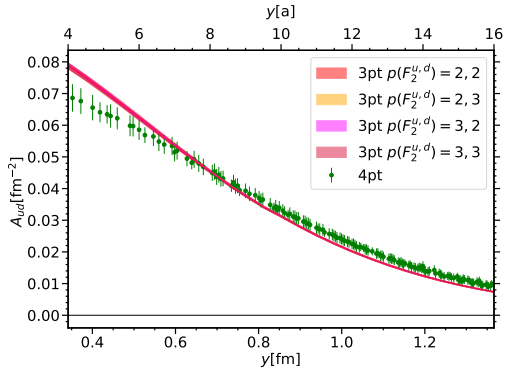

(a) A_{ud} vs $\int F_u F_d$, $py = 0$, $p(F_1^{u,d}) = 2, 3$

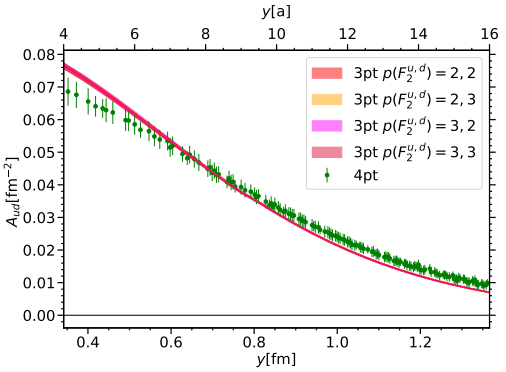

(b) A_{ud} vs $\int F_u F_d$, $py = 0$, $p(F_1^{u,d}) = 3, 4$

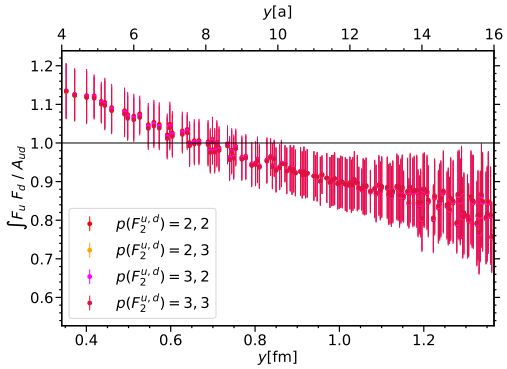

(c) $\int F_u F_d / A_{ud}$, $py = 0$, $p(F_1^{u,d}) = 2, 3$

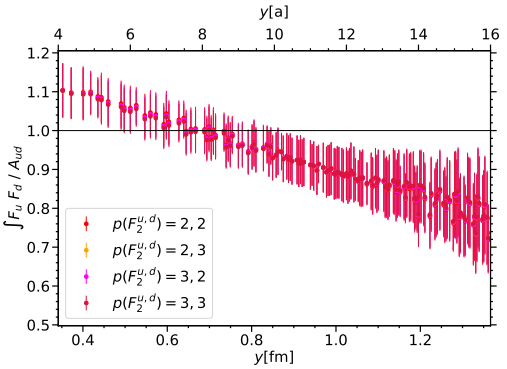

(d) $\int F_u F_d / A_{ud}$, $py = 0$, $p(F_1^{u,d}) = 3, 4$

Figure 6.6: (a,b): Comparison between the results for A_{ud} calculated from two-current matrix elements (green data points) and those obtained from the convolution (6.11) of FFs (continuous curves). The latter is shown for different form factor parameterizations differing in the exponent p. (c,d): Ratio of the FF convolution and the two-current data for A_{ud}

considering the ratio of the FF convolution and the two-current data, which is plotted in panel (c) and (d) in Figure 6.6 and Figure 6.7. Here we observe discrepancies of at most $20 - 30\%$ for A_{ud}. For A_{uu} and A_{dd} it is a bit larger. The result for A_{ud} is comparable to its analogue for the pion, which has been evaluated in the past [46].
In the case of two longitudinally polarized quarks $A_{\Delta u \Delta d}$ we observe a remarkably good coincidence of the data obtained from two-current matrix elements and the curves resulting from the corresponding convolution of axial form factors, which is shown in Figure 6.8 (a) and (b). This is quite surprising, since it indicates absence of direct spin correlations between the quarks, meaning that the only source of spin-spin correlations

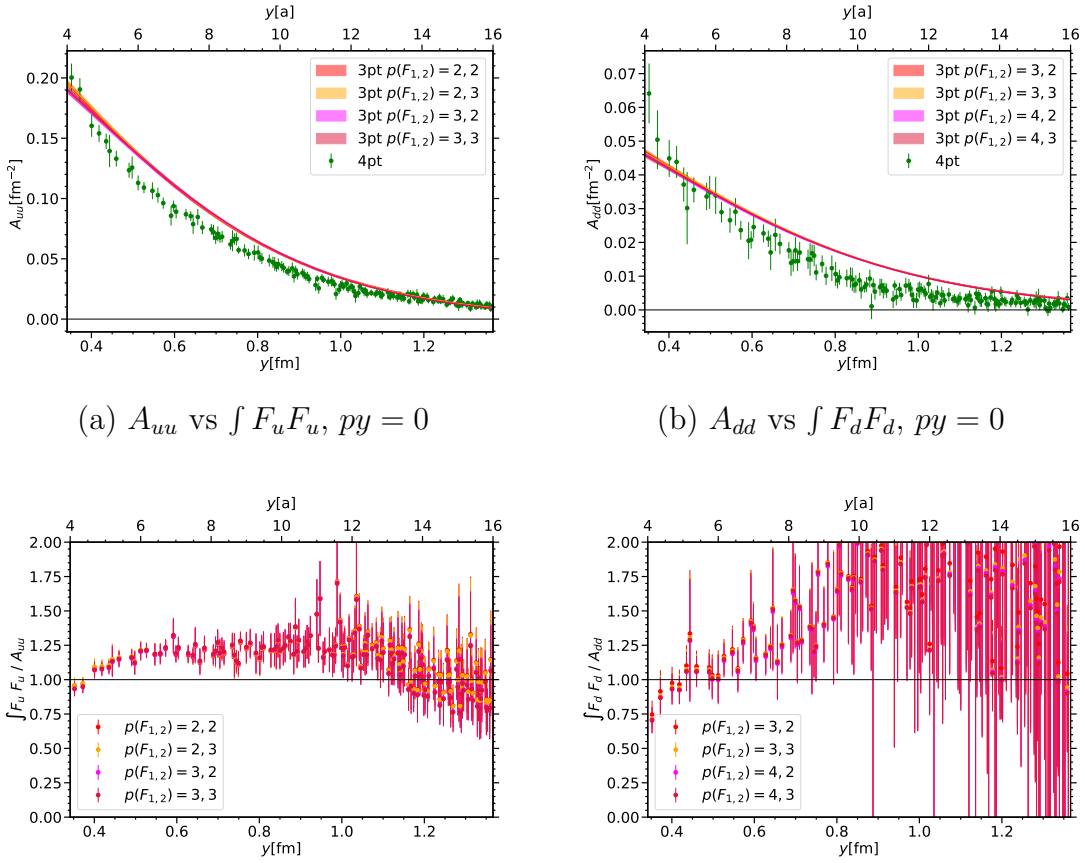

(a) A_{uu} vs $\int F_u F_u$, $py = 0$

(b) A_{dd} vs $\int F_d F_d$, $py = 0$

(c) $\int F_u F_u / A_{uu}$, $py = 0$

(d) $\int F_d F_d / A_{dd}$, $py = 0$

Figure 6.7: Comparison between the two-current data for the twist-2 functions A_{uu} (a) and A_{dd} (b) and the corresponding results obtained from the FF convolution (6.11) for several parameterizations. Again we show the ratio of the FF convolution and the corresponding twist-2 function A_{uu} (c) and A_{dd} (d).

is the correlation between one quark spin and the proton. For $A_{\Delta u \Delta u}$ (panel (c)) the agreement is not that perfect but still reasonable for $y > 6a$. In the case of $A_{\Delta d \Delta d}$ (panel (d)) the values for both, the four-point result and the convolution, are close to zero, where the errors of the four-point data are quite large.
Finally, we want to discuss the second kind of factorization we introduced in section 6.1. This concerns the matrix elements of two local currents, where we consider zero components of the vector or the axial vector current, see (6.19). We show the corresponding results in Figure 6.9 for $\langle V_u^0 V_d^0 \rangle$ and Figure 6.10 for $\langle V_u^0 V_u^0 \rangle$ and $\langle V_d^0 V_d^0 \rangle$. Again we plot the convolution results for several possible combinations of FF parameterizations. The variation of the result caused by changing this exponent turns out to be small compared to the absolute value of the signal. The plotted four-point data corresponds to those that have been shown in section 4.4, where only C_1 and C_2 contributions are taken into

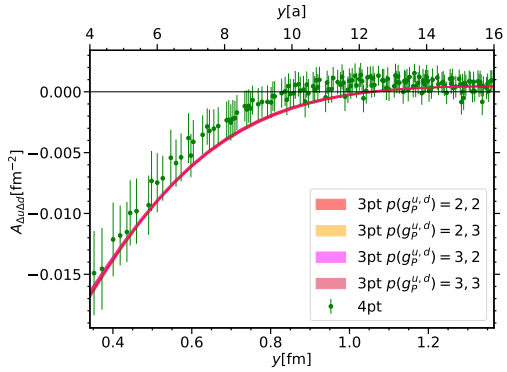

(a) $A_{\Delta u\Delta d}$ vs $\int F_{\Delta u}F_{\Delta d}$, $p(g_A^{u,d}) = 2,2$

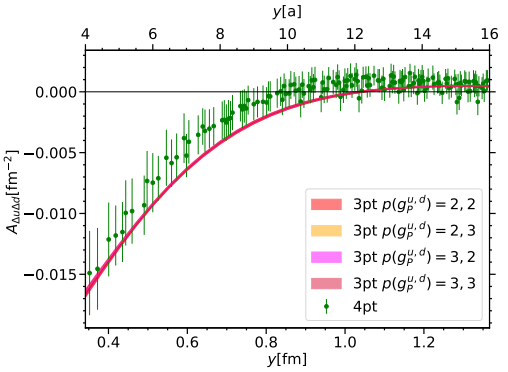

(b) $A_{\Delta u\Delta d}$ vs $\int F_{\Delta u}F_{\Delta d}$, $p(g_A^{u,d}) = 3,3$

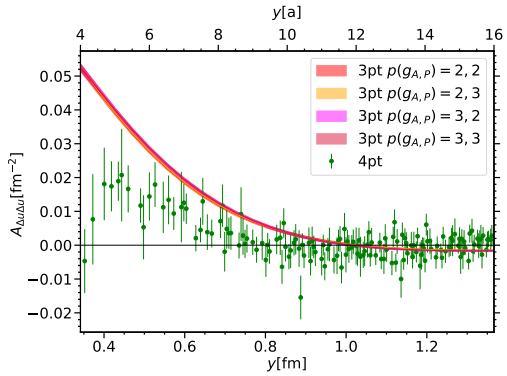

(c) $A_{\Delta u\Delta u}$ vs $\int F_{\Delta u}F_{\Delta u}$

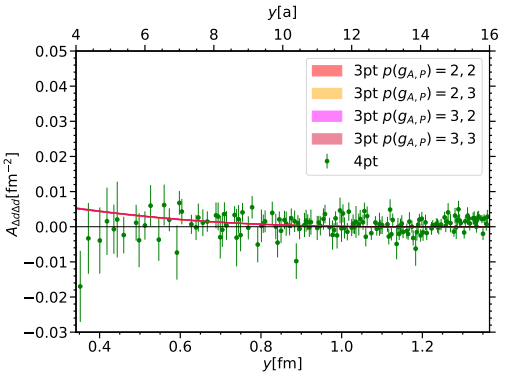

(d) $A_{\Delta d\Delta d}$ vs $\int F_{\Delta d}F_{\Delta d}$

Figure 6.8: Comparison between the two-current results for a given twist-2 function and the corresponding convolution (6.11) of FFs for several parameterizations. This is shown for $A_{\Delta u\Delta d}$ (a,b), $A_{\Delta u\Delta u}$ (c) and $A_{\Delta d\Delta d}$ (d)

account.
Again the convolution is of roughly the same size as the corresponding two-current data in the case of two vector currents V^0V^0, see Figure 6.9 (a,b). However, we are able to observe significant discrepancies. The corresponding ratio, which is plotted in Figure 6.9 (c,d), is different from one for each current distance y. It is observed to be at most $30 - 40\%$ in the case of ud. The differences are extreme for uu and dd at small distances, which can be seen in Figure 6.10 (c,d).
In the case of two axial vector currents A^0A^0 we can make two observations, see Figure 6.11: The first one is that for uu and dd the signals of both, the convolution and the two-current data, are relatively small compared to the statistical error if y is large, such that the two results are consistent with each other. However, they tend to different directions if y becomes small. The second observation is that in the case of ud the factorization hypothesis clearly fails. The convolution even predicts the opposite sign

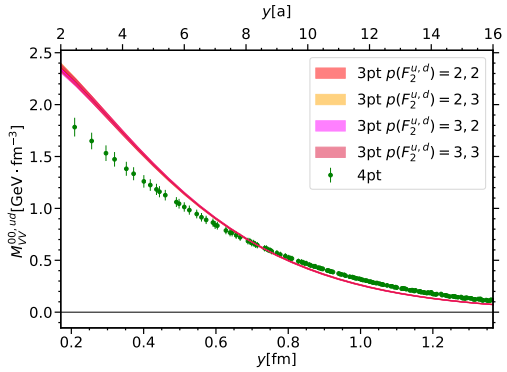

(a) $\langle V_u^0 V_d^0 \rangle$ vs $\int F_u F_d$, $p(F_1^{u,d}) = 2,3$

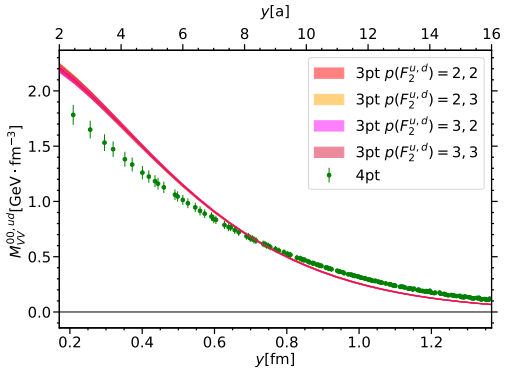

(b) $\langle V_u^0 V_d^0 \rangle$ vs $\int F_u F_d$, $p(F_1^{u,d}) = 3,4$

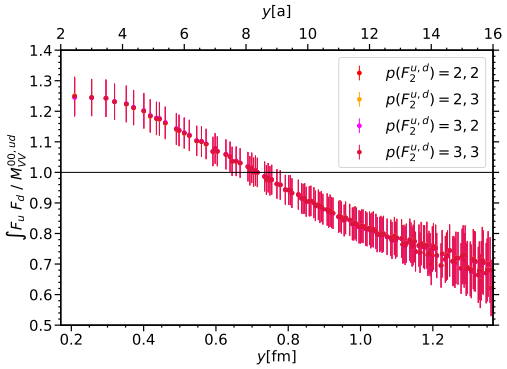

(c) $\int F_u F_d / \langle V_u^0 V_d^0 \rangle$, $p(F_1^{u,d}) = 2,3$

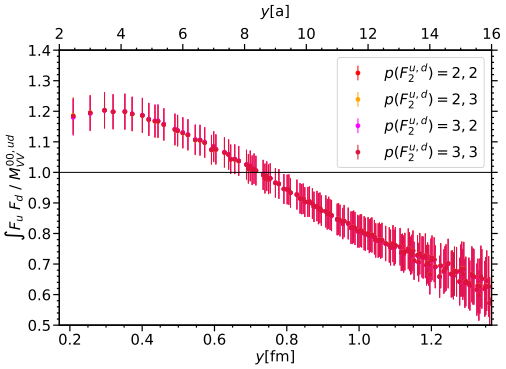

(d) $\int F_u F_d / \langle V_u^0 V_d^0 \rangle$, $p(F_1^{u,d}) = 3,4$

Figure 6.9: Data of the matrix element $\langle V_u^0 V_d^0 \rangle$ compared to the corresponding convolution (6.19) of FFs for several FF parameterizations (a,b). (c) and (d) show the ratio of the convolution and the matrix element.

as the corresponding two-current result.

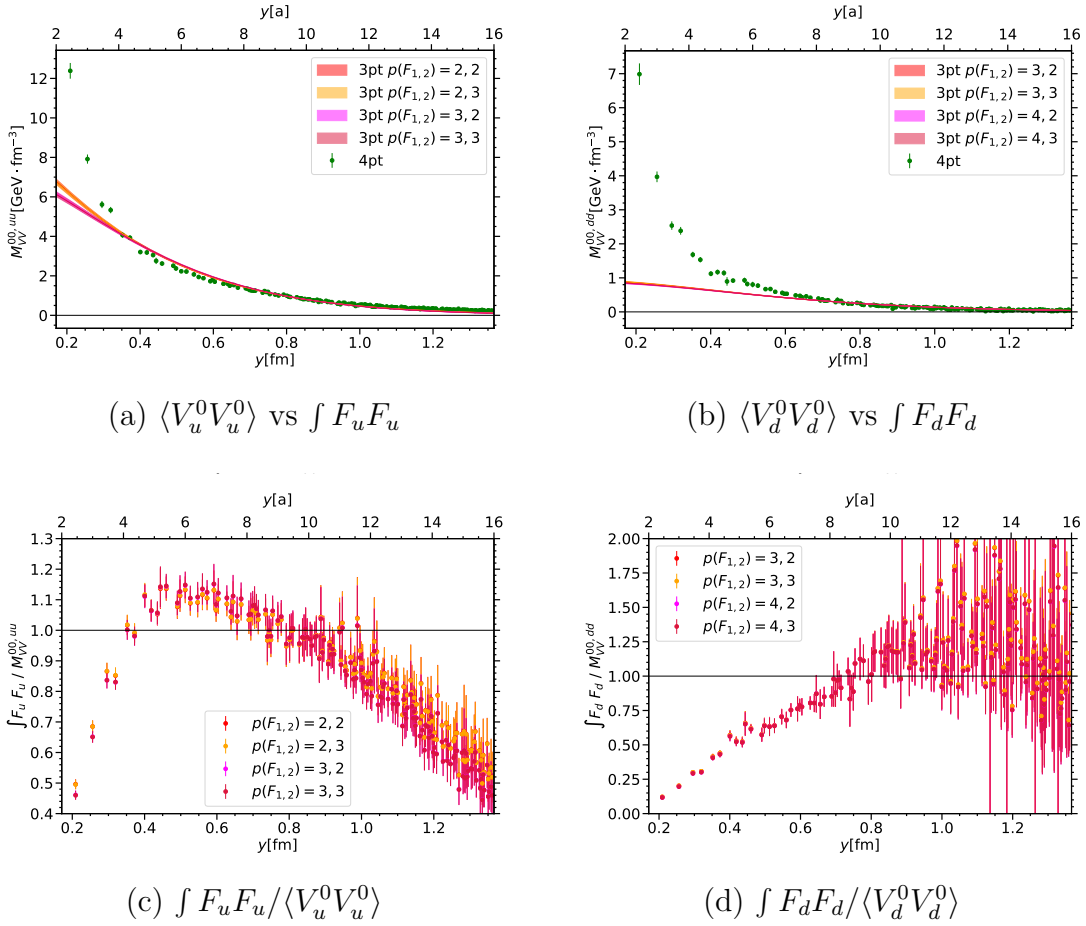

(a) $\langle V_u^0 V_u^0 \rangle$ vs $\int F_u F_u$

(b) $\langle V_d^0 V_d^0 \rangle$ vs $\int F_d F_d$

(c) $\int F_u F_u / \langle V_u^0 V_u^0 \rangle$

(d) $\int F_d F_d / \langle V_d^0 V_d^0 \rangle$

Figure 6.10: Comparison between $\langle V_u^0 V_u^0 \rangle$ and the corresponding convolution (6.19) (a). The same is shown for the matrix element $\langle V_d^0 V_d^0 \rangle$ (b). We plot the ratio of the convolution and the matrix element in (c) for $\langle V_u^0 V_u^0 \rangle$ and (d) for $\langle V_d^0 V_d^0 \rangle$.

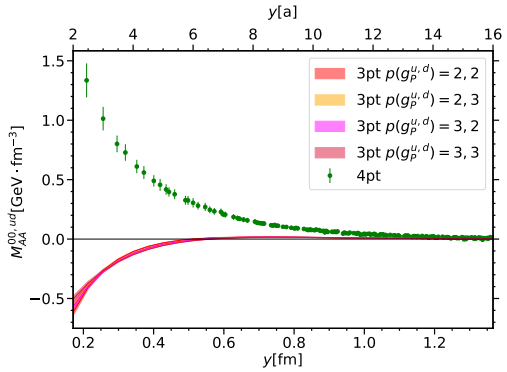

(a) $\langle A_u^0 A_d^0 \rangle$ vs $\int F_{\Delta u} F_{\Delta d}$, $p(g_A^{u,d}) = 2,2$

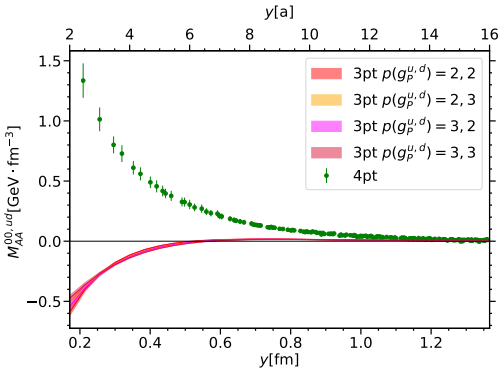

(b) $\langle A_u^0 A_d^0 \rangle$ vs $\int F_{\Delta u} F_{\Delta d}$, $p(g_A^{u,d}) = 3,3$

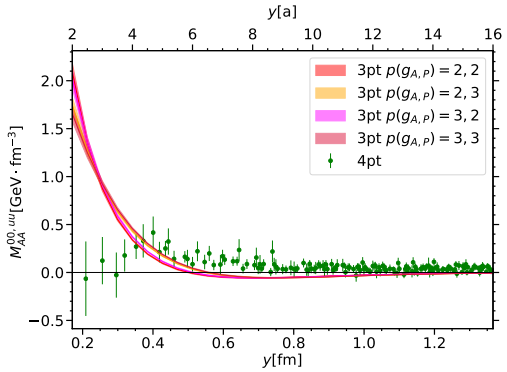

(c) $\langle A_u^0 A_u^0 \rangle$ vs $\int F_{\Delta u} F_{\Delta u}$

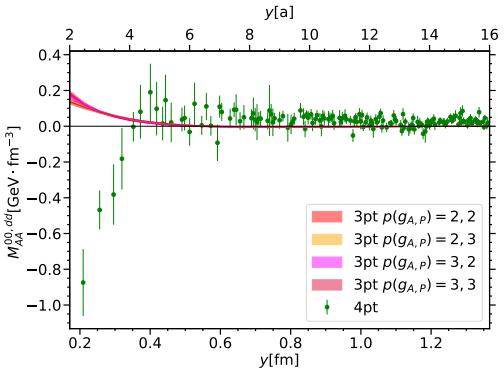

(d) $\langle A_d^0 A_d^0 \rangle$ vs $\int F_{\Delta d} F_{\Delta d}$

Figure 6.11: Comparison of the convolution (6.19) and the corresponding two-current matrix element for several parameterizations. This is plotted in (a,b) for $\langle A_u^0 A_d^0 \rangle$, as well as for $\langle A_u^0 A_u^0 \rangle$ (c) and $\langle A_d^0 A_d^0 \rangle$ (d).

7 Conclusions

A brief summary of the results being obtained in this thesis, as well as remarks on future perspectives regarding the research on DPDs on the lattice, shall be given in this chapter.
A general review on subjects regarding the hadronic structure has been given in chapter 2, where we also defined DPDs. The concept of LQCD was explained in chapter 3. In chapter 4 we defined hadronic matrix elements of two spatially separated local currents for the case of the proton, which can also be related to matrix elements for the neutron by isospin symmetry. These matrix elements have been found to be real-valued in the case of flavor conserving currents. In order to evaluate them on the lattice, we related the matrix elements to four-point functions. It has been found that there are five types of Wick contractions, which we call C_1, C_2, S_1, S_2 and D. The exact contraction depends on the quark flavor of the operators. For each contraction we derived an explicit expression to be calculated on the lattice. For a better overlap with the ground state we employed the momentum smearing technique. Moreover, stochastic propagators combined with the hopping parameter expansion have been used. Each contraction has been evaluated on 990 configurations on the H102 ensemble generated by the CLS collaboration. Here we took into account several proton momenta up to $\vec{p}^2 = 2.47\ \mathrm{GeV}^2$. With the exception of the D contraction, which yielded large error bars, we obtained clear signals for each contraction. The corresponding results have been presented in section 4.4. We analyzed anisotropy effects caused by mirror charges and the anisotropic behavior of the lattice propagator. It has been found that anisotropy effects are least significant close to the lattice diagonals. The corresponding data was used subsequently to evaluate the physical results. We observed dominance of the the connected contributions C_1 and C_2. In the case of the axial vector currents $\langle A^0 A^0 \rangle$ only C_1 for ud yielded a large signal. S_1 was found to be comparable with zero in all considered cases. The S_2 contraction is observed to steeply increase at small distances between the currents, whereas it is very small otherwise. For the matrix elements $\langle V^0 V^0 \rangle$ and $\langle A^0 A^0 \rangle$ we also calculated physically relevant sums of contractions, taking into account the contributions of C_1, C_2 and S_2. For $\langle V^0 V^0 \rangle$ we observed clear signals for all flavor combinations, where the uu and dd correlations become very large at small current distances. The data of $\langle A^0 A^0 \rangle$ was observed to be smaller and have been seen to be strongly dependent on the S_2 contribution for uu and dd.
Chapter 5 was concerned with the relation of the previously calculated two-current matrix elements with Mellin moments $I_{ab}(\zeta, \boldsymbol{y}^2)$ of DPDs. The corresponding twist-2 functions $A_{ab}(py, y^2)$ have been extracted by solving the defining system of equations in section 5.2. In order to obtain results for the Mellin moment themselves, the twist-2

data has been fitted to a suitable parameterization of the py-dependence. We varied the choices of parameters in order to get an estimate of the model dependence of the final results. It has turned out that in the cases where the data is not too small compared to the statistical error the results of the Mellin moments are quite robust w.r.t. to the choice of parameters. We analyzed the dependence of the twist-2 functions, as well as that of the extracted Mellin moments, on quark flavor and polarization. This was discussed in section 5.4. It was observed that uu and ud contributions dominate for large current distances, whereas uu and dd become very large if the distance is small. In particular, the considered flavor combinations showed marked differences in their $\boldsymbol{y}^2$ dependence, which is in contradiction to postulations that are made in order to derive the pocket formula (1.3). Polarization effects are prominent for ud, whereas they are small for other quark flavors. The largest contribution was found for the spin-orbit correlation $A_{q\delta q'}$ and the corresponding Mellin moment. Spin-spin correlations have been observed to be much smaller than predicted by simple quark model assumptions. In section section 5.5 we verified the consistence with the DPD number sum rule, which was well fulfilled within the statistical error.

An important aspect regarding the strength of quark-quark correlations has been investigated in chapter 6. For the local two-current matrix elements $\langle V^0 V^0 \rangle$ and $\langle A^0 A^0 \rangle$, as well as for the twist-2 functions A_{qq} and $A_{\Delta q \Delta q'}$, we derived a factorized expression involving only one-current matrix elements being related to nucleon form factors. This has been achieved by inserting a complete set of states between the two currents. Furthermore, we assumed that nucleon states dominate and neglected the remaining contributions. The form factor data has been generated in another simulation [110], its t-dependence was fitted to a p-pole function, where several integer values of p were taken in order to control the model dependence. The agreement of the convolution results with the two-current data was discussed in section 6.3. For the twist-2 functions we obtained values which were quite close to the two-current data. This was observed for A_{qq} and also $A_{\Delta q \Delta q'}$. The latter indicates that the two longitudinal quark spins are only correlated via spin correlations of each quark and the proton. The results regarding the factorization of a local matrix element were similar in the case of $\langle V^0 V^0 \rangle$, where the convolution result has the same order of magnitude as the corresponding two-current data. Deviations were seen to be large for small y for uu and dd. The situation is different for the case of two axial vector currents $\langle A^0 A^0 \rangle$, where the convolution did not reproduce the results of the two-current calculations.

Beyond this pilot study of quark correlations and DPDs in the nucleon, there remains a variety of aspects that have not been considered within this thesis, but are certainly interesting to be investigated in future research. Our calculations did not take into account operators containing derivatives. Including them would offer the possibility of analyzing higher Mellin moments, which would provide a first insight into the x_i-dependence of DPDs. Our study has been restricted to operators conserving the quark flavor. Matrix elements of flavor changing operators appear in contributions corresponding to flavor interference. There are further objects related to several kinds of interferences, like fermion number interference distributions. Although not accessible in

LHC experiments, it might be interesting to explore matrix elements of polarized nucleons in order to investigate the corresponding DPDs. The present study only includes the analysis for valence quark flavors of the proton, i.e. u or d. The CLS ensembles take into account $n_f = 3$ dynamic quark flavors, which basically allows a dynamical simulation of matrix elements of strange quark operators, and subsequently of non-valence quark DPDs. A general exploration of the quark mass dependence, as well as the investigation of possible excited state contributions by varying the source-sink separation, is still outstanding. Corresponding analyses have been performed for the pion in [45, 46]. So far our analysis includes only one gauge ensemble. Repeating the simulations on further ensembles is advisable for the following reasons. The calculation on ensembles employing finer and larger lattices would allow a more detailed study of discretization artifacts and finite volume effects. The final aim would be to take the physical limit, i.e. to decrease the masses and the lattice spacing towards the physical point.

A Appendix

A.1 Notations and conventions

Within this thesis, the following notations and conventions are used:

- We use natural units, i.e. Planck's constant and the speed of light are set to one:

$$\hbar = c = 1 \tag{A.1}$$

- Tensor component labeling: For Minkowski (Euclidean) spacetime the tensor components are labeled with Greek indices $(\mu, \nu, \lambda, ...)$, which run from 0 to d-1 (1 to d) with the 0-th (d-th) component being interpreted as the time component. Spatial or transverse components are labeled with Latin indices $(i, j, k, ...)$.

- Further index conventions: Spinor indices are labeled by $\alpha, \beta, \gamma, \ldots$, color indices by $a, b, c, \ldots$, not to be confused with the quark polarization channels, which are also labeled by $a, b, \ldots$.

- Symmetrization and antisymmetrization of indices: By writing square brackets we denote antisymmetrization of indices, by writing curly brackets we denote symmetrization of indices. In both cases a normalization factor $1/(n!)$ is included:

$$a^{[\mu_1 \ldots \mu_n]} = \frac{1}{n!} \sum_{P \in S_n} \text{sign}(P)\ a^{\mu_{P(1)} \cdots \nu_{P(n)}}\ , \tag{A.2}$$

$$a^{\{\mu_1 \ldots \mu_n\}} = \frac{1}{n!} \sum_{P \in S_n} a^{\mu_{P(1)} \cdots \nu_{P(n)}}\ . \tag{A.3}$$

- The Minkowski metric:

$$(g_{\mu\nu}) = \text{diag}(1, -1, -1, -1)\ . \tag{A.4}$$

- Euclidean Gamma matrices:

$$\gamma_E^4 = \begin{pmatrix} 0 & \mathbb{1}_2 \\ \mathbb{1}_2 & 0 \end{pmatrix}\ , \qquad \gamma_E^j = (-1)^j \begin{pmatrix} 0 & -i\sigma^j \\ i\sigma^j & 0 \end{pmatrix}\ , \tag{A.5}$$

where the σ^j are the Pauli matrices. This basis is chiral.
Furthermore we define the commutator of gamma matrices:

$$\sigma^{\mu\nu} = \frac{i}{2}\left[\gamma^\mu, \gamma^\nu\right] \ . \tag{A.6}$$

In the basis (A.5) we can give explicit definitions of the C (charge conjugation) and T (time reflection) matrix:

$$C = \gamma_2\gamma_4 \ , \qquad T = \gamma_1\gamma_3\gamma_4 \ . \tag{A.7}$$

- Kronecker-Delta and Levi-Civita-Symbol:

$$\delta^{ij} = \begin{cases} 1 & i = j \\ 0 & i \neq j \end{cases} \ , \tag{A.8}$$

$$\epsilon^{i_1\cdots i_n} = \begin{cases} 1 & i_1\cdots i_n \text{ even permutation of } 1\cdots n \\ -1 & i_1\cdots i_n \text{ odd permutation of } 1\cdots n \\ 0 & \text{else} \end{cases} \ . \tag{A.9}$$

- Einstein sum convention:

$$a_\mu b^\mu = \sum_{\mu=0(1)}^{d-1(d)} a_\mu b^\mu \ , \tag{A.10}$$

for any quantity a or b having d components labeled by μ in this case. The up-down notation may be dropped if there is no distinction between elements - dual elements, covariant - contravariant, etc.

- Feynman slash notation:

$$\not{a} = a_\mu\gamma^\mu \ . \tag{A.11}$$

- Notation for an arbitrary 4-vector x^μ:

$$(x^\mu) = (x^0, \vec{x}) \ , \tag{A.12}$$

where $x_0 = t$ is the time component and $\vec{x}$ represents the three space components. Sometimes we use light-cone coordinates:

$$(x^\mu) = \left(x^+, x^-, \boldsymbol{x}\right) \ , \quad x^\pm = \frac{x^0 \pm x^3}{\sqrt{2}} \ , \quad \boldsymbol{x} = \left(x^1, x^2\right) \ , \tag{A.13}$$

with the scalar product:

$$xy = x^\mu y_\mu = x^+ y^- + x^- y^+ - \boldsymbol{xy} \ . \tag{A.14}$$

Depending on the context, we use the following short notation for absolute values of 3-vectors $\vec{x}$ or transverse vectors $\boldsymbol{x}$, respectively:

$$x = |\vec{x}| \quad \text{or} \quad x = |\boldsymbol{x}| \ . \tag{A.15}$$

In order to avoid confusions, we denote powers of x by

$$(x)^n := |\vec{x}|^n \quad \text{or} \quad (x)^n := |\boldsymbol{x}|^n \ . \tag{A.16}$$

If $x^0 = 0$ or $x^+ = 0$, this is equivalent to

$$(x)^n := \sqrt{-x^\mu x_\mu}^{\,n} = \sqrt{-x^2}^{\,n} \ . \tag{A.17}$$

where $x^2 = -\vec{x}^2$ or $x^2 = -\boldsymbol{x}^2$, respectively.
A Euclidean vector has the form

$$x_E = (x_E^\mu) = (\vec{x}, x^4) \ . \tag{A.18}$$

- Lattice vectors: $\hat{\mu}$ denotes a vector that points from one lattice site to the next neighboring site in the μ-direction.

- Lattice propagators $M = \mathcal{D}^{-1}$ for a given Dirac operator $\mathcal{D}$: The propagator from point x to y is denoted by $M(y|x)$. For a point-to-all propagator from fixed x to y we write $M_x(y)$.
  In any case, the propagator carries two spinor and two color indices (sometimes not explicitly written).

- Unless stated otherwise, traces and transpositions are taken w.r.t. spinor and color indices, i.e. for an expression X carrying two spinor indices α, β and two color indices a, b we define

$$\mathrm{tr}\,\{X\} = X^{ab}_{\alpha\beta}\delta_{\alpha\beta}\delta_{ab} \ , \qquad \left(X^T\right)^{\alpha\beta}_{ab} = X^{\beta\alpha}_{ba} \ . \tag{A.19}$$

- Negative indices: In the context of LQCD we use negative Lorentz indices to abbreviate:

$$U_{-\mu}(x) = U_\mu^\dagger(x - \hat{\mu}) \ , \qquad \gamma_{-\mu} = -\gamma_\mu \ , \tag{A.20}$$

  for a gauge link $U_\mu(x)$ and a Dirac matrix γ_μ.

A.2 Wick contraction symmetries

We use the relations (3.34) to determine the behavior under discrete symmetry operations of the constituents (4.16) entering the expressions for lattice contractions of four-point functions. In the following, we consider $\mathcal{PT}$ transformations and the combination of complex conjugation and $\mathcal{CP}$ transformation. The relations are understood to be valid after integrating over the gauge fields:

$$\begin{aligned} K_1^i(z'|y|z) &\xrightarrow{\mathcal{PT}} \eta_{PT}^i \; S^{-1} \; K_1^{i,T}(-z|-y|-z') \; S \; , \\ \Big[K_1^i(z'|y|z)\Big]^* &\xrightarrow{\mathcal{CP}} \eta_{PT}^i \; \eta_4^i \; A^{-1} \; K_1^i(z'|y|z) \; A \; , \\ K_2^{ji}(z'|y|z) &\xrightarrow{\mathcal{PT}} \eta_{PT}^{ij} \; S^{-1} \; K_2^{ij,T}(-z|y|-z') \; S \; , \\ \Big[K_2^{ji}(z'|y|z)\Big]^* &\xrightarrow{\mathcal{CP}} \eta_{PT}^{ij} \; \eta_4^{ij} \; A^{-1} \; K_2^{ji}(z'|y|z) \; A \; . \end{aligned} \tag{A.21}$$

where

$$S := \gamma_4 T \qquad A := \gamma_4 C \gamma_5 \; , \tag{A.22}$$

and η_{PT}, η_4 are defined in (3.71) and (4.25), respectively. Considering the generic connected baryon contractions (4.14) we find for the nucleon:

$$\Big[G^{ijk}[X,Y,Z]\Big]^* \xrightarrow{\mathcal{CP}} G^{ijk}[\mathcal{CP}(X^*),\mathcal{CP}(Y^*),\mathcal{CP}(Z^*)] \; , \tag{A.23}$$

and, moreover

$$\begin{aligned} G^{ijk}[X,Y,Z] &\xrightarrow{\mathcal{PT}} G^{ijk}[\mathcal{PT}X,\mathcal{PT}Y,\mathcal{PT}Z] \quad \text{for } (ijk) = (123),(213) \; , \\ G^{ijk}[X,Y,Z] &\xrightarrow{\mathcal{PT}} G^{ijk}[\mathcal{PT}Z,\mathcal{PT}Y,\mathcal{PT}X] \quad \text{for } (ijk) = (321),(231) \; , \\ G^{ijk}[X,Y,Z] &\xrightarrow{\mathcal{PT}} G^{ijk}[\mathcal{PT}X,\mathcal{PT}Z,\mathcal{PT}Y] \quad \text{for } (ijk) = (132),(312) \; . \end{aligned} \tag{A.24}$$

A.3 Tensor Parameterizations

This is an overview of the tensor structures being used to decompose the two-current matrix elements, see (5.5). The structures are the same in the case of the vector-vector and axial-axial channel:

$$\begin{aligned} u_{VV,A}^{\mu\nu}(p,y) &:= 2p^\mu p^\nu - \frac{m^2}{2} g^{\mu\nu} \; , \\ u_{VV,B}^{\mu\nu}(p,y) &:= 2p^{\{\mu} y^{\nu\}} - \frac{py}{2} g^{\mu\nu} \; , \\ u_{VV,C}^{\mu\nu}(p,y) &:= 2y^\mu y^\nu - \frac{y^2}{2} g^{\mu\nu} \; . \end{aligned} \tag{A.25}$$

For the tensor-vector channel we have two tensor combinations:

$$\begin{aligned} u^{\mu\nu\rho}_{TV,A}(p,y) &:= 4y^{[\mu}p^{\nu]}p^{\rho} + \frac{4m^2}{3}g^{\rho[\mu}y^{\nu]} - \frac{4py}{3}g^{\rho[\mu}p^{\nu]} \ , \\ u^{\mu\nu\rho}_{TV,B}(p,y) &:= 4y^{[\mu}p^{\nu]}y^{\rho} + \frac{4py}{3}g^{\rho[\mu}y^{\nu]} - \frac{4y^2}{3}g^{\rho[\mu}p^{\nu]} \ . \end{aligned} \tag{A.26}$$

In the case of the tensor-tensor channel we have to consider five terms, where the corresponding tensor structures read[1]

$$\begin{aligned} u^{\mu\nu\rho\sigma}_{TT,A}(p,y) &:= -8p^{[\nu}g^{\mu][\rho}p^{\sigma]} \ , \\ u^{\mu\nu\rho\sigma}_{TT,B}(p,y) &:= -16y^{[\mu}p^{\nu]}y^{[\rho}p^{\sigma]} + 8y^2\ p^{[\nu}g^{\mu][\rho}p^{\sigma]} \ , \\ u^{\mu\nu\rho\sigma}_{TT,C}(p,y) &:= -4p^{[\nu}g^{\mu][\rho}y^{\sigma]} - 4y^{[\nu}g^{\mu][\rho}p^{\sigma]} \ , \\ u^{\mu\nu\rho\sigma}_{TT,D}(p,y) &:= -8y^{[\nu}g^{\mu][\rho}y^{\sigma]} \ , \\ u^{\mu\nu\rho\sigma}_{TT,E}(p,y) &:= 2g^{\mu[\rho}g^{\sigma]\nu} \ . \end{aligned} \tag{A.27}$$

For brevity we use the symmetrization or anti-symmetrization notation of indices being introduced in section A.1.

A.4 Fourier transform $h_n(x)$ of polynomial terms

Let $F(\zeta)$ be a function defined as follows:

$$F(\zeta) = \begin{cases} \sum_{n=0}^{N} a_n \zeta^{2n} & |\zeta| \leq 1 \\ 0 & |\zeta| > 1 \end{cases} \ , \tag{A.28}$$

$$\sum_{n=0}^{N} a_n = 0 \ \Leftrightarrow F(\zeta) \text{ continuous at } |\zeta| = 1. \tag{A.29}$$

For the n-th term of the sum above, the Fourier transform may be obtained by partial integration:

$$\begin{aligned} \frac{1}{2}\int_{-1}^{1} \mathrm{d}\zeta e^{ix\zeta}\zeta^{2n} &= (\sin(x)s_n(x) + \cos(x)c_n(x)) \\ &=: h_n(x) \ , \end{aligned} \tag{A.30}$$

[1] Compared to the definition we give in this thesis, the definition in [46] includes a shift w.r.t. trace terms ($\propto g^{\mu[\rho}g^{\sigma]\nu}$), i.e. the invariant function E is not the same in the two cases.

with

$$\begin{aligned} s_n(x) &:= (2n)! \sum_{m=0}^{n} \frac{(-1)^m}{(2n-2m)!\; x^{1+2m}} \ , \\ c_n(x) &:= (2n)! \sum_{m=0}^{n-1} \frac{(-1)^m}{(2n-2m-1)!\; x^{2+2m}} \ . \end{aligned} \tag{A.31}$$

The limit $x \to 0$ for $h_n(x)$ yields:

$$\lim_{x\to 0} h_n(x) = \frac{1}{1+2n} \ . \tag{A.32}$$

For the second derivative of $h_n(x)$ it holds that:

$$\frac{\partial^2}{\partial x^2} h_n(x) = -h_{n+1}(x) \ , \tag{A.33}$$

which can be easily found by applying the derivatives before performing the Fourier transformation. The same can be done for the first derivative, where one finds:

$$\frac{\partial}{\partial x} h_n(x) = \frac{1}{2(n+1)} \left(x h_{n+1}(x) - \sin(x) \right) \ . \tag{A.34}$$

Combining (A.34) with (A.33) and integrating yields the differential equation:

$$(2n+1) h_n(x) + x \frac{\partial}{\partial x} h_n(x) = \cos(x) \ . \tag{A.35}$$

Moreover we can give an explicit form of the Taylor expansion of $h_n(x)$ around $x = 0$ by using (A.32) in (A.33):

$$h_n(x) = \sum_{m=0}^{N} \frac{(-1)^m x^{2m}}{(2m)!(1+2n+2m)} + \mathcal{O}\left(x^{2N+1}\right) \ , \tag{A.36}$$

such that $h_n(x)$ can also be written as:

$$h_n(x) = \sum_{m=0}^{\infty} \frac{(-1)^m x^{2m}}{(2m)!(1+2n+2m)} \ . \tag{A.37}$$

Notice that $\frac{1+2n}{2} h_n(x)$ can be identified with the hypergeometric function ${}_1F_2(\frac{1}{2}+n; \frac{1}{2}, \frac{3}{2}+n; -\frac{x^2}{2})$.

A.5 Statistical analysis

For a consistent treatment of error propagation in observables created from strongly correlated data we employ the Jackknife method. Let us assume that we have N measurements $\mathcal{O}_j$ of an observable $\mathcal{O}$. These measurements are resampled in the following way:

$$c_i = \frac{1}{(N-1)} \sum_{j \neq i} \mathcal{O}_j \ . \tag{A.38}$$

The mean value is given by:

$$\overline{c} = \frac{1}{N} \sum_i c_i = \frac{1}{N} \sum_i \mathcal{O}_i = \langle \mathcal{O} \rangle \ , \tag{A.39}$$

with variance:

$$\sigma^2 = \frac{N-1}{N} \sum_i (\overline{c} - c_i)^2 \ . \tag{A.40}$$

For a derived quantity $f(\mathcal{O})$ with mean $f(\overline{c})$ the variance is written as:

$$\sigma^2 = \frac{N-1}{N} \sum_i (f(\overline{c}) - f(c_i))^2 \ . \tag{A.41}$$

Notice that in general $f(\overline{c}) \neq \sum_i f(c_i)$, non-vanishing differences indicate a bias.

A.6 Fitting methods

In the following, we review the standard method of χ^2 minimization being used to fit the data obtained from our simulations by a certain function or system of functions.

A.6.1 χ^2 minimization

Let X_i be a data point of an observable X with mean $\langle X_i \rangle$ and variance σ_i^2 at position i and f the desired functional description of this observable depending on fit parameters collected in the vector $\vec{A}$. An optimal description of the data is obtained if

$$\chi^2(\vec{A}) = \sum_{ij} \left(f_i(\vec{A}) - X_i \right) \left(C^{-1} \right)_{ij} \left(f_j(\vec{A}) - X_j \right) \tag{A.42}$$

is minimal. C is the covariance matrix

$$C_{ij} = \langle (X_i - \langle X_i \rangle)(X_j - \langle X_j \rangle) \rangle \ . \tag{A.43}$$

Neglecting off-diagonal elements, i.e. correlations between the data points, we obtain a diagonal matrix where the entries are given by the variance $C_{ij} = \delta_{ij}\sigma_i^2$ of the corresponding data point. Hence:

$$\chi^2(\vec{A}) = \sum_i \frac{\left(f_i(\vec{A}) - X_i\right)^2}{\sigma_i^2} \ . \tag{A.44}$$

For all non-linear problems in our analysis we used the MIGRAD method of Minuit[117] for χ^2 minimization.

A.6.2 Linear fits and equation systems

A special case of χ^2 minimization described above is given if the dependence on the fit parameters A_j is purely linear. This might be e.g. the solution of an overdetermined linear system of equations, which is determined by a fit. We consider data points X_i, which are supposed to be fitted to a function of the form

$$X_i = \sum_j a_{ij} A_j \ , \tag{A.45}$$

where a_{ij} are known coefficients. The χ^2 (A.44) can be written as:

$$\chi^2 = \sum_i \sigma_i^{-2} \left[\sum_j a_{ij} A_j - X_i\right]^2 \ , \tag{A.46}$$

and the χ^2 minimization problem translates to requiring the gradient w.r.t. to the fit variables A_j to vanish:

$$\frac{\partial \chi^2}{\partial A_k} = 2 \sum_i \sigma_i^{-2} \left[\sum_j a_{ij} A_j - X_i\right] a_{ik} \stackrel{!}{=} 0 \ . \tag{A.47}$$

This is equivalent to

$$\sum_j \alpha_{kj} A_j = \gamma_k \ , \tag{A.48}$$

with the matrix α:

$$\alpha_{kj} = \sum_i \sigma_i^{-2} a_{ij} a_{ik} \ , \tag{A.49}$$

and the source vector γ:

$$\gamma_k = \sum_i \sigma_i^{-2} X_i a_{ik} \ . \tag{A.50}$$

Hence, an overdetermined linear equation system (A.45) can be fitted by inverting α on γ

$$\alpha A = \gamma \ , \tag{A.51}$$

yielding the solution A, where the components are the fit parameters A_j. Two special cases should be considered at this point: The case of fitting the data $X(y)$ to a linear function $f(y) = ay + b$, where α and γ take the form:

$$\alpha = \sum_i \sigma_i^{-2} \begin{pmatrix} y_i^2 & y_i \\ y_i & 1 \end{pmatrix} \ , \qquad \gamma = \sum_i \sigma_i^{-2} X(y_i) \begin{pmatrix} y_i \\ 1 \end{pmatrix} \ . \tag{A.52}$$

The second and most trivial case is that of a fit to constant c. Here the equation (A.51) reduces to

$$c = \frac{\sum_i \sigma_i^{-2} X(y_i)}{\sum_i \sigma_i^{-2}} \ . \tag{A.53}$$

List of Figures

List of Tables

Acronyms

BSM beyond the Standard Model

DDY double Drell-Yan

DGLAP Dokshitzer Gribow Lipatow Altarelli Parisi

DIS deep inelastic scattering

DPD double parton distribution

DPS double parton scattering

DVCS deeply virtual Compton scattering

DY Drell-Yan

EIC Electron Ion Collider

FF form factor

GFF generalized form factor

GPD generalized parton distribution

HMC hybrid Monte Carlo

HPE hopping parameter expansion

LHC Large Hadron Collider

LQCD lattice QCD

OFPD off-forward parton distribution

OPE operator product expansion

PDF parton distribution function

QCD Quantum Chromodynamics

RHIC Relativistic Heavy Ion Collider

RHMC rational HMC

SIDIS semi-inclusive DIS

SM Standard Model

SPS single parton scattering

TMD transverse momentum dependent

Bibliography

[1] Christine A. Aidala et al. “The Spin Structure of the Nucleon”. In: *Rev. Mod. Phys.* 85 (2013), pp. 655–691. arXiv: 1209.2803 [hep-ph].

[2] A. Accardi et al. “Electron Ion Collider: The Next QCD Frontier: Understanding the glue that binds us all”. In: *Eur. Phys. J. A* 52.9 (2016). Ed. by A. Deshpande, Z.E. Meziani, and J.W. Qiu, p. 268. arXiv: 1212.1701 [nucl-ex].

[3] Serguei Chatrchyan et al. “Observation of a New Boson at a Mass of 125 GeV with the CMS Experiment at the LHC”. In: *Phys. Lett. B* 716 (2012), pp. 30–61. arXiv: 1207.7235 [hep-ex].

[4] Georges Aad et al. “Observation of a new particle in the search for the Standard Model Higgs boson with the ATLAS detector at the LHC”. In: *Phys. Lett. B* 716 (2012), pp. 1–29. arXiv: 1207.7214 [hep-ex].

[5] Mieczyslaw Witold Krasny and Wieslaw Placzek. “On the contribution of the double Drell-Yan process to WW and ZZ production at the LHC”. In: *Acta Phys. Polon. B* 47 (2016), pp. 1045–1056. arXiv: 1501.04569 [hep-ph].

[6] S.D. Drell and Tung-Mow Yan. “Massive Lepton Pair Production in Hadron-Hadron Collisions at High-Energies”. In: *Phys. Rev. Lett.* 25 (1970). [Erratum: Phys.Rev.Lett. 25, 902 (1970)], pp. 316–320.

[7] Jun Gao, Lucian Harland-Lang, and Juan Rojo. “The Structure of the Proton in the LHC Precision Era”. In: *Phys. Rept.* 742 (2018), pp. 1–121. arXiv: 1709.04922 [hep-ph].

[8] Huey-Wen Lin et al. “Parton distributions and lattice QCD calculations: a community white paper”. In: *Prog. Part. Nucl. Phys.* 100 (2018), pp. 107–160. arXiv: 1711.07916 [hep-ph].

[9] T. Åkesson et al. “Double Parton Scattering in pp Collisions at $\sqrt{s} = 63$-GeV”. In: *Z. Phys. C* 34 (1987), p. 163.

[10] J. Alitti et al. “A Study of multi - jet events at the CERN anti-p p collider and a search for double parton scattering”. In: *Phys. Lett. B* 268 (1991), pp. 145–154.

[11] F. Abe et al. “Study of four jet events and evidence for double parton interactions in $p\bar{p}$ collisions at $\sqrt{s} = 1.8$ TeV”. In: *Phys. Rev. D* 47 (1993), pp. 4857–4871.

[12] F. Abe et al. “Measurement of double parton scattering in $\bar{p}p$ collisions at $\sqrt{s} = 1.8$ TeV”. In: *Phys. Rev. Lett.* 79 (1997), pp. 584–589.

[13] F. Abe et al. “Double parton scattering in $\bar{p}p$ collisions at $\sqrt{s} = 1.8$TeV”. In: *Phys. Rev. D* 56 (1997), pp. 3811–3832.

[14] V.M. Abazov et al. "Double parton interactions in γ+3 jet events in pp^- bar collisions $\sqrt{s} = 1.96$ TeV." In: *Phys. Rev. D* 81 (2010), p. 052012. arXiv: 0912.5104 [hep-ex].

[15] R Aaij et al. "Observation of double charm production involving open charm in pp collisions at $\sqrt{s} = 7$ TeV". In: *JHEP* 06 (2012). [Addendum: JHEP 03, 108 (2014)], p. 141. arXiv: 1205.0975 [hep-ex].

[16] Georges Aad et al. "Measurement of hard double-parton interactions in $W(\rightarrow l\nu)$+ 2 jet events at $\sqrt{s}$=7 TeV with the ATLAS detector". In: *New J. Phys.* 15 (2013), p. 033038. arXiv: 1301.6872 [hep-ex].

[17] Serguei Chatrchyan et al. "Study of Double Parton Scattering Using W + 2-Jet Events in Proton-Proton Collisions at $\sqrt{s} = 7$ TeV". In: *JHEP* 03 (2014), p. 032. arXiv: 1312.5729 [hep-ex].

[18] Morad Aaboud et al. "Study of hard double-parton scattering in four-jet events in pp collisions at $\sqrt{s} = 7$ TeV with the ATLAS experiment". In: *JHEP* 11 (2016), p. 110. arXiv: 1608.01857 [hep-ex].

[19] Victor Mukhamedovich Abazov et al. "Double Parton Interactions in $\gamma + 3$ Jet and $\gamma + b/cjet + 2$ Jet Events in $p\bar{p}$ Collisions at $\sqrt{s} = 1.96$ TeV". In: *Phys. Rev. D* 89.7 (2014), p. 072006. arXiv: 1402.1550 [hep-ex].

[20] Georges Aad et al. "Observation and measurements of the production of prompt and non-prompt J/ψ mesons in association with a Z boson in pp collisions at $\sqrt{s} = 8$ TeV with the ATLAS detector". In: *Eur. Phys. J. C* 75.5 (2015), p. 229. arXiv: 1412.6428 [hep-ex].

[21] Roel Aaij et al. "Production of associated Y and open charm hadrons in pp collisions at $\sqrt{s} = 7$ and 8 TeV via double parton scattering". In: *JHEP* 07 (2016), p. 052. arXiv: 1510.05949 [hep-ex].

[22] Victor Mukhamedovich Abazov et al. "Study of double parton interactions in diphoton + dijet events in $p\bar{p}$ collisions at $\sqrt{s} = 1.96$ TeV". In: *Phys. Rev. D* 93.5 (2016), p. 052008. arXiv: 1512.05291 [hep-ex].

[23] Roel Aaij et al. "Measurement of the J/ψ pair production cross-section in pp collisions at $\sqrt{s} = 13$ TeV". In: *JHEP* 06 (2017). [Erratum: JHEP 10, 068 (2017)], p. 047. arXiv: 1612.07451 [hep-ex].

[24] Albert M Sirunyan et al. "Constraints on the double-parton scattering cross section from same-sign W boson pair production in proton-proton collisions at $\sqrt{s} = 8$ TeV". In: *JHEP* 02 (2018), p. 032. arXiv: 1712.02280 [hep-ex].

[25] Victor Mukhamedovich Abazov et al. "Observation and Studies of Double J/ψ Production at the Tevatron". In: *Phys. Rev. D* 90.11 (2014), p. 111101. arXiv: 1406.2380 [hep-ex].

[26] Victor Mukhamedovich Abazov et al. "Evidence for simultaneous production of J/ψ and Υ mesons". In: *Phys. Rev. Lett.* 116.8 (2016), p. 082002. arXiv: 1511.02428 [hep-ex].

[27] Morad Aaboud et al. "Measurement of the prompt J/ ψ pair production cross-section in pp collisions at $\sqrt{s} = 8$ TeV with the ATLAS detector". In: *Eur. Phys. J. C* 77.2 (2017), p. 76. arXiv: 1612.02950 [hep-ex].

[28] Morad Aaboud et al. "Study of the hard double-parton scattering contribution to inclusive four-lepton production in *pp* collisions at $\sqrt{s} = 8$ TeV with the ATLAS detector". In: *Phys. Lett.* 790 (2019), p. 595. arXiv: 1811.11094 [hep-ex].

[29] Anna Kulesza and W.James Stirling. "Like sign W boson production at the LHC as a probe of double parton scattering". In: *Phys. Lett. B* 475 (2000), pp. 168–175. arXiv: hep-ph/9912232.

[30] Jonathan R. Gaunt et al. "Same-sign W pair production as a probe of double parton scattering at the LHC". In: *Eur. Phys. J. C* 69 (2010), pp. 53–65. arXiv: 1003.3953 [hep-ph].

[31] Federico Alberto Ceccopieri, Matteo Rinaldi, and Sergio Scopetta. "Parton correlations in same-sign W pair production via double parton scattering at the LHC". In: *Phys. Rev. D* 95.11 (2017), p. 114030. arXiv: 1702.05363 [hep-ph].

[32] P. Bartalini et al. "Multi-Parton Interactions at the LHC". In: Nov. 2011. arXiv: 1111.0469 [hep-ph].

[33] Hsi-Ming Chang, Aneesh V. Manohar, and Wouter J. Waalewijn. "Double Parton Correlations in the Bag Model". In: *Phys. Rev.* D87.3 (2013), p. 034009. arXiv: 1211.3132 [hep-ph].

[34] M. Rinaldi, S. Scopetta, and V. Vento. "Double parton correlations in constituent quark models". In: *Phys. Rev.* D87 (2013), p. 114021. arXiv: 1302.6462 [hep-ph].

[35] Wojciech Broniowski and Enrique Ruiz Arriola. "Valence double parton distributions of the nucleon in a simple model". In: *Few Body Syst.* 55 (2014), pp. 381–387. arXiv: 1310.8419 [hep-ph].

[36] Matteo Rinaldi et al. "Double parton correlations and constituent quark models: a Light Front approach to the valence sector". In: *JHEP* 12 (2014), p. 028. arXiv: 1409.1500 [hep-ph].

[37] Matteo Rinaldi et al. "Correlations in Double Parton Distributions: Perturbative and Non-Perturbative effects". In: *JHEP* 10 (2016), p. 063. arXiv: 1608.02521 [hep-ph].

[38] Matteo Rinaldi and Federico Alberto Ceccopieri. "Relativistic effects in model calculations of double parton distribution function". In: *Phys. Rev.* D95.3 (2017), p. 034040. arXiv: 1611.04793 [hep-ph].

[39] Tomas Kasemets and Asmita Mukherjee. "Quark-gluon double parton distributions in the light-front dressed quark model". In: *Phys. Rev.* D94.7 (2016), p. 074029. arXiv: 1606.05686 [hep-ph].

[40] Wojciech Broniowski, Enrique Ruiz Arriola, and Krzysztof Golec-Biernat. "Generalized Valon Model for Double Parton Distributions". In: *Few Body Syst.* 57.6 (2016), pp. 405–410. arXiv: 1602.00254 [hep-ph].

[41] Matteo Rinaldi et al. "A model calculation of double parton distribution functions of the pion". In: *Eur. Phys. J.* C78.9 (2018), p. 781. arXiv: 1806.10112 [hep-ph].

[42] Wojciech Broniowski and Enrique Ruiz Arriola. "Double parton distribution of valence quarks in the pion in chiral quark models". In: *Phys. Rev.* D101.1 (2020), p. 014019. arXiv: 1910.03707 [hep-ph].

[43] Aurore Courtoy, Santiago Noguera, and Sergio Scopetta. "Double parton distributions in the pion in the Nambu–Jona-Lasinio model". In: *JHEP* 12 (2019), p. 045. arXiv: 1909.09530 [hep-ph].

[44] Christian Zimmermann. "Double Parton Distributions of the Pion". In: *PoS* LATTICE2016 (2016), p. 152. arXiv: 1701.05479 [hep-lat].

[45] Gunnar S. Bali et al. "Two-current correlations in the pion on the lattice". In: *JHEP* 12 (2018), p. 061. arXiv: 1807.03073 [hep-lat].

[46] Gunnar S. Bali et al. "Double parton distributions in the pion from lattice QCD". In: (June 2020). arXiv: 2006.14826 [hep-lat].

[47] Christian Zimmermann. "Two-current correlations and DPDs for the nucleon on the lattice". In: *PoS* LATTICE2019 (Nov. 2019), p. 040. arXiv: 1911.05051 [hep-lat].

[48] Michael E. Peskin and Daniel V. Schroeder. *An Introduction to quantum field theory*. Reading, USA: Addison-Wesley, 1995. ISBN: 9780201503975, 0201503972. URL: http://www.slac.stanford.edu/~mpeskin/QFT.html.

[49] David Griffiths. *Introduction to elementary particles*. 2008. ISBN: 978-3-527-40601-2.

[50] M. Tanabashi et al. "Review of Particle Physics". In: *Phys. Rev. D* 98.3 (2018), p. 030001.

[51] Matthias Burkardt. "Light front quantization". In: *Adv. Nucl. Phys.* 23 (1996), pp. 1–74. arXiv: hep-ph/9505259.

[52] M. Burkardt and B. Pasquini. "Modelling the nucleon structure". In: *Eur. Phys. J. A* 52.6 (2016), p. 161. arXiv: 1510.02567 [hep-ph].

[53] Markus Diehl. "Introduction to GPDs and TMDs". In: *Eur. Phys. J.* A52.6 (2016), p. 149. arXiv: 1512.01328 [hep-ph].

[54] Markus Diehl and Thierry Gousset. "Time ordering in off diagonal parton distributions". In: *Phys. Lett. B* 428 (1998), pp. 359–370. arXiv: hep-ph/9801233.

[55] Markus Diehl, Daniel Ostermeier, and Andreas Schäfer. "Elements of a theory for multiparton interactions in QCD". In: *JHEP* 03 (2012). [Erratum: JHEP03,001(2016)], p. 089. arXiv: 1111.0910 [hep-ph].

[56] Robert L. Jaffe. "Spin, twist and hadron structure in deep inelastic processes". In: *Ettore Majorana International School of Nucleon Structure: 1st Course: The Spin Structure of the Nucleon*. Jan. 1996, pp. 42–129. arXiv: hep-ph/9602236.

[57] C.J. Bomhof, P.J. Mulders, and F. Pijlman. "The Construction of gauge-links in arbitrary hard processes". In: *Eur. Phys. J. C* 47 (2006), pp. 147–162. arXiv: hep-ph/0601171.

[58] M. Diehl. "Generalized parton distributions". In: *Phys. Rept.* 388 (2003), pp. 41–277. arXiv: hep-ph/0307382 [hep-ph].

[59] Xiang-Dong Ji. "Off forward parton distributions". In: *J. Phys.* G24 (1998), pp. 1181–1205. arXiv: hep-ph/9807358 [hep-ph].

[60] Gerald A. Miller. "Charge Density of the Neutron". In: *Phys. Rev. Lett.* 99 (2007), p. 112001. arXiv: 0705.2409 [nucl-th].

[61] Markus Diehl and Jonathan R. Gaunt. "Double parton scattering theory overview". In: vol. 29. 2019, pp. 7–28. arXiv: 1710.04408 [hep-ph].

[62] Jonathan R. Gaunt and W. James Stirling. "Double Parton Distributions Incorporating Perturbative QCD Evolution and Momentum and Quark Number Sum Rules". In: *JHEP* 03 (2010), p. 005. arXiv: 0910.4347 [hep-ph].

[63] Markus Diehl, P. Plößl, and A. Schäfer. "Proof of sum rules for double parton distributions in QCD". In: *Eur. Phys. J.* C79.3 (2019), p. 253. arXiv: 1811.00289 [hep-ph].

[64] Markus Diehl et al. "Cancellation of Glauber gluon exchange in the double Drell-Yan process". In: *JHEP* 01 (2016), p. 076. arXiv: 1510.08696 [hep-ph].

[65] Ted C. Rogers and Piet J. Mulders. "No Generalized TMD-Factorization in Hadro-Production of High Transverse Momentum Hadrons". In: *Phys. Rev. D* 81 (2010), p. 094006. arXiv: 1001.2977 [hep-ph].

[66] Aneesh V. Manohar and Wouter J. Waalewijn. "A QCD Analysis of Double Parton Scattering: Color Correlations, Interference Effects and Evolution". In: *Phys. Rev. D* 85 (2012), p. 114009. arXiv: 1202.3794 [hep-ph].

[67] Kenneth G. Wilson. "Confinement of Quarks". In: *Phys. Rev.* D10 (1974). [,45(1974); ,319(1974)], pp. 2445–2459.

[68] Christof Gattringer and Christian B. Lang. "Quantum chromodynamics on the lattice". In: *Lect. Notes Phys.* 788 (2010), pp. 1–343.

[69] Rajan Gupta. "Introduction to lattice QCD: Course". In: *Les Houches Summer School in Theoretical Physics, Session 68: Probing the Standard Model of Particle Interactions*. July 1997, pp. 83–219. arXiv: hep-lat/9807028.

[70] Holger Bech Nielsen and M. Ninomiya. "No Go Theorem for Regularizing Chiral Fermions". In: *Phys. Lett.* 105B (1981), pp. 219–223.

[71] Peter Hasenfratz and Moritz Bissegger. "CP, T and CPT in the non-perturbative formulation of chiral gauge theories". In: *Phys. Lett. B* 613 (2005), pp. 57–60. arXiv: hep-lat/0501010.

[72] B. Sheikholeslami and R. Wohlert. "Improved Continuum Limit Lattice Action for QCD with Wilson Fermions". In: *Nucl. Phys.* B259 (1985), p. 572.

[73] John Bulava and Stefan Schaefer. "Improvement of N_f=3 lattice QCD with Wilson fermions and tree-level improved gauge action". In: *Nucl. Phys. B* 874 (2013), pp. 188–197. arXiv: 1304.7093 [hep-lat].

[74] M. Luscher and P. Weisz. "On-Shell Improved Lattice Gauge Theories". In: *Commun. Math. Phys.* 97 (1985). [Erratum: Commun. Math. Phys.98,433(1985)], p. 59.

[75] S. Duane et al. "Hybrid Monte Carlo". In: *Phys. Lett.* B195 (1987), pp. 216–222.

[76] Mattia Bruno et al. "Simulation of QCD with $N_f = 2 + 1$ flavors of non-perturbatively improved Wilson fermions". In: *JHEP* 02 (2015), p. 043. arXiv: 1411.3982 [hep-lat].

[77] Martin Luscher and Filippo Palombi. "Fluctuations and reweighting of the quark determinant on large lattices". In: *PoS* LATTICE2008 (2008), p. 049. arXiv: 0810.0946 [hep-lat].

[78] Thomas A. DeGrand. "A Conditioning Technique for Matrix Inversion for Wilson Fermions". In: *Comput. Phys. Commun.* 52 (1988), pp. 161–164.

[79] A. D. Kennedy, Ivan Horvath, and Stefan Sint. "A New exact method for dynamical fermion computations with nonlocal actions". In: *Nucl. Phys. Proc. Suppl.* 73 (1999). [,834(1998)], pp. 834–836. arXiv: hep-lat/9809092 [hep-lat].

[80] C. Best et al. "Pion and rho structure functions from lattice QCD". In: *Phys. Rev. D* 56 (1997), pp. 2743–2754. arXiv: hep-lat/9703014.

[81] G. Martinelli et al. "A General method for nonperturbative renormalization of lattice operators". In: *Nucl. Phys.* B445 (1995), pp. 81–108. arXiv: hep-lat/9411010 [hep-lat].

[82] M. Gockeler et al. "Nonperturbative renormalization of composite operators in lattice QCD". In: *Nucl. Phys. B* 544 (1999), pp. 699–733. arXiv: hep-lat/9807044.

[83] K. Barad, M. Ogilvie, and C. Rebbi. "Quark - Anti-quark Charge Distributions and Confinement". In: *Phys. Lett. B* 143 (1984), pp. 222–226.

[84] K. Barad, M. Ogilvie, and C. Rebbi. "QUARK - ANTI-QUARK CHARGE DISTRIBUTIONS". In: *Annals Phys.* 168 (1986), p. 284.

[85] Walter Wilcox and Keh-Fei Liu. "Charge Radii From Lattice Relative Charge Distributions". In: *Phys. Lett. B* 172 (1986), p. 62.

[86] Walter Wilcox et al. "Relative Charge Distributions for Quarks in Lattice Mesons". In: *Phys. Rev. D* 34 (1986), p. 3882.

[87] Walter Wilcox. “Current overlap methods in lattice QCD”. In: *Phys. Rev. D* 43 (1991), pp. 2443–2446.

[88] M. Burkardt, J.M. Grandy, and John W. Negele. “Calculation and interpretation of hadron correlation functions in lattice QCD”. In: *Annals Phys.* 238 (1995), pp. 441–472. arXiv: `hep-lat/9406009`.

[89] M.C. Chu, Marcello Lissia, and John W. Negele. “Hadron structure in lattice QCD. 1. Correlation functions and wave functions”. In: *Nucl. Phys. B* 360 (1991), pp. 31–66.

[90] Marcello Lissia et al. “Comparison of hadron quark distributions from lattice QCD and the MIT bag model”. In: *Nucl. Phys. A* 555 (1993), pp. 272–292.

[91] C. Alexandrou, P. de Forcrand, and A. Tsapalis. “Probing hadron wave functions in lattice QCD”. In: *Phys. Rev. D* 66 (2002), p. 094503. arXiv: `hep-lat/0206026`.

[92] C. Alexandrou, P. de Forcrand, and A. Tsapalis. “The Matter and the pseudoscalar densities in lattice QCD”. In: *Phys. Rev. D* 68 (2003), p. 074504. arXiv: `hep-lat/0307009`.

[93] Constantia Alexandrou and Giannis Koutsou. “A Study of Hadron Deformation in Lattice QCD”. In: *Phys. Rev. D* 78 (2008), p. 094506. arXiv: `0809.2056 [hep-lat]`.

[94] Raza Sabbir Sufian et al. “Pion Valence Quark Distribution from Matrix Element Calculated in Lattice QCD”. In: *Phys. Rev.* D99.7 (2019), p. 074507. arXiv: `1901.03921 [hep-lat]`.

[95] Meinulf Göckeler. *private communication.*

[96] Gunnar S. Bali et al. “Novel quark smearing for hadrons with high momenta in lattice QCD”. In: *Phys. Rev.* D93.9 (2016), p. 094515. arXiv: `1602.05525 [hep-lat]`.

[97] S. Gusken et al. “Nonsinglet Axial Vector Couplings of the Baryon Octet in Lattice QCD”. In: *Phys. Lett.* B227 (1989), pp. 266–269.

[98] M. Falcioni et al. “AGAIN ON SU(3) GLUEBALL MASS”. In: *Nucl. Phys.* B251 (1985), pp. 624–632.

[99] Gunnar S. Bali, Sara Collins, and Andreas Schäfer. “Effective noise reduction techniques for disconnected loops in Lattice QCD”. In: *Comput. Phys. Commun.* 181 (2010), pp. 1570–1583. arXiv: `0910.3970 [hep-lat]`.

[100] Benjamin Gläßle. *private communication.*

[101] G. Martinelli and Christopher T. Sachrajda. “A Lattice Study of Nucleon Structure”. In: *Nucl. Phys.* B316 (1989), pp. 355–372.

[102] Robert G. Edwards and Balint Joo. “The Chroma software system for lattice QCD”. In: *Nucl. Phys. Proc. Suppl.* 140 (2005). [,832(2004)], p. 832. arXiv: `hep-lat/0409003 [hep-lat]`.

[103] R. Babich et al. “Adaptive multigrid algorithm for the lattice Wilson-Dirac operator”. In: *Phys. Rev. Lett.* 105 (2010), p. 201602. arXiv: 1005.3043 [hep-lat].

[104] Andreas Frommer et al. “Adaptive Aggregation Based Domain Decomposition Multigrid for the Lattice Wilson Dirac Operator”. In: *SIAM J. Sci. Comput.* 36 (2014), A1581–A1608. arXiv: 1303.1377 [hep-lat].

[105] Simon Heybrock et al. “Adaptive algebraic multigrid on SIMD architectures”. In: *PoS* LATTICE2015 (2016), p. 036. arXiv: 1512.04506 [physics.comp-ph].

[106] Daniel Richtmann, Simon Heybrock, and Tilo Wettig. “Multiple right-hand-side setup for the DD-αAMG”. In: *PoS* LATTICE2015 (2016), p. 035. arXiv: 1601.03184 [hep-lat].

[107] Peter Georg, Daniel Richtmann, and Tilo Wettig. “DD-αAMG on QPACE 3”. In: *EPJ Web Conf.* 175 (2018), p. 02007. arXiv: 1710.07041 [hep-lat].

[108] Gunnar S. Bali et al. “Pion distribution amplitude from Euclidean correlation functions: Exploring universality and higher-twist effects”. In: *Phys. Rev.* D98.9 (2018), p. 094507. arXiv: 1807.06671 [hep-lat].

[109] Krzysztof Cichy, Karl Jansen, and Piotr Korcyl. “Non-perturbative renormalization in coordinate space for $N_f = 2$ maximally twisted mass fermions with tree-level Symanzik improved gauge action”. In: *Nucl. Phys.* B865 (2012), pp. 268–290. arXiv: 1207.0628 [hep-lat].

[110] Gunnar S. Bali et al. “Nucleon axial structure from lattice QCD”. In: (2019). arXiv: 1911.13150 [hep-lat].

[111] Matteo Rinaldi. “Double parton correlations in mesons within AdS/QCD soft-wall models: a first comparison with lattice data”. In: (Mar. 2020). arXiv: 2003.09400 [hep-ph].

[112] Thomas Wurm. *private communication.*

[113] C. Alabiso and G. Schierholz. “Asymptotic Behavior of Form-Factors for Two-Body and Three-Body Bound States. 2. Spin 1/2 Constituents”. In: *Phys. Rev. D* 11 (1975), p. 1905.

[114] Stanley J. Brodsky and Glennys R. Farrar. “Scaling Laws at Large Transverse Momentum”. In: *Phys. Rev. Lett.* 31 (1973), pp. 1153–1156.

[115] T. Hahn. “CUBA: A Library for multidimensional numerical integration”. In: *Comput. Phys. Commun.* 168 (2005), pp. 78–95. arXiv: hep-ph/0404043 [hep-ph].

[116] Brian Gough. *GNU Scientific Library Reference Manual - Third Edition.* 3rd. Network Theory Ltd., 2009. ISBN: 0954612078.

[117] F. James and M. Roos. “Minuit: A System for Function Minimization and Analysis of the Parameter Errors and Correlations”. In: *Comput. Phys. Commun.* 10 (1975), pp. 343–367.

Acknowledgments

A successful making of this thesis would not have been possible without support from various sides, which I want to gratefully acknowledge:
First of all, I want to thank my supervisor Andreas Schäfer, who gave me the possibility to work on this very interesting research field for the last six years, starting with my Bachelor's thesis through to my PhD.
Furthermore, I want to thank Markus Diehl, who was my second supervisor, for a multitude of helpful discussions and suggestions regarding the project my thesis is part of, and, furthermore, for useful explanations on theory and phenomenology of (multi) parton interactions.
For fruitful discussions and explanations regarding lattice techniques I want to thank Gunnar Bali. The input I got from him was essential for a successful calculation of the four-point data.
Furthermore, I want to thank Benjamin Gläßle, who gave me very useful hints when implementing the source code being used for the production of the nucleon four-point data. Some parts of the code have been already implemented by him within previous projects and I am very thankful for the possibility to reuse those parts.
I also give thanks to Thomas Wurm for providing the form factor data, which he produced in the context of his work, and which I needed for comparisons with my calculations, see chapter 6.
Moreover, I thank Meinulf Göckeler for providing the renormalization constants required for the calculation of the two-current matrix elements.
For help with the usage of various computational resources I want to thank our system administrators, in particular Peter Georg, with whom I had lots of discussions on writing performant code.
I also want to thank the Deutsche Forschungsgemeinschaft (DFG) for funding the SFB TRR55, from which I profit very much during the last years. Within this context the KNL cluster QPACE 3 has been built, which was used for the production of the data being required for this work.
I thankfully acknowledge the the CLS effort of generating the $n_f = 2 + 1$ gauge ensembles, which have been used in my simulations.
Furthermore, I thank all people of our group and the RQCD collaboration for the nice atmosphere. For this I want to thank, in particular, my fellow graduate students, with whom I spent lots of time during coffee and lunch breaks, swapping ideas on our work and beyond.
Moreover, I thank my friends, who spent a lot of time with me, such that I had a beautiful life outside the university.

Last, but not least, I want to thank my family and especially my parents, who always supported and motivated me during the last decades.